UNIVERSITY OF CALIFORNIA

Santa Barbara

Phase Equilibria and Toughness of ZrO_2-$(Y/Yb)O_{1.5}$-$TaO_{2.5}$ Thermal Barrier Coatings

A Dissertation submitted in partial satisfaction of the requirements for the degree of

Doctor of Philosophy

in

Materials

By

Stefan Gerardo Heinze

Committee in charge:

Professor Carlos G. Levi, Chair

Professor Anton Van der Ven

Professor Matthew R. Begley

Professor Michael J. Gordon

December 2018

The dissertation of Stefan Gerardo Heinze is approved.

Carlos G. Levi, Committee Chair

Anton Van der Ven

Matthew R. Begley

Michael J. Gordon

November 2018

Phase Equilibria and Toughness of ZrO_2-$(Y/Yb)O_{1.5}$-$TaO_{2.5}$ Thermal Barrier Coatings

Copyright © 2018

by

Stefan Gerardo Heinze

ACKNOWLEDGEMENTS

This dissertation marks the end of a six-and-a-half year journey that has encompassed what I consider to be, to date, the best years of my life. I would like to take a moment to thank the many people who have contributed to these amazing years in Santa Barbara.

It is difficult to overstate my gratitude to my Ph.D. advisor, Prof. Carlos Levi, whose constant support, encouragement, and guidance made this work possible. His inquisitive nature and penchant for detailed analysis has transformed me into the scientist I am today. I am especially appreciative that his office door was always open and that he would pause what he was doing to take time to answer my "quick" questions.

I would also like to express my deepest appreciation to the rest of my dissertation committee, Profs. Anton Van der Ven, Matt Begley, and Mike Gordon, whose advice and ideas during numerous discussions provided critical insights into my research. Special thanks goes to Prof. Van der Ven for fostering me in his research group and for supporting my computational work when I knew nothing about first-principles calculations.

A number of previous teachers and professors sculpted the path towards my doctorate long before I could see it coming. In particular, I want to give an enormous thank you to my high school chemistry teacher, Dr. Carol Brown, for informing me about a career she thought I might be interested in, materials science. Her passion for chemistry and ability to relay that passion to her students undoubtedly and profoundly impacted my path in life. I am also grateful to Dr. Peter Loos, Dr. Jay Jacobson, and Dr. Stephen Johnson, among others.

I was extremely lucky to work with incredibly intelligent graduate students, post-doctoral researchers, and lab managers who were always willing to support me in various ways. Jason Van Sluytman, Chandra Macauley, Najeb Abdul Jabbar, Daesung Park, Kaylan

Wessels, David Poerschke, Wesley Jackson, Sarah Miller, Collin Stewart, Colin Hollgate, Mayela Aldaz, Tom Drtina, Rebecca Reitz, Abel Fernandez, Anirudh Raju Natarajan, Pete Maxwell, Deryck Stave, Stephen Kramer, and Mark Cornish were among those who made the day-to-day life of working in a research lab an absolute pleasure. Thank you for always being patient and kind around the office and for listening to my hit-and-miss jokes.

I am blessed to have shared my time in Santa Barbara with lifelong friends, Michael Trogdon, Abel Barragan, Colin Barker, Kate Hake, Surahbi Ram, Simone Beede, Humberto Foronda, Michael Gotrik, Sean Harrington, Brian Evanko, and Mitchell Maier. I want to give a special thank you to Michael Trogdon, who has been my best friend for the past four years and who taught me the importance of introspection. Whenever I think back on this time, I'll always remember Fetty Wap x Documentary mash-ups (bug on a bug), rides down to the kickball field on the bus, nights at Cadiz, camping in Yosemite and Sequoia, beach chilling on the Tommy Bahama's, and hands-down crushing Ladies Slalom.

Finally, I cannot begin to express my thanks to my family, who have provided immense emotional and financial support throughout this journey even though they had no idea what I was doing. Thank you to my dad for instilling in me a great appreciation and enthusiasm for quantitative reasoning, which started by quizzing me daily on the squares of numbers 1-20. Thank you to my mom for always reminding me that there are bigger things in life than work and that true happiness is found with friends and family. Thank you to my brothers for being trailblazers, which has made me unafraid to forge my own path. Lastly, I am extremely grateful for Kelsey Olafson, with whom I've spent the past 7 years of my life over the phone, on FaceTime, at weddings, and for weeklong periods of time throughout different parts of the world. This accomplishment is special because I get to share it with you.

VITA OF STEFAN GERARDO HEINZE

November 2018

EDUCATION

University of California Santa Barbara

- Ph.D. Candidate, Materials Department, 2012-2018

Rice University

- B.S. Materials Science and Engineering, 2008-2012

FELLOWSHIPS

- University of California Chancellor's Fellowship (2012-2018)
- Institute of Energy Efficiency Holbrook Fellowship (2012-2013)

PUBLICATIONS

Heinze, S.G., A. Raju Natarajan, C.G. Levi, A. Van der Ven. "Crystallography and substitution patterns in the ZrO_2-$YTaO_4$ system." *Phys. Rev. Mat.*, 2 073607-1-9 (2018). DOI: 10.1103/PhysRevMaterials.2.073607

Heinze, S.G., J.V. Sluytman, V.K. Tolypgo, C.G. Levi. "Microstructure Evolution and Physical Properties of ZrO_2-$(Y/Yb)O_{1.5}$-$TaO_{2.5}$ Thermal Barrier Coatings." *Surf Coat & Tech.* (2019) In Preparation.

Heinze, S.G., M. Pressacco, C.G. Levi. "Toughness of Multi-Phase Materials in the ZrO_2-$YO_{1.5}$-$TaO_{2.5}$ System." *Journal of the American Ceramic Society.* (2019) In preparation.

Heinze, S.G., D. Park, N. Abdul-Jabbar, C.G. Levi. "Domain Structure of the Non-Transformable Tetragonal Phase in the ZrO_2-$YO_{1.5}$-$TaO_{2.5}$ System ." *Journal of the American Ceramic Society.* (2019) In Preparation.

PRESENTATIONS - INVITED

Heinze, S.G., N. Abdul-Jabbar, D. Park, M. Pressacco, C.G. Levi. "Design and Selection of Materials in the ZrO_2-$REO_{1.5}$-$TaO_{2.5}$ System for Advanced Thermal Barrier Coatings." 2018, *HRL*

PRESENTATIONS - CONTRIBUTED

Heinze, S.G., N. Abdul-Jabbar, D. Park, C.G. Levi. "Toughening Mechanisms in the ZrO_2-$YO_{1.5}$-$TaO_{2.5}$ system." 2017, Pacific Rim Conference on Ceramic and Glass Technology .

Heinze, S.G., A. Raju Natarajan, C.G. Levi, A. Van der Ven. "Effect of Atomic Configuration on Phase Stability and Toughness in the ZrO_2-$YTaO_4$ System." 2016, International Conference on Advanced Ceramics and Composites.

Heinze, S.G., J.V. Sluytman, V.K. Tolypgo, C.G. Levi. "Phase Stable $REO_{1.5}$-$TaO_{2.5}$-ZrO_2 EB-PVD Thermal Barrier Coatings." 2015, International Conference on Metallurgical Coatings and Thin Films.

Sluytman, J.V., S.G. Heinze, C.G. Levi. "EB-PVD TBCs based on the ZrO_2-Yb_2O_3-Ta_2O_5 System." 2015, International Conference on Metallurgical Coatings and Thin Film.

PRESENTATIONS - POSTERS

Heinze, S.G., N. Abdul-Jabbar, D. Park, C.G. Levi. "Toughness and Toughening Mechanisms in the ZrO_2-$YO_{1.5}$-$TaO_{2.5}$ System" 2018, *UCSB Winter Study Group of High Temperature Materials*, Santa Barbara, CA.

Heinze, S.G., N. Abdul-Jabbar, D. Park, C.G. Levi. "Toughening Mechanisms in the ZrO_2-$YO_{1.5}$-$TaO_{2.5}$ Ternary System" 2018, *UCSB Materials Research Outreach Program*, Santa Barbara, CA.

Heinze, S.G., A. Raju Natarajan, C.G. Levi, A. Van der Ven. "Effect of Atomic Configuration on Phase Stability and Ferroelastic Switching in the ZrO_2-$YTaO_4$ System" 2016, *UCSB Winter Study Group of High Temperature Materials*, Santa Barbara, CA.

Heinze, S.G., J.V. Sluytman, V.K. Tolpygo, C.G. Levi. "Phase Stable ZrO_2-$REO_{1.5}$-$TaO_{2.5}$ Thermal Barrier Coatings" 2016, *UCSB Winter Study Group of High Temperature Materials*, Santa Barbara, CA.

ABSTRACT

Phase Stability and Toughness of ZrO_2-$(Y/Yb)O_{1.5}$-$TaO_{2.5}$ Thermal Barrier Coatings

Stefan G. Heinze

Materials based on the non-transformable tetragonal phase in the ZrO_2-$(Y/Yb)O_{1.5}$-$TaO_{2.5}$ systems are of significant interest for next-generation thermal barrier coatings (TBCs) owing to their thermodynamic stability at high temperature, resistance to deleterious phase transformations on thermal cycling, low thermal conductivity, and potentially adequate toughness. The current study investigates fundamental issues pertaining to the implementation of these compositions for TBC applications and associated concerns potentially impacting coating durability. Topics explored include: (i) material processability by electron beam physical vapor deposition (EB-PVD), (ii) TBC microstructure evolution, (iii) relationships between toughness and composition, and (iv) toughening mechanisms, including ferroelastic domain switching.

Key challenges identified in the fabrication of ZrO_2-$(Y/Yb)O_{1.5}$-$TaO_{2.5}$ TBCs by EB-PVD are compositional variability throughout the coating thickness and the development of suboptimal columnar microstructures. The former prevents deposition of single-phase materials and potentially compromises the phase stability of the structure and the latter degrades the strain tolerance of the coating. Despite these complications, compositions in the two-phase *t*-ZrO_2 + *c*-ZrO_2 and three-phase *t*-ZrO_2 + *c*-ZrO_2 + *M'*-$YTaO_4$ phase fields can be deposited by EB-PVD such that the columnar microstructure is adequate and the stability of the tetragonal phase is retained for at least 400 hours at 1250°C and 1500°C.

The toughness of the investigated multi-phase compositions, which is expected to influence the durability of thermal barrier coatings based on these materials, is demonstrated to be significantly dependent on composition and microstructure. The influence of composition arises from the relative fractions of the phases present at equilibrium and the differences between their intrinsic toughness. Minimizing the amount of secondary phases (*c*-ZrO_2 and *M'*-$YTaO_4$), particularly *c*-ZrO_2, is a path to optimize the toughness of the tetragonal-phase material. The role of microstructure is related to the fracture pathway and prevalence of toughening mechanisms such as crack deflection, grain bridging, grain pullout, and microcracking, which had not been previously reported. It is shown for the first time that domains suggestive of ferroelastic switching are contained within non-transformable tetragonal grains. The domains form on growth and/or densification of precursor-derived powder compacts as a result of short-range ordering between Y^{3+} and Ta^{5+} cations, as predicted by first-principle calculations. The ordering patterns in the zirconia solid solution are reminiscent of those predicted and observed for the various forms of the yttrium tantalate. However, direct evidence of ferroelastic switching within the process zone of a crack remains elusive. The results suggest that additional understanding of the relationship between toughness and microstructure is required for the implementation of materials based on the non-transformable tetragonal phase in thermal barrier coatings.

TABLE OF CONTENTS

CHAPTER 1: INTRODUCTION

The demand for increased efficiency in gas turbine engines is motivated by considerable economic and environmental incentives. Energy generated by burning natural gas in turbines currently accounts for 20% of the total energy production in the world today, and that fraction is expected to increase to 25% by 2040 [1]. The gross domestic product associated with this market share is valued at over $1 trillion. The aviation industry utilizes gas turbines to transport 4.3 billion passengers every year, releasing 874 million tonnes of CO_2 into the atmosphere in the process [2]. The annual cost of jet fuel is nearly $150 billion. As a result of the enormous size of these industries, even small increases in efficiency can produce massive cost savings and substantially reduced environmental impact.

The efficiency of modern gas turbine engines is limited in large part by the thermal capabilities of structural components in the hot gas path [3]. Consequently, there is relentless demand to develop new, advanced structural materials capable of withstanding higher gas temperatures. The structure of an airfoil located in the hot section of a modern gas turbine engine is schematically depicted in Figure 1.1. The airfoil consists of a superalloy substrate and a thermal barrier coating (TBC) system. The primary role of the superalloy is to bear load, whereas the primary role of the TBC system is to provide thermal insulation and oxidation protection to the underlying superalloy. The TBC is a multilayered material system consisting of three layers: (i) a ceramic topcoat that provides thermal insulation to an actively cooled substrate, (ii) a thin, thermally grown oxide (TGO) that acts as an oxidation barrier, and (iii) a metallic bond coat that serves as an aluminum reservoir for the TGO and prevents diffusion from the superalloy [4]. Although improvements to both the superalloy

and TBC system can increase the temperature capabilities of the overall component, as shown in the historical data in Figure 1.2, this dissertation will focus only on exploring ways to enhance the performance of the oxide topcoat, referred to as a TBC for the remainder of this thesis.

A thermal barrier coating must exhibit a wide array of properties in order to serve its purpose. These include low thermal conductivity, phase stability for prolonged times at temperature and thermal cycles, processability, and resistance to molten silicates (CMAS) [5]. The current industrial standard, ZrO_2-8±1 mol% $YO_{1.5}$ (8YSZ), which has been used as the material-of-choice for thermal barrier coatings for nearly 40 years, exhibits a suitable balance of the requisite properties [6,7]. However, the exceptional performance of the material relies on a metastable tetragonal phase, *t'*, that is susceptible to deleterious phase decomposition at elevated temperatures [8,9]. The transformation kinetics are known to increase with increasing temperature, such that decomposition becomes an important consideration above ~1200°C [8]. As next-generation turbines are targeting 1300-1500°C, 8YSZ is evidently not a suitable materials option for the topcoat [10].

Next-generation materials for thermal barriers coating would ideally improve upon the already-favorable aspects of 8YSZ, namely its low thermal conductivity and processability, while mitigating its failure mechanisms, such as phase destabilization, spallation due to impact, and molten silicate attack. It has been reported that the ZrO_2-$YO_{1.5}$-$TaO_{2.5}$ system contains a tetragonal phase that exhibits a combination of lower thermal conductivity [11,12], phase stability [13-15], and comparable or higher toughness than 8YSZ [16]. Therefore, the ZrO_2-$YO_{1.5}$-$TaO_{2.5}$ system and other related ZrO_2-$REO_{1.5}$-$TaO_{2.5}$ (RE = rare-earth) systems are candidate materials of interest for next-generation TBCs. However, little

is known about the processability of these materials by conventional methods or about the toughening mechanisms that lead to enhanced toughness. The primary objectives of this dissertation are to explore the processability of ZrO_2-$REO_{1.5}$-$TaO_{2.5}$ (RE = rare-earth) materials by conventional coating methods as well as to investigate the toughness and toughening mechanisms of the tetragonal phase and related materials based on the tetragonal phase.

To address these topics, this dissertation is structured as follows. A review of concepts and relevant literature is presented in Chapter 2. Experimental methods, characterization techniques, and mechanical testing procedures are described in Chapter 3.

Local ordering patterns that affect material behavior in the ZrO_2-$YO_{1.5}$-$TaO_{2.5}$ system is investigated by first-principles methods in Chapter 4.

The amenability of ZrO_2-$YbO_{1.5}$-$TaO_{2.5}$ materials to electron beam physical vapor deposition (EB-PVD) and the microstructure evolution of select ZrO_2-$(Y/Yb)O_{1.5}$-$TaO_{2.5}$ thermal barrier coatings are discussed in Chapter 5 and Chapter 6.

The focus shifts to understanding how compositional inhomogeneity encountered during processing affects the toughness of ZrO_2-$YO_{1.5}$-$TaO_{2.5}$ materials in Chapter 7. The indentation toughness results for the single tetragonal phase motivate a more thorough investigation into ferroelastic switching in the tetragonal phase, discussed in Chapter 8. Transmission electron microscopy is used to examine the grain-level microstructure of the non-transformable tetragonal phase and search for microstructural evidence of ferroelastic switching.

Finally, conclusions and recommendations for future work are given in Chapter 9.

1.1 Figures

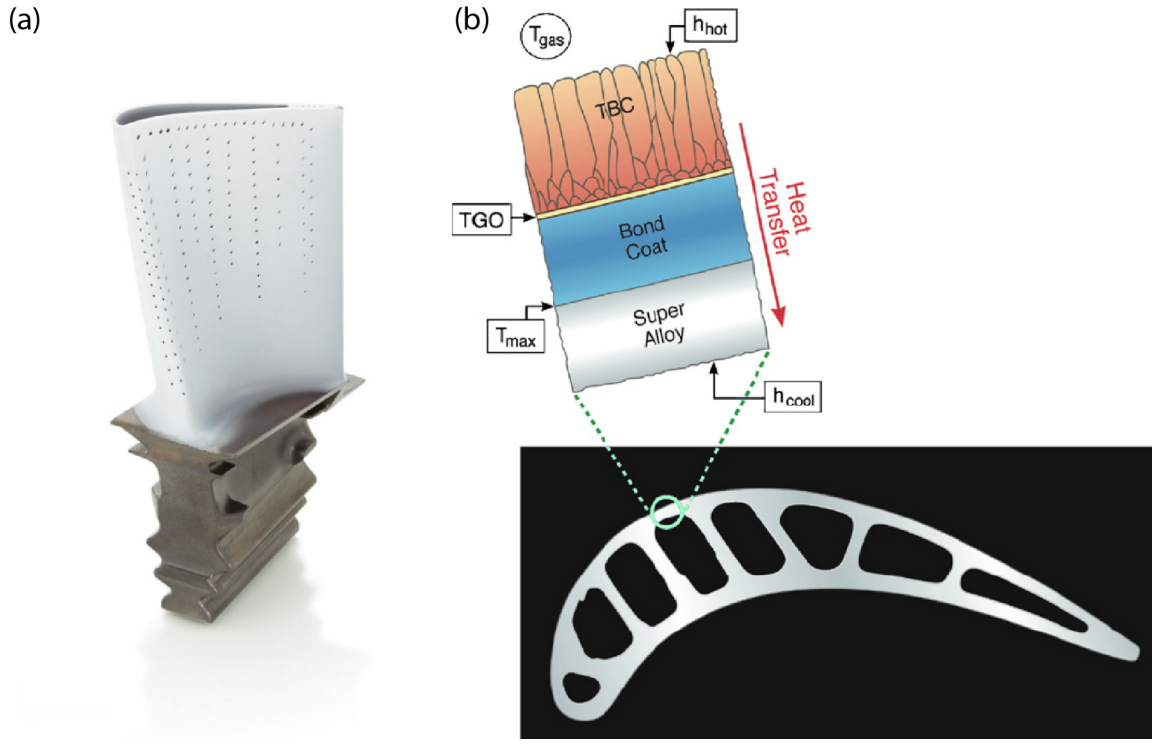

Figure 1.1: An airfoil located in the hot section of a gas turbine engine, (a), is constructed of a superalloy and a thermal barrier system, (b). The thermal barrier system is the bond coat, the thermally grown oxide (TGO), and the oxide topcoat, most commonly referred to as a thermal barrier coating (TBC).

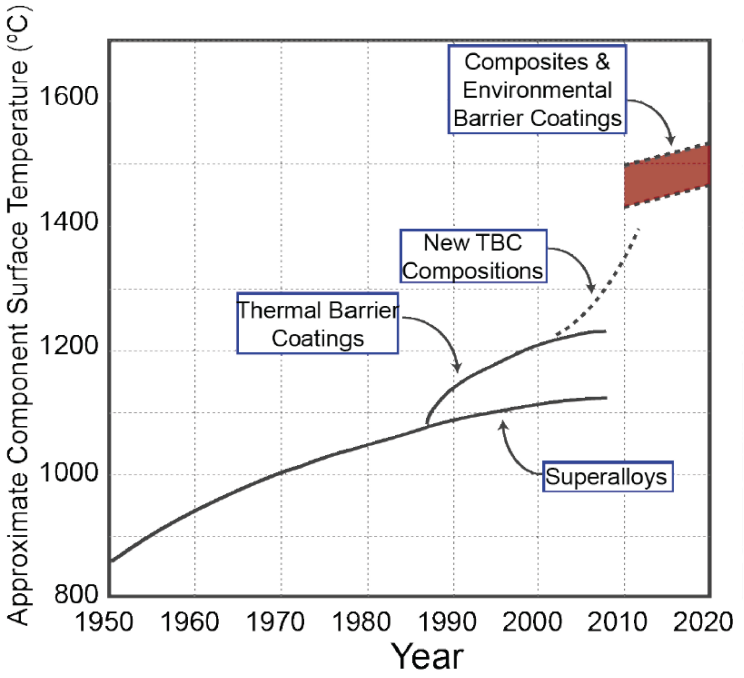

Figure 1.2: Development of advanced structural materials, notably superalloys and thermal barrier coatings, has led to increased component temperatures in the hot section of gas turbine engines. Increases to the gas temperature lead to increases in the engine efficiency.

CHAPTER 2: BACKGROUND

Next-generation materials for advanced thermal barrier coatings (TBCs) must exhibit a lower thermal conductivity at high temperature, superior phase stability, processability, and comparable or higher toughness than the state-of-the-art ZrO_2-8±1 mol% $YO_{1.5}$ (8YSZ). This chapter will review the current understanding of these properties in zirconia-based thermal barrier oxides, highlighting the deficiencies of 8YSZ that motivate the search for alternative TBC materials. A fundamental description of the zirconia crystal structures and crystallographic stabilization mechanisms will be developed in order to explain the impact of various dopants on the aforementioned material properties. The discussion will reveal opportunities for novel thermal barrier oxides in zirconia systems co-doped with trivalent and pentavalent stabilizers, particularly the ZrO_2-$REO_{1.5}$-$TaO_{2.5}$ (RE = rare-earth) systems. Finally, the current knowledge of phase equilibria, toughness, and toughening mechanisms exhibited by these materials will be examined.

2.1 Crystal Structures and Stabilization Mechanisms

Pure ZrO_2 exhibits three polymorphs at ambient pressure. A monoclinic phase (*m*, $P2_1/c$) is thermodynamically stable from absolute zero to 1180°C, at which point a transformation to tetragonal symmetry (*t*, $P4_2/nmc$) takes place. Cubic symmetry (*F*, $Fm\bar{3}m$) is adopted above 2370°C and until melting near 2700°C [17,18]. As will become evident throughout this chapter, only the high temperature tetragonal phase exhibits the desired combination of properties for thermal barrier technology and thus it must be stabilized over the monoclinic and cubic phases in the expected range of operating temperatures. To understand the mechanisms by which stabilization of the tetragonal phase is achieved, it is necessary to

have a detailed understanding of the zirconia crystal structures. The combined knowledge of crystal structures and stabilization mechanisms enables design of novel phase-stable materials with enhanced performance.

2.1.1 Crystal Structures of ZrO_2

Schematic depictions of the ZrO_2 crystal structures are shown in Figure 2.1. The cubic polymorph is a fluorite-type crystal structure with an FCC cation sublattice and oxygen anions filling the tetrahedral interstitial sites. Each zirconium cation is cubically coordinated by oxygen and each oxygen anion is tetrahedrally coordinated by zirconium. The tetragonal and monoclinic phases are close derivatives of the fluorite structure and can be obtained from *F*-ZrO_2 through a combination of lattice strains and internal atomic shuffles, described comprehensively in [19].

The tetragonal phase is generated from the cubic phase by a shuffling of oxygen atoms along a single axis of the cubic structure, seen as arrows overlaid onto the oxygen atoms in Figure 2.1(b). The displacement of the oxygen atoms elongates the structure along the shuffle direction, establishing a c-axis that is slightly larger than the a-axes that define the base. Four Zr-O bonds are elongated (Zr-O_I) and four are shortened (Zr-O_{II}), generating two nested tetrahedra and the tetragonal symmetry. The difference between the Zr-O_I and Zr-O_{II} bond lengths is related to the tetragonality of the unit cell. These shuffles notwithstanding, each atom is commonly regarded as maintaining the same coordination number.

The transformation from *t* to *m* involves a complex motion of both zirconium and oxygen atoms that severely distorts the coordination polyhedra and changes the coordination number of the atoms. The displacements result in a layer-like structure where oxygen anions on

alternating (100)-type planes are coordinated by four and then three zirconium cations while each zirconium cation is coordinated by seven oxygen anions.

The stability of pure *m*-ZrO_2 over *t* and *F*-ZrO_2 at low temperature is typically attributed to the size of the zirconium cation, which is slightly undersized relative to that necessary for eightfold coordination by oxygen according to Pauling's rules of coordination (Zr^{4+} = 0.84Å, O^{2-} = 1.38Å, r^{Zr2+}/r^{O2-} = 0.608, in between criteria for six and eightfold coordination, namely 0.414 and 0.732, respectively) [20]. Hence the oxygen anions are "overcrowded" around the zirconium cations in the cubic polymorph. To reduce the overcrowding and to achieve a more energetically preferred structure, the atoms shuffle and the crystal structure distorts as described in the previous paragraphs. Although the oxygen anions in *t*-ZrO_2 are distorted from their perfect tetrahedral positions in an attempt to relieve the oxygen overcrowding, further relief is achieved in *m*-ZrO_2, where each zirconium achieves its preferred sevenfold coordination.

In order to stabilize the tetragonal and cubic phases to lower temperatures, oxygen overcrowding must be reduced. This is commonly achieved by the introduction of dopant oxides. The dopants can broadly be divided into two categories: (i) those that stabilize the cubic structure and (ii) those that stabilize the tetragonal structure. The preferred oxidation state of the dopant cation and its size relative to the zirconium cation largely determines into which category it falls [21-23].

2.1.2 Oxides of Trivalent Cations

The oxides of trivalent cations, notably Y_2O_3, are the most common dopants used in state-of-the-art thermal barrier coatings. Substituting these materials into zirconia stabilizes the cubic phase primarily by introducing charge-compensating oxygen vacancies into the anion

sublattice [21]. The formation of oxygen vacancies is related to the higher valence of the dopant relative to the host cation according to the mechanism represented by the following Kroger-Vink equation:

$$M_2O_3 \xrightarrow{ZrO_2} 2M'_{Zr} + 3O_O^X + V_O^{\bullet\bullet} \quad (2.1)$$

The vacancies preferentially associate with the Zr^{4+} cations and therefore reduce oxygen overcrowding [21,24]. If the cation is larger than Zr^{4+}, additional stabilization is achieved as a result of the local dilation of the crystal structure surrounding the substitutional dopants. However, empirical evidence suggests that the introduction of anion vacancies is the more potent stabilizer of the cubic symmetry. Figure 2.2 plots the tetragonality of the zirconia unit cell against dopant concentration for a number of different trivalent cations. The observation that the tetragonality of the unit cell is independent of trivalent dopant choice indicates that stabilization of the cubic phase can be achieved at approximately the same dopant concentration regardless of dopant size [25].

2.1.3 Oxides of Tetravalent Cations

Stabilization can be achieved in the absence of anion vacancies by introducing substitutional defects on the cation lattice that disrupt the local crystal structure. This type of behavior is exemplified by the oxides of homovalent (4+) cations, which undergo a substitution process represented by the following Kroger-Vink equation:

$$MO_2 \xrightarrow{ZrO_2} M_{Zr}^X + 2O_O^X \quad (2.2)$$

Figure 2.3, which plots the tetragonality of the zirconia crystal structure against dopant concentration for a number of tetravalent dopant species [26], illustrates that the size of the dopant cation determines whether the cubic or tetragonal phase is stabilized. Tetravalent

cations larger than the Zr^{4+}, typified by Ce^{4+}, stabilize the cubic symmetry. The dopants adopt cubic oxygen coordination and also dilate the local crystal structure, leading to a reduction of oxygen overcrowding for nearby Zr^{4+} cations [22]. The stabilization effect is evidently not as strong as the introduction of oxygen vacancies, since, for example, the concentration of CeO_2 needed to stabilize the cubic phase in the ZrO_2-CeO_2 system is much larger than the amount of $YO_{1.5}$ needed to stabilize the cubic phase in the ZrO_2-$YO_{1.5}$ system, Figure 2.4(a) and (b). Tetravalent cations smaller than Zr^{4+}, typified by Ti^{4+}, instead adopt tetrahedral oxygen coordination and therefore stabilize tetragonal symmetry. A key aspect of this stabilization mechanism is that the host and dopant cations form ordered regions with local structures similar to that displayed in the ordered phases at higher dopant concentrations, e.g. $ZrTiO_4$, which can be seen in the phase diagram in Figure 2.4(c) [22]. The combination of cation ordering and oxygen displacement partially relieves the internal strain of the tetragonal structure that drives the monoclinic distortion but the tetragonal zirconia structure cannot be stabilized to room temperature.

Importantly, the stabilization mechanisms outlined above can be exploited simultaneously by co-doping zirconia with tetravalent cations of varying ionic radii. The prototypical example is co-doping with CeO_2 and TiO_2. By appropriately choosing the amount of each dopant, tetragonal structures with exceptional combinations of stability and tetragonality can be produced in the ZrO_2-CeO_2-TiO_2 system [27].

2.1.4 Charge-compensating Oxides

The oxides of pentavalent cations must be co-substituted in equimolar amounts with the oxides of trivalent cations in order to prevent the formation of cation vacancies that would substantially increase oxygen overcrowding and therefore prevent stabilization of the

tetragonal and cubic phases [28]. The co-substitution process is represented by the following Kroger-Vink equation:

$$M_2O_3 + L_2O_5 \xrightarrow{ZrO_2} 2M'_{Zr} + 2L^{\bullet}_{Zr} + 8^{X}_{O} \quad (2.3)$$

Doping zirconia with these "charge-compensating oxides" stabilizes the tetragonal phase via a mechanism that is hypothesized to involve a combination of oxygen displacements surrounding the substitutional dopants and short-range ordering between the trivalent and pentavalent cations [28]. Although the mechanism is qualitatively similar to that outlined for undersized tetravalent dopants, tetragonal structures containing charge-compensating dopants can be stabilized over the monoclinic structure. For example, regions of the tetragonal phase field in the ZrO_2-$YO_{1.5}$-$TaO_{2.5}$ system are non-transformable to monoclinic zirconia at room temperature [13-15]. Developing thermal barrier coatings based on tetragonal materials in the ZrO_2-$YO_{1.5}$-$TaO_{2.5}$ system and related ZrO_2-$REO_{1.5}$-$TaO_{2.5}$ systems is a focus of this dissertation.

2.2 Considerations for Thermal Barrier Oxides

Although the primary function of a thermal barrier coating is to provide thermal insulation to the underlying metallic component, it must be able to do so under aggressive service environments for prolonged times and repeated thermal cycling. This requires the use of a material system with a remarkable combination of properties beyond just low thermal conductivity. In many applications coatings are expected to survive up to tens of thousands of hours over a range of temperatures up to 1300°C and hundreds of thermal cycles [5]. The imposed thermal profile demands that the TBC exhibit phase stability over the course of the thermal exposure, in-plane compliance to reduce thermal expansion mismatch stresses

between the topcoat and the superalloy substrate under thermal cycling, and adequate toughness to prevent spallation of the coating due to thermomechanical stresses and debris impact. Each of these properties is dependent on the coating microstructure and hence the microstructure imparted during deposition and the amenability of the material to these conventional deposition processes is also important. The following sections present an overview of the design strategy for each of these key properties. Material systems that offer improvements in properties over 8YSZ are highlighted.

2.2.1 Low Thermal Conductivity

Low thermal conductivity is essential to a thermal barrier coating, given that its primary function is to provide thermal insulation. Zirconia exhibits one of the lowest thermal conductivities of any pure oxide, e.g. ~ 8W/m/K for *m*-ZrO_2 versus ~ 30 W/m/K for Al_2O_3 [29-31], and hence serves as a suitable base material for TBCs. Appropriate modifications to topcoat composition and microstructure can reduce the thermal conductivity of the system by more than an order of magnitude [32].

The intrinsic thermal conductivity of a material is approximately given by:

$$k_p = \frac{1}{3} C_V v l \tag{2.4}$$

where C_v is the heat capacity at constant volume, v is the phonon velocity, and l is the phonon mean free path. Although the model ignores the frequency dependence of each term, it provides a framework by which to decrease the conductivity of any material. The most common strategy employs reducing the phonon mean free path via the incorporation of various defects at the atomic and microstructural levels. Relevant point defects include oxygen vacancies and lattice dopants, while microstructural defects include pores, cracks,

and grain boundaries [33-38]. The following sections first consider atomic scale defects and then discuss larger-scale microstructural imperfections.

Oxygen vacancies are extremely effective phonon scatters in virtue of their large mass contrast with the Zr^{4+} cations, the missing interatomic linkages, and the local disorder related to the surrounding bond distortions [39,40]. Such vacancies are typically formed in zirconia via the addition of trivalent stabilizers to the pure oxide, as described by Equation (2.1). Increasing the concentration of oxygen vacancies by increasing the yttria content of the material results in a marked reduction of the thermal conductivity of dense ZrO_2, as seen in Figure 2.5. The thermal conductivity rapidly drops with increasing dopant content and is reduced to ~2 W/m/K (a factor of 4 decrease) for a stabilizer content of 12 mol% $YO_{1.5}$ (11 wt% Y_2O_3). The effectiveness of this approach is in part due to the fact that even modest concentrations of trivalent stabilizers result in a relatively short average vacancy spacing, on the order of the unit cell dimensions, 1-2 nm, creating many scattering centers that yield a very short mean free path for phonons. Although this trend would suggest that materials with high yttria content should be used in TBCs, compositions with high yttria concentrations also have lower durability, as shown in Figure 2.6.

Introducing substitutional defects on the cation lattice can also generate reduced thermal conductivity. It is important that the substitutional cations have a larger mass than Zr^{4+} since the thermal conductivity of a material at high temperature is inversely proportional to the square root of its average atomic mass, as dictated by the following equation:

$$\kappa_{\min} = 0.87 k_b \bar{\Omega}^{-2/3} \left(E / \rho \right)^{1/2} \tag{2.5}$$

where κ_{min} is the minimum achievable thermal conductivity of a material, k_b is the Boltzmann constant, E is Young's modulus, ρ is the density, and Ω is an effective atomic volume that is linearly proportional to the average atomic mass and inversely proportional to the density [4,41]. Therefore, substituting a heavier tetravalent oxide like HfO_2 into ZrO_2 (Hf: 178.49 amu vs. Zr: 91.2 amu) can reduce the intrinsic thermal conductivity of ZrO_2 by 25% or more [42]. Partially substituting $YbO_{1.5}$ (Yb: 173.0 amu) for $YO_{1.5}$ (Y: 88.9 amu) in YSZ compositions can also reduce thermal conductivity by an additional 30% even though the oxygen vacancy concentration remains unchanged [43]. When utilized skillfully, high-mass substitutional defects can reduce thermal conductivity as much as that achieved by using oxygen vacancies. The solid solution tetragonal phase in the ZrO_2-$YO_{1.5}$-$TaO_{2.5}$ system, which lacks oxygen vacancies because it is stabilized by equimolar concentrations of $YO_{1.5}$ and $TaO_{2.5}$, is an excellent example. These materials can exhibit thermal conductivities as low as or lower (ca. 1.5 W/m/k) than 8YSZ due to the large atomic masses of the Ta cation (Ta: 180.9 amu) [11,12]. Substituting small amounts of heavier trivalent cations like Gd^{3+} for Y^{3+} can reduce the thermal conductivity even further [44].

Microstructural defects can further reduce the effective thermal conductivity of the thermal barrier system by up to 45% for electron-beam physical vapor deposited (EB-PVD) coatings and up to 80% for air plasma spray (APS) deposited coatings [45]. This substantial reduction in thermal conductivity is attributed to the substantial volume fraction of pores, cracks, and grain boundaries that are introduced into the structure [32,46]. Figure 2.7 shows micrographs of both EB-PVD and APS coatings and identifies the common types of defects exhibited. The porosity also generally increases the compliance of the coating, decreasing the stored elastic energy upon thermal cycling, but degrades its erosion resistance [47].

In summary, the thermal conductivity of zirconia-based thermal barrier coatings can be reduced by doping with trivalent, tetravalent, and combinations of charge-compensating oxides and by tailoring the fraction, size, and shape of pores and other boundary defects in the microstructure. Although the thermal conductivity of 8YSZ is adequately low, there are opportunities in other compositions to substantially reduce κ, providing a driving force for their implementation as next-generation thermal barrier oxides. However, the reductions in thermal conductivity are often accompanied by trade-offs in other properties, as discussed in the following sections.

2.2.2 Phase Stability

Phase stability is an important attribute of the topcoat material both because of the large temperature range in which the thermal barrier system is meant to operate (ambient to ~1300°C) and the prolonged exposure to high temperature (thousands of hours at T > 1000°C). Phase changes involving significant volume changes (>1%) are particularly deleterious as they can generate severe stresses in the coating that can cause cracking and spallation. The prototypical example is the tetragonal (*t*) to monoclinic (*m*) transformation in zirconia. The transformation from *t* to *m* involves a dilation of about 4% and generates internal stresses several GPa (~3 GPa for linear strain) in magnitude due to the large elastic modulus of zirconia (E ≈ 200 GPa). Doping zirconia with other oxides that stabilize the tetragonal phase relative to the monoclinic phase can eliminate this issue. As previously mentioned, the most common dopants are trivalent oxides like $YO_{1.5}$.

The stabilizing nature of yttria can be seen schematically in the zirconia-rich portion of the ZrO_2-$YO_{1.5}$ phase diagram in Figure 2.8. The T_0(t/m) curve towards the bottom left of the figure represents the temperature at which the Gibbs free energy of the tetragonal phase is

equal to that of the monoclinic phase if the same composition. Above T_0(t/m), the tetragonal phase is stable, and below it, the monoclinic phase is stable against diffusionless transformations. Notably, the T_0(t/m) decreases with increasing yttria content and crosses the ambient temperature isotherm at ~6 mol% $YO_{1.5}$, indicating that any tetragonal composition with > 6 mol% $YO_{1.5}$ would be stable against the monoclinic transformation on cooling to room temperature [18]. However, the maximum solubility of yttria in the tetragonal phase is lower than that required concentration. This means that a thermodynamically stable, non-transformable tetragonal phase does not exist in the YSZ system. To overcome this hurdle, TBCs made from 8YSZ are deposited as a metastable single phase, *t'*, that is supersaturated with yttria. Such microstructures are thermodynamically stable against the transformation to *m* on cooling. However, *t'*-8YSZ is located in a two-phase field between the yttria-lean *t* and yttria-rich *c* phases at high temperature, so that there is a thermodynamic driving force to separate into these equilibrium phases. The kinetics and mechanism by which the *t'* phase decomposes depends on the processing method, i.e. EB-PVD vs. APS [10,48,49], but eventually results in the formation of incoherent globules or grains of equilibrium tetragonal and cubic phases at high temperature, with the tetragonal grains being transformable to the monoclinic phase on cooling. Thus the metastable nature of *t'*-8YSZ places an inherent limit on the temperatures at which it can be used for a specified lifetime, with the achievable lifetime decreasing as the operating temperatures increase due to more rapid partitioning of *t'*, as inferred from Figure 2.9.

To continue pushing engine-operating temperatures higher and improve the overall efficiency of the engine, it is necessary that next-generation thermal barrier coatings be

fabricated from materials that display improved phase stability. Two classes of such materials can be distinguished, namely: (i) those that exhibit a thermodynamically stable tetragonal crystal structure and (ii) those that exhibit a thermodynamically stable cubic crystal structure. The former class is differentiated from 8YSZ by the fact that the tetragonal phase is not only non-transformable to the monoclinic phase at room temperature but also thermodynamically stable against phase separation at elevated temperature. Tetragonal materials that satisfy this phase stability criterion are often referred to as non-transformable tetragonal phases. Several materials systems are known to contain non-transformable tetragonal phases, most notably the ZrO_2-CeO_2-TiO_2 and ZrO_2-$YO_{1.5}$-$TaO_{2.5}$ systems. Although the compositional space where a non-transformable tetragonal structure can be generated is quite large in the ZrO_2-CeO_2-TiO_2 system, the Ce^{4+} cation is susceptible to reduction at elevated temperatures ($T \geq 1420°C$) and the change in valence is accompanied by deleterious modifications to the phase equilibria [50]. The compositional space where a non-transformable phase can be formed in the ZrO_2-$YO_{1.5}$-$TaO_{2.5}$ system is much smaller than in the ZrO_2-CeO_2-TiO_2 system, Figure 2.10, but the tetragonal phase is stable up to at least 1500°C [13,15]. The class of materials exhibiting a phase stable cubic crystal structure encompasses a variety of oxides of diverse compositions, including *F*-ZrO_2 doped with numerous rare-earth oxides, e.g. those lanthanides between Sm and Lu, and combinations thereof [51], as well as compounds in ZrO_2-$REO_{1.5}$ systems. Notable among them are δ-$Zr_3Y_4O_{12}$, a fluorite derivative with ordered oxygen vacancies and partial cation ordering [52], and pyrochlore phases such as $Gd_2Zr_2O_7$ [17] and $La_2Zr_2O_7$ [53].

Identifying which phase stable compositions are appropriate for TBC development requires additional information about how other material properties are influenced by chemistry and

structure. For example, it is important that next-generation thermal barrier oxides retain the remarkable durability of 8YSZ. As will be seen in the next section, the durability of a TBC is linked to the intrinsic toughness of the oxide material, which is itself tied to chemistry and crystal structure.

2.2.3 Toughness

Examination of components removed from aero engines reveals that in many cases the durability of the thermal barrier system is ultimately governed by spallation of the topcoat and hence the toughness of the oxide material is of central importance [6]. Many mechanisms exist by which the integrity of the coating can be compromised. These can generally be divided into two categories as shown in Figure 2.11: extrinsic and intrinsic. Intrinsic mechanisms are those arising from the evolution of the system over time, e.g. by TGO growth, sintering or morphological instabilities in the bond coat. They are generally governed by the thermal strain misfits between the constituent layers of the system under thermal cycling. The residual stresses can drive crack formation and propagation in the form of vertical cracking and delamination throughout the entire thickness of the thermal barrier oxide.

Extrinsic mechanisms are governed by physical or chemical interactions with contaminants in the combustion environment [6]. Prominent examples include damage by particle impact and attack by molten deposits, typically arising from the ingestion of siliceous debris with the intake air. Damage associated with particle impact is generally classified as erosion if it evolves incrementally over multiple cycles, but can also lead to massive loss of coating in a single impact, typically known as FOD (for foreign object damage) which may also include "domestic" particles that come from the upstream engine sections, e.g. a small piece of

combustor TBC that detaches and impacts the airfoils [54]. The latter involves detrimental microstructure changes like densification and kink bank formation [55-57]. The abundance of failure mechanisms and variables that contribute to the magnitude of the residual stresses highlight the complexity of toughness-related issues. The ensuing discussion will focus primarily on the role of the bulk toughness of the topcoat material since it affects the ability of the thermal barrier to resist both delamination and erosion and because characterizing the intrinsic toughness of novel compositions is a primary goal of this dissertation.

The strain energy density expected from thermal strain mismatch between the TBC and underlying superalloy substrate serves as a useful metric of the required TBC toughness to prevent spontaneous delamination. The thermal strain, ε_T, can be approximated by

$$\varepsilon_T = \pm\left(\alpha_{TBC} - \alpha_{sub}\right)\Delta T \tag{2.6}$$

where α_{TBC} is the coefficient of thermal expansion (CTE) of the TBC material, α_{sub} is the CTE of the superalloy substrate, and ΔT is the change in temperature. The difference in CTE between the TBC and superalloy is roughly ±3 ppm/K. The "±" sign indicates that the TBC will be in tension upon heating ("+") and in compression upon cooling ("-"), depending on the originally stress-free state. The resulting residual stress, σ_R, can be estimated by:

$$\sigma_R \approx E_{TBC}\varepsilon_T / \left(1 - \nu_{TBC}\right) \tag{2.7}$$

where E_{TBC} is the in-plane modulus of the TBC and ν_{TBC} is Poisson's ratio for the TBC material. The strain energy density, U_R, can then be predicted by:

$$U_{TBC} = \sigma_R^2 H_{TBC} / 2E_{TBC} \tag{2.8}$$

where H_{TBC} is the thickness of the TBC coating. Assuming a dense YSZ material was used as the topcoat material, $E_{TBC} \approx 200$ GPa and $\nu_{TBC} \approx 0.2$ [6]. For a typical thermal cycle of ΔT

≈ 1100°C and topcoat thickness H_{TBC} ≈ 100-200 μm, σ_R ≈ 0.8 GPa and U_{TBC} ≈ 170-340 J/m^2, an extremely large value given that most ceramics display toughness $G_c \leq 50$ J/m^2. However, as discussed previously, the microstructure imparted by EB-PVD and APS contains a substantial amount of intentional porosity, leading to a substantially reduced in-plane modulus. For typical EB-PVD and APS topcoats, E_{TBC} ≈ 30 GPa [58], instead leading to σ_R ≈ 0.1 GPa and $U_{TBC} \approx$ 25-50 J/m^2 for H_{TBC} = 100-200 μm. In essence, the topcoat must have a minimum toughness G_{TBC} ≈ 25-50 J/m^2 to resist propagation of delamination cracks. This calculation neglects the thermal expansion of the other constituent layers and the stress experienced during thermal transients but more sophisticated methods that take this to account have been developed and suggest that it is of the correct order [59].

The reported range of intrinsic toughness in the YSZ system is shown in Figure 2.12 and spans $1 \leq G_C \leq 300$ J/m^2. The toughness is generally dependent both on composition and microstructure. The highest toughness values, $40 \leq G_c \leq 200$ J/m^2, are displayed by materials containing tetragonal phase, e.g. tetragonal zirconia polycrystals (TZP) and EB-PVD *t'*-8YSZ, while the lowest values, $G_C \leq 10$ J/m^2, are displayed by materials containing only cubic phases, e.g. all compositions within the cubic phase field, including the only compound in the system, δ-$Zr_3Y_4O_{12}$. The largest toughness values are ascribed to tetragonal materials that experience transformation toughening, e.g. tetragonal zirconia polycrystals (TZP), wherein metastable tetragonal crystallites transform to the monoclinic form under the stress field of an approaching crack. The transformation results in compressive stresses in the process zone, which reduces the effective driving force on the crack tip [60-62]. This mechanism is not suitable for TBC applications because (i) the transformation is thermodynamically forbidden above the T_0(t/m) line in Figure 2.8, which includes most of

the relevant range for engine operation, and (ii) the transformation at lower temperatures leads to repeated microcracking in the coating upon thermal cycling. The next largest values are ascribed to tetragonal materials that experience ferroelastic switching, e.g. *t'*-8YSZ, a process whereby the tetragonal domains are reoriented due to the stress field of a nearby crack, Figure 2.13, placing a compressive residual stress on the crack tip. The toughness of these materials are substantially lower than those susceptible to transformation toughening, typically displaying values of order ~40 J/m^2 [27], but the toughening mechanism is operative in a large range of temperatures and in principle should not cause internal cracking because there is no volume change involved. Materials displaying a cubic (fluorite) structure, e.g. *F*-ZrO2, exhibit the lowest toughness, G ≈ 1-10 J/m^2. These low values are ascribed to a lack of intrinsic toughening mechanisms beyond those expected in all polycrystalline materials, e.g. surface energy generated by the two new crack surfaces and some contribution from crack tortuosity due to preferred cleavage planes. In principle, this extends to all cubic materials, including all rare-earth fluorites and zirconates [63].

Based on the above discussion, materials with adequate intrinsic toughness for TBC applications are limited to tetragonal materials that experience ferroelastic switching. However, in practice, even materials with low intrinsic toughness can be used in thermal barrier coatings, e.g. (cubic) pyrochlore $Gd_2Zr_2O_7$ [64,65], although those with higher intrinsic toughness are still preferred. This is because the effective toughness of the topcoat can be increased by an order of magnitude via larger-scale microstructure-related toughening mechanisms like crack bridging and pullout in segmented structures [66]. As a result, proper design of the coating microstructure plays a key role in the durability of the thermal barrier system. The next section describes the critical features of EB-PVD and APS

microstructures that enable TBCs to achieve higher effective toughness, low thermal conductivity, and high strain tolerance.

2.2.4 Amenability to Conventional Coating Processes

Thermal barrier coatings are commercially produced by two main processes: electron beam physical vapor deposition (EB-PVD) and air plasma spray (APS). Both techniques generate microstructures that are enabling to the strain tolerance and thermal resistivity of the topcoat, as shown by the examples in Figure 2.7, and so it is crucial that any candidate thermal barrier oxide be amenable to be deposited by these processes.

EB-PVD coatings are distinguished by columnar grain morphologies where single crystalline grains span the entire thickness of the topcoat [67]. The columns are produced when vapor having the desired composition condensates onto a rotating substrate. The growth of voided regions that separate the columns, termed intercolumnar porosity or intercolumnar gaps, is concomitant with the growth of the columns themselves [68]. Typical coating thicknesses range from 100-300 μm, with lateral column dimensions below 1 μm at the base and ~10 μm at the surface; the average columnar gap widths are typically ≤1 μm. The intercolumnar porosity provides EB-PVD TBCs with a low in-plane modulus that affords the coatings their excellent strain tolerance [69]. Due to the parallel orientation of the columnar gaps relative to the thermal gradient, these features do not contribute significantly to the thermal resistivity, but additional fine-scale porosity that is contained within the columns themselves, termed intracolumnar of "feathery" porosity, lowers the effective thermal conductivity of the coating significantly, cf. Figure 2.7(c). Measured thermal conductivities are as low as 1.0 W/m/K but are more typically in the range of 1.3-1.8 W/m/K [45].

In contrast, APS coatings are distinguished by as assemblage of "splats" produced when molten droplets impact a substrate and solidify on top of one another [45]. The "splats" are separated by a combination of microcracks that form due to the stresses arising from the constrained volume change during solidification, as well as intersplat porosity that arises from poor bonding during deposition. Typical coatings thicknesses are in the range of ~200 μm to over 1 mm. Similar to EB-PVD, the microcracks and porosity are instrumental in achieving the desired in-plane compliance and thermal resistivity of the thermal barrier coating. However, unlike in the case of EB-PVD materials, the porosity and splat microcracks tend to be oriented perpendicularly to the thermal gradients, which very effectively reduces the thermal conductivity of the coating. Typical achievable thermal conductivities for APS 7-8YSZ are in the range of 0.8-1.0 W/m/K [45], generally lower than EB-PVD.

In general, EB-PVD coatings substantially outperform APS coatings in terms of durability, as measured in cyclic burner rig testing [70,71]. There are several reasons for this difference. Firstly, strain compliance garnered from standard APS microstructures is not as large as that garnered from standard PVD microstructures [45]. To this end, a variant of the APS structure has been developed where vertical segmentation cracks are periodically generated along the in-plane dimensions of the coating [45]. These "dense vertically cracked" (DVC) microstructures aim to mimic the vertical segmentation of EB-PVD coatings and exhibit significantly improved thermal cycling life compared to the standard APS structure, albeit at the expense of higher thermal conductivity. Secondly, the effective toughness of the coatings may be different. It has been observed that the steady-state toughness of dense vertically cracked APS structures can be larger than the bulk value of conventional APS

YSZ by higher than a factor of five [66]. As the cracks propagate through the microstructure they are deflected by pre-existing flaws, namely the vertical cracks, creating large-scale columnar pullout that toughens the topcoat via crack bridging and frictional dissipation. Although it is hypothesized that such a mechanism could exist for the columnar EB-PVD structures, it has not been experimentally confirmed in the literature.

2.2.5 Motivation for Novel TBC Compositions in the ZrO_2-$REO_{1.5}$-$TaO_{2.5}$ Systems

8YSZ has been the state-of-the-art thermal barrier oxide because of its low thermal conductivity, its ability to be deposited via conventional techniques as a single, metastable tetragonal phase that does not undergo phase transformations upon (limited) thermal cycling, and its superior durability, imparted by a combination of high intrinsic toughness and microstructure-related toughening mechanisms. The superior durability of 8YSZ is especially important as many other compositions exhibit low thermal conductivity and phase stability but have low intrinsic toughness and are not used in TBCs. Nevertheless, the decomposition of the metastable tetragonal phase *t'* places an inherent limit on the temperatures and time at temperature that 8YSZ can be utilized. Preliminary studies suggest that non-transformable tetragonal materials in the ZrO_2-$YO_{1.5}$-$TaO_{2.5}$ system are phase stable to temperatures exceeding 1500°C and also exhibit lower thermal conductivity (ca 1.5 W/m/K [11,12] than 8YSZ. Therefore, these materials offer significant promise in the development of next generation thermal barrier coatings. The subsequent sections of this chapter focus on exploring what is known about the phase equilibria, deposition, and toughness of ZrO_2-$YO_{1.5}$-$TaO_{2.5}$ and related ZrO_2-$REO_{1.5}$-$TaO_{2.5}$ materials.

2.3 Phase Equilibria in the ZrO_2-$YO_{1.5}$-$TaO_{2.5}$ System

Predicting the microstructure and property evolution of a thermal barrier oxide requires a fundamental understanding of phase equilibria. As most of this dissertation focuses on materials in the ZrO_2-$YO_{1.5}$-$TaO_{2.5}$ and ZrO_2-$REO_{1.5}$-$TaO_{2.5}$ systems, attention will be directed towards understanding phase equilibria in these systems. Isothermal slices of the ZrO_2-$YO_{1.5}$-$TaO_{2.5}$ system at 1500°C and 1250°C are shown in Figure 2.14 [14,15]. The ternary equilibria and quaternary equilibria with other rare-earth sesquioxides are expected to be qualitatively similar but with different solubilities depending on the size of the rare-earth cation [72]. There are no ternary phases at either temperature but all of the terminal oxides and most of the binary phases exhibit some solubility of the other oxides into the ternary diagram. The most notable feature of the diagrams is the equilibrium between the *t*-ZrO_2 phase and the $YTaO_4$ phases that divides the diagram in half.

There are several important features of the tetragonal zirconia phase field. The solid solution penetrates deeply into the ternary at both 1250°C and 1500°C, with a maximum reported solubility of ~$18.5YO_{1.5}$-$18.5TaO_{2.5}$ at 1500°C [14,15]. The solubility recedes asymmetrically at 1250°C so that the equilibrium composition at the tip varies between ~$15.4YO_{1.5}$-$14.9TaO_{2.5}$ and ~$12.5YO_{1.5}$-$12.6TaO_{2.5}$. The narrow shape of the tetragonal phase field reflects the stabilization of *t*-ZrO_2 by charge-compensating cations that must be added in a near 1:1 molar ratio. Any significant amount of excess yttria or tantala (>1 mol%) is not tolerated in the solid solution and causes the formation of multiphase mixtures with the *F*-ZrO_2 or *O*-$Zr_6Ta_2O_7$ solid solutions.

The asymmetric recession of the solubility limit at 1250°C has important implications on the transformability of materials in and around the tip of the tetragonal phase field. The

transformability of the tetragonal phase is dictated by the $C_0(t/m)$ line on the diagram, which is the locus of all compositions that have equal Gibbs free energy in the tetragonal and monoclinic phases at room temperature.[1] Tetragonal compositions closer to the ZrO_2 corner than compositions on the *$C_0(t/m)$* curve are transformable and those that are further are stable. The $C_0(t/m)$ line crosses the yttria-rich portion of the tetragonal phase field at around 26% total dopant concentration (i.e. mol% $YO_{1.5}$ + mol% $TaO_{2.5}$) [13,14,16] and beneath 25% total dopant concentration in the tantala-rich portion [14]. At 1500°C, a moderately sized part of the tetragonal phase field is non-transformable on cooling. The non-transformable region spans a range of ~5 mol% $YTaO_4$ and the solid solution can accommodate slight amounts of excess yttria or tantala. At the more realistic engine operating temperature of 1250°C, the reduced solubility of the tetragonal phase and the asymmetry of the phase field results in a much smaller part of the tetragonal phase field being non-transformable. Specifically, only the leftmost edge of the tip and some portion of the tip in the *t + M'* two-phase field is stable against the monoclinic transformation. Thus the equilibrium tetragonal phases in the two-phase *t+O* and three-phase *t+O+M'* are susceptible to transforming to *m* on cooling. Conversely, the equilibrium tetragonal phases in the three-phase *t+F+M'* field and in part of the two-phase *t+F* field are stable. The regions that exhibit a stable tetragonal phase are marked by a speckled pattern in the phase diagrams of Figure 2.14.

[1] Or the lowest temperature at which the tetragonalto monoclinic transformation is kinetically feasible. The transformation is nominally martensitic but it is thermally activated [61] J.

2.3.1 Relevance to Novel TBCs in the ZrO_2-$REO_{1.5}$-$TaO_{2.5}$ Systems

A key driving force for the development of ZrO_2-$REO_{1.5}$-$TaO_{2.5}$ thermal barrier coatings is the existence of a thermodynamically stable, non-transformable tetragonal phase in these systems. However, the compositional space where the tetragonal phase is stable and non-transformable at realistic engine operating temperatures, ca. 1250°C, is quite small for RE = Y^{3+} or Yb^{3+} [14,72]. As a result, tight compositional control during processing is required to make thermal barrier coatings from these materials. Previous research has shown that thermal barrier coatings made from ZrO_2-$YbO_{1.5}$-$TaO_{2.5}$ materials exhibit a significant degree of compositional fluctuation throughout their thickness, as demonstrated in Figure 2.15. The deviations in chemistry can be severe enough to cause local areas within the coating to fall into regions of the phase diagram where a transformable tetragonal phase is expected at equilibrium, which could impact the durability of the coating. However, it is not clear if or how the compositional fluctuations change with choice of composition, including total rare-earth content and rare-earth choice. It is also not known how these compositional fluctuations impact coating microstructure evolution. Further research into these concepts is needed in order to identify the appropriate design space for TBCs in the ZrO_2-$REO_{1.5}$-$TaO_{2.5}$ systems.

2.4 Toughness and Toughening Mechanisms

Thermal barrier coatings must be able to withstand the thermomechanical stresses generated during engine operation. The stresses produce a wide variety of fracture-type failure mechanisms described previously. Resistance to these modes of failure, and hence enhanced durability of the thermal barrier system, is linked to the toughness of the TBC [6]. Therefore, thermal barrier oxides with comparable or enhanced toughness relative to 7-

8YSZ are desired. The intrinsic toughness of TBCs can be improved through the use of controlled structural transformations that activate during fracture and consume energy and/or place a compressive stress on the crack tip [73]. Ferroelastic switching is one such mechanism and it is responsible for the elevated toughness of tetragonal thermal barrier oxides like *t'*-8YSZ [74]. Various factors influence the amount of toughening provided by ferroelastic switching, including thermal barrier oxide chemistry, microstructure at several length scales, and interactions between the microstructure and crack. This section reviews the current understanding of ferroelastic toughening in tetragonal TBC materials, highlighting the effects of chemistry and microstructure. Techniques to characterize ferroelastic switching and determine toughness are also discussed.

2.4.1 Ferroelastic Switching Fundamentals

Pure tetragonal zirconia may exist in three energetically equivalent orientation states relative to a reference (or parent) cubic structure, one for each orthonormal direction of the c-axis, Figure 2.16. The three orientation states are often referred to as variants. Application of a non-hydrostatic stress breaks the energetic equivalence of the orientation states such that at least one of the variants becomes energetically stabilized. Ferroelastic switching occurs when a sufficiently large stress causes tetragonal domains of one orientation to change to a more energetically favored orientation [19]. If the stress is associated with a nearby crack, the change in orientation places a compressive stress on the crack tip, hindering further crack propagation [73] (Figure 2.10). The net result is that a larger global stress is required to advance the crack and hence the material is toughened. The increase in toughness is proposed to follow the following relationship:

$$\Delta\Gamma_{ss} = 2hf\tau_T\gamma_T \tag{2.9}$$

where h is the process zone size, f is the fraction of switched domains, τ_T is the coercive stress required to initiate the transformation, and γ_T is the transformation strain [73]. The approach towards designing thermal barrier oxides with improved toughness involves understanding how each of these variables depends on tetragonality. The simplest relationship is between the transformation strain and tetragonality. Switching a single domain produces a strain equal to (c/a - 1) along the direction of the new c-axis. Therefore, much work over the past decade has focused on generating tetragonal structures with large tetragonality [16,75]. However, the observed toughness is often much lower than that predicted considering the transformation strain alone. It has been proposed the coercive stress also depends on tetragonality but the relationship remains unclear [16,27,75]. Non-linear increases in toughness have been reported with increasing tetragonality in the ZrO_2-$YO_{1.5}$-TiO_2 system [75] and non-linear decreases in toughness have been reported with increasing tetragonality in the ZrO_2-$YO_{1.5}$-$TaO_{2.5}$ system [13,16], suggesting that the scaling may be material-specific. Thus it is not known whether tetragonal structures with increasing or decreasing tetragonality should be pursued.

2.4.2 Microstructure Effects

The grain-level microstructure of thermal barrier oxides plays a critical role in determining the mechanism by which ferroelastic toughening may occur, which in turn affects the amount of toughening generated. Two types of microstructure are distinguished (Figure 2.17). In the first, each "grain" is composed of fine-scale domains of the three possible tetragonal variants and toughening occurs by the motion of the domain boundaries. New domains are not created; rather, domains of a particular variant grow at the expense of the others. In the second, each grain is itself a single tetragonal domain and new, fine-scale

domains having the favored orientation must first be formed for ferroelastic domain switching to be feasible. The new domains can subsequently grow by motion of their boundaries. The stress needed to create domains is expected to be larger than that to propagate domain boundaries [76]. A concomitant reduction in toughening is expected since the process zone width, h, scales as the $1/\tau_c^2$ [73].

Ferroelastic switching is most commonly observed in materials where each grain is composed of fine-scale tetragonal domains. The domains are generated by rapidly cooling a high-temperature cubic phase below the $T_0(c/t)$ line, inducing the displacive $c \rightarrow t$ transformation. The latter yields a microstructure where roughly equal proportions of the three possible tetragonal variants are contained within each grain, Figure 2.18. The size of the domains is sensitive to the composition and quench rate [74,77,78]. The domains are twin related, exhibiting 90° $(101)_t$ and $(011)_t$ twin boundaries, and the size of the domains are on the order of one to several microns in length and several hundred nanometers in width. Reported toughness values span a large range, 100-700 J/m^2 [74,79]. The critical stress necessary to move the twin boundaries is reported to be ~600-700 MPa at 500°C and is weakly sensitive to temperature, decreasing ~300 MPa at 1400°C [78].

Ferroelastic switching has also been reported in materials that do not have fine-scale domains within each grain. This class of materials is relevant to thermal barrier coatings since most TBC microstructures exhibit large, single-crystal grains without small domains. Examples include *t'*-8YSZ deposited by EB-PVD [76] and most tetragonal compositions created from precursors [16,27,75,80]. Reported toughness values in polycrystalline samples are in the range of 40-80 J/m^2, suggesting that the toughening generated by domain formation is substantially lower than that by domain boundary motion [16,27,75].

2.4.3 Chemistry Effects

Ferroelastic switching has been reported in several different zirconia-based systems, including ZrO_2-$YO_{1.5}$ [27], ZrO_2-$YO_{1.5}$-TiO_2 [75], ZrO_2-CeO_2-TiO_2 [27,80], and ZrO_2-$YO_{1.5}$-$TaO_{2.5}$ [16]. The role of chemistry on the toughness generated by ferroelastic switching is typically understood in relation to its effect on the tetragonality of zirconia structure, with larger tetragonalities expected to increase toughness due to the enhanced transformation strain. However, as previously noted, increases in tetragonality are not always accompanied by increases in toughness. It is hypothesized that this is a consequence of the relationship between chemistry and coercive stress. The effect of chemistry on coercive stress is best understood from a crystal structure perspective. Ferroelastic switching requires each ion to move to a new location in order to facilitate reorientation of the crystal structure. The coercive stress is related to the energy barrier for these atomic shuffles to occur. The most important shuffles are those of the oxygen anions since they provide the primary resistance for reorientation in *t*-ZrO_2 [19]. Dopant atoms in zirconia alter the local positions of the oxygen anions in the crystal structure and hence they modify the transformation pathway and the corresponding energy barrier. Doping *t*-ZrO_2 with $YO_{1.5}$ decreases the energy barrier substantially whereas doping with TiO_2 increases the barrier substantially [81]. Therefore it is expected that YSZ will have a lower coercive stress than TiSZ. It is possible that the coercive stress can become so large than ferroelastic switching occurs by a different mechanism entirely, requiring diffusive rearrangement of the cations to generate stable atomic configurations in the new orientation of the crystal structure.

2.4.4 Multi-phase Structures

The presence of brittle secondary phases in materials containing *t*-ZrO_2 can significantly influence the amount of toughening generated by ferroelastic switching. The effect is a result of interactions between the microstructure and crack that alters the crack propagation pathways. For example, two-phase (*t* + *F)*- CeTiSZ materials containing a large majority of *t*-ZrO_2 phase exhibit toughness close to that of the brittle *F*-ZrO_2 phase, ~10 J/m^2, rather than that of the tough *t*-ZrO_2 phase. In this material, the crack propagates almost entirely through the brittle *F*-ZrO_2 grains despite the fluorite phase being a minor constituent [27]. The inference is that the ferroelastic switching mechanism is never activated because the crack does not cut through the tetragonal grains, which could reduce the elastic stress they experience. By a similar reasoning, toughening could also be reduced if cracking occurs intergranularly rather than transgranularly. A fundamental understanding of the effect of multiphase structures on ferroelastic switching has not been developed.

2.4.5 Characterization

Several characterization techniques are used to determine whether or not ferroelastic switching is an active mechanism in a thermal barrier oxide. The methods analyze samples before and after fracture experiments or compare results from bulk material to data nearby a fracture location. X-ray diffraction is a commonly utilized technique. In this approach, the relative intensities of the 200/002 or 400/004 diffraction peaks before and after mechanical testing are compared [66,74,82]. The peak intensities are linked to the proportion of each tetragonal variant so that the relative intensities change if switching has taken place. The method has been used to demonstrate switching in materials with pre-existent tetragonal variants under grinding stresses [74], uniaxial compression [77,82], and nearby indentation

cracks [77,82] and in materials without pre-existent tetragonal domains after fracture experiments [66].

Raman spectroscopy is another commonly utilized technique. Raman spectroscopy is sensitive to anion displacements in the ZrO_2 crystal structures and therefore can distinguish between out-of-plane and in-plane *t*-ZrO_2 variants with respect to the sample surface [80,83]. To determine if ferroelastic switching has occurred, the relative intensity of the A_{1g} and B_{1g} peaks (located at ~250 and 300 cm^{-1}, Raman shift) is analyzed as a function of distance from the crack. The intensity of the B_{1g} peak is associated with the perpendicularity of the c-axis to the sample surface so that B_{1g}/A_{1g} decreases as the fraction of domains in the plane of the sample surface increases [80]. Given that the process zone can be quite small (<5μm), the volume sampled by the Raman laser relative should be minimized to clearly identify changes in the peak intensity with distance [76].

The most common technique to investigate the microstructural changes occurring during ferroelastic switching is TEM examination, particularly by selected area electron diffraction (SAED) and dark field (DF) imaging. To determine the number of variants within a specific area of the microstructure, SAED patterns along the [111] zone axis are collected. In pure ZrO_2 and YSZ, each tetragonal variant produces one symmetrically unique (211)-type reflection in the [111] zone axis and thus the number of (211)-type reflections corresponds directly with the number of variants, Figure 2.19. Ferroelastic switching is demonstrated by showing that the number or intensity of (211)-type reflections is different before and after a mechanical test or near and far from a fracture site. Using this method, domain boundary motion has been reported in polydomain tetragonal YSZ subjected to uniaxial compression

[77] and domain formation has been reported in EB-PVD *t'*-8YSZ [76] and *t*-CeTiSZ [27] compacts made from precursor-derived powders.

A less commonly employed technique to study ferroelastic behavior is simple uniaxial tension and compression mechanical tests [78]. The stress-strain curves obtained by such tests are highly desired because they give insight into the coercive stress and the amount of switching that takes place. Unfortunately, these tests require material derived from a single fluorite crystal so all the domains present are orthogonal to each other and coherent. For some microstructures, such as those where each grain is composed of small tetragonal domains, obtaining a large single crystal is difficult but feasible; in others, such as those typical of TBCs, obtaining a large single crystal has not been possible.

2.4.6 Methods to Determine Toughness

One obstacle in clearly assessing the effects of chemistry and microstructure on ferroelastic switching is obtaining accurate, statistically relevant toughness measurements. The most common technique to determine the toughness of thermal barrier oxides is microindentation. The predominant method involves using a Vickers indenter to generate radial cracks on the surface of a material. The equilibrium crack lengths, the residual indentation size, and the applied load are used to calculate the toughness through the semi-empirical formula:

$$\Gamma = K_C^2 / E = 2\zeta^2 P\left(d^2 / c^3\right) \tag{2.10}$$

where P is the applied load, d is the size of the residual indent, c is the length of the cracks, and ζ is a dimensionless constant that depends on the indenter geometry and nature of the deformation [84]. The technique is attractive because of its expediency, the small volume of material required (many measurements are possible), and the relatively short sample

preparation time, but there are several caveats about its accuracy and applicability that often go overlooked. The coefficient ζ, which was determined experimentally in [85], is only applicable to materials that exhibit ideal deformation response and crack geometry, namely small grained (<1 μm), dense, non-transforming, isotropic ceramics free of residual stress and with a Young's modulus to hardness ratio (E/H) of 10-20. Furthermore, deformation underneath the indenter must be volume conserving, cracking must only occur on the corners of the indent, the length of the cracks must be large relative to the indentation size ($c < 2d$), the cracks must assume a half penny-like geometry normal to the surface, and no lateral cracking must occur. Any departure from these criteria can lead to significant error in the toughness predicted by indentation. For example, a difference by factor of two between the toughness predicted by indentation and that predicted by other standard methods has been observed for glasses undergoing non-volume conserving deformation [86]. Even when all the requirements of indentation toughness are met, the predicted toughness is only accurate to about 30-40%. However, comparative measurements within a single material class are expected to be fairly accurate relative to one another [85]. Therefore indentation toughness testing is meant to be an exploratory tool to rank the relative toughness of materials within the same material class and not as a quantitative predictor of absolute toughness.

2.4.7 Relevance to Novel TBCs in the ZrO_2-$REO_{1.5}$-$TaO_{2.5}$ Systems

Ferroelastic toughening is the currently accepted mechanism for the enhanced toughness and therefore enhanced durability of tetragonal-based thermal barrier coatings. Non-transformable tetragonal materials in the ZrO_2-$YO_{1.5}$-$TaO_{2.5}$ system exhibit indentation toughness similar to or greater than *t'*-8YSZ (ca. 39-53 J/m^2), suggesting that TBCs made

from these materials could also exhibit adequate or improved durability [13,16]. The high indentation toughness exhibited by these materials has been used to infer ferroelastic behavior but microstructural evidence of ferroelastic switching is lacking. Additionally, when taking into consideration the accuracy of the indentation toughness method and the fact that the toughness measurements exhibited standard deviations larger than 25% of the mean toughness value, it becomes clear that additional investigations of the toughness of tetragonal materials in the ZrO_2-$YO_{1.5}$-$TaO_{2.5}$ system are required [16].

2.5 Summary and Scope

The extremely aggressive thermochemical and thermomechanical environment encountered in commercial gas turbines requires that thermal barrier coating materials exhibit many properties, including low thermal conductivity, phase stability, toughness, and amenability to conventional processing techniques. Materials in the ZrO_2-$YO_{1.5}$-$TaO_{2.5}$ system have been reported to exhibit lower thermal conductivity, improved phase stability, and similar or better toughness than 8YSZ, providing a driving force for their implementation into TBCs. This dissertation focuses on understanding the behavior of materials in the ZrO_2-$REO_{1.5}$-$TaO_{2.5}$ system and the application of this understanding to assess their potential for utilization in next-generation thermal barrier coatings. In particular, the research concentrates on assessing and understanding phase stability, toughness, and amenability to conventional coating processes for materials in and around the tip of the tetragonal phase field. The dissertation examines the connections between substitution patterns, stabilization mechanisms, and toughness in single-phase tetragonal materials, explores the deposition and subsequent microstructure evolution of ZrO_2-$REO_{1.5}$-$TaO_{2.5}$ thermal barrier coatings

fabricated by EB-PVD, and investigates the toughness and toughening mechanisms of single and multi-phase materials.

2.6 Figures

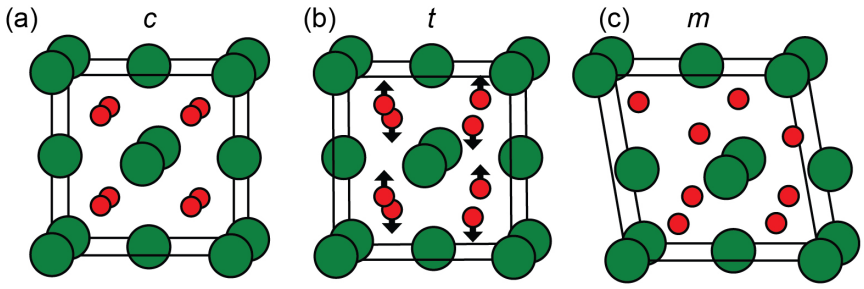

Figure 2.3: Schematic depictions of the ZrO_2 crystal structures. A combination of internal oxygen shuffles and strains can be applied to the high symmetry (a) cubic polymorph to produce the (b) tetragonal and (c) monoclinic polymorphs.

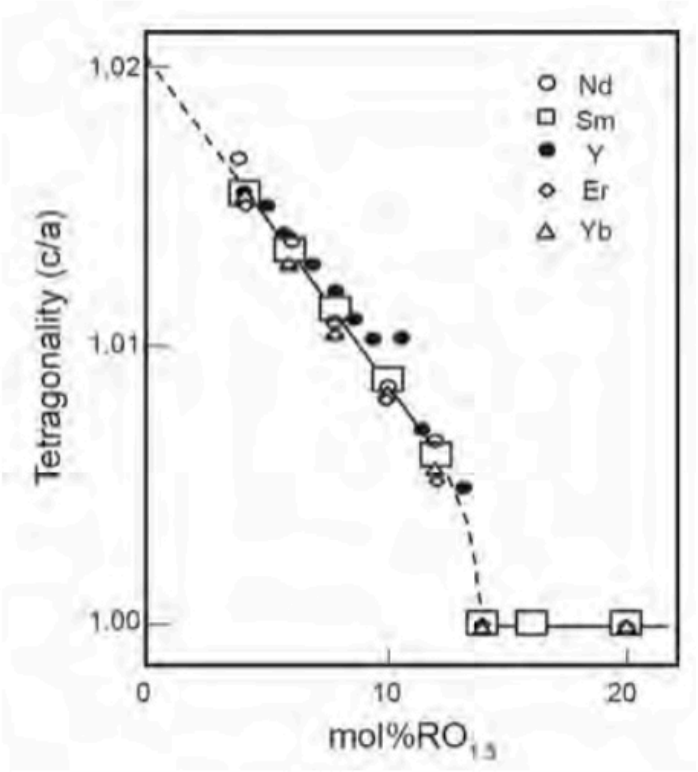

Figure 2.2: Tetragonality as a function of trivalent dopant content [25].

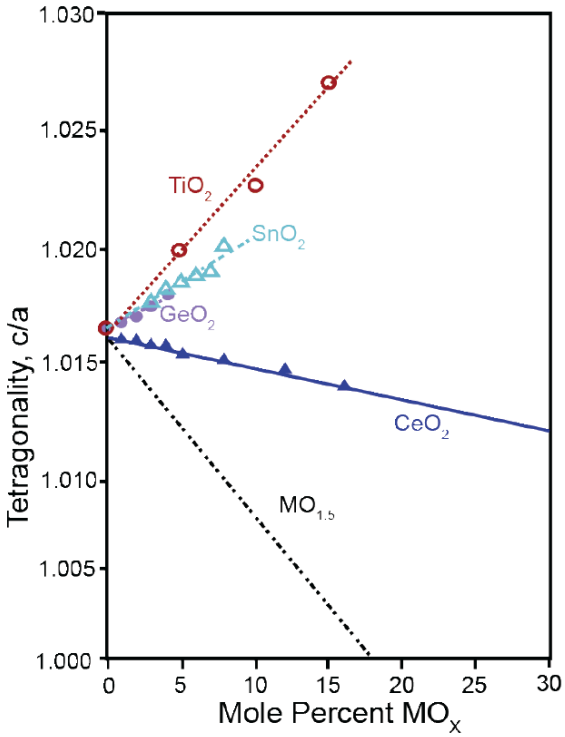

Figure 2.3: Tetragonality as a function of tetravalent dopant content. Oversized tetravalent cations like Ce^{4+} stabilize the cubic phase and therefore the tetragonality decreases with increasing Ce^{4+} concentration. Undersized tetravalent cations like Ti^{4+} stabilize the tetragonal phase and therefore the tetragonality increases with increasing Ti^{4+} concentration. Adapted from [26].

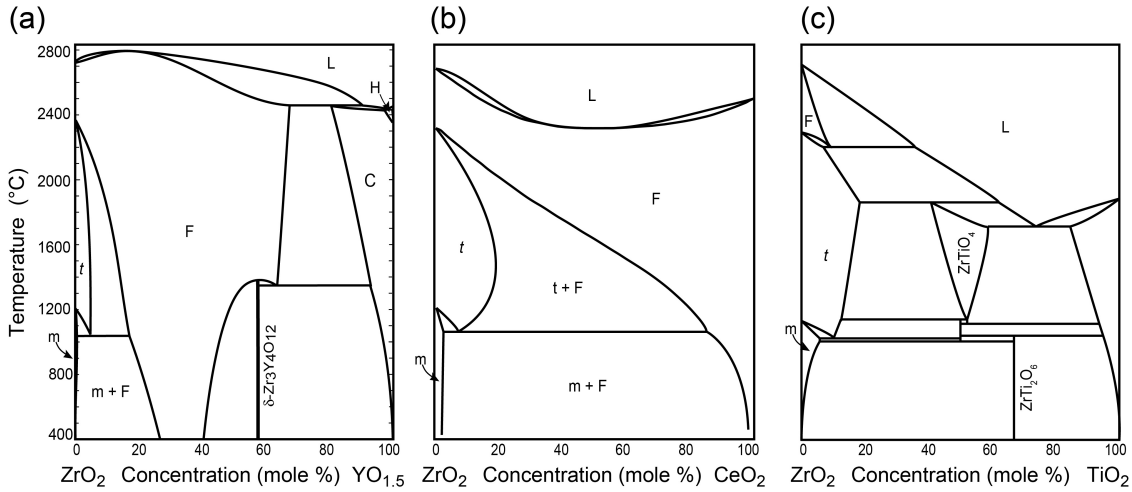

Figure 2.4: Phase diagrams for the (a) ZrO_2-$YO_{1.5}$ system [18,87] , (b) ZrO_2-CeO_2 system [88], (c), ZrO_2-TiO_2 system [89].

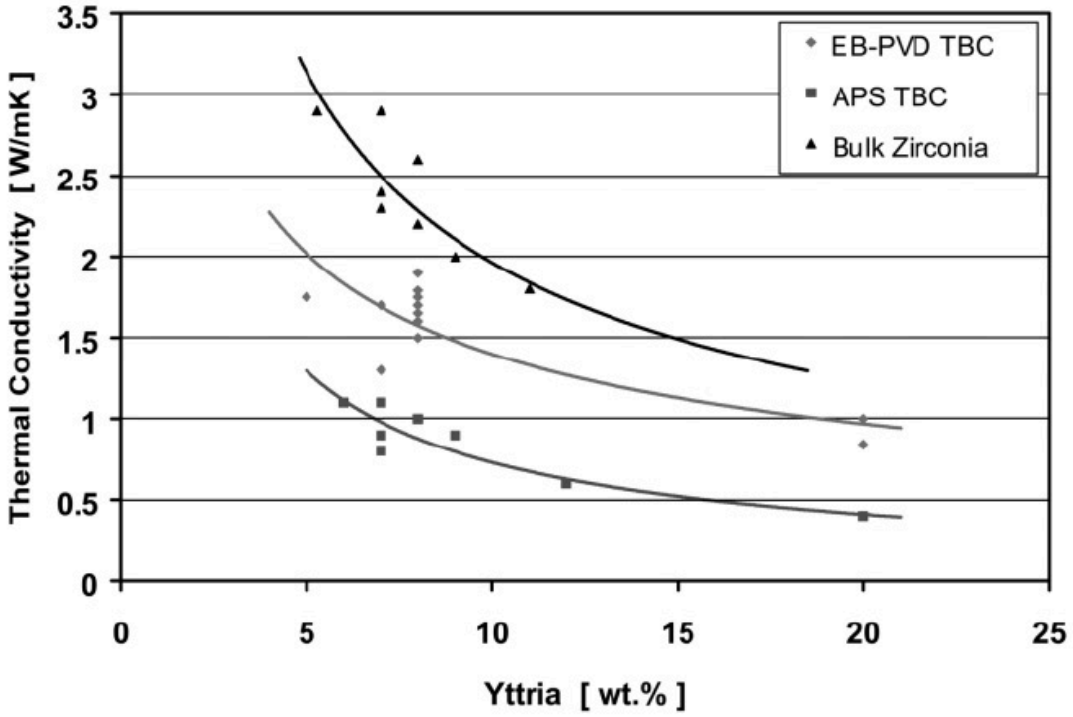

Figure 2.5: Thermal conductivity as a function of yttria weight percent [37]. Decreasing thermal conductivity is observed with increasing yttria weight percent.

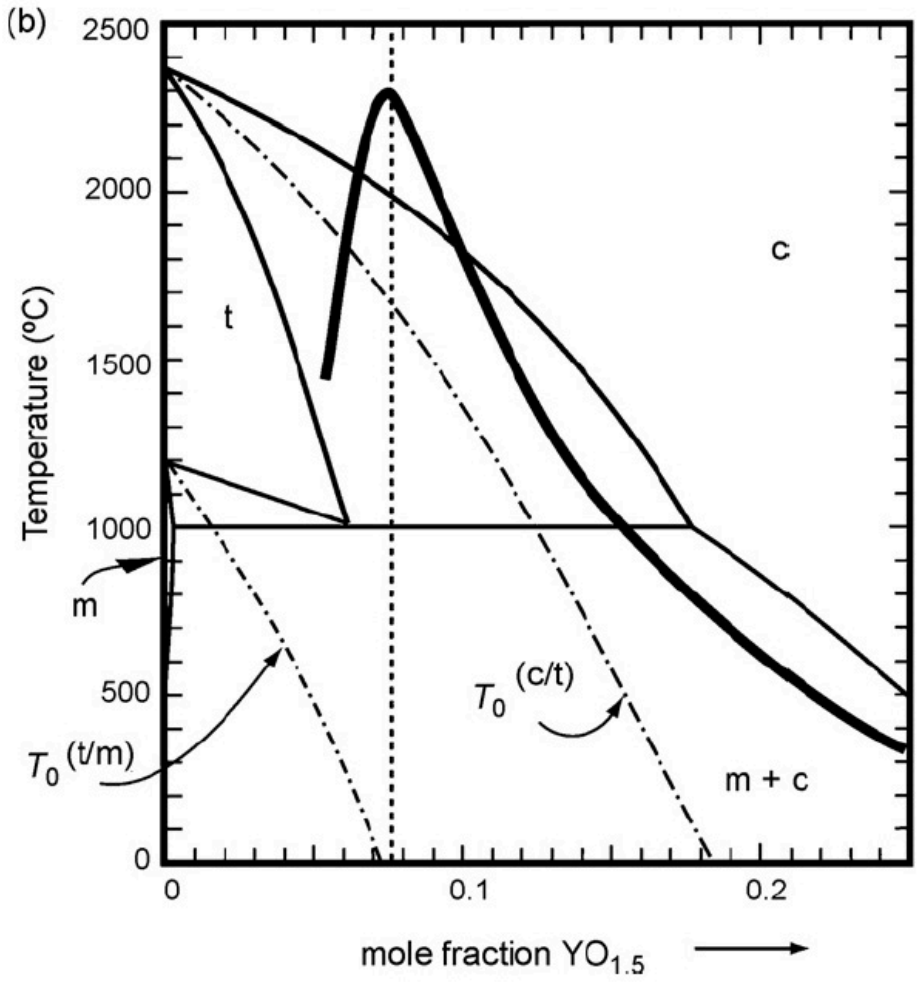

Figure 2.6: The bold line shows the relative lifetime of YSZ thermal barrier coatings exposed to cyclic burner rig [6]. A maximum in lifetime is obtained for ~8YSZ.

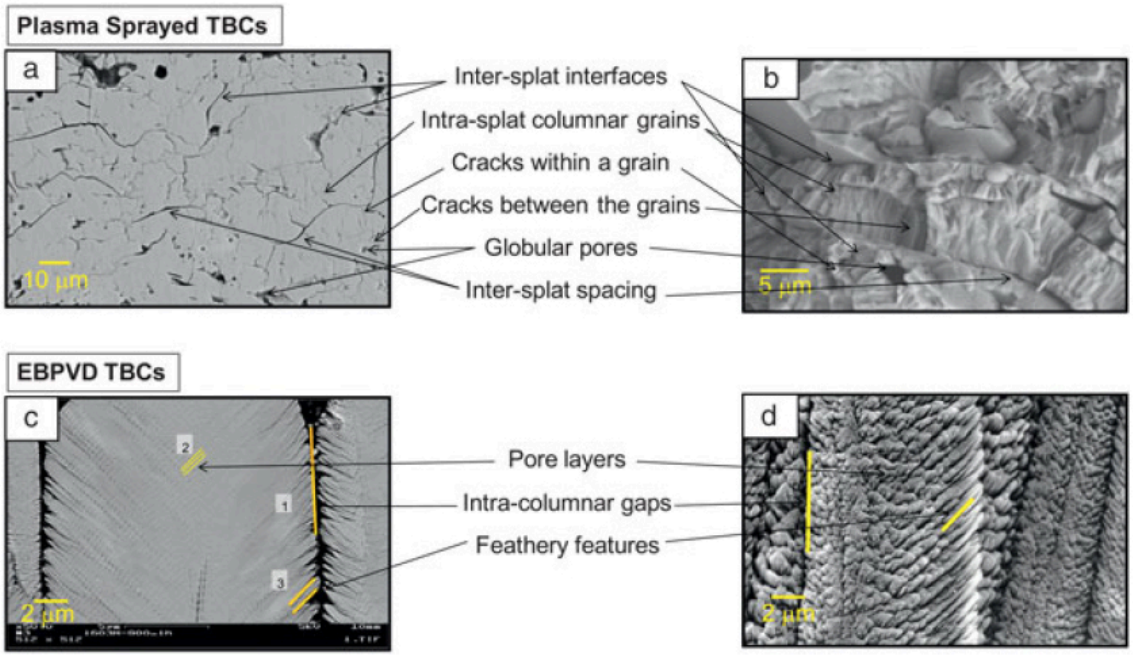

Figure 2.7: SEM micrographs of APS (a, b) and EB-PVD microstructures (c, d) [45]. Different types of pores, cracks, and grain boundaries are highlighted. These defects serve to increase strain compliance and reduce thermal conductivity.

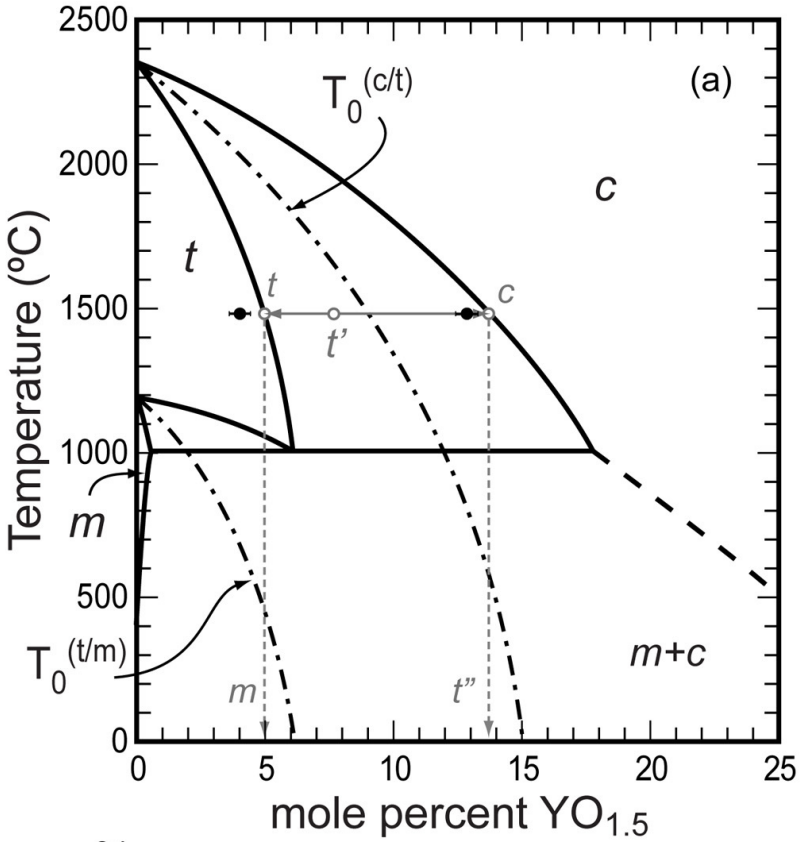

Figure 2.8: Zirconia right portion of the ZrO_2-$YO_{1.5}$ phase diagram [48]. The $T_0(t/m)$ curve [18], which represents the temperature at which the tetragonal and monoclinic phases have equivalent energy, dives rapidly with increasing yttria content. Above ~6YSZ, the tetragonal phase is stable over the monoclinic phase at room temperature and is hence non-transformable on cooling.

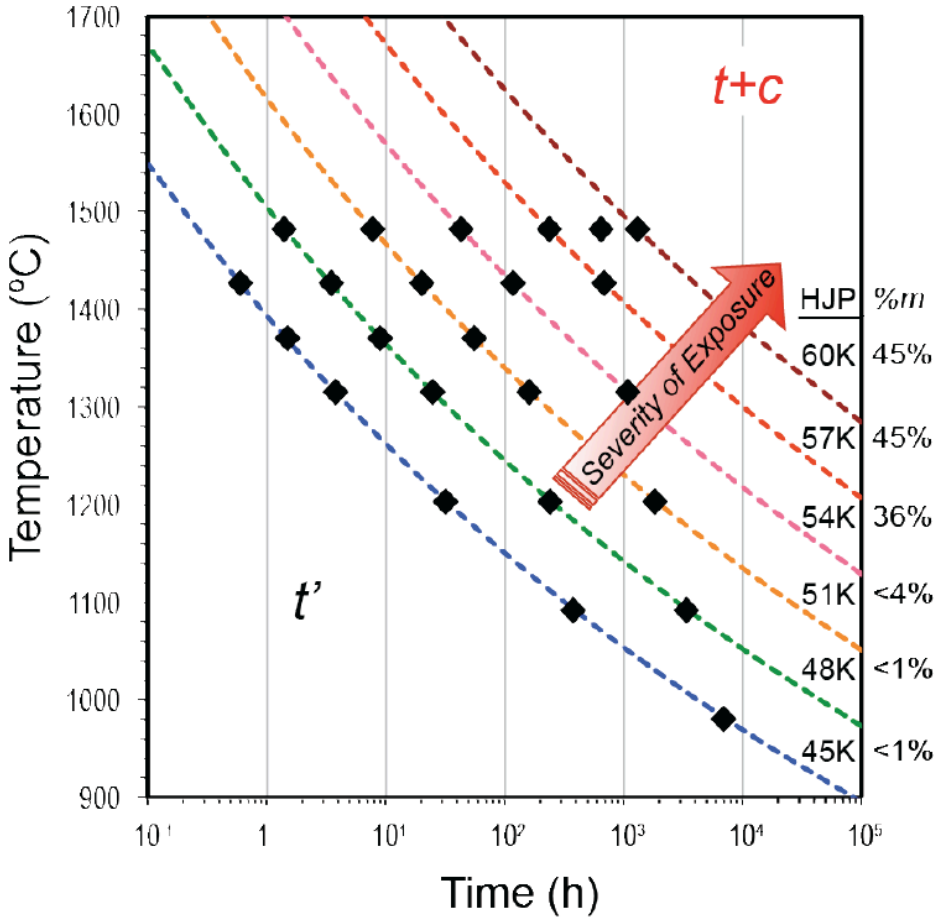

Figure 2.9: The achievable lifetime of a *t'*-8YSZ TBC is linked to the time at temperature it takes for the decomposition of *t'* and formation of *m*-ZrO_2, assuming that other mechanisms do not cause TBC failure. A Hollomon-Jaffe parameter (HJP) is useful for understanding the kinetics of phase evolution in *t'*-8YSZ. A single HJP represents a series of time(s) at temperature(s) for which the phase evolution is equivalent. Any colored iso-contour in the above plot depicts a single HJP. The phase fractions of *m*-ZrO_2 associated with the iso-contours are shown on the bottom right of the plot. The plot can be used to determine the lifetime of a TBC if failure is dictated by the formation of a certain amount of *m*-ZrO_2. The lifetime generally decreases rapidly with increasing temperature. [10]

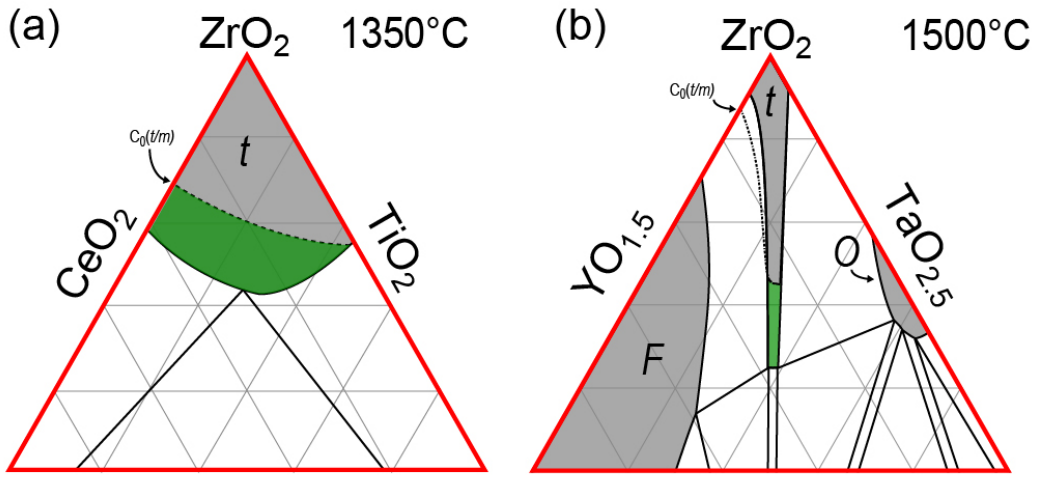

Figure 2.10: Isothermal slices of (a) the ZrO_2-CeO_2-TiO_2 phase diagram at 1350°C [50] and (b) the ZrO_2-$YO_{1.5}$-$TaO_{2.5}$ phase diagram at 1500°C [15]. Both of the systems have regions where the tetragonal phase field is non-transformable to monoclinic on cooling, highlighted in green, but the compositional space where such a phase exists is much smaller in the ZrO_2-$YO_{1.5}$-$TaO_{2.5}$ system.

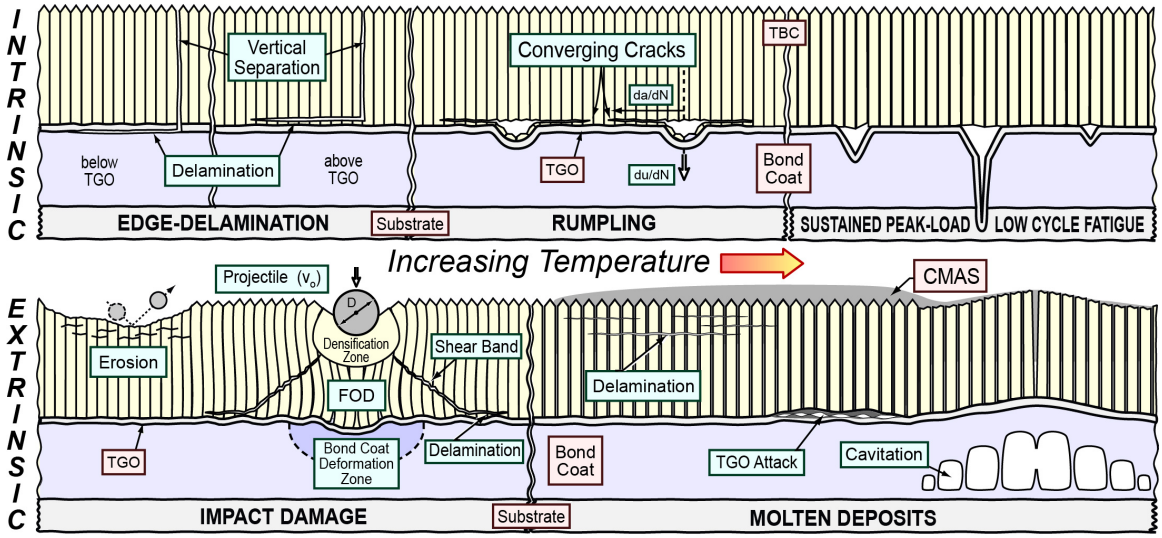

Figure 2.11: A summary of the various mechanisms that can cause spalling of the TBC on turbine airfoils. Strain misfits between the constituent layers upon thermal cycling govern the intrinsic mechanisms. Material properties and external factors govern the extrinsic mechanisms. Taken from [6].

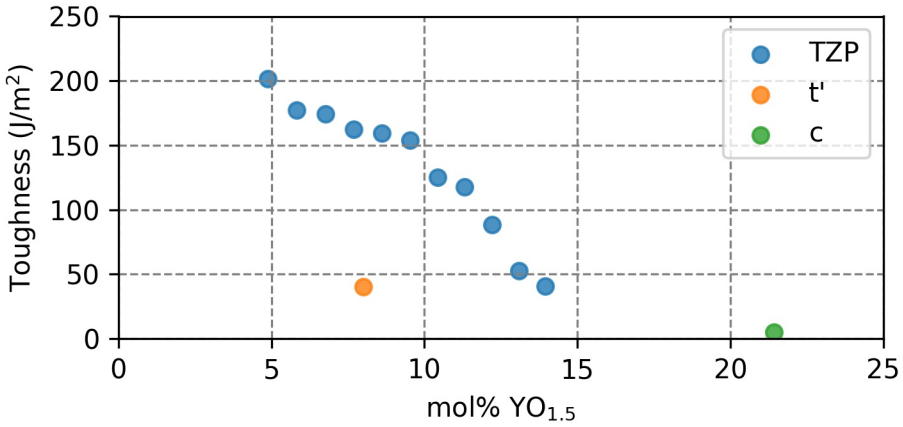

Figure 2.12: Toughness for several different compositions and microstructures in the YSZ system. Adapted from [6] assuming a constant modulus of E = 200 GPa. TZP compositions are toughened by transformation toughening and have the highest toughness, *t'* is toughened by ferroelastic switching and has moderate toughness, and *c* is not toughened by any significant toughening mechanism.

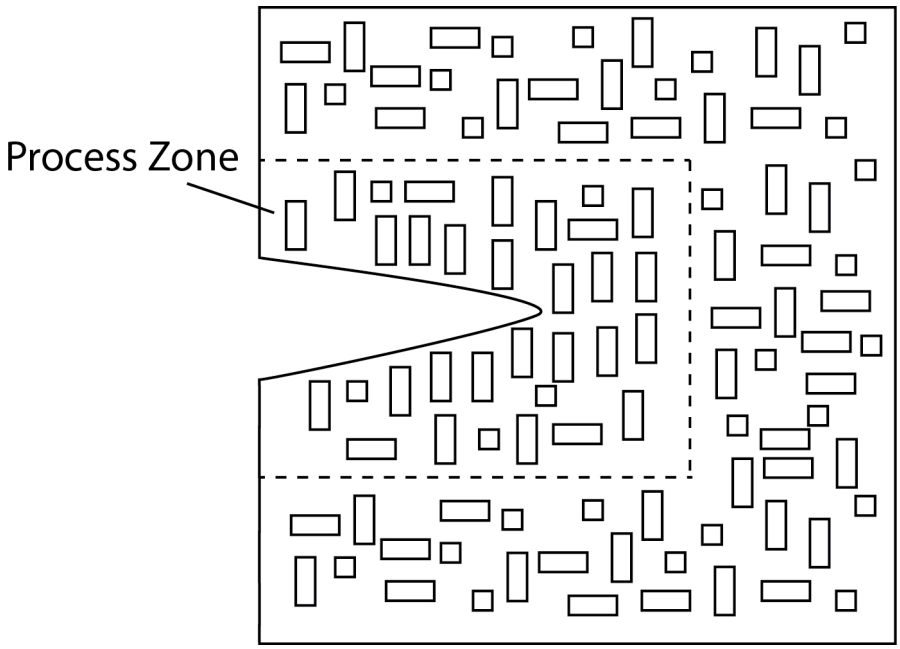

Figure 2.13: Schematic illustration of ferroelastic switching in *t'*-YSZ. Each variant is represented by a rectangle (c-axis in the plane of the page) or by a square (c-axis out of the plane of the page). In the bulk material outside of the process zone, equal fractions of all three tetragonal variants exist. Within the process zone, a majority of the tetragonal variants have reoriented such that their c-axis is now aligned perpendicular to the crack plane. The reorientation places a compressive stress on the crack tip and causes toughening.

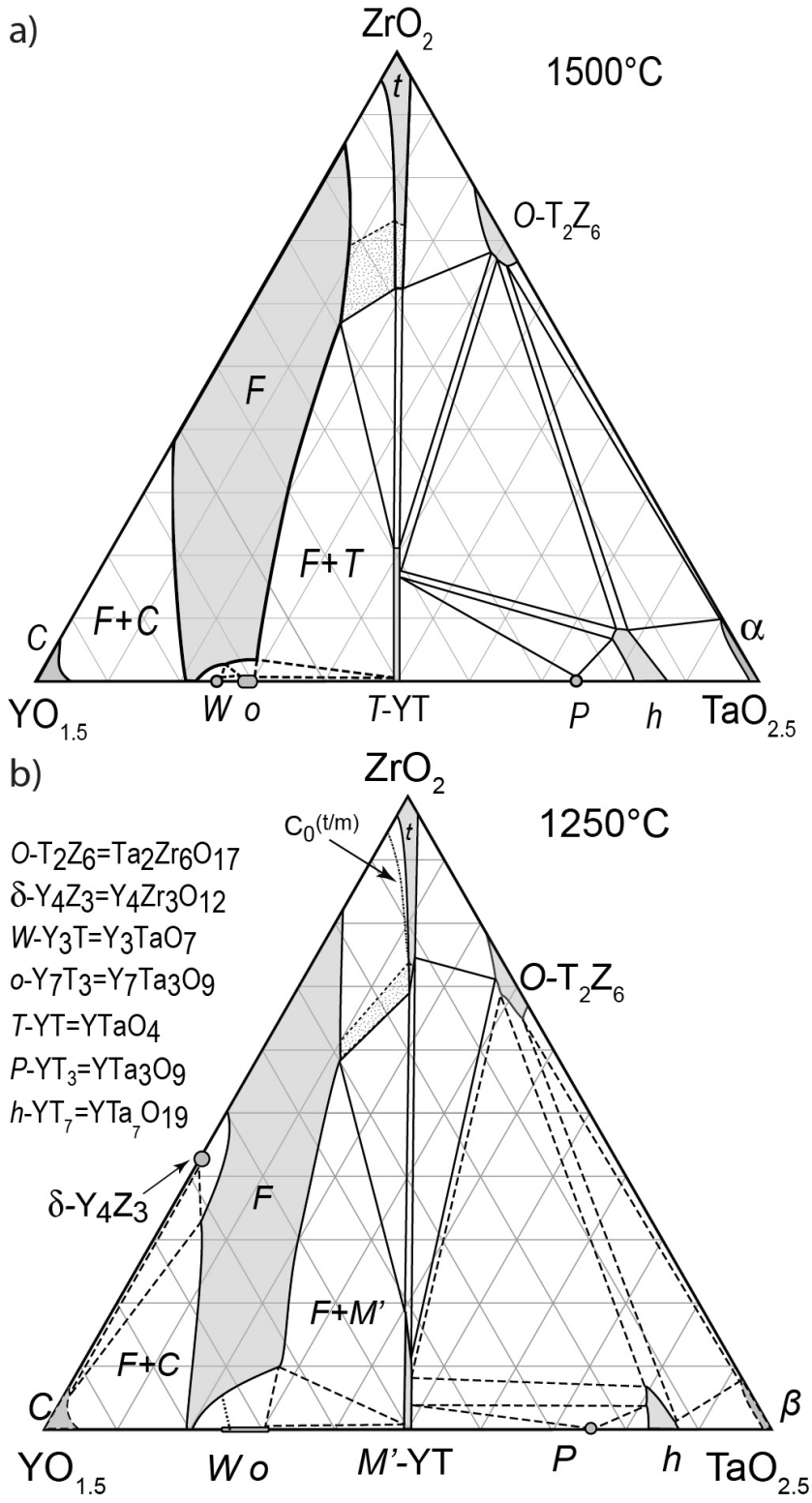

Figure 2.14: Isothermal slices of the ZrO_2-$YO_{1.5}$-$TaO_{2.5}$ phase diagram at (a) 1500°C and (b) 1250°C. Adapted from [14,15].

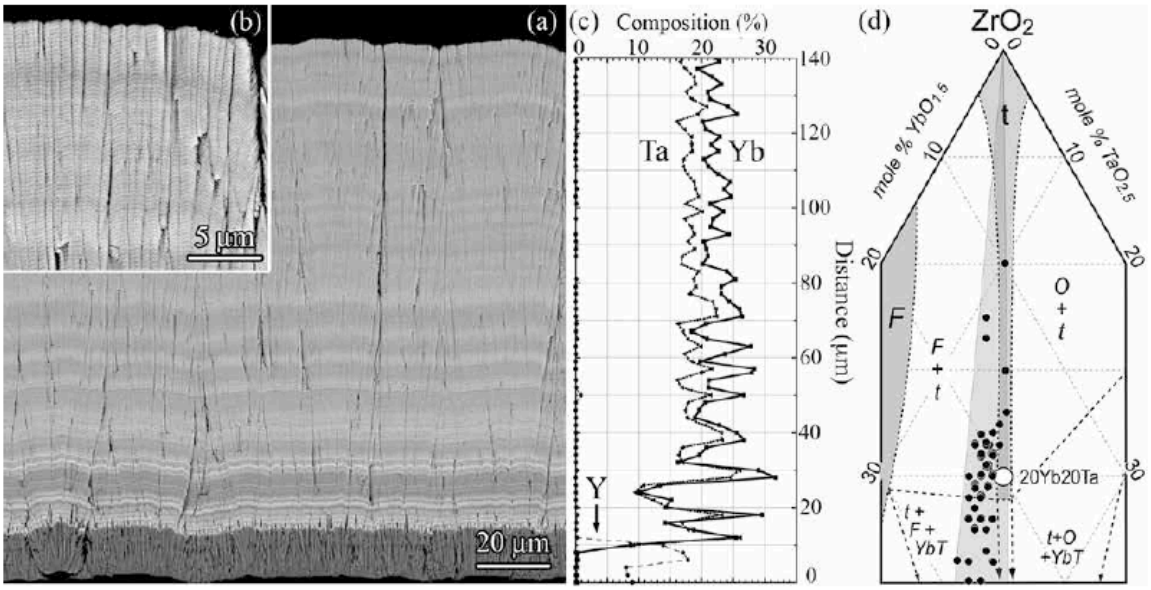

Figure 2.15: A thermal barrier coating made from $60ZrO_2$-$20YbO_{1.5}$-$20TaO_{2.5}$ exhibits chemical fluctuations throughout the thickness of the coating, seen as contrast variations in the backscatter electron image shown in (a). A high magnification image of the column tips is shown (b). The compositional fluctuations can be measured by electron probe microanalysis, (c), and plotted onto the phase diagram (d). The chemical fluctuations produce select areas in the coating that are expected to be extremely rich in ZrO_2 and therefore reside in a region of the phase diagram where a transformable tetragonal phase is expected at equilibrium.

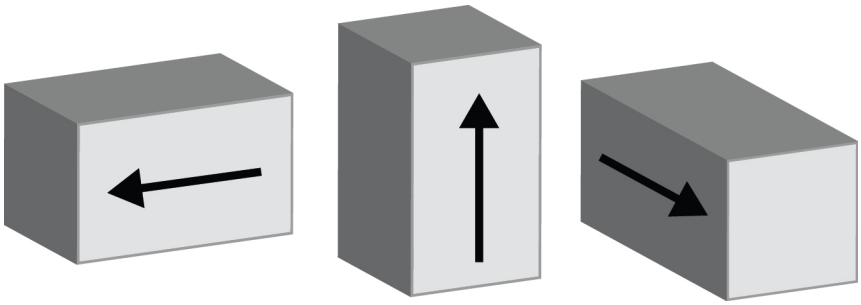

Figure 2.16: The three tetragonal variants. The arrows depict the direction of the c-axis.

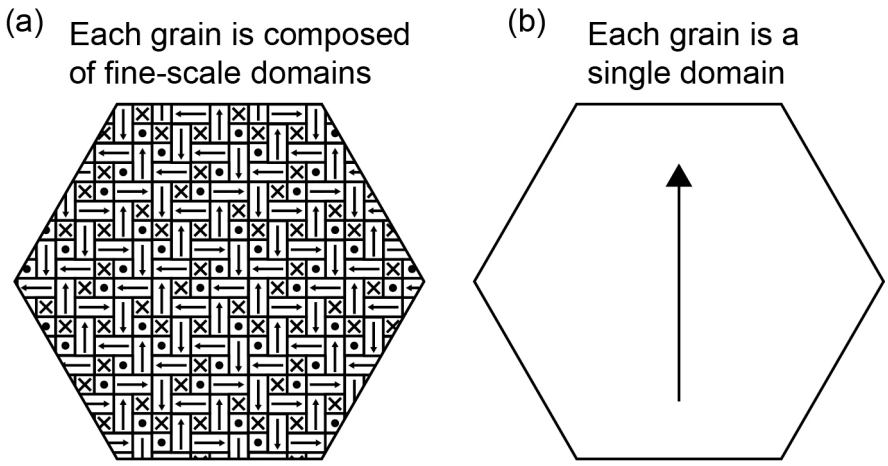

Figure 2.17: Schematic illustrations of the two types of microstructures pertinent to ferroelastic switching in zirconia based materials. (a) Each grain is composed of fine-scale domains of all three tetragonal variants. (b) Each grain is itself a single, large tetragonal variant.

Figure 2.18: Dark field images showing the distribution of the three tetragonal variants in a ~6YSZ material that has been subjected to the $c \rightarrow t$ transformation. Adapted from [77].

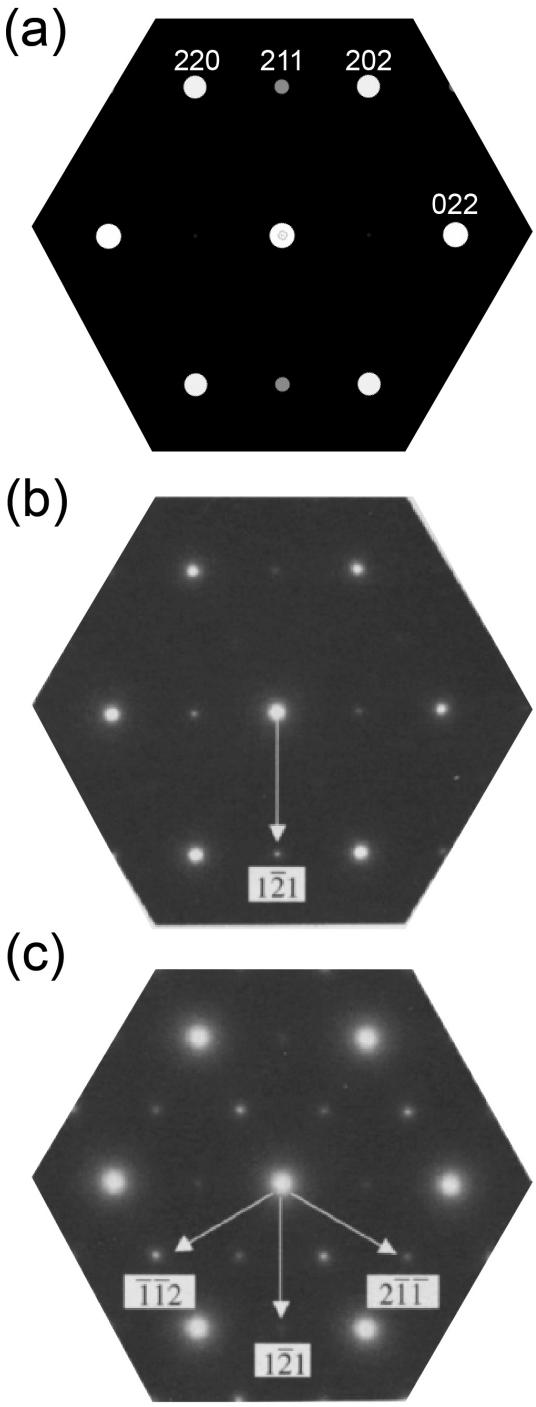

Figure 2.19: (a) Simulated diffraction pattern from the [111] zone axis in ZrO_2. Note that a single symmetrically unique 211-type reflection is present. (b) Experimental [111] diffraction pattern from a single domain-free grain in bulk *t'*-8YSZ. A single 211 reflection is observed. (c) Experimental [111] diffraction pattern from the same material in (b) but from a region near an indentation crack. All three 211-type reflections are observed, suggesting that ferroelastic switching has occurred. Adapted from [76]

CHAPTER 3: METHODS

Identifying and optimizing materials within the ZrO_2-$REO_{1.5}$-$TaO_{2.5}$ (RE = rare-earth) system for next generation thermal barrier coatings requires a comprehensive understanding of the complex relationships between crystal structure, phase equilibria, microstructure, and properties. A combined computational and experimental approach was utilized to develop such an understanding, beginning with first principles calculations to gain insight into the equilibria and atomic structure of phases relevant for thermal barrier coatings, then exploring the microstructure evolution and thermomechanical properties of deposited coatings, and finally investigating the toughness and toughening mechanisms of polycrystalline compacts. The equipment, general techniques, and methods that were used are described in this chapter, with additional information provided in subsequent chapters as necessary.

3.1 Material Synthesis

3.1.1 Synthesis and Refinement of Oxide Powders

Oxide powders used as starting material for the toughness studies were synthesized by reverse co-precipitation [16,90,91]. The precursors utilized were zirconyl nitrate (Sigma Aldrich, 99% purity, metals basis), yttrium nitrate hexahydrate (Sigma Aldrich, 99.9% purity, metals basis), ytterbium nitrate pentahydrate (Fischer Scientific, 99.9% purity, metals basis), and tantalum chloride (Fischer Scientific, 99.99% purity, metals basis). Individual solutions were prepared by dissolving the Zr, Y or Yb precursors in deionized water, or the Ta precursor in ethanol, similar to the procedures described in [16]. The solutions were then assayed to determine the exact oxide yield and subsequently mixed in the appropriate

proportions to yield the desired composition. Each mixed solution was then added drop-wise to a large, stirred reservoir of ammonium hydroxide while maintaining a pH above 10 to ensure the precipitation of a homogenous molecularly mixed hydroxide. The resultant mixture was separated into supernatant and precipitate by spinning in a centrifuge (Unico PowerSpin® MX Centrifuge) at 300 RPM for 3 minutes. The collected precipitate was mixed with an excess of ethanol and separated by centrifuge; the cycle was repeated twice to minimize any residual reactants, especially ammonium or chloride ions. The cleaned product was finally dried at 150°C and pyrolized at 700°C for 4 hours in air.

3.1.2 Ball Milling

In order to break up particulate agglomerates created during pyrolysis, the calcined powders were attrition milled using a planetary ball mill (Across International PQ-N04). In the typical procedure, a yttria-stabilized zirconia jar was loaded halfway by volume with 1 mm spherical yttria-stabilized zirconia milling media and subsequently to about the two-thirds mark with ethanol. Approximately 5 grams of powder was added to the jar, which was then sealed and allowed to spin in the planetary mill at 350 RPM for 90 minutes. The milling media was extracted from the suspension by coarse filtration and the remaining product was allowed to dry overnight at 50-80°C.

In one case, discussed in Chapter 5, a similar procedure was used to grind EB-PVD material. The EB-PVD material, which had been deposited onto graphite paddles by an industrial collaborator, was removed from the graphite by burning the graphite at low temperature. The resulting powder was then ball milled in a similar manner as outlined above but the milling media consisted of a mixture of 10 mm, 5 mm, and 2 mm yttria-stabilized zirconia

spheres in order to more effectively crush the relatively large starting particles (columnar crystals >200 μm).

3.2 Material Processing

3.2.1 Consolidation and Heat Treatment of Powders for Toughness Testing

Pellets for toughness testing were fabricated using spark plasma sintering (SPS)[2] [92] in a Field Assisted Sintering System (FAST) model HPD 5 (FCT Systeme GmbH, Rauerstein, Germany) and also by sinter forging [93] in a modified mini-hot press model FR210 (Oxygon, Epsom, New Hamsphire). Because both processes are performed in a partially reducing environment, the samples underwent a subsequent heat treatment to re-oxidize and further densify the material.

For SPS, approximately 1-1.2 g of precursor-derived powder was loaded into a 9.15 mm graphite die lined with grafoil, the rest of the die set assembly was configured, and the assembly was loaded into the FAST system, Figure 3.1. A compressive uniaxial pressure of ~130 MPa was loaded over the course of two minutes and then heated at 100°C/min to 1250°C. The compact was held at this temperature for 2 minutes, and then allowed to cool to room temperature at 100°C/min, with the pressure being released over the course of the cooling period. The current was not pulsed during the experiments. Following release of the pellet from the cooled SPS die set, residual grafoil on the surface of the compact was largely removed by mechanical grinding. Even after this step, pellets made via SPS often appeared grey or black, suggesting partial reduction of the some cations and presumably incorporation of oxygen vacancies. In order to re-oxidize the pellet and promote further densification

[2] Also known in the literature as Current Assisted Densification (CAD) or Field Assisted Sintering (FAST).

(without pressure), the pellet was subsequently heated in a box furnace (1700°C model 51 314, Lindberg, Riverside, Missouri) at a rate of 10°C/min up to 1250°C in air, held for 12 hours, and then cooled at 10°C/min.

For sinter forging (SF), approximately 1-1.5 g of precursor-derived or EB-PVD powder were uniaxially cold pressed at 250 MPa into pellets ~12.7 mm in diameter and ~3 mm thick. (Specimens fabricated from EB-PVD powder subsequently underwent cold isostatic pressing at 300 MPa.) The pellets were then heated at 10°C/min up to 1250°C, held for 30 minutes in order to lightly sinter the material, and then cooled at 10°C/min. The resulting pellet was placed in between two pieces of ZYF-100 zirconia felt (Zircar, Florida, USA), which was then placed in between two pieces of grafoil, and the entire assembly was inserted into the Oxy-gon unit, Figure 3.2. Prior to evacuation and heating to 1250°C at 5°C/min, the rams were lowered into contact with pellet such that a light stress (~5 MPa) was applied. After the maximum temperature was reached, the full uniaxial compressive pressure of 15 MPa was applied and the system was allowed to dwell for 17 h. The load was then released but the temperature kept at 1250°C in order to help relax any residual stresses, and finally the chamber was cooled at 5°C/min. Similar to the SPS procedure, residual grafoil and zirconia felt were removed by mechanical grinding. Even after removal of the grafoil and felt, pellets made via sinter forging often appeared grey, although not as dark as those made by SPS. The pellets were subjected to the same re-oxidation treatment as those produced by SPS, as described above, but the dwell at 1250°C was for 100 h. The dwell time for the SPS specimens was shorter than that for the SF specimens because preliminary studies had revealed that several of the SPS compacts displayed cracking after aging at

1250°C for 100 h. It is important to note that the cracking was not associated with the tetragonal-to-monoclinic transformation.

3.2.2 Electron Beam Physical Vapor Deposition (EB-PVD)

Thermal barrier coatings in the ZrO_2-$YbO_{1.5}$-$TaO_{2.5}$ system were deposited at UCSB using an in-house evaporator (Consarc, Inc., Rancocas, NJ), depicted in Figure 3.3, and ingots procured from TCI Ceramics, Inc. (Bethlehem, PA). Ingots of three different compositions, ZrO_2-$8YbO_{1.5}$, ZrO_2-$25YbO_{1.5}$-$15TaO_{2.5}$, and ZrO_2-$15YbO_{1.5}$-$25TaO_{2.5}$ (all in mole percent) were deposited onto 1 inch Fecralloy discs (Goodfellow, Coraopolis, PA) that had been pre-oxidized in air at 1100°C for 3 h to produce a thin layer of adherent alumina. The system was operated with an accelerating voltage of 40 kV, beam current in the range 160-200 mA, chamber pressure of 5 mTorr, and oxygen intake of 40 sccm. The substrates were attached to a hollow alumina tube (which acts as the substrate stage) by Fecralloy wire, heated in the back by a silicon carbide cartridge heater to a surface temperature of 1100°C, and rotated along its axis at 8 RPM. Typical deposition rates were in the range 1-1.5 μm/min with total thicknesses ranging from 100-160 μm.

Thermal barrier coatings of nominal composition ZrO_2-$12YO_{1.5}$-$13YbO_{1.5}$-$14TaO_{2.5}$ (in mole percent) were deposited onto 1 cm sapphire discs by electron beam physical vapor deposition at an industrial facility. All processing parameters, such as deposition rate, rotation rate, oxygen partial pressure, etc., are proprietary. The TBCs were shipped to UCSB in the as-deposited condition for further characterization and aging treatments.

3.2.3 Phase Stability Studies

To assess their phase stability, EB-PVD coatings underwent isothermal heat treatments in air at 1250°C and 1500°C for cumulative time increments until the total time at temperature for a given sample was 400 h. For these treatments a box furnace (1700°C model 51 314, Lindberg, Riverside, Missouri) was preheated to the prescribed temperature. The sample, which was placed inside an alumina crucible within an approximately 50x50x50 mm cube of Fiberfrax insulation (Unifrax, Tonawanda, NY), was directly inserted into the furnace, held for the specified time, and then removed from the furnace and allowed to cool at ambient temperature within the holder. Similar procedures were followed for compacts from precursor-derived powders.

3.2.4 Surface Preparation for XRD, Raman, Indentation, and Microscopy

The surfaces of compacted samples were prepared for toughness testing and microstructural observation by mechanical polishing using standard metallographic techniques. In all cases, the MultiPrep Polishing System (Allied High Tech) was utilized to ensure reproducibility of the surface polish and parallelism of the pellet faces. The compacts were mounted to a parallel polishing fixture using crystal bond or wax, the fixture was inserted onto the MultiPrep system, and the compacts lowered into contact with diamond lapping films. In most cases the final diamond lapping film used was 0.25 μm.

To prepare coatings for microstructural observation, the columnar gaps were first infiltrated with M-Bond 610 adhesive (Micro-Measurements, Windell, NC) to preserve the TBC microstructure during subsequent sectioning and polishing, mounted in epoxy resin, cross-sectioned using a slow speed diamond saw, and polished to a 1 μm finish.

3.3 Characterization

3.3.1 X-ray Diffraction

Standard x-ray diffraction techniques were used to assess the phase evolution of specimens in both coated and compacted form (Empyrean Powder Diffractometer, PANalytical, Westborough, MA). Phases were identified by comparison to published powder diffraction data (ICCD PDF-4 Database) and to material standards fabricated via reverse co-precipitation at UCSB. In most cases, a goniometer was used to scan reciprocal space from $2\theta = 20°$ to 80° with a step size of 0.013° and 13 minute scan time.

To characterize the texture of deposited coatings, pole figures were collected utilizing an x-ray diffractometer with capabilities of rotating in Φ (phi, in-plane) and φ (psi, out-of-plane) (X'Pert Pro, PANalytical). A step size of 1° was used for Φ and a step size of 2.5° was used for φ. The (200) and (220) peaks were used to determine the texture, similar to the procedure employed for 7YSZ in earlier works [68].

3.3.2 Raman Spectroscopy

Due to its sensitivity to small volumes of tetragonal grains that have transformed to the monoclinic phase [80,94], Raman spectroscopy (Triple Monochromator Jobin-Yvon; 633 nm excitation) was used specifically to determine whether or not *m*-ZrO_2 was present in coatings and compacts throughout aging treatments. The microscope was operated with a hole size of 500 μm, a slit size of 500 μm, and a grating size of 1200 cm^{-1}. The spectrometer was centered on 600 cm^{-1} and the signal was collected for 10 seconds 5 times, for a total collection length of 50 s.

3.3.3 Dilatometry

The bulk, linear coefficient of thermal expansion (CTE) was measured using a push-rod type Orton 2016 HU differential dilatometer in an air atmosphere. A 25 mm alumina bar with a 9.5 mm cross-section was used as a standard. 25 mm long bars of various materials were fabricated by uniaxially pressing ~5 g of powder into a bar, followed by annealing at 1250°C for 24 h. The temperature and hold time were chosen to allow the initial, rapid stages of sintering to occur while also preserving the as-fabricated microstructure. The measurements were in the temperature range 30°C-1250°C at a heating and cooling rate of 3°C/min with a sampling time of 20 s. The bar was subjected to seven identical runs. The mean coefficient of thermal expansion at a given temperature was calculated using the expression:

$$\alpha_{mean} = 1/L_0 \bullet (\Delta L/\Delta T) \tag{3.1}$$

where L_0 is the original length of the bar at 30°C, ΔL is the change in length from the reference (ambient) temperature to the temperature of interest, and ΔT is the temperature interval over which the measurement was performed.

3.3.4 Density Measurements

The densities of compacted specimens were measured by Archimedes method [95] using water as the immersion medium. Each pellet was submerged in water and heated to ~80-90°C for 4 hours. The water was cooled and measurements of the apparent mass when submerged and wet mass in air were taken. The density was calculated as:

$$\rho = \frac{m_{sub}}{m_{sub} - m_{wet}} \tag{3.2}$$

where m_{sub} is the apparent mass when submerged and m_{wet} is the wet mass in air.

3.3.5 Electron Microscopy

Microstructure observations and dimensional measurements of microindentations were conducted using scanning electron microscopy (SEM) on a XL30-FEG SEM (FEI, Hillsboro, OR) and a FEI Nova Nano 650 FEG SEM in both secondary and backscatter imaging modes.

Chemical analysis along the thickness of deposited coatings was conducted via electron probe microanalysis (EPMA) in a CAMECA system model SX-100 (Gennevilliers-Cedex, France) equipped with five wavelength dispersive spectrometers (WDS). Pure oxide standards were used as reference samples to calibrate the WDS detectors. Spot scans were collected using a 1 μm beam spot size and 15 kV source.

Lamellae for transmission electron microscopy were extracted using a Helios Dualbeam Nanolab 600 (FEI). Mo grids were used to hold the FIB specimens instead of the conventional Cu grids to avoid overlap between the Ta L_α = 8.2 and Cu K_α = 8.0 keV emission lines.

Transmission electron microscopy was performed using two FEI 200kV Tecnai G2 Sphera microscopes. The set of microscopes was used for compositional analysis, diffraction pattern investigation, and complementary bright/dark field imaging. A FEI Titan 300 kV FEG TEM/STEM system and FEI Titan 80-300 microscope with a spherical aberration (Cs) corrector for the objective lens were used for high-resolution work involving bright field, high angle annular dark field (HAADF), and scanning tunneling electron microscopy (STEM) imaging as well as fine-scale chemical analysis. The majority of the work in

Chapter 8 was performed with the FEI Titan 80-300 microscope at the Central Facility for Electron Microscopy (GFE) and Ernst Ruska-Centre (ER-C)-2 for Microscopy and Spectroscopy with Electrons in Aachen, Germany.

Energy dispersive spectroscopy (EDS) was carried out using an Oxford spectroscope (Oxfordshire, United Kingdom). Contributions from Ga from the FIBing process to the EDS spectra were deconvoluted using the INCA software. The K series principal emission lines were used for Zr and Y while the L series lines were used to quantify Ta and Yb. Two samples with composition ZrO_2 - 16.62 mol% $YO_{1.5}$ -16.59 mol% $TaO_{2.5}$ and ZrO_2 - 18.73 mol% $YbO_{1.5}$ -19.46 mol% $TaO_{2.5}$ were utilized as standards for EDS. The compositions of the samples were determined by inductively coupled plasma optical emission spectroscopy at an external laboratory (Dirats Laboratories, Westfield, MA).

3.4 Toughness Measurements

Microindentation with a Vickers indenter was used to estimate specimen toughness according to the method outlined in [85]. The starting distance from the specimen surface and the indenter tip was fixed at 1 mm. Loads of 4 kg were used to produce indents and at least 6 indents showing the right attributes were analyzed for each sample. Immediately following indentation, the dimensions of the indents and the cracks propagating from the corners of the indents were measured by scanning electron microscopy (FEI Nova Nano 650 FEG SEM). The toughness (Γ, J/m^2) was then calculated from the equation [85]:

$$\Gamma = K_c^2 / E = 2\zeta^2 P\left(d^2 / c^3\right) \tag{3.3}$$

where K_c (MPa m$^{1/2}$) is the fracture toughness, E (GPa) is the Young's modulus, $\zeta = 0.016$ is a term that is often cited as a "geometrical constant" but is calibrated and hence it is a

calibration constant, P is the load, $2d$ is the average length of the diagonal of the indentation, and $2c$ is the average crack length, as depicted in Figure 3.4.

As outlined in [85], the following guidelines were abided by in order to validate the underlying assumptions implicit in the calculation of toughness via indentation:

(i) All indentations were made on freestanding pellets.

(ii) The thickness of the pellet was at least 10 times greater than the dimension of the radial crack, c, in accordance with the semi-infinite body assumption of linear elastic mechanics. Most cracks were ~100-130 μm, so all specimens were at least 1.3 mm thick.

(iii) The ratio of the radial crack length, c, to the indent diagonal, d, was always greater than 1.

(iv) The grain size was ideally less than 1% of the average crack dimensions. Most, but not all, specimens had sub-micron grain size.

3.5 Figures

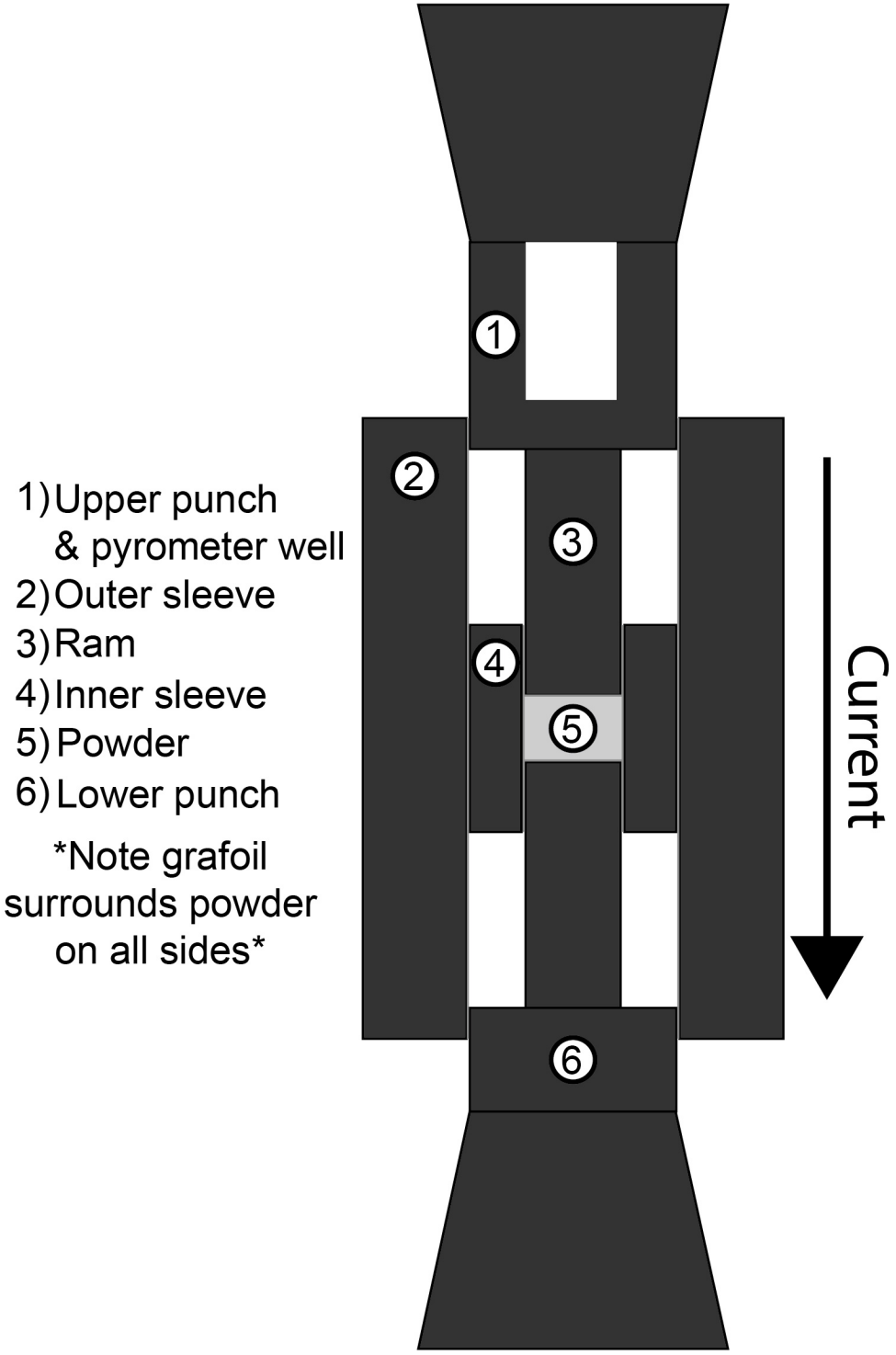

Figure 3.4: Schematic of the spark plasma sintering (SPS) assembly used for densification experiments. All parts are made out of graphite.

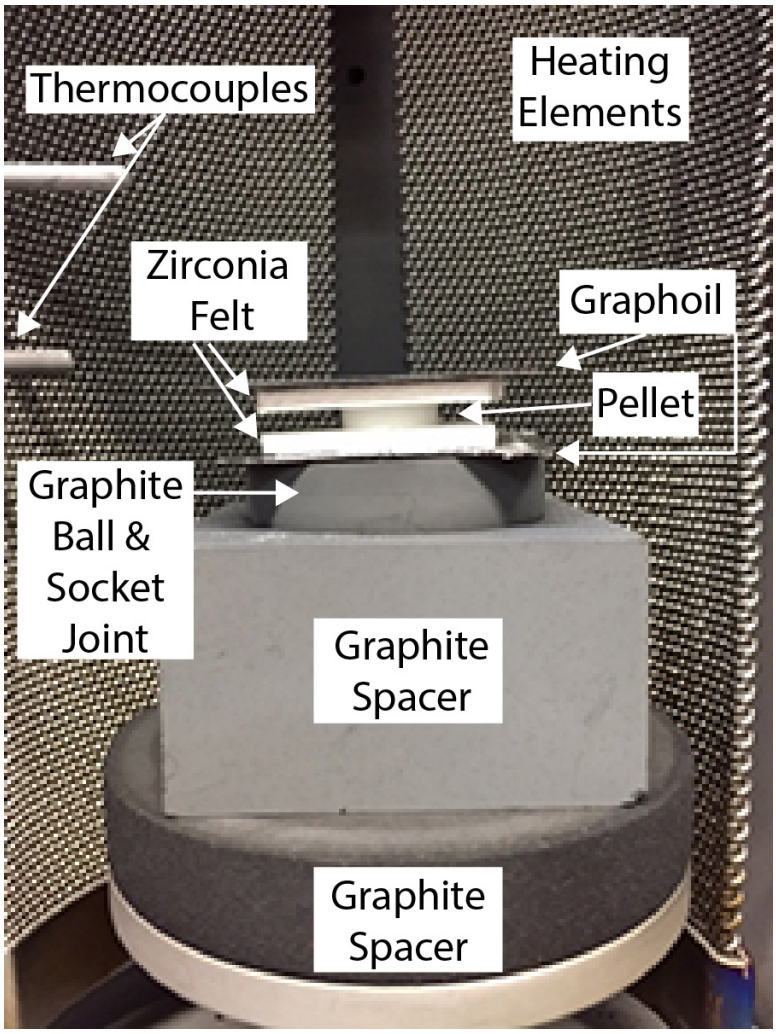

Figure 3.2: Image depicting the sandwich of grafoil (thin grey), zirconia felt (thick white), and sample used for the sinter forging process.

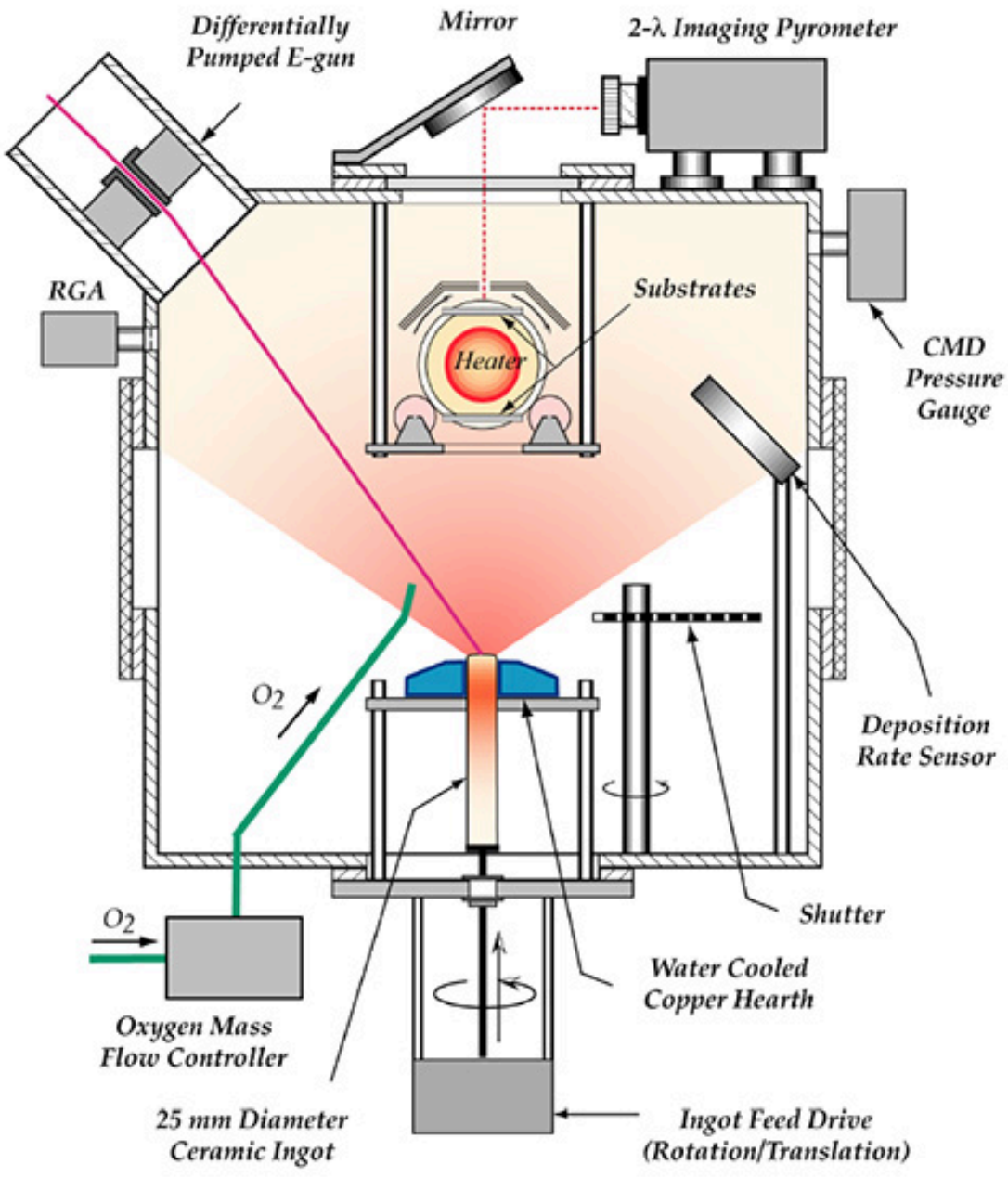

Figure 3.3: Scehmatic representation of UCSB EB-PVD TBC coater configured for high rate deposition on rotating subtrates.

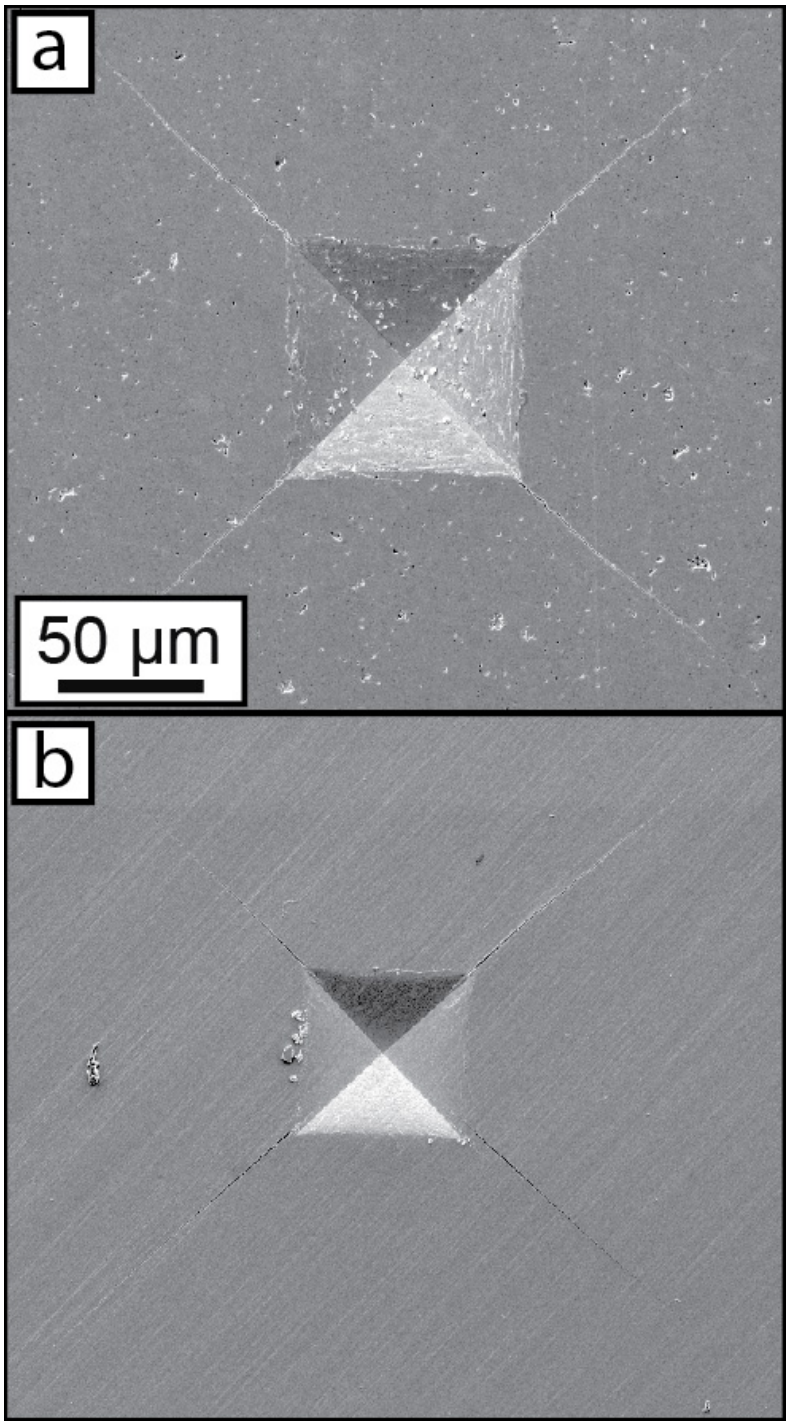

Figure 3.4: Secondary electron images showing two typical, valid micro-indentations with relavant dimensions for toughness testing depicted. (a) Typical microindentation for ZrO_2-$REO_{1.5}$-$TaO_{2.5}$ ternary and quaternary materials and (b) ZrO_2-$YO_{1.5}$ binary materials.

CHAPTER 4: CRYSTALLOGRAPHY IN THE ZrO_2-$YTaO_4$ SYSTEM

Many properties that underpin the utility of materials in the ZrO_2-$YTaO_4$ system, such as the toughness of non-transformable *t*-ZrO_2, are significantly influenced by the crystal structure. A detailed knowledge of the crystallography of ZrO_2 and $YTaO_4$ is therefore fundamental to understanding the behavior of thermal barrier oxides based on these and related compositions. The crystal structures of ZrO_2 and $YTaO_4$ share many similarities. Both materials exhibit a monoclinic phase at low temperature and a tetragonal phase at higher temperature, where each phase forms a distorted fluorite lattice with small atomic shuffles. A key difference between the structures is the presence of multiple atomic species on the $YTaO_4$ cation sublattice, which produces ordering in the $YTaO_4$ structures. It is generally expected that the preference for order in the $YTaO_4$ phases will influence a wide range of properties in both the pure and alloyed materials. However, the ordering patterns and their relative energies are not well understood.

This chapter presents a first-principles investigation of crystallography, phase stability, and transformation pathways in the ZrO_2-$YTaO_4$ system at 0 K. The focus of this work is to elucidate and understand trends between stability and configurational degrees of freedom across the ZrO_2-$YTaO_4$ binary, as well as compare and contrast the tetragonal and monoclinic phases at the compositional extremes. The stable orderings in $YTaO_4$ are resolved and a 2D checkerboard arrangement of yttrium and tantalum cations is found to serve as a basic structural motif. The preference for yttrium and tantalum cations to order in this pattern persists when $YTaO_4$ is alloyed into ZrO_2, implying a tendency for short-range ordering. The stability of the preferred ordering patterns is driven by oxygen coordination

and is therefore coupled to the direction of the oxygen shuffle in *t*-ZrO_2. Finally, the tetragonal *T*-$YTaO_4$ phase is found to be dynamically unstable at 0 K, implying that anharmonic vibrations are critical to its stabilization at high temperature.

4.1 Methods

Establishing the ground states and preferred ordering patterns in the ZrO_2-$YTaO_4$ system requires a comparison of the energies of many symmetrically distinct orderings of yttrium and tantalum in the relevant phases. The experimentally observed crystal structures at both compositional extremes of the quasi-binary and at pertinent temperatures (0-1800K) are tetragonal and monoclinic distortions of an FCC cation sublattice with oxygen residing in the tetrahedral interstitial sites. The Clusters Approach to Statistical Mechanics (CASM) software package [96-98] was used to enumerate symmetrically distinct ZrO_2-$YTaO_4$ orderings over *m*-ZrO_2, the monoclinic polymorph of ZrO_2 with 12 atoms per unit cell, and *t*-ZrO_2, the tetragonal polymorph of ZrO_2 with 6 atoms per unit cell[3], allowing Y and Ta to substitute for Zr. Only configurations on the quasi-binary, i.e. those that have equal atomic fractions of yttrium and tantalum, were enumerated. Tetragonal supercells up to volume 4 (having four times the volume relative to the primitive *t*-ZrO_2 cell) and monoclinic supercells up to volume 2 (having two times the volume relative to the primitive *m*-ZrO_2 cell) were considered, amounting to 2,053 symmetrically distinct configurations. An additional tetragonal supercell of volume 16 relative to the primitive tetragonal cell and an additional monoclinic supercell of volume 8 relative to the primitive monoclinic cell were used to investigate the effect of dilute additions of $YTaO_4$ into the ZrO_2 phases.

[3] The ZrO_2 unit cells described here are the primitive versions of the *t*-ZrO_2 and *m*-ZrO_2 structures. A non-primitive version of the *t*-ZrO_2 unit cell having 12 atoms, referred to as the pseudocubic unit cell, is sometimes referenced in this publication and is useful to compare and contrast the *t*-ZrO_2 structure with the primitive *m*-ZrO_2 structure (Figure 4.1).

First-principles density functional theory (DFT) calculations were used to assess the stability of each ordering at 0 K, allowing relaxations of the lattice shape, volume, and atomic coordinates. The Perdew-Burke-Ernzehof (PBE) parameterization of the generalized gradient approximation (GGA) was utilized, as implemented in the Vienna Ab Initio Simulation Package (VASP) [99-103]. Projector augmented wave [104,105] pseudo-potentials with valence-electron configurations of $2s^2\ 2p^4$, $4s^2\ 4p^6\ 5s^2\ 4d^1$, $6s^2\ 5d^3$, and $4s^2\ 4p^6\ 5s^2\ 4d^2$ for the O, Y, Ta, and Zr atoms, respectively, were used. The energy cutoff for the plane wave basis was set to 600 eV. A k-point grid generated with the Monkhorst-Pack method [106] of 11 x 11 x 9 was found to converge energies within 0.1 meV/atom for both the monoclinic and tetragonal cells. Larger supercells maintained the same k-point density by scaling the grid. The formation energies were calculated relative to the lowest energy end-states, *m*-ZrO_2 and *M'*-$YTaO_4$, and normalized per number of atoms according to:

$$\Delta E_f = E^{DFT} - 2X_{YO_{1.5}} E^{DFT}_{YTaO_4} - (1-2X_{YO_{1.5}}) E^{DFT}_{ZrO_2} \tag{4.1}$$

where E^{DFT} without subscript refers to the relaxed energy per atom of a particular configuration and with subscript refers to the relaxed energy per atom of one of the two pure end-states. The units of these energies are meV/atom. The composition, X, is specified in terms of single cation mol fraction to facilitate comparison with the reported ZrO_2-$YO_{1.5}$-$TaO_{2.5}$ ternary phase diagram in [15]. Pure $YTaO_4$, for example, has a composition of 50 mol% $YO_{1.5}$.

4.2 Results

The crystal structures of ZrO_2 are shown in Figure 4.1. Each phase forms a distorted fluorite structure where the cations are in an FCC-like arrangement and oxygens fill the tetrahedral

interstitial sites. In this work, yttrium and tantalum atoms were allowed to substitute for Zr into supercells derived from the primitive *m* and *t*-ZrO_2 unit cells, and the relaxed energies were used to assess the stabilities of various ordering patterns. Figure 4.2 shows the calculated formation energies of all enumerated configurations investigated in this study. The crystal structures for the lowest energy $YTaO_4$ orderings are first identified and explored. The pathways connecting the tetragonal and monoclinic phases in pure ZrO_2 and $YTaO_4$ are then considered. Finally, clustering patterns between Y and Ta in the alloyed materials are examined, beginning with dilute additions of $YTaO_4$ into ZrO_2 and ending with more concentrated additions.

4.2.1 Pure Crystal Structures

The formation energies in Figure 4.2 reveal that a miscibility gap exists between *m*-ZrO_2 and a monoclinic $YTaO_4$ structure at 0 K with no intermediate compounds. In the following sections, the lowest energy ordering of $YTaO_4$ is identified and compared to several of the other low-energy $YTaO_4$ orderings. Subsequently, the pathways connecting the low energy monoclinic structures to their respective tetragonal structures in both ZrO_2 and $YTaO_4$ are analyzed.

The crystal structures of yttrium tantalate

Figure 4.3(a) shows the calculated formation energies of all $YTaO_4$ orderings considered in this study. The three lowest energy orderings, *M*, *M'*, and *M''*, are labeled on the figure and all have monoclinic symmetry, with $E_{M'} < E_M < E_{M''}$. Here *M''* only represents a hypothetical structure that has not been reported in the literature, whereas *M* and *M'* have been experimentally observed. The FINDSYM extension to the ISOTROPY software suite [107] was used to determine the space group for *M'* and *M*, which were found to be P2/c

(#13) and C2/c (#15), in agreement with reference [108]. Although *M'* is the most stable ordering of $YTaO_4$, *M* and *M''* are within 15 meV/atom of *M'*. Schematic depictions of the crystal structures are shown in Figure 4.3(c-e). A common motif in *M*, *M'*, and *M''* is a 2D checkerboard pattern of Y and Ta cations, schematically drawn in Figure 4.3(b). This layer motif serves as the basic building block of the most stable yttrium tantalate phases, whereby each phase is constructed by stacking multiple checkerboard layers and shifting the positions of the layers relative to one another. The checkerboard pattern can be characterized as an ordering of yttrium and tantalum cations over an FCC {100}-type plane. In the monoclinic structures, however, the shape of the layers and positions of the atoms within the layers are slightly distorted relative to their shape and position in the perfect FCC structure.

For each of the monoclinic phases *M*, *M'*, and *M''*, there exists a tetragonal structure with equivalent cation ordering. Pairs of tetragonal and monoclinic structures with the same cation configuration are designated by the same prime notation, e.g. *T* and *M* have the same cation ordering, as do *T'* and *M'*, and *T''* and *M''*. These structures are shown in Figure 4.3(c-e). The space groups of *T'* and *T* were found to be P4/nmb (#125) and $I4_1/a$ (#88), respectively. Interestingly, the tetragonal analogues of the most stable monoclinic orderings are themselves among the most stable tetragonal orderings. However, whereas *M'* is found to be the most stable monoclinic structure, *T* is found to be the most stable tetragonal structure, followed by *T'* and then *T''* ($E_T < E_{T'} < E_{T''}$).

Each pair of tetragonal and monoclinic tantalate phases contain two or more checkerboard layers stacked on top of each other and the shifts between each layer completely characterize the cation ordering (Figure 4.4). The stacking patterns that lead to each pair of phases are best described in reference to the tetragonal structures. In the following notation, a unit cell

vector is shown in bold and the magnitude of each vector, shown in italic font, is the lattice constant. Each tetragonal phase is defined such that $a = b \neq c$. In *T'*, each checkerboard layer forms a {100} plane and the checkerboard layers are stacked along **a**. There are only two layers in the unit cell of this phase and the second is translated relative to the first by **b**/2. In *T''* and *T*, each layer instead forms a (001) plane and the planes are stacked along **c**. Besides the difference in stacking direction, there are distinct shifts of the layers in both structures that lead to a doubling of the unit cell size along the stacking direction **c**. It is instructive to visually compare the structures in Figure 4.4(b-d) in order to understand the similarities and differences between *T'*, *T''*, and *T*. Compared to *T'*, the fourth layer in *T''* is translated so that the yttrium and tantalum cations exchange locations relative to their positions in *T'*. In *T*, both the third and fourth layers are translated. The fourth layer is translated identically to *T''* and the third layer is translated so that the yttrium and tantalum cations also exchange locations compared to their positions in the third layer of *T'*.

Transformation pathways

The differences in both chemistry and atomic configuration between the yttrium tantalate and zirconia phases affect the transition pathways between the tetragonal and monoclinic polymorphs. The pathways are important because they reveal additional contrast between the ZrO_2 and $YTaO_4$ structures and give insight into the dynamical stability of the tetragonal phases. The pathways connecting the *t*-ZrO_2, *T*-$YTaO_4$, and *T'*-$YTaO_4$ phases to their respective monoclinic phases were found by performing nudged elastic band (NEB) calculations, relaxing both strain and atomic coordinates within each cell. For these calculations, 12 atom versions of each structure were used (non-primitive pseudocubic *t*-ZrO_2, primitive *m*-ZrO_2, and primitive *T*, *T'*, *M*, and *M'*-$YTaO_4$).

The minimum energy pathways between *t* and *m*-ZrO_2, *T* and *M*-$YTaO_4$, and *T'* and *M'*-$YTaO_4$ are shown in Figure 4.5(a). The plot shows the energy per atom relative to the stable phases at the compositional extremes (*m* for ZrO_2 and *M'* for $YTaO_4$). A collective distortion path involving both a strain of the lattice and internal shuffles of the atoms within the basis of the unit cell can be tracked with an order parameter η, which is zero for the tetragonal phase and one for the monoclinic phase. The distortions and displacements are taken relative the tetragonal reference frame. Figure 4.5(a) shows that the monoclinic ZrO_2 structure is nearly 40 meV per atom more stable than the tetragonal ZrO_2 structure, which is consistent with the fact that *m*-ZrO_2 is the stable polymorph at 0 K. An energy barrier separates *t*-ZrO_2 from *m*-ZrO_2 along the connecting pathway, a result of the locally positive curvature at $\eta = 0$. The magnitude of the energy barrier, approximately 0.8 meV/atom (10 meV per unit cell), is relatively small but the existence of an energy barrier implies that the tetragonal form of ZrO_2 is dynamically stable. This result is consistent with other estimations of the energy barrier for this structural phase transformation [109,110] and previous phonon calculations that found only real vibrational frequencies in the phonon dispersion curves of *t*-ZrO_2 [19]. In contrast, both the $T \rightarrow M$ and $T' \rightarrow M'$ transition pathways display a qualitatively different shape than that observed for zirconia. The energy curves for both transformations exhibit a negative curvature at $\eta = 0$, showing that there is no energy barrier separating the *T* and *M,* and *T'* and *M'* phases. The implication is that the tetragonal $YTaO_4$ phases are dynamically unstable at absolute zero and only become stable at elevated temperature as a result of large-scale anharmonic vibrational excitations.

A larger slice of the energy landscape, providing broader insight than the minimum energy pathway, can be captured by utilizing strain order parameters (SOPs) [111]. The SOPs track variations in the lattice relative to the high symmetry tetragonal structure and are defined as:

$$\vec{e} = \begin{pmatrix} e_1 \\ e_2 \\ e_3 \\ e_4 \\ e_5 \\ e_6 \end{pmatrix} = \begin{pmatrix} \varepsilon_{xx} + \varepsilon_{yy} + \varepsilon_{zz} \big/ \sqrt{3} \\ \varepsilon_{xx} - \varepsilon_{yy} \big/ \sqrt{2} \\ 2\varepsilon_{zz} - \varepsilon_{xx} - \varepsilon_{yy} \big/ \sqrt{6} \\ \sqrt{2}\varepsilon_{yz} \\ \sqrt{2}\varepsilon_{xz} \\ \sqrt{2}\varepsilon_{xy} \end{pmatrix} \tag{4.2}$$

where *e*'s are the SOPs and the epsilons refer to the individual components of the Hencky strain tensor [111]. The Hencky strain tensor is defined in a Cartesian coordinate system with the *z* axis aligned parallel to the **c** axis of the tetragonal cell and the *x* and *y* axes aligned along **a** and **b**. When the reference crystal has tetragonal symmetry, e_1 and e_3 preserve symmetry, with e_1 describing dilational strain and e_3 describing volume-preserving variations of the c/a ratio of the tetragonal reference crystal. The e_2 strain order parameter describes orthorhombic distortions, while e_4, e_5, and e_6 describe shear strains that further lower the structural symmetry to monoclinic and triclinic.

The $T \rightarrow M$ transformation is special in that the strains taking *T* to *M* can almost fully be captured by e_2 and e_6 ($e_1 = 0.2\%$, $e_2 = 4.5\%$, $e_3 = 0.04\%$, $e_4 = 0$, $e_5 = 0$, $e_6 = 6.7\%$). Thus, the energy landscape for this transformation in six-dimensional strain space can be approximated by a two-dimensional slice through it, varying e_2 and e_6 but setting all other strain metrics equal to 0. The e_2 SOP reduces the symmetry of the tetragonal lattice to orthorhombic by stretching or compressing the square base of the tetragonal lattice. The e_6

SOP further reduces the symmetry to monoclinic by shearing the lattice in the same x-y plane. A total of 231 strained unit cells were created with e_2 ranging from 0 to 0.1 in increments of 0.01 and e_6 from -0.1 to 0.1 in increments of 0.01 relative to the *T* reference cell. The energy of each cell was computed by DFT, allowing only the positions of the atoms to relax. The energy landscape as a function of e_2 and e_6, Figure 4.5(b), exhibits the same qualitative features as that observed in the minimum energy pathway calculated by NEB. However, the tetragonal structure is properly identified as a saddle point in the larger space spanned by e_2-e_6. The absence of an energy barrier for the $T \rightarrow M$ transformation is qualitatively consistent with previous first-principles calculations [112].

4.2.2 Substitution of Yttrium Tantalate into Zirconia

While a miscibility gap between ZrO_2 and $YTaO_4$ is predicted at 0 Kelvin, experiments reveal the existence of a significant degree of $YTaO_4$ solubility in ZrO_2 at elevated temperature [13-15]. Entropy due to the large number of ways of distributing Y and Ta over the cation sublattice of ZrO_2 is responsible for the finite $YTaO_4$ solubility at high temperature. Most solid solutions, while lacking long-range order, nevertheless still exhibit some degree of short-range order at intermediate temperatures due to energetic interactions that favor particular local arrangements over others. To provide insight as to the type of short-range order that might be expected at finite temperature, substitution patterns as yttrium and tantalum are added into ZrO_2 are explored next, beginning with dilute substitutions of $YTaO_4$ and ending with more concentrated additions. Of particular interest is whether or not specific ordering patterns are energetically favored in the tetragonal and monoclinic polymorphs.

Dilute substitution

Dilute orderings of Y and Ta within zirconia were enumerated in 96-atom supercells of the *t* and *m* zirconia unit cells. One yttrium atom and one tantalum atom were allowed to substitute onto the cation lattice. The yttrium atom was placed at the corner of the unit cell and the position of the tantalum atom was variable, effectively changing the yttrium-tantalum pair distance. All degrees of freedom were relaxed in the ~3.2 mol% $YTaO_4$ (3.125 mol% $YO_{1.5}$) configurations. Figure 4.6(a) plots the energy of each tetragonal supercell versus the yttrium-tantalum pair distance. The energy of each configuration is taken relative to the energy of the configuration where the yttrium and tantalum atoms were separated as far apart as possible. The results indicate that the energy is relatively insensitive to the distance between the dopant cations until they become nearest neighbors, where a stabilization of ~0.3 eV/cell (~3 meV/atom) is achieved. Intriguingly, the Y and Ta cations are separated by virtually the same distance in both the nearest neighbor (NN) and next-nearest neighbor (NNN) configurations, yet the orderings exhibit substantially different energies. An important difference in these configurations is the orientation of the Y-Ta pair relative to the oxygen shuffle in *t*-ZrO_2. The shuffle can be viewed as a displacement of the oxygen atoms along the **c**-axis of the tetragonal structure relative to their positions in the cubic phase, depicted by white arrows in Figure 4.1(b) [19]. In the NN configuration, the pair lies in the (001) plane along the [110] direction and hence the pair is oriented perpendicular to the direction of the oxygen shuffle. This configuration is henceforth denoted P$\perp$ and is schematically represented in the second cell drawn in Figure 4.6(e). In the NNN configuration, the pair is instead on a {100}-type plane along a [101]-type direction and thus the pair lies on a plane oriented parallel to the direction of the oxygen

shuffle. This configuration is henceforth denoted P|| and schematically represented in the first cell drawn in Figure 4.6(e). P⊥ is stabilized by ~0.3 eV/cell whereas P|| is stabilized only by ~0.05 eV/cell, suggesting that there is a preference for yttrium and tantalum pairs to be oriented perpendicular to the oxygen shuffle.

Two additional supercells were sampled to further investigate clustering patterns similar to the P⊥ configuration: one in which the P⊥ pair was extended into a single row of alternating yttrium and tantalum atoms and one in which the P⊥ pair was extended into the checkerboard layer of yttrium and tantalum atoms described previously for pure $YTaO_4$, all cells having the same ~3.2 mol% $YTaO_4$ (2 dopant cations out of 32) composition. Row and layer ordering patterns are illustrated in the last two cells drawn in Figure 4.6(e), noting that the depicted cells have larger $YTaO_4$ concentration, namely ~6.7 mol% $YTaO_4$ (4:32 cations) for the row configuration and ~14.3 mol% $YTaO_4$ (8:32 cations) for the layer configuration, so that they can be depicted in the same pseudocubic supercell. In both cases the cells are further stabilized as compared to the P⊥ pair but the checkerboard layer shows the largest stabilization of ~0.6 eV/cell. Therefore, there is a preference for yttrium and tantalum cations to cluster into checkerboard-type arrangements in the *t*-ZrO_2 phase. Similar calculations for the monoclinic ZrO_2 phase, Figure 4.6(b), reveal that configurations where the yttrium and tantalum cations are separated by large distances are energetically competitive with paired configurations in *m*-ZrO_2. Grouping the yttrium and tantalum cations into checkerboard layers results in stabilization (~0.2-0.25 eV/cell) but not as much as that observed for the tetragonal phase. Therefore, the preference for yttrium and tantalum to cluster into checkerboard-type arrangements is stronger in *t*-ZrO_2 than *m*-ZrO_2.

The question arises as to what drives the preference for yttrium and tantalum to cluster into pairs, rows, and layers. The fact that different orientations of yttrium-tantalum nearest neighbor pairs having essentially the same bond length exhibit significantly different energies suggests that size considerations of the cations cannot alone explain the observations. The coordination of the cations by oxygen is dependent on the local arrangement of cations and hence coordination by oxygen serves as a meaningful metric. The coordination of cations by oxygen in various configurations was analyzed via their radial distribution functions (RDFs), as determined by the ASAP extension to the Atomic Simulation Environment (ASE) toolkit [113]. The average effective coordination numbers (ECNs) of each cation by oxygen were calculated using the methodology developed by Hoppe et al. [114], but a value of 8 rather than 6 for the power coefficient was implemented to reflect the eightfold coordination of the zirconium cation in cubic ZrO_2:

$$ECN = \sum_i \exp\left[1 - \left(\frac{l_i}{l_{av}}\right)\right]^8 \tag{4.3a}$$

$$l_{av} = \frac{\sum_i l_i \exp\left[1 - \left(\frac{l_i}{l_{\min}}\right)\right]}{\sum_i \exp\left[1 - \left(\frac{l_i}{l_{\min}}\right)\right]} \tag{4.3b}$$

where i is an index for each oxygen anion, l_i represents the bond length between the cation of interest and ith oxygen, l_{av} is the average weighted bond distance, and l_{min} is the minimum bond distance.

Figure 4.6(c) and (d) show the relaxed energy of each dilute supercell as a function of the ECN of each cation. Overlaid in dotted lines are the ECNs of yttrium and tantalum in *M'*,

M, *T'*, and *T*-$YTaO_4$ as well as the ECN of zirconium in *t* and *m*-ZrO_2. To understand the correlation between the energy of the dilute supercells and the ECN of the cations, it is important to recognize that the yttrium and tantalum cations have preferred coordination by oxygen in the pure $YTaO_4$ structures, with the yttrium ions exhibiting a relatively high ECN (~8, distorted cubic coordination) and the tantalum ions a relatively low ECN (~4, tetrahedral coordination). In the dilute tetragonal cells, the lowest energy configuration is one in which each cation achieves its preferred coordination. Therefore, the checkerboard Y-Ta ordering displayed in this configuration, which is identical to the checkerboard ordering characteristic of the stable $YTaO_4$ structures, allows each cation to adopt its preferred oxygen coordination. More generally, the results suggest that the energy of the dilute tetragonal phase is strongly correlated with the yttrium ECN, which approaches eight as yttrium and tantalum are clustered into pairs, rows, and layers. In contrast, the tantalum and zirconium cations are able to achieve their preferred coordinations in all orderings and hence the energy does not correlate with their ECN. In the monoclinic structures, there is no definitive correlation between the average ECN of any cation and the energy of the supercell even though the most stable checkerboard configuration has tantalum achieving coordination closer to 4 and yttrium closer to 8. The fact that the ECNs in the monoclinic polymorph are relatively insensitive to the atomic ordering is consistent with the fact that the energy of the monoclinic phase is also less sensitive to the ordering pattern in the dilute supercells.

Non-dilute substitution

To determine if the preference to have yttrium and tantalum cluster into checkerboard-type configurations persists at higher doping concentrations, non-dilute orderings of Y and Ta

within *t*-ZrO_2 and *m*-ZrO_2 supercells were enumerated and relaxed. The extent of clustering between Y and Ta cations in each configuration was determined by calculating the average number of tantalum cations within the first cation coordination sphere around yttrium (or equivalently, the average number of yttrium cations within the first cation coordination sphere around tantalum). The average number of Ta cations within the first cation coordination sphere around Y, denoted χ, was calculated using the equation:

$$\chi = \frac{N_{Y-Ta\,pairs}}{N_Y} = \frac{N_{Y-Ta\,pairs}}{N_{Ta}} \tag{4.4}$$

where $N_{Y\text{-}Ta\ pairs}$ is the number of Y-Ta pairs in a particular configuration, N_Y is the number of Y cations in a particular configuration, and N_{Ta} is the number of Ta cations in a particular configuration. Note that $N_Y = N_{Ta}$ in every enumerated configuration. Clustering between Y and Ta cations into pairs, rows, and checkerboard layers results in increasingly larger χ. For example, in the P$\perp$ and P$\parallel$ configurations, $N_{Y\text{-}Ta\ pairs} = 1$, $N_Y = N_{Ta} = 1$, and $\chi = 1$. In the row configuration shown in 4.5(e), $N_{Y\text{-}Ta\ pairs} = 4$, $N_Y = N_{Ta} = 2$, and $\chi = 2$, and in the checkerboard configuration shown in Figure 4.6(e), $N_{Y\text{-}Ta\ pairs} = 16$, $N_Y = N_{Ta} = 4$, and $\chi = 4$. The energy of each configuration was plotted as a function of χ for four different compositions: 12.5, 25, 37.5, and 50 mol% $YO_{1.5}$. Figure 4.7 shows these plots only for structures initialized in the tetragonal phase but those initialized in the monoclinic phase show qualitatively similar features. In this figure, it can be seen that as the composition increases, the average χ increases, as should be expected given the higher probability of having yttrium and tantalum as nearest neighbor pairs for larger atomic fractions of yttrium and tantalum. Most importantly, the low energy configurations for any single composition tend to be those that high values of χ. Visual inspection of a number of the lowest energy

configurations confirmed that these lowest energy supercells had yttrium and tantalum cations clustered in patterns similar to those previously discussed in the dilute region and to the most stable $YTaO_4$ orderings. Therefore, the preference to have yttrium and tantalum cluster into pairs, rows, and checkerboard-type ordering patterns persists in both the *t* and *m*-ZrO_2 phases at higher doping concentrations. Nevertheless, it is notable that some configurations that have large χ have very high energy, indicating that the energy is not solely dependent on the number of Y-Ta pairs. This finding is in agreement with the substitution analysis in the dilute region, which showed that nearest neighbor pairs oriented differently relative to the tetragonal oxygen shuffle have substantially different energies. Thus, although a correlation between energy and number of Y-Ta pairs exists, the energy is also influenced by cation coordination by oxygen, electrostatic interactions, and covalent bonding, which are not taken into account in the clustering metric χ.

4.3 Discussion

The salient findings of this work are: (1) the stability of *M'*-$YTaO_4$ over *M*-$YTaO_4$ at 0 K and the prediction that *T*-$YTaO_4$ is dynamically unstable at absolute zero as opposed to locally metastable, (2) the stability of checkerboard orderings of yttrium and tantalum throughout the entire binary and the associated tendency for short-range order, and (3) the coupling between the orientation of the preferred ordering patterns and the oxygen shuffle in *t*-ZrO_2, which is driven partly by optimizing the cation coordination by oxygen.

The most stable orderings of yttrium tantalate in order of lowest to highest energy at 0 K are found to be *M'*, *M*, and *M''*. Each of these unit cells display monoclinic symmetry and is built by stacking checkerboard layers of yttrium and tantalum. The order of stability for the tetragonal analogues differs from the monoclinic polymorphs: *T*, *T'*, *T''*, in order of lowest

to highest energy. Of the most stable monoclinic and tetragonal $YTaO_4$ structures, only *M'*, *M*, and *T* are experimentally observed, with and without ZrO_2 doping. There has been some confusion in the literature as to whether *M'* or *M* is the stable phase of $YTaO_4$ at low temperature, likely stemming from the variety of different processes and temperatures that are used to synthesize the material [14,15,108,115]. The calculations unequivocally show that *M'* is the stable phase at 0 K. Notably, the stability of *M'* over *M* was also predicted with several other exchange and correlation potentials, including LDA, GGA, and PBEsol. The *M'* structure is stable until T ≈ 1700K [15], where it undergoes a transformation to *T*-$YTaO_4$. Upon cooling, the structure does not transform back to *M'* but rather to *M* [116]. To fully understand the phase evolution pathway, it is necessary to calculate the contribution of vibrational entropy to the Gibbs energy of each phase. However, the first-principles results show that *T* is dynamically unstable at 0 K and hence its vibrational entropy cannot be calculated using conventional phonon theories like the quasi-harmonic approximation. It is thus likely that *T*-$YTaO_4$ is stabilized at high temperature by large-scale anharmonic vibrations [96,117] and that more sophisticated methods to approximate the vibrational entropy must be applied to clarify the transformation pathway.

The formation energies of the alloyed materials suggest that there is a strong tendency for short-range ordering when mixing $YTaO_4$ into *m* and *t*-ZrO_2. The short-range order is related to the checkerboard orderings formed in the low-energy structures of $YTaO_4$, i.e. *M'* and *M*. The most stable configurations are those where the yttrium and tantalum cations form checkerboard layers but other associated configurations such as rows and pairs are also low in energy. Indications of this type of short-range order have been experimentally observed by x-ray techniques in a related system, *viz*. ZrO_2-$YNbO_4$ [23]. In *t*-ZrO_2, the

energy of the ordering patterns is sensitive to the orientation of the Y-Ta clusters relative to the oxygen shuffle. Configurations where the checkerboards are oriented perpendicular to the oxygen shuffle are substantially lower in energy compared to those where they are oriented parallel to the shuffle. The energy difference is partially linked to the ability of each cation to achieve its preferred coordination ($ECN_{Zr} \approx 5$, $ECN_{Y} \approx 8$, $ECN_{Ta} \approx 4$). When the checkerboard is oriented perpendicular to the shuffle, every cation realizes its preferred coordination, whereas a suboptimal coordination is realized for the parallel configuration. The stability of particular orientations of the short-range ordering patterns relative to the tetragonal oxygen shuffle could significantly affect the ferroelastic toughening of *t*-ZrO_2. To understand the effect of the short-range ordering on ferroelastic switching, consider attempting to switch a domain where the cations are ordered like that in the $P\perp$ configuration. Reorientation of the **c**-axis would produce a structure where the cations are instead ordered like that in the $P\parallel$ configuration, which is energetically unfavorable relative to the $P\perp$ configuration. Therefore, the driving force for switching is decreased and a reduction in the extent of ferroelastic toughening is expected. Preliminary toughness measurements confirm that the toughness of the tetragonal phase in the ZrO_2-$YTaO_4$ system is lower than would be predicted based on extrapolations from other systems where short-range order is not observed, for example ZrO_2-$YO_{1.5}$ [16,76]. It is also possible that reorientation can occur by a different mechanism entirely, whereby cations are redistributed by diffusion so that the ordering pattern is oriented favorably to the oxygen shuffle in the switched state.

It is hypothesized that the preference to exhibit checkerboard-like ordering in both the pure and alloyed ZrO_2-$YTaO_4$ materials is related to the valences of the Y^{3+} and Ta^{5+} cations.

Experimentally, all ABO_4 compounds, where A represents a trivalent rare-earth cation and B represents a group five transition metal (Nb, Ta), are reported to form *M′* or *M* [108,118,119]. The ubiquity of the *M'* and *M* crystal structures suggests that the checkerboard pattern is energetically preferred throughout these charge-compensated systems. This likely extends to the formation of checkerboard-type short-range order when dissolving equimolar ratios of these cations into zirconia, but this hypothesized trend merits careful investigation in future work.

4.4 Synopsis

A first-principles study of ordering patterns in the ZrO_2-$YTaO_4$ system was conducted. The results clarify the stability of *M'*-$YTaO_4$ over both *M* and *T*-$YTaO_4$ at 0 K and describe a cation ordering pattern from which the most stable tetragonal and monoclinic $YTaO_4$ polymorphs are built. A preference for Y and Ta to cluster into configurations similar to those observed in the most stable, pure $YTaO_4$ structures is observed as $YTaO_4$ is substituted into *t* and *m*-ZrO_2, with the tendency to cluster being larger in the tetragonal phase. The propensity to order in this manner is attributed to the effect of these ordering patterns on the ability of each cation to achieve its favored anion coordination. The short-range order between Y and Ta could have detrimental effects on the toughening generated by ferroelastic switching in the *t*-ZrO_2 phase. A comparison between the pathways connecting the tetragonal and monoclinic phases in ZrO_2 and $YTaO_4$ demonstrates that the most stable tetragonal $YTaO_4$ phases are dynamically unstable, unlike *t*-ZrO_2, suggesting that ZrO_2 and $YTaO_4$ tetragonal phases likely have substantially different thermodynamics, with implications on which statistical mechanics methods can be used to calculate their finite-temperature properties.

4.5 Figures

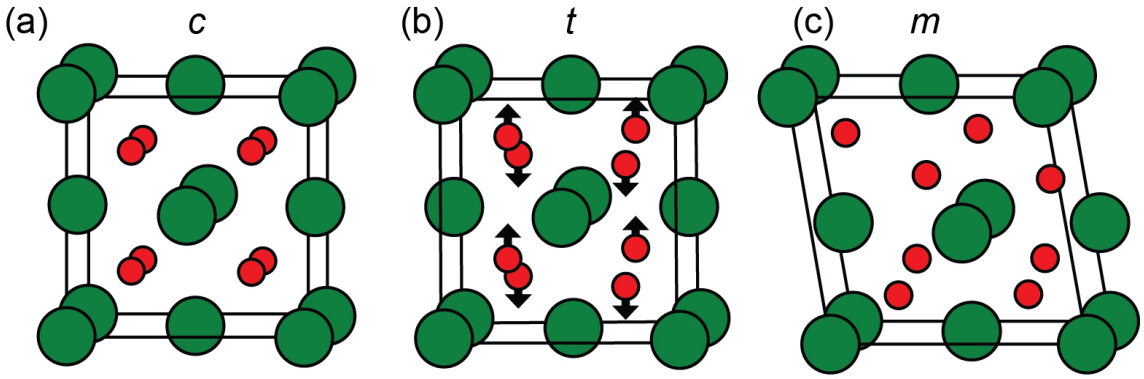

Figure 4.1: Schematic depictions of the ZrO_2 crystal structures. A combination of internal oxygen shuffles and strains can be applied to the high symmetry (a) cubic polymorph to produce the (b) tetragonal and (c) monoclinic polymorphs. Note that the depicted tetragonal structure is the non-primitive (pseudocubic) unit cell, which is shown to illustrate the similarities and difference between each polymorph.

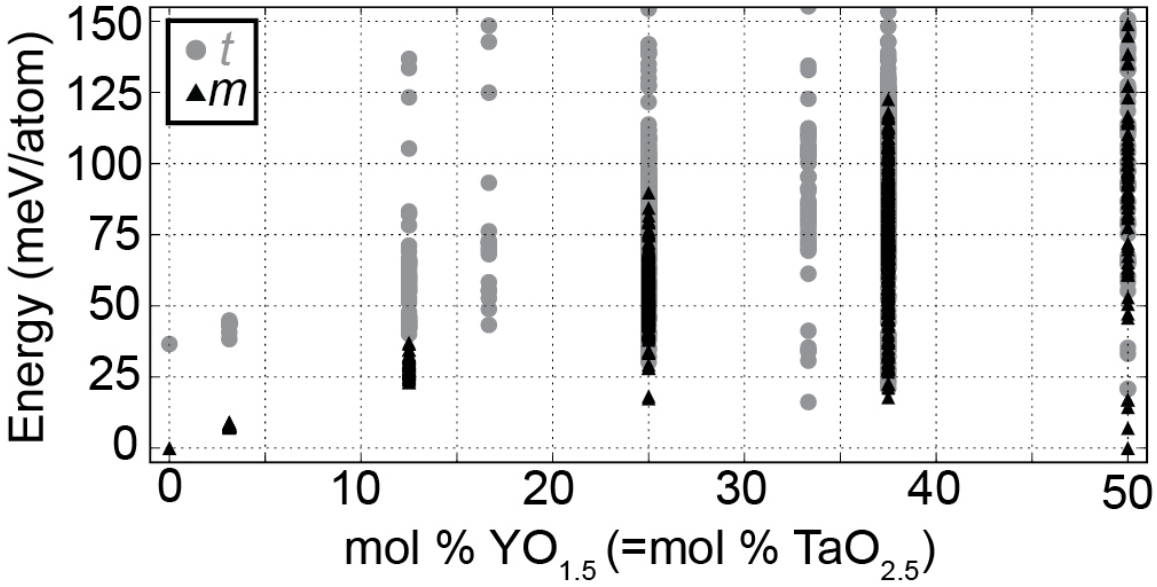

Figure 4.2: Calculated formation energies as a function of composition for every configuration that was initiated as a ordering over *t*-ZrO_2 supercells (grey circles) and *m*-ZrO_2 supercells (black triangles). Energies are taken with respect to the energies of *m*-ZrO_2 and *M'*-$YTaO_4$.

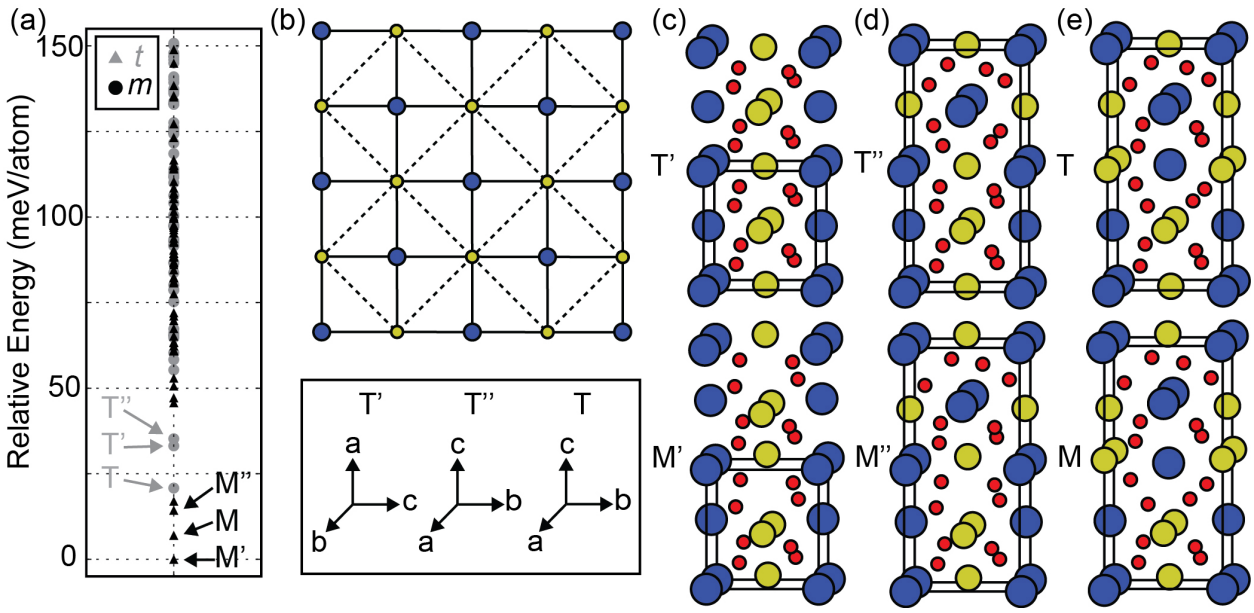

Figure 4.3: (a) Calculated formation energies of all $YTaO_4$ orderings. (b) A checkerboard layer of Y and Ta atoms, which is an ordering over a {100}-type FCC layer, serves as the basic building block of the low energy $YTaO_4$ phases. The dashed lines indicate the lattice vectors for the FCC cation sublattice. Schematic depictions of the (c) *T′* and *M′*-$YTaO_4$ structures, (d) *T″* and *M″*-$YTaO_4$ structures, and (e) *T* and *M*-$YTaO_4$ structures. Blue atoms represent yttrium cations, yellow atoms represent tantalum cations, and red atoms represent oxygen anions. The crystal orientation for the tetragonal polymorphs are displayed below (b). Note that the orientations are chosen to emphasize how each phase is built by stacking the checkerboard layers and that the monoclinic distortions are not evident because of this.

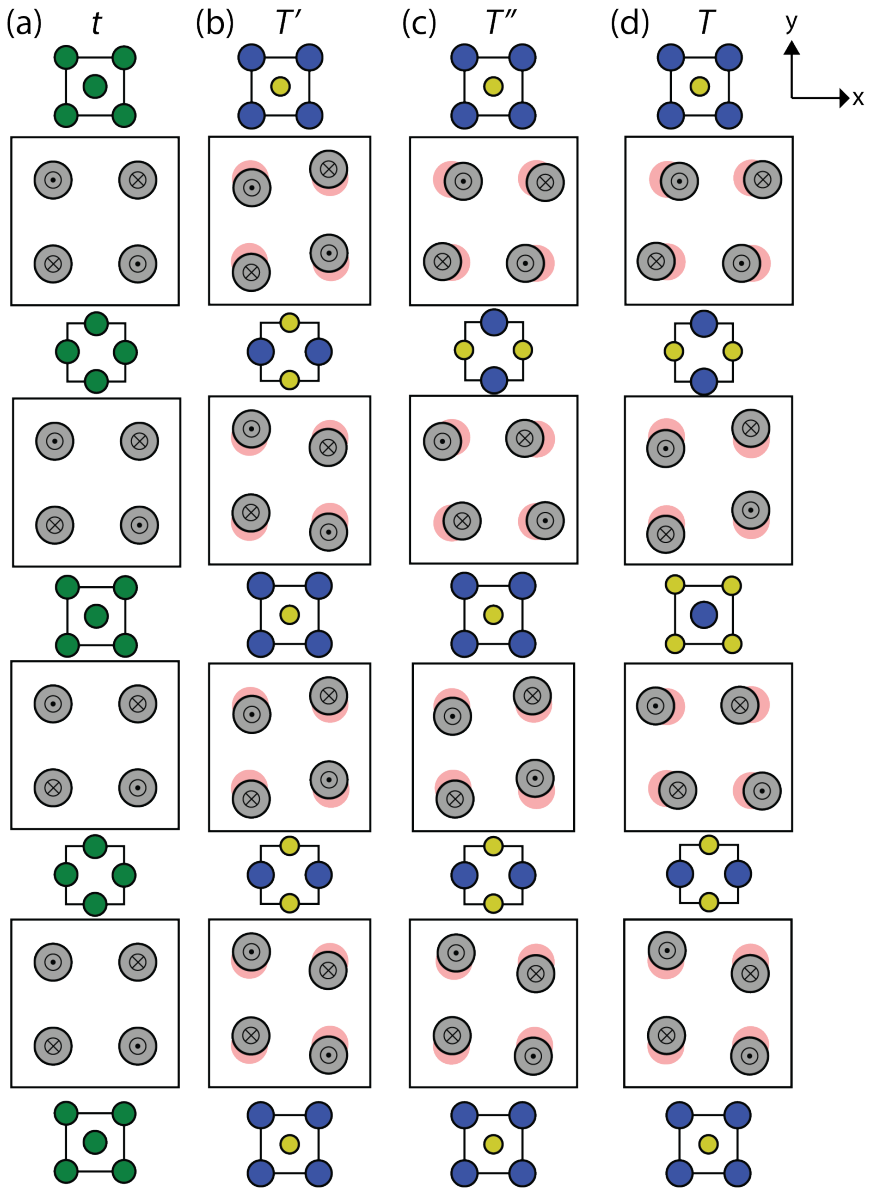

Figure 4.4: Layer-by-layer breakdown of the (a) *t*-ZrO_2, (b) *T′*-$YTaO_4$, (c) *T″*-$YTaO_4$, and (d) *T*-$YTaO_4$ crystal structures. Grey atoms represent oxygen atoms. Layers of oxygen atoms, enlarged to clearly indicate the internal shuffles, are situated between layers of cations. Pink atoms in (b), (c), and (d) represent the in-plane position of the oxygen atoms in cubic and tetragonal zirconia. In and out-of-plane vector notation is used to depict the out-of-plane shuffles, which are qualitatively similar to *t* in all of the depicted structures. A dot represents and upwards shuffle, towards the cation layer above it, and an "x" represents a downwards shuffle, towards the cation layer below it. All in-plane oxygen shuffles move the oxygen atoms closer to the nearest Ta cation, increasing its coordination at the expense of the Y cation. The closest Ta cation is in the layer above it if the out-of-plane shuffle is upwards and visa versa for any given oxygen atom. To a first-order approximation, the oxygens in any one layer shuffle only in the x or y direction, not both.

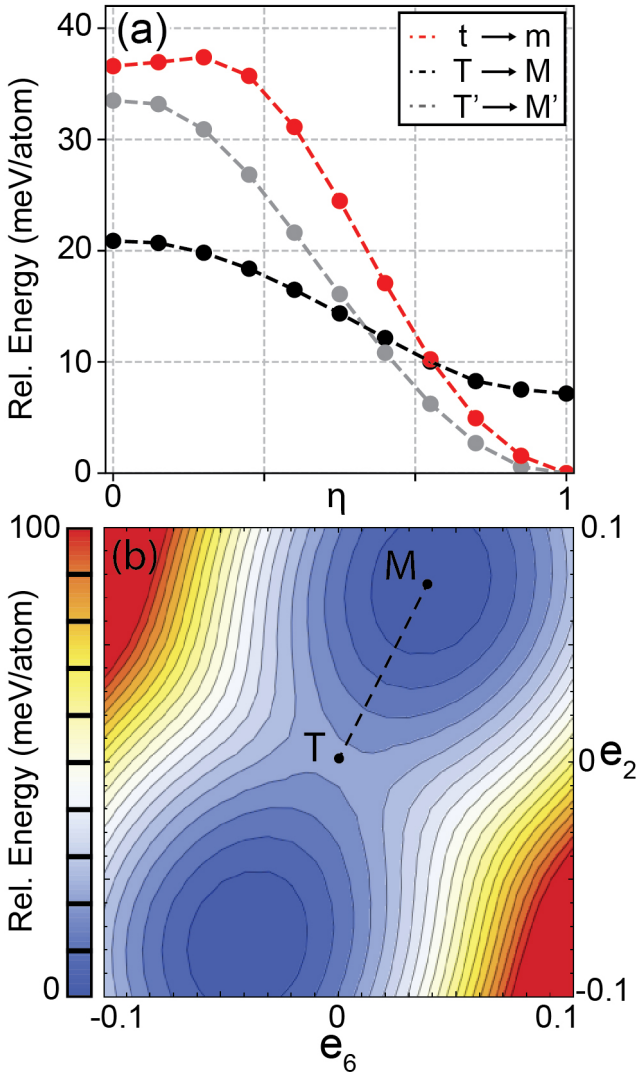

Figure 4.5: (a) The NEB transformation pathways for the *T*-to-*M* and *T*′-to-*M*′ transformations in $YTaO_4$ show qualitatively different behavior than that for *t*-to-*m* transformation in ZrO_2. There is no energy barrier to transform from *T*-to-*M* and from *T*′-to-*M*′; hence both structures are dynamically unstable at 0 K. A larger slice of the energy landscape for the *T*-to-*M* transition can be calculated in e_2-e_6 strain space, (b), where the *T* phase at the origin can be correctly characterized as a saddle point. The dashed black line in (b) approximates the minimum energy pathway for the *T*-to-*M* transformation in (a).

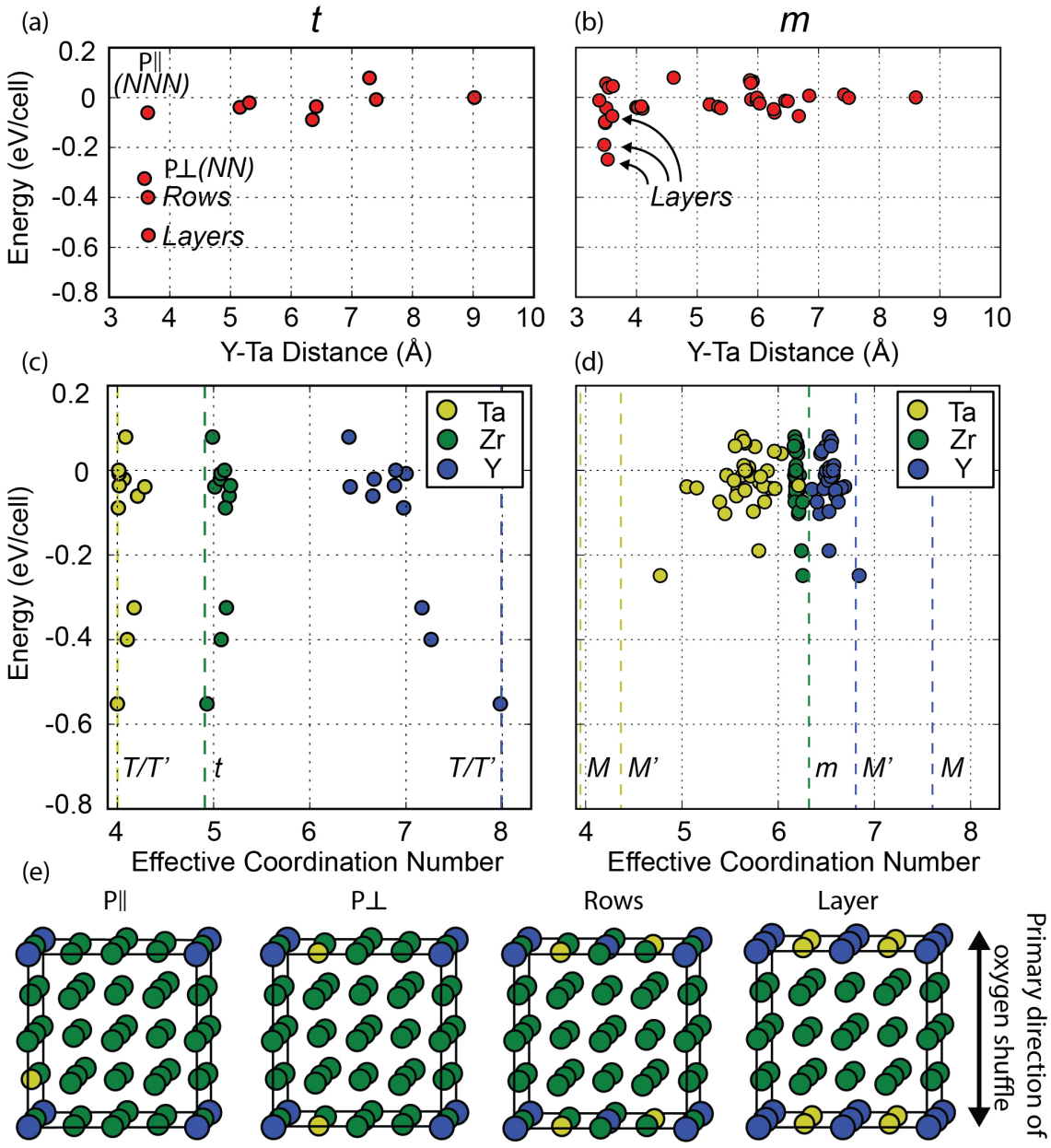

Figure 4.6: Calculated energy variation for supercells of *t*-ZrO_2 (a) and *m*-ZrO_2 (b) doped with 1 yttrium cation and 1 tantalum cation as a function of yttrium-tantalum pair distance. Energies are taken relative to the energy of the cell with Y and Ta separated as far as possible. Energy of each configuration is also plotted as a function of the average effective coordination number (ECN) of each cation in the (c) tetragonal structures and (d) monoclinic structures. Dashed lines indicate the ECNs for the Zr^{4+}, Y^{3+}, and Ta^{5+} cations in *t* and *m*-ZrO_2 and *T*, *T'*, *M*, and *M'*-$YTaO_4$. The most stable configurations are those where all three cations are able to achieve oxygen coordination similar to that in *t* and *m*-ZrO_2 and *T*, *T'*, *M*, and *M'*-$YTaO_4$. Schematic depictions of the P||, P⊥, row, and layer configurations are shown in (e).

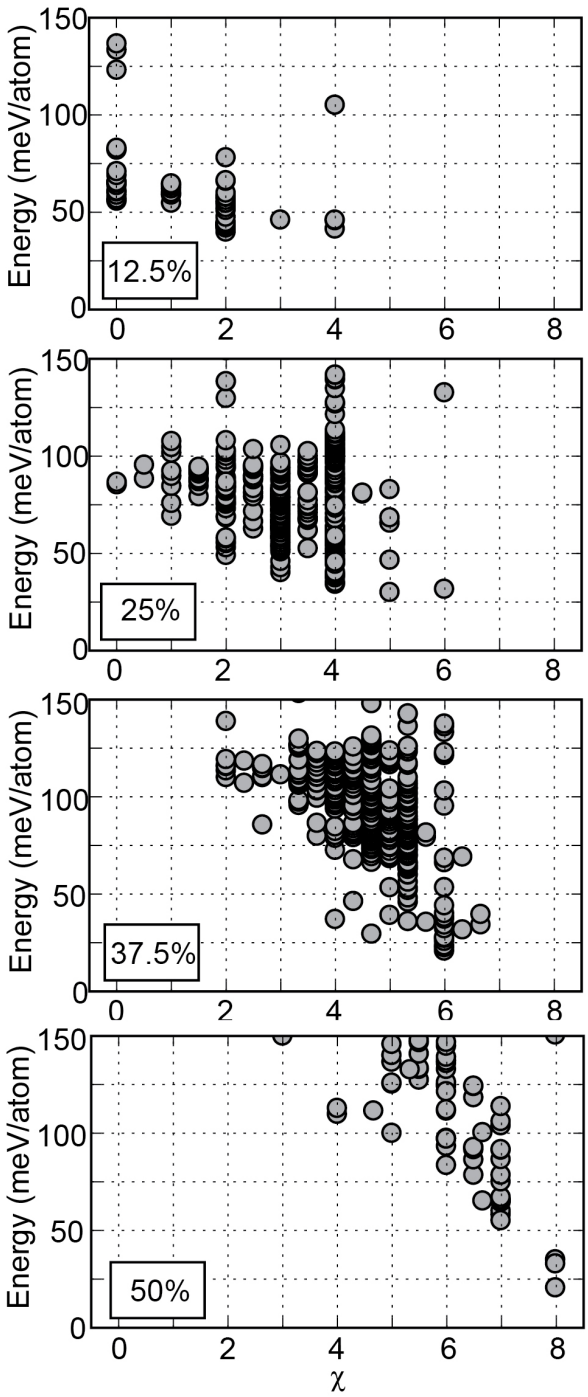

Figure 4.7: Energy as a function of χ for four different *t*-ZrO_2 compositions. The low energy configurations for any single composition tend to exhibit high values of χ and therefore have yttrium and tantalum cations clustered into pairs, rows, and checkerboard-type ordering patterns.

CHAPTER 5: MICROSTRUCTURE OF ZrO_2-$YbO_{1.5}$-$TaO_{2.5}$ EB-PVD THERMAL BARRIER COATINGS

Developing a new family of oxide compositions for thermal barrier coating (TBC) applications requires fundamental understanding of the processability of the materials by established industrial technologies, such as electron-beam physical vapor deposition (EB-PVD). Key issues include conservation of the source material stoichiometry in the deposit, the uniformity of the coating composition, and the development of a sufficiently strain tolerant microstructure. Thermal barrier coatings made from materials in the ZrO_2-$YbO_{1.5}$-$TaO_{2.5}$ system are of particular interest because of the reduced thermal conductivity of the tetragonal phase with equimolar additions of Yb+Ta, ~1.5 $W{\cdot}m^{-1}K^{-1}$, compared to that with equimolar additions of the more explored, Y+Ta combination, i.e. ~2.0 $W{\cdot}m^{-1}K^{-1}$ [11]. Previous work has demonstrated that ZrO_2-$YbO_{1.5}$-$TaO_{2.5}$ TBCs can be deposited by EB-PVD, but found that the coatings exhibit substantial compositional scatter in addition to columns that are broader and more internally segmented than that characteristic of current 8YSZ coatings [72]. The compositional inhomogeneity is potentially problematic, as it is inferred from studies on the ZrO_2-$YO_{1.5}$-$TaO_{2.5}$ system [14,15] and the similarity in chemical behavior between Y and Yb that suggests phase stability is only achievable in a very narrow compositional window. There are also possible deleterious effects on the strain tolerance of the coating from the modifications to the columnar microstructure. However, it has not been reported how the compositional scatter and features of the columnar microstructure change with composition.

This chapter focuses on exploring the influence of composition on the as-deposited microstructure of ZrO_2-$YbO_{1.5}$-$TaO_{2.5}$ EB-PVD TBCs. Three distinct compositions within

the ZrO_2-$YbO_{1.5}$-$TaO_{2.5}$ system were deposited by EB-PVD. The uniformity of the coating chemistry and characteristics of the columnar microstructure were analyzed for each coating. It was found that chemical fluctuations occur only in coatings made from compositions containing tantala and that the scatter increases with the tantala concentration. Compositions with Yb:Ta < 1 (i.e. located on the left side of the ZrO_2-$YbO_{1.5}$-$TaO_{2.5}$ phase diagram in Figure 5.1) exhibit as-deposited microstructures morphologically similar to conventional EB-PVD 8YSZ, while those with Yb:Ta > 1 (located on the right side of the phase diagram) exhibit cauliflower-like microstructures [120] with broader columns comprising many thin and tightly packed elongated crystallites. The segmentation is usually concomitant with a loss of biaxial texture. These observations are used to determine the design space within the ZrO_2-$REO_{1.5}$-$TaO_{2.5}$ that is suitable for thermal barrier coating development.

5.1 Experimental Details

Thermal barrier coatings of nominal compositions ZrO_2-$8YbO_{1.5}$, ZrO_2-$25YbO_{1.5}$-$15TaO_{2.5}$, and ZrO_2-$15YbO_{1.5}$-$25TaO_{2.5}$, henceforth referred to as 8YbSZ, 25Yb15Ta, and 15Yb25Ta, were deposited by EB-PVD at UCSB. The chemical composition and microstructure of each coating were characterized using a combination of techniques including EPMA, SEM, TEM, XRD, and Raman, as described in Chapter 3. For EPMA, the composition of each coating was measured at intervals of 2 μm starting from the thermally grown oxide (TGO). The linear correlations between the Zr, Yb, and Ta concentrations were calculated using the Pearson correlation coefficient:

$$\chi_{X-Y} = \frac{E[(X-\mu_X)(Y-\mu_Y)]}{\sigma_X \sigma_Y} \tag{5.1}$$

where χ is the correlation coefficient, E is the expected value, X and Y are the concentration data points for two of three cations, μ_X and μ_Y are the mean values of the concentrations, and σ_X and σ_Y are the standard deviations of the concentrations.

Several standards were prepared to assist in phase identification of the XRD and Raman spectra. These standards include a non-transformable single-phase tetragonal composition, 16Y16Ta, and a single-phase fluorite (cubic) composition 30Y11Ta. Both of these compositions were synthesized by reverse co-precipitation of mixed precursor solutions but the tetragonal phase was sintered at 1500°C for 24 h while the cubic one was sintered at 1240°C for 100 h. Although the standards contain $YO_{1.5}$ rather than $YbO_{1.5}$, for the purposes of qualitative phase identification, no significant differences in the XRD or Raman spectra are expected.

5.2 Results

Figure 5.1 illustrates the locations of the deposited compositions, 8YbSZ, 25Yb15Ta, and 15Yb25Ta, on the 1500°C isothermal slice of the tentative ZrO_2-$YbO_{1.5}$-$TaO_{2.5}$ phase diagram. It has been shown by earlier work [72] that the ZrO_2-$YbO_{1.5}$-TaO_2 exhibits similar features to the ZrO_2-$YO_{1.5}$-$TaO_{2.5}$ system [14,15] with a slightly extended tetragonal field along the quasi-binary and also a slightly shifted non-transformable region. The 8YbSZ chemistry, which is the Yb-equivalent to 8YSZ, serves as a reference material to understand the microstructure of ZrO_2-$YbO_{1.5}$ EB-PVD coatings (i.e. those without $TaO_{2.5}$ additions). The ternary materials are located close to the compositional region of interest, namely the non-transformable part of the tetragonal phase field, and encompass a moderate range of Ta concentrations while keeping the Zr concentration fixed. The 25Yb15Ta composition is located in the two-phase $t + F$ field and is therefore located in the same phase field as the

8YbSZ composition at 1500°C. The 15Yb25Ta composition is instead located in the three-phase $t + O + T$-$YbTaO_4$ field. The chemical homogeneity of the coatings and the characteristics of the columnar microstructures are detailed below.

5.2.1 Compositional Homogeneity

Figure 5.2 shows cross-sectional overviews of the as-deposited coatings in back scattered electron (BSE) imaging mode. A thin, ~10-20 μm 8YSZ layer was deposited under each ZrO_2-$YbO_{1.5}$-$TaO_{2.5}$ topcoat to serve as a thermochemical compatibility layer with the alumina TGO. (In typical applications this layer also provides increased toughness near the TGO interface, but durability assessment was beyond the scope of this study). Z-contrast fluctuations are evident in the 25Yb15Ta and 15Yb25Ta coatings but not the 8YbSZ coating, suggesting the chemical fluctuations are arising from the co-doping with Ta. Given the relative atomic numbers of the components ($Z_{Zr} = 40$, $Z_{Yb} = 70$, $Z_{Ta} = 73$), the contrast fluctuations reflect primarily variations in the Zr concentration.

In order to quantify the variability of each atomic component in the three TBCs, compositional profiles across the thickness of the coatings were measured by EPMA. The Yb and Ta profiles for each coating are superposed on the cross-sectional images in Figure 5.3. Mean values (μ) and standard deviations (σ) for the Zr, Yb, and Ta concentrations are summarized in Table 5.1. The Zr and Yb concentrations along the thickness of the 8YbSZ coating, Figure 5.3(a), exhibit small fluctuations ($\sigma_{Zr} < 1$ mol% Zr, $\sigma_{Yb} < 1$ mol% Yb) around the mean values of μ_{Zr} = 92 mol% ZrO_2 and μ_{Yb} = 8 mol% $YbO_{1.5}$. The similarity between the nominal and measured compositions in addition to the limited compositional variability demonstrates the exceptional compositional stability of 8YbSZ when deposited by EB-PVD. In contrast, the average measured compositions of the tantala-containing

coatings differ substantially from their nominal compositions and the Zr, Yb, and Ta profiles exhibit significant compositional fluctuations. The magnitude of the fluctuations in the 25Yb15Ta coating (σ_{Zr} = 4 mol% Zr, σ_{Yb} = 2 mol% Yb, σ_{Ta} = 2 mol% Ta) and the difference between the measured and nominal values ($\Delta\mu_{Zr}$ = 0 mol% ZrO_2, $\Delta\mu_{Yb}$ = -2 mol% $YbO_{1.5}$, and $\Delta\mu_{Yb}$ = 2 mol% $TaO_{2.5}$) show that even moderate additions of tantala produce compositional inhomogeneity during EB-PVD deposition. The inhomogeneity becomes more severe when the tantala concentration is increased. The difference between the measured and nominal composition in the 15Yb25Ta coating ($\Delta\mu_{Zr}$ = -7 mol% ZrO_2, $\Delta\mu_{Yb}$ = 1 mol% $YbO_{1.5}$, and $\Delta\mu_{Yb}$ = -4 mol% $TaO_{2.5}$) is significantly larger than in the 25Yb15Ta coating and the magnitude of the fluctuations (σ_{Zr} = 17 mol% Zr, σ_{Yb} = 6 mol% Yb, σ_{Ta} = 12 mol% Ta) are about four, three, and six times as large for Zr, Yb, and Ta, respectively.

Significant linear correlations between the Zr, Yb, and Ta concentrations are observed in the EPMA data. The correlations in the 25Yb15Ta TBC are calculated to be $\chi_{Zr\text{-}Yb}$ = -0.97, $\chi_{Zr\text{-}Ta}$ = -0.94, and $\chi_{Yb\text{-}Ta}$ = 0.81 and those in the 15Yb25Ta TBC are found to be $\chi_{Zr\text{-}Yb}$ = -0.88, $\chi_{Zr\text{-}Ta}$ = -0.97, and $\chi_{Yb\text{-}Ta}$ = 0.74. The signs of the correlations indicate that the Yb and Ta concentrations fluctuate in-phase (i.e. when the Yb concentration increases, so does the Ta concentration) while the Zr and Yb or Ta concentrations fluctuate out-of-phase (i.e. when the Yb or Ta concentrations increase, the Zr concentration decreases). Overlaying the composition profile of the coatings onto the phase diagram, Figure 5.4, clearly shows that the fluctuations are oriented towards and away from zirconia.

5.2.2 Columnar Microstructure and Texture

8YbSZ

Micrographs illustrating the morphology of the 8YbSZ columns after deposition are shown in Figure 5.5. Fracture surfaces along the rotation direction of the coating, Figure 5.5(a), reveal that the columnar structure is uninterrupted at the transition from the 8YSZ sublayer to the 8YbSZ topcoat ; the structure of the latter is generally well defined, exhibiting clear intercolumnar gaps. Based on this micrograph, the columns are tilted approximately 11° relative to the substrate normal. Images of the growth surface in plan view, Figure 5.5(b), reveal that the tips of the columnar grains in the 8YbSZ coating are rough, asymmetric three-sided pyramids with edge lengths ~5-10 μm and inclusion angles of ~120°. A high magnification side-on view of the tips, Figure 5.5(c), helps visualize the shape. Large (~0.05-0.5 μm) faceted steps (sheets) inclined at an angle relative to the columnar axis are evident in the micrograph. The terraces of these steps define one of the faces of the three-sided pyramids, while the ledges of the steps define the other two. The terraces between the steps are not smooth and contain even finer steps that appear to evolve by island-type nucleation and growth.

The shapes of the column tips are related to the crystallographic texture of the coatings [68]. X-ray goniometer scans taken from the coating surface is shown in Figure 5.6. The coating was aligned such that the rotation axis was parallel to the x-ray scanning direction in accordance with previous work [68]. X-ray scans from randomly oriented polycrystalline *t*-ZrO_2 and *m*-ZrO_2 are also displayed as references. The 8YbSZ coating is highly textured in the out-of-plane direction, exhibiting a single prominent reflection belonging to the $(311)_t$ crystal plane. This indicates that the columns are single-phase (*t*-ZrO_2) and oriented along

the $[311]_t$ direction, at variance with the normal out-of-plane texture for 8YSZ which is along the <100] direction [121]. The tetragonality of the crystal structure was also confirmed by Raman spectroscopy (Figure 5.7(a)). Columns oriented along the $[311]_t$ direction in zirconia-based EB-PVD TBCs are expected to display asymmetric three-sided pyramidal tips, assuming that the growth facets in this material have {111}-type habits as they do in zirconia [68]. Therefore, the shape of the tips in this coating are reasonably consistent with that predicted based on the coating texture.

XRD pole figure scans were performed to examine the degree of in-plane orientation and thus allow characterization of the texture as fiber (preferred out-of-plane texture but no preferred in-plane orientation) or biaxial (preferred out-of-plane and in-plane orientation). A {311} pole figure for the 8YbSZ coating, Figure 5.8(a), shows a single strong peak located near the center of the pole figure, confirming the [311] out-of-plane texture. Based on the deviation of the peak from the center of the diagram, the columnar grains responsible for producing the texture are inclined relative to the substrate normal at an angle $\beta \approx 13°$, close to that estimated from the micrograph in Figure 5.5(a). Figure 5.8(b) shows the [220] pole figure for the same coating. Superposing the standard [311] stereographic projection and tilting the projection axis $\varphi = 13°$ would yield an almost equivalent pattern of 220-type spots. The presence of these discrete spots therefore indicates the existence of an in-plane orientation in addition to the out-of-plan texture. The sharpness of the 220-type spots is in agreement with the observation that the ridges of the three-sided pyramids are generally aligned with one another, as can be seen in Figure 5.5(b), which indicates that the columns share similar crystallographic orientations. Based on the standard [311] stereographic

projection, the ridges of the columns are aligned with [110]-type directions and the rotation axis is parallel to a [332]-type direction.

25Yb15Ta

Micrographs illustrating the morphology of the 25Yb15Ta columns after deposition are shown in Figure 5.9. Similar to 8YbSZ, the fracture surface along the rotation direction of the coating, Figure 5.9(a), illustrates that the columnar structure is generally well developed. A variety of column tip shapes, all of which are highly faceted, are observed in the plan view image of Figure 5.9(b). One of the more frequent morphologies is a truncated triangular prism with edge length ~5 μm and inclusion angles of ~90° and ~120°. These prisms are much like the four-sided pyramids typically observed in 8YSZ EB-PVD TBCs but stretched along one of the ⟨110] ridges contained in the (100) plane. It is noted that the direction of the prism ridge is comparable for each column exhibiting that tip morphology. Of the remaining column tips, a substantial fraction of the columns terminate without an easily definable shape. There does not appear to be a significant shared directionality between the ridges of these tips.

The x-ray diffraction spectrum in Figure 5.6 reveals that the 25Yb15Ta coating is highly textured in the out-of-plane direction, exhibiting a single dominant reflection belonging to the $(002)_t$ crystal plane. This indicates that the columns are single-phase (t-ZrO_2) and oriented along the c-axis of the tetragonal crystal structure. The tetragonality of the crystal structure was confirmed by Raman spectroscopy in Figure 5.7(b). The out-of-plane c-axis texture is consistent with that previously reported for 8YSZ EB-PVD TBCs at growth temperatures of 1100°C [68] but the expected shape of the column tips based on the observed texture for 8YSZ was that of a four-sided pyramid, which was not observed in this

co-doped material. The [200] pole figure for the 25Yb15Ta material, Figure 5.8(c), clearly demonstrates the strong out-of-plane texture seen in the goniometer scan. The expected column inclination based on this pole is $\beta \approx 10°$, which is close to $\approx 9°$ tilt predicted from a number of cross-sectional SEM images such as that in Figure 5.2(b). An important distinction between the 25Yb15Ta and 8YbSZ materials is the strength of the biaxial texture. The [220] pole figure for the 25Yb15Ta coating, Figure 5.8(d), exhibits more diffuse diffraction spots relative to those observed in the [220] pole figure for the 8YbSZ coating, suggesting that the in-plane texture in the 25Yb15Ta coating is somewhat weaker. The columnar crystallites are therefore strongly oriented along the [200] direction out-of-plane but exist in a moderate range of in-plane orientations (rotations of the crystal structure about the [200] direction).

15Yb25Ta

The microstructure of the 15Yb25Ta coating is broadly columnar but with notable differences relative to the 8YbSZ and 25Yb15Ta coatings. When viewed along the fracture surface at low magnification, Figure 5.10(a), the columns are coarse and poorly defined, and the intercolumnar gaps are not easily identifiable. A high magnification image near the surface of the coating, Figure 5.10(b), reveals that each column (5-10 μm) is highly segmented and consists of a number of smaller crystallites that are densely packed. Both the size of the column tips (< 1 μm) and the porosity that separates the tips from one another (<< 1 μm) are extremely fine in scale. The high density of the columns results in the relatively planar fracture surface seen in Figure 5.10(a). The small scale of the crystallites precludes detailed examination of their tip morphology by SEM but based on Figure 5.10(c), the column tips are relatively blunt in comparison to those in the 8YbSZ and 25Y15Ta

materials. This “cauliflower”-like microstructure appears to be the effect of the high tantala concentration in the coating, since both the binary material (8YbSZ) and ternary material with lower tantala concentration (25Yb15Ta) exhibited a more typical columnar microstructure.

The cauliflower microstructure is indicative of repetitive nucleation during deposition [120]. Evidence of renucleation can be seen in Figure 5.11(a), which highlights a region of the polished cross-section ~30 μm above TGO. A columnar structure is observed in the bottom third of the image, where the material appears dark in contrast. Based on the chemical profile in Figure 5.3(c), the composition in this region is ~10Yb20Ta. The columns continue to grow until the composition changes abruptly to ~40Yb55Ta, marked by a bright, ~3 μm thick band in Figure 5.11(a). Within this high-Z band, no evidence of the columnar structure can be found. The columns renucleate in the dark layer above this bright band and continue to grow until another high-Z band is reached. To further probe the grain structure of these layers, a lamella was taken from the area indicated by a dashed black line in Figure 5.11(a). The bright field image of the lamella, Figure 5.11(b), demonstrates that small, equiaxed grains exist in the high-Z regions of the coating while columnar grains exist in the lower-Z region. The identity and orientation of the crystallites in the equiaxed region could not be determined due to their fine scale, but the bulk chemistry in this region is so far from the nominal composition (in equilibrium with *T*-$YbTaO_4$ and *P*-$YbTa_3O_9$ [14,15]) that secondary phases should be expected. Nevertheless, the cumulative evidence suggests that re-nucleation is tied to the microstructure of the high-Z bands and therefore the compositional fluctuations that occur during deposition.

The x-ray spectrum from the 15Yb25Ta coating in Figure 5.6 displays a multiplicity of peaks that cannot be attributed solely to *t*-ZrO_2 and *m*-ZrO_2, indicating that the coating is multi-phase. Only a single peak at $2\theta \approx 50°$ can be confidently indexed to the *t*-ZrO_2 phase. The presence of *t*-ZrO_2 was confirmed by Raman spectroscopy as shown in Figure 5.7(c). Although the identity of the second phase(s) could not be determined with the available XRD and Raman data, the existence of multiple peaks in the XRD data demonstrates that a number of orientations of the secondary phase(s) must be present. The location of the *t*-ZrO_2 diffraction peak suggests that the coating has a strong $[220]_t$ out-of-plane texture. The [220] pole figure confirms the $[220]_t$ out-of-plane texture and indicates that the "columns" are oriented nearly perfectly parallel to the substrate normal, which is consistent with the cross sectional micrograph in Figure 5.10. The ring of equal intensity in the $[200]_t$ pole figure indicates that all in-plane orientations of the tetragonal crystal structure are equally likely and therefore that the coating has a fiber rather than biaxial texture. It is hypothesized that the fiber texture is tied to the renucleation of the columns throughout the growth of the coating, since the evolutionary selection process that normally dictates which orientations of the columns survive growth must restart every time renucleation occurs following a layer with higher Ta concentration. It is generally expected that the out-of-plane texture in EB-PVD coatings is generated prior to the in-plane texture [68]. Given the attenuation length of $Cu_{K\alpha}$ radiation in ZrO_2 (6-14 μm in the range 30°-70° 2θ) and the bright compositional bands near the surface in Figure 5.10(a), the $[220]_t$ out-of-plane texture must be generated over a thickness of approximately 5 μm or less. It is not clear over what thickness the in-plane texture would be developed if the columns grow without interruption, but evidently it must be larger than 5 μm.

5.3 Discussion

The salient findings of this part of the dissertation research include the increasing variability of the coating chemistry with increasing nominal concentration of tantala, the preservation of a typical columnar microstructure for compositions with moderate tantala content (Yb:Ta > 1), and the loss of a typical columnar microstructure for materials with high tantala content (Yb:Ta < 1). Several topics pertaining to these observations warrant further discussion: (i) the origin of the chemical fluctuations during EB-PVD deposition, (ii) the implications of the compositional scatter on phase stability of the coatings, (iii) the source of the deviations in columnar morphology, and (iv) the potential significance of the observed microstructures to coating durability.

5.3.1 Origin of the Compositional Variability

Coatings made from binary ZrO_2-$YbO_{1.5}$ materials (8YbSZ) were found to be chemically homogenous within the precision of the EPMA measurements (≈1 mol% of each cation) while those made from ternary ZrO_2-$YbO_{1.5}$-$TaO_{2.5}$ materials (25Yb15Ta and 15Yb25Ta) exhibited significant compositional scatter. Qualitatively similar variability has been observed in a number of multi-component TBC systems such as ZrO_2-CeO_2 [67], ZrO_2-Sm_2O_3 [122,123], ZrO_2-La_2O_3 [124]}, and ZrO_2-$YO_{1.5}$-$NbO_{1.5}$ [125]. The chemical fluctuations are generally attributed to the varying vapor pressures of the oxides in the melt pool of the source material. Compositional fluctuations occur when preferential evaporation of high vapor pressure compounds takes place, which is concomitant with an enrichment of low vapor pressure compounds in the melt pool [67]. Since the vapor pressures dictate the flux of each component over the TBC, they directly determine the composition of the deposit. One method to estimate the vapor pressures of the species during deposition is to

assume that the oxide mixtures decompose into their constituent elements [126] and then calculate the equilibrium partial pressure of the constituent oxide and sub-oxides using relevant thermodynamic data. It is important to note that this approach approximates the activity coefficients as unity, which is increasingly questionable especially when the oxides tend to form compounds like pyrochlores. Figure 5.12 shows the calculated vapor pressures for a number of pure sesquioxide materials in addition to ZrO_2 [126]. The vapor pressures of ZrO_2 and $YbO_{1.5}$ differ by less than an order of magnitude at common pool temperatures (≈3500°C for YSZ [127]). The experimental observation that ZrO_2 and $YbO_{1.5}$ thermal barrier coatings exhibit relatively uniform composition suggests that this difference between vapor pressures is low enough to allow deposition of a compositionally homogenous coating. Although the vapor pressure of $TaO_{2.5}$ is not included in Figure 5.12, it can be estimated in a similar fashion from available thermodynamic data [128]. For simplicity, tantala was assumed to vaporize either as gaseous TaO_2 or TaO but not both:

$$Ta_2O_5(l) \rightarrow 2\,TaO_2(g) + \frac{1}{2}O_2(g) \tag{5.2}$$

$$Ta_2O_5(l) \rightarrow 2\,TaO(g) + \frac{3}{2}O_2(g) \tag{5.3}$$

In order to calculate the partial pressure of the gaseous tantalum species, the partial pressure of oxygen was set to the pressure of the chamber during EB-PVD deposition (5 mTorr). In reality, this value represents an upper limit for the partial pressure of oxygen. Tantalum monoxide is predicted to be the prevalent species at ~3500°C. However, it was found that regardless of the identity of the vaporization product, the vapor pressure of the tantala-containing species in the relevant temperature range is two to three orders of magnitude larger that that of gaseous ZrO_2, which is the reported dominant sublimation product of

molten ZrO_2 [129]. The partial pressures of the tantala suboxide species represent a lower bound, since decreasing the partial pressure of oxygen further increases the suboxide partial pressure. The difference in partial pressure is similar to that between ZrO_2 and La_2O_3, which when deposited together by EB-PVD are known to produce coatings with compositional variability [124].

Although the calculations suggest that preferential evaporation of pure tantala is thermodynamically feasible, the orientation of the chemical fluctuations on the phase diagram in Figure 5.4 suggests that preferential evaporation of tantala alone is not occurring; if this were the case, the concentration data should be scattered along a line of approximately constant tantala. Instead, the orientation of the data suggests that the vapor may contain (sub)oxides originating from vaporization of compounds along the $YbO_{1.5}$-$TaO_{2.5}$ binary. Thermochemical data for these (sub)oxides have not been reported and therefore their vapor pressures cannot be rigorously estimated. It is worth noting that the directionality of the compositional scatter may depend on the rare-earth choice. Most $REO_{1.5}$ sesquioxides vaporize as gaseous REO [129,130] whereas $YbO_{1.5}$ tends to vaporize as gaseous Yb^+ [131]. The propensity of the rare-earth to vaporize in different valence species could influence which species volatilize in the ternary compositions. Lastly, it is possible that two-source evaporation as well as enhanced melt pool control, beam pattern, and crucible design could minimize the composition fluctuations. These strategies have been used to reduce the deviation in chemistry from 20 mol% to 5 mol% in ZrO_2-CeO_2 compositions [67].

5.3.2 Implications of Chemical Variability on Phase Stability

Irrespective of the cause of the compositional fluctuations, their existence has important implications on the phase stability of the coatings. The primary concern involves the stability of the tetragonal phase that forms upon equilibration of the coatings at elevated temperature. The stability of the coating is assessed by comparing the predicted compositions of the equilibrium tetragonal phase (based EPMA data points in Figure 5.4) to the position of the estimated $C_0(t/m)$ line at room temperature. The coating is considered phase stable if each measured EPMA data point produces a non-transformable tetragonal phase after equilibration, noting that transformations from *T* to *M*-$YbTaO_4$ may still be possible when cooling from temperatures of order ~1500°C. The 8YbSZ composition, although being deposited as a kinetically stabilized non-transformable tetragonal phase, *t'*, is located in the two-phase *t*-ZrO_2 + *c*-ZrO_2 field and therefore decomposes upon aging into equilibrium tetragonal and cubic phases along the ZrO_2-$YbO_{1.5}$ binary. The equilibrium concentration of $YbO_{1.5}$ in *t*-ZrO_2 is less than that required for non-transformability, similar to the ZrO_2-$YO_{1.5}$ system, and therefore this composition is not phase stable [132]. The 25Yb15Ta composition is also deposited as a non-transformable tetragonal single phase in the two-phase *t*-ZrO_2 + *c*-ZrO_2 field but, unlike 8YbSZ, the expected tetragonal phase after equilibration at 1500°C is non-transformable. Compositional fluctuations during deposition results in a range of chemistries being deposited but all measured compositions fall into a region of the phase diagram where the equilibrium tetragonal phase that is generated upon decomposition is non-transformable. In principle, the 15Yb25Ta composition should behave similarly to the 25Yb15Ta chemistry despite its location in a different phase field, *t*-ZrO_2 + *O*-$Zr_6Ta_2O_7$ + *T*-$YbTaO_4$. However, the increased amount of compositional scatter produces

select regions of the coating that are sufficiently rich in ZrO_2 to equilibrate into a mixture of phases containing transformable *t*-ZrO_2. As a result, coatings with nominal composition located close to the non-transformable phase field but with Yb:Ta < 1 (i.e. on the right side of the phase diagram) are susceptible to the tetragonal-to-monoclinic phase transformation upon equilibration. This likely extends to coatings with nominal compositions located in the non-transformable part of the tetragonal phase field (Yb:Ta =1). However, it must be noted that constraint from surrounding non-transformable material may delay or prevent the tetragonal-to-monoclinic transformation from occurring in these coatings, but this remains the subject of future work [61].

5.3.3 Source of the Microstructural Variations

A number of factors related to coating composition could drive the observed variation in the columnar morphology, including the homologous temperature of the material (T_{dep} / $T_0(L/S)$) [126,133], the energies of crystalline defects such as dislocations and surfaces[68,134], and the nucleation of secondary phases.

The most likely cause of the [311] texture and three-sided morphology of the column tips in the 8YbSZ coating is a modification of defect energies because the homologous temperature of 8YbSZ is very close to that of 8YSZ at 1100°C (0.454 vs 0.446, respectively) [135,136]. The multitude of aligned growth steps on the column tips suggests the occurrence of dislocations during deposition. The dislocations could act as preferential attachment sites for the condensing adatom species and promote the growth of a particular crystalline facet.

Factors pertaining to the melting temperature and crystalline defect energies could be at play for the 25Yb15Ta material. Although the liquidus surface for the ZrO_2-$YbO_{1.5}$-$TaO_{2.5}$ ternary system has not been calculated, the relatively lower melting point of $RETaO_4$

compared to ZrO_2 and Yb_2O_3 (2050°C for $YTaO_4$ [137] compared to 2700°C and 2400°C for ZrO_2 and Yb_2O_3) suggests that both the 25Yb15Ta and 15Yb25Ta compositions likely have a lower, albeit different, melting point and hence higher homologous temperature than 8YSZ and 8YbSZ. This speculation is supported by the flatness and high degree of faceted growth observed on the column tips of the 25Yb15Ta coating. The variability in the in-plane orientation of the columns could be a result of changes to the relative surface energies of the crystal, which determine the growth facets of the columnar crystallites. Short-range ordering between the Yb^{3+} and Ta^{5+} cations, which should be expected given the results in Chapter 4, could influence the distribution of cations in the crystalline lattice and therefore modify the surface energies

The loss of the classic columnar morphology in the 15Yb25Ta coating is likely a result of the chemical fluctuations that occur on deposition. Figure 5.11 clearly shows that regions of increased $YbO_{1.5}$ and $TaO_{2.5}$ content contain equiaxed secondary phases that would interrupt the development of the columnar morphology. The columns renucleate above these regions and grow by the usual evolutionary selection mechanism until another chemical fluctuation again causes termination of the columnar structure.

5.3.4 Potential Implications of Microstructure Variability on Durability

Since the columnar structure is integral to the strain compliance of EB-PVD TBCs, the observed columnar morphologies have important consequences on coating durability. Aside from the peculiarities in the shape and texture of the 8YbSZ and 25Yb15Ta topcoats, the general similarity in appearance of the columns and intercolumnar gaps to that typical of 8YSZ TBCs suggests that the coatings have the requisite in-plane compliance to survive thermal cycling. In contrast, the dense packing of crystallites in the 15Yb25Ta coating likely

results in a relatively larger in-plane elastic modulus, thereby increasing any thermomechanical stresses on top of the transformation stresses. This is exacerbated in the regions of the coating that are enriched in $YbO_{1.5}$ and $TaO_{2.5}$, as Figure 5.11 shows that these regions are particularly dense. Although the relative densities of the coatings were not measured, the relatively flat fracture surface of the 15Yb25Ta coating relative to the 8YbSZ and 25Yb15Ta materials, particularly in the high-Z bands, supports the idea that the 15Yb25Ta coating is substantially more dense and hence has a higher in-plane modulus. Therefore, coatings made from chemistries with Yb:Ta > 1 likely have shortened lifetimes relative to 8YbSZ and 25Yb15Ta.

5.4 Synopsis

The results in this chapter highlight the difficulties in fabricating ZrO_2-$YbO_{1.5}$-$TaO_{2.5}$ thermal barrier coatings by electron beam physical vapor deposition. Compositional fluctuations are observed in coatings made from Ta-containing materials. The variations in chemistry are undesirable from the point of view of phase stability, as local parts of the coating may drift into a region of the phase diagram where a transformable tetragonal phase is expected. Based on the increasing amounts of compositional scatter with increasing $TaO_{2.5}$ concentration, coatings made from compositions close to the non-transformable tetragonal phase field but with Yb:Ta > 1 can be fabricated so that phase stability is retained at equilibrium while those with Yb:Ta ≈ 1 and Yb:Ta < 1 could be susceptible to transformations upon thermal cycling. The variations in chemistry are also undesirable from the point of view of microstructural strain tolerance, since the large compositional fluctuations that occur in high-tantala content materials can prevent the formation of a well-defined columnar structure. The loss of the classic columnar structure occurs due to

renucleation of the columns following severe compositional fluctuations. The continual termination and renucleation of the columns in these areas leads to a very finely segmented columnar structure that is denser than that characteristic of 8YSZ TBCs. It is anticipated that the tight packing of the columns would lead to a debit in the durability of these coatings.

The results help identify the most promising region of compositional space for TBC development in ZrO_2-$REO_{1.5}$-$TaO_{2.5}$ systems. The cumulative evidence supports the idea that EB-PVD TBCs in the ZrO_2-$REO_{1.5}$-$TaO_{2.5}$ systems will need to be fabricated in the multi-phase regions where RE:Ta > 1. Therefore, the nominal compositions of these materials will be located in the two-phase field with *t*-ZrO_2 + *c*-ZrO_2 or in the three-phase field with *t*-ZrO_2 + *c*-ZrO_2 + *M'*-$YbTaO_4$. The choice of rare-earth stabilizer is expected to change the size of the compositional region that is safe for EB-PVD deposition, but qualitatively similar compositional fluctuations and changes to the columnar microstructure are expected for trivalent rare-earth cations of size similar to that of Y^{3+} and Yb^{3+}. The study illustrates why probing and understanding the processability of thermal barrier oxides to conventional deposition techniques is vital towards developing next-generation thermal barrier coatings.

5.5 Tables and Figures

Table 5.1: The measured average values (μ) and standard deviations (σ) of the Zr, Yb, and Ta cations in the EB-PVD ZrO_2-$YbO_{1.5}$-$TaO_{2.5}$ thermal barrier coatings.

Nominal Composition	μ_{Zr} mol%	σ_{Zr} mol%	μ_{Yb} mol%	σ_{Yb} mol%	μ_{Ta} mol%	σ_{Ta} mol%
8YbSZ	92	< 1	8	<1	-	-
60Zr25Yb15Ta	60	4	23	2	17	2
60Zr15Yb25Ta	53	17	16	6	31	12

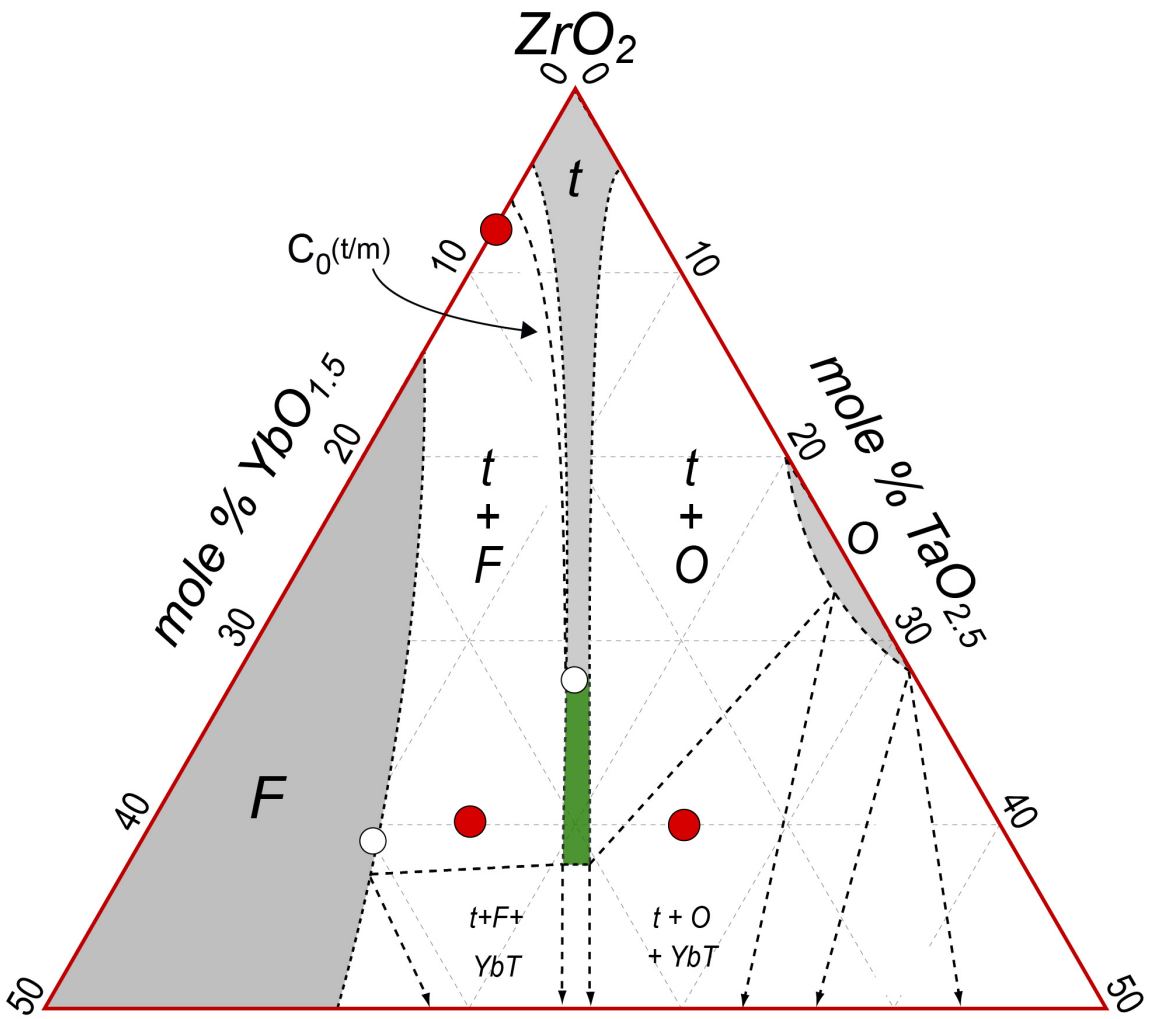

Figure 5.5: The compositions deposited by EB-PVD, 8YbSZ, 25Yb15Ta, and 15Yb25Ta, are shown by red dots overlaid onto the tentative 1500°C isothermal slice of the ZrO_2-$YbO_{1.5}$-$TaO_{2.5}$ phase diagram. White dots indicate the compositions of the standards used for phase identification, 16Y16Ta and 30Y11Ta. The features of the diagram are generally adapted from that for ZrO_2-$YO_{1.5}$-$TaO_{2.5}$ with the solubility and transformability range of the tetragonal phase adjusted from experimental results. The green part of the tetragonal phase field highlights the proposed region of non-transformability.

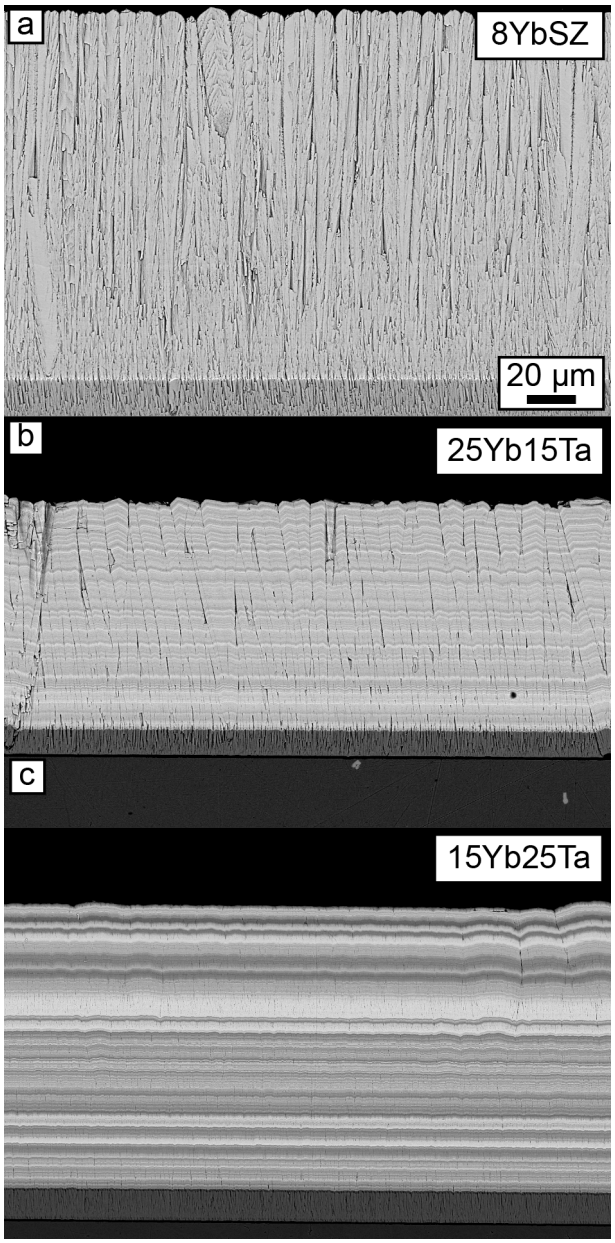

Figure 5.6: Back scatter electron images from the 8YbSZ, 25Yb15Ta, and 15Yb25Ta thermal barrier coatings (top-to-bottom, respectively) reveal progressively larger contrast fluctuations throughout the thickness of the coatings. The images suggest increasing chemical scatter at higher Ta concentrations.

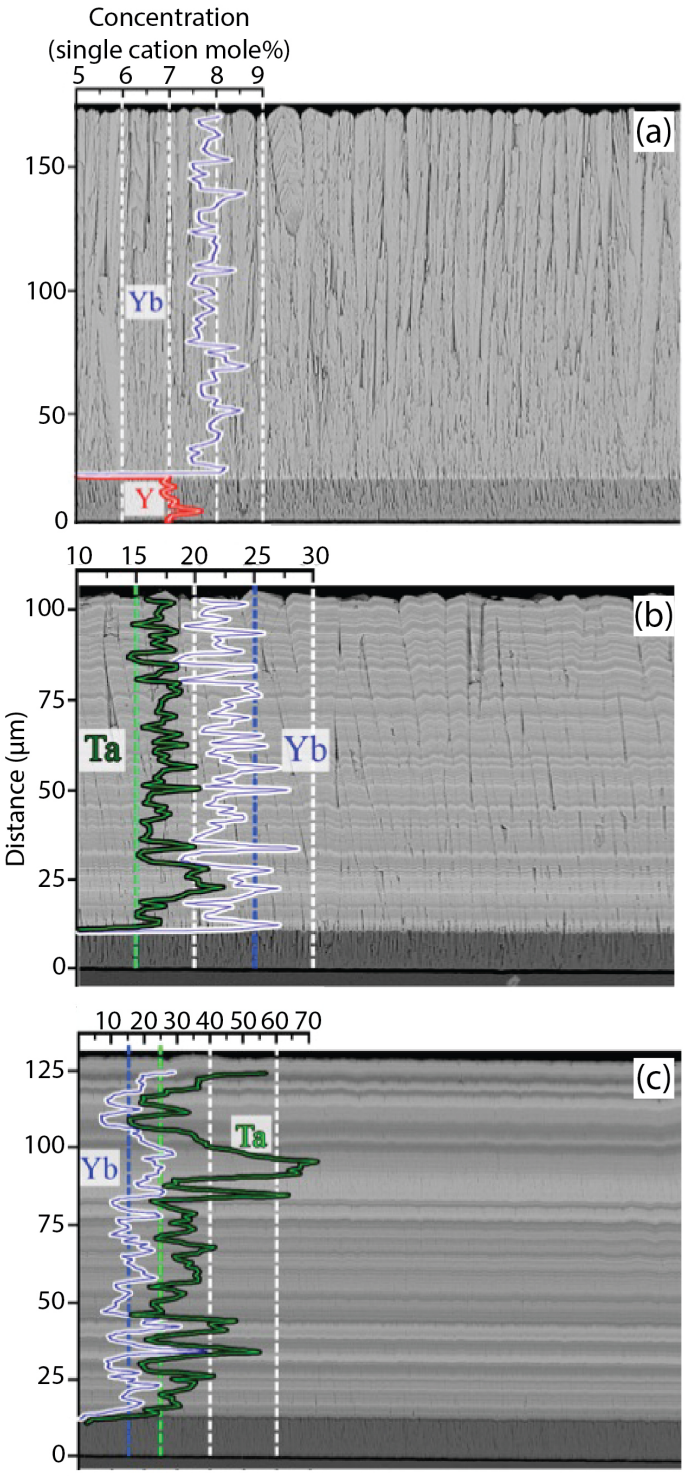

Figure 5.3. Yb and Ta compositional profiles in the (a) 8YbSZ, (b) 25Yb15Ta, and (c) 15Yb25Ta EB-PVD coatings. The nominal concentration of Yb and Ta are shown by blue and green dotted lines. Increasing Yb and Ta fluctuations are observed as the Ta concentration increases. Note the difference in composition scales among the 3 different microstructures.

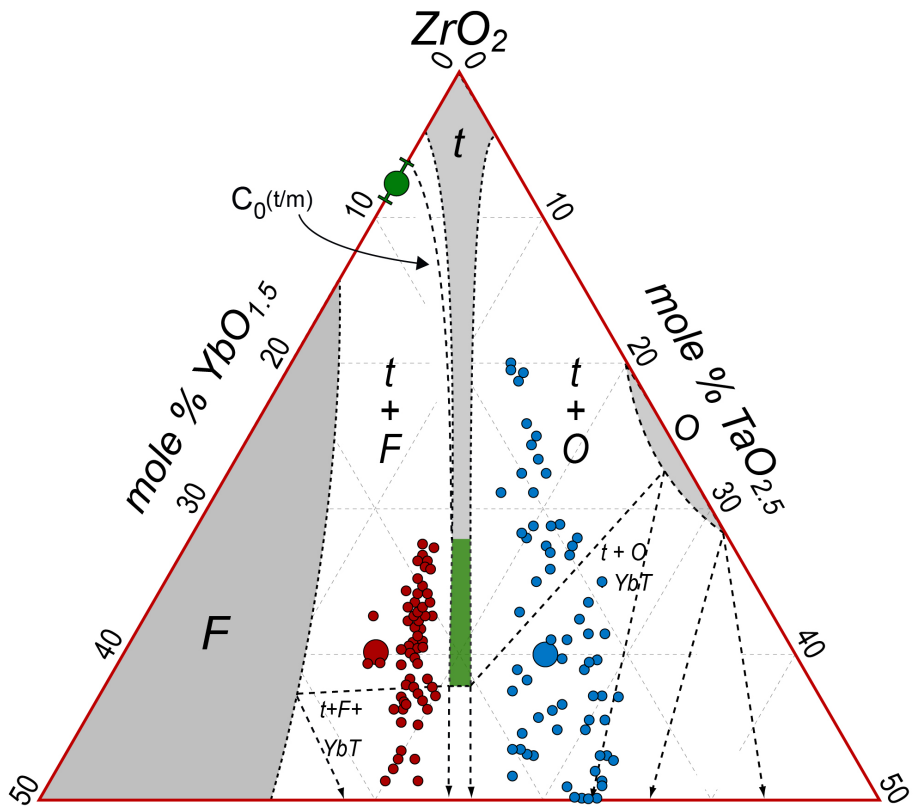

Figure 5.4: The composition profiles of the 8YbSZ (green), 25Yb15Ta (red), and 15Yb25Ta (blue) coatings superposed onto the proposed 1500°C isothermal slice of the ZrO_2-$YbO_{1.5}$-$TaO_{2.5}$ phase diagram.

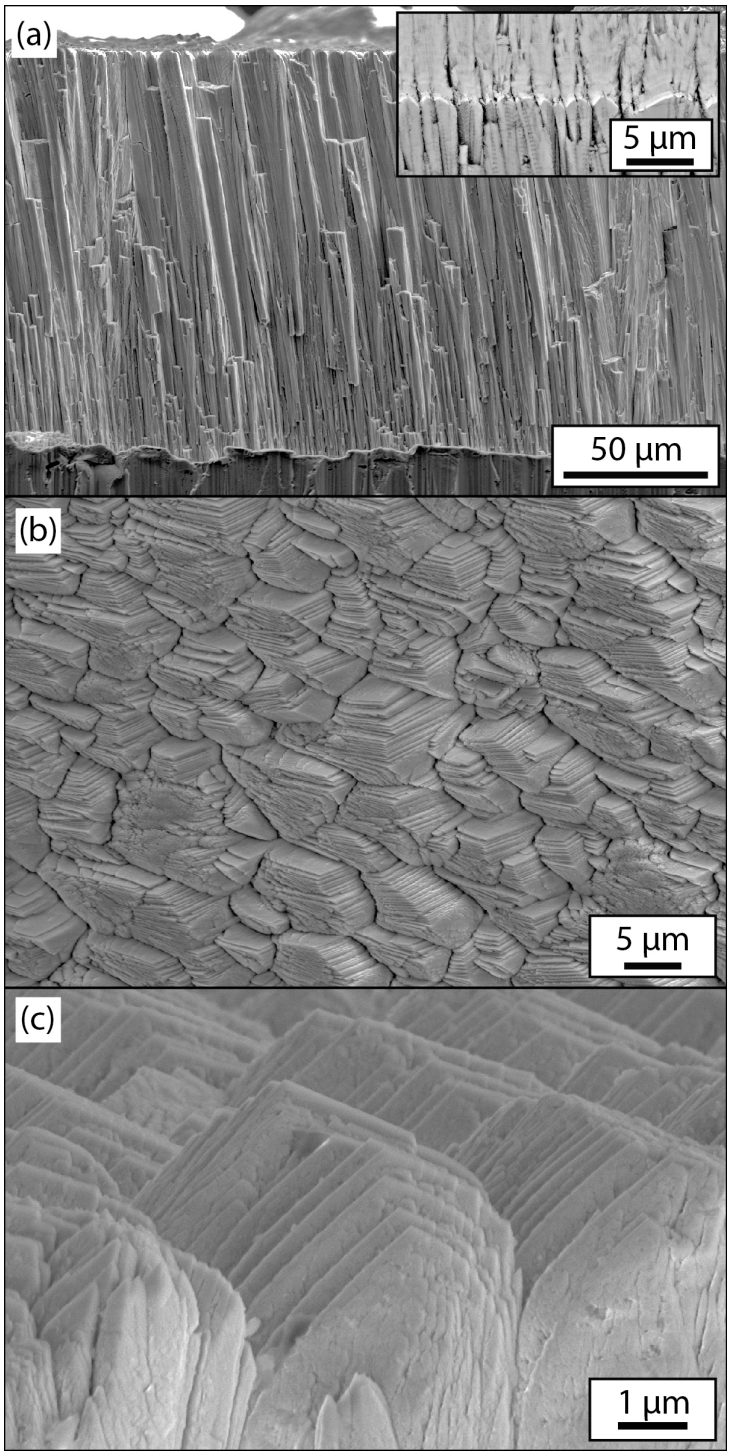

Figure 5.5: (a) A cross-sectional fracture surface along the rotation direction of the 8YbSZ coating reveals a fully developed columnar structure. The columnar structure is uninterrupted at the transition from the 8YSZ sublayer to the 8YbSZ topcoat (inset). The column tips, shown in plan view in (b) and from the side in (c), have an irregular appearance described best as asymmetric three sided pyramids. The tips are formed by steps or sheets oriented at an angle to the columnar axis.

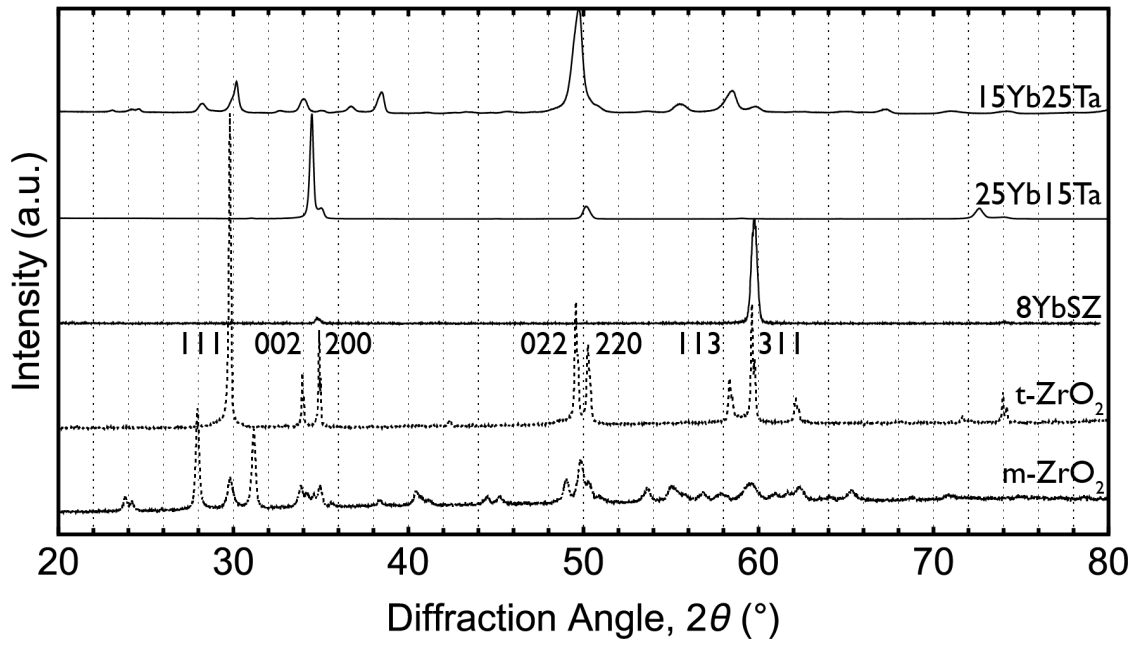

Figure 5.6: Goniometer x-ray diffraction scans for the three coatings were used to determine the out-of-plane texture. The 8YbSZ coating has a strong $[311]_t$ out-of-plane orientation, the 25Yb15Ta has a strong $[002]_t$ out-of-plane orientation, and the 15Yb25Ta has a strong $[220]_t$ out-of-plane orientation. While the 8YbSZ and 25Yb15Ta coatings appear to be single phase (t-ZrO_2), the 15Yb25Ta is multiphase (t-ZrO_2 + …) The secondary phase could not be identified by XRD.

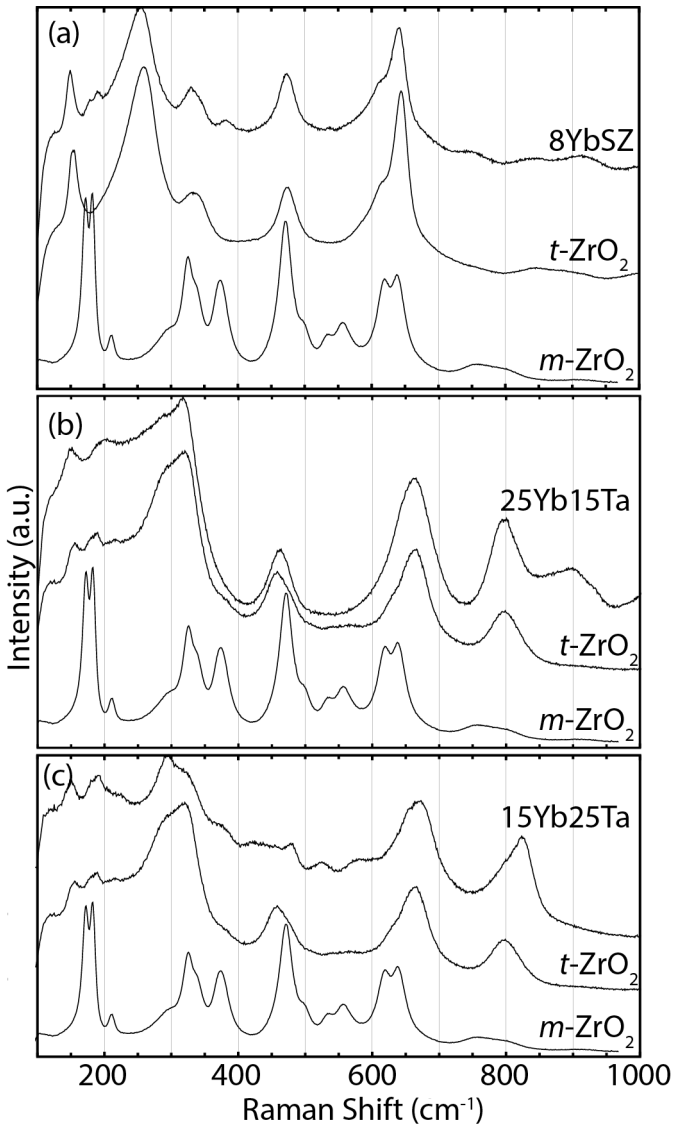

Figure 5.7: Raman spectra from the coatings were used to confirm the tetragonality in the coatings, since the tetragonality cannot be established from the XRD scans due to the out-of-plane texture. Peaks belonging to *t*-ZrO_2 are seen in all of the coatings, but additional peaks that cannot be ascribed to *t*-ZrO_2 nor *m*-ZrO_2 are observed in the 15Yb25Ta coating. Note that the *t*-ZrO_2 scan shown in (a) is for that for a binary YSZ tetragonal phase while that shown in (b) and (c) is that for a ternary ZrO_2-$YO_{1.5}$-$TaO_{2.5}$ tetragonal phase.

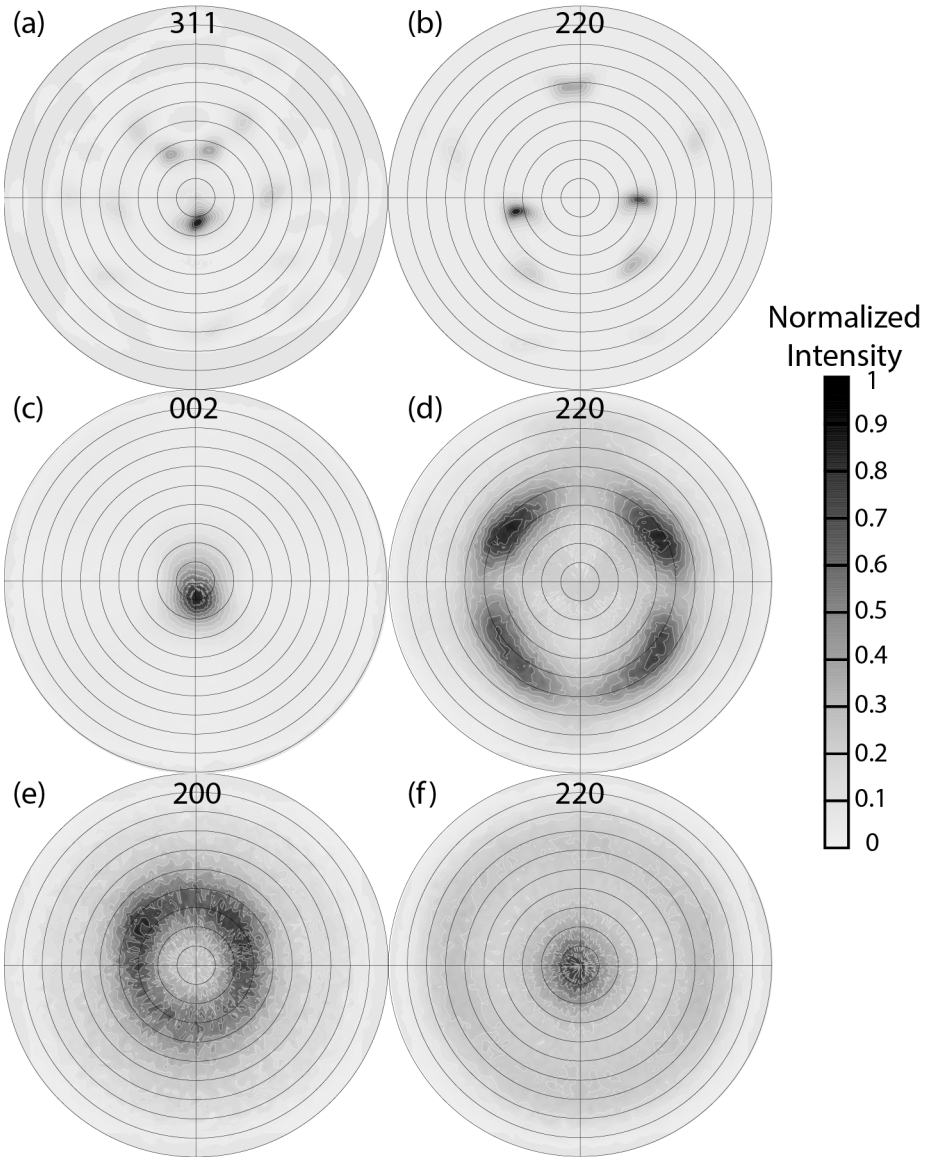

Figure 5.8: Pole figures were used to confirm the out-of-plane texture established by XRD and determine any in-plane texture of each coating. The 311 pole figure for the 8YbSZ coating, (a), confirms the 311 out-of-plane texture for this TBC and the 220 pole figure, (b) indicates a strong biaxial texture. Similarly, the 200 and 220 pole figures for the 25Yb15Ta coating, (c) and (d), confirm a biaxial texture in the 25Yb15Ta coating; however, the diffusivity of the 220 diffraction spots suggest that a range of orientations of the 220 planes exist at the surface of the coating. The 15Yb25Ta coating has a moderate 220 out-of-plane texture, (f), but a fiber (200) in-plane texture, (e). The fiber texture is garnered from the ring-like appearance of the 200 pole.

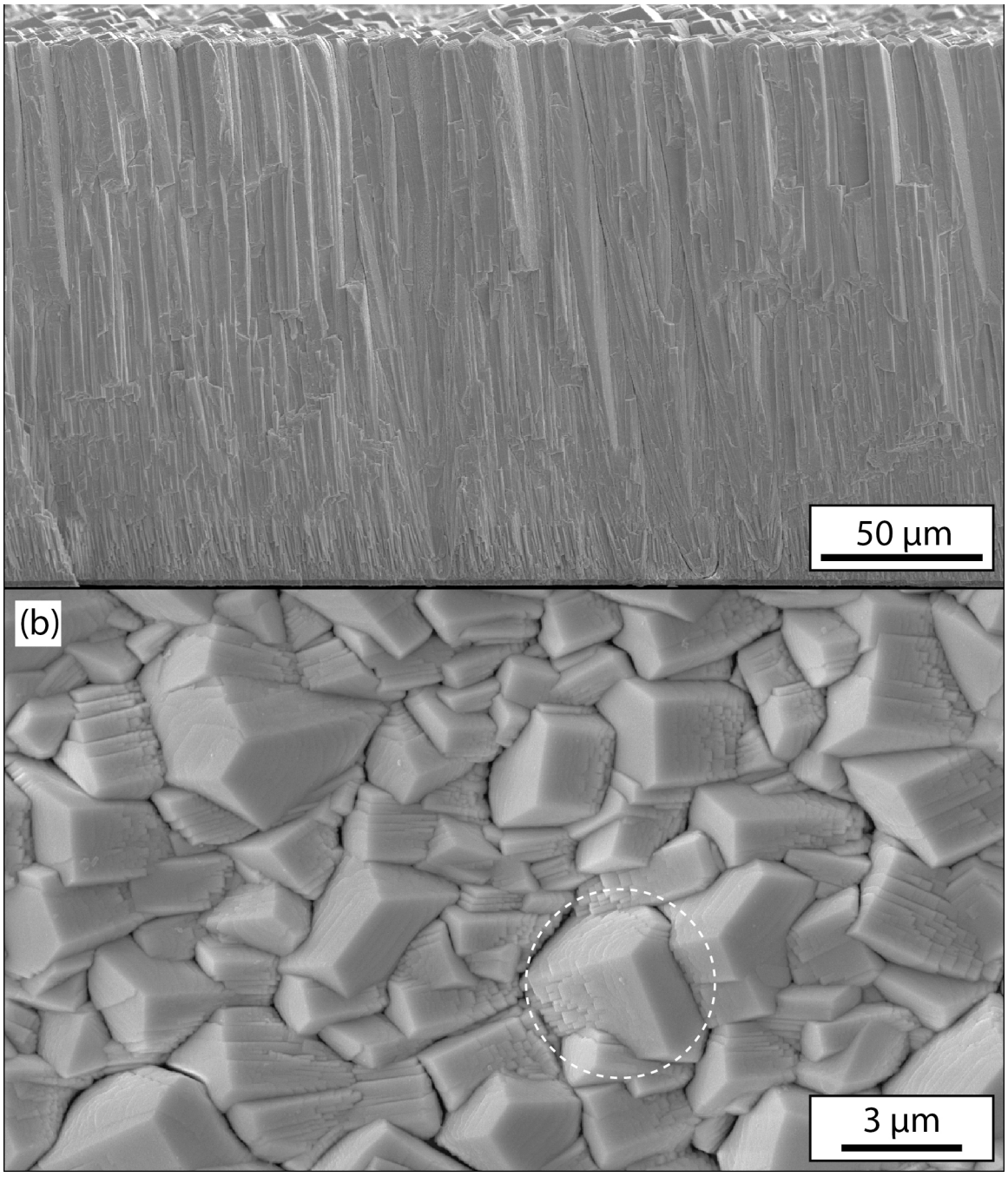

Figure 5.9: (a) A cross-sectional fracture surface along the rotation direction of the 25Yb15Ta coating reveals a fully developed columnar structure near the surface of the coating. Faceted column tips are observed when looking at the coating in plan view, (b), but the shapes of the tips are highly variable. The dashed white circle illustrates a tip having the truncated triangular prism shape.

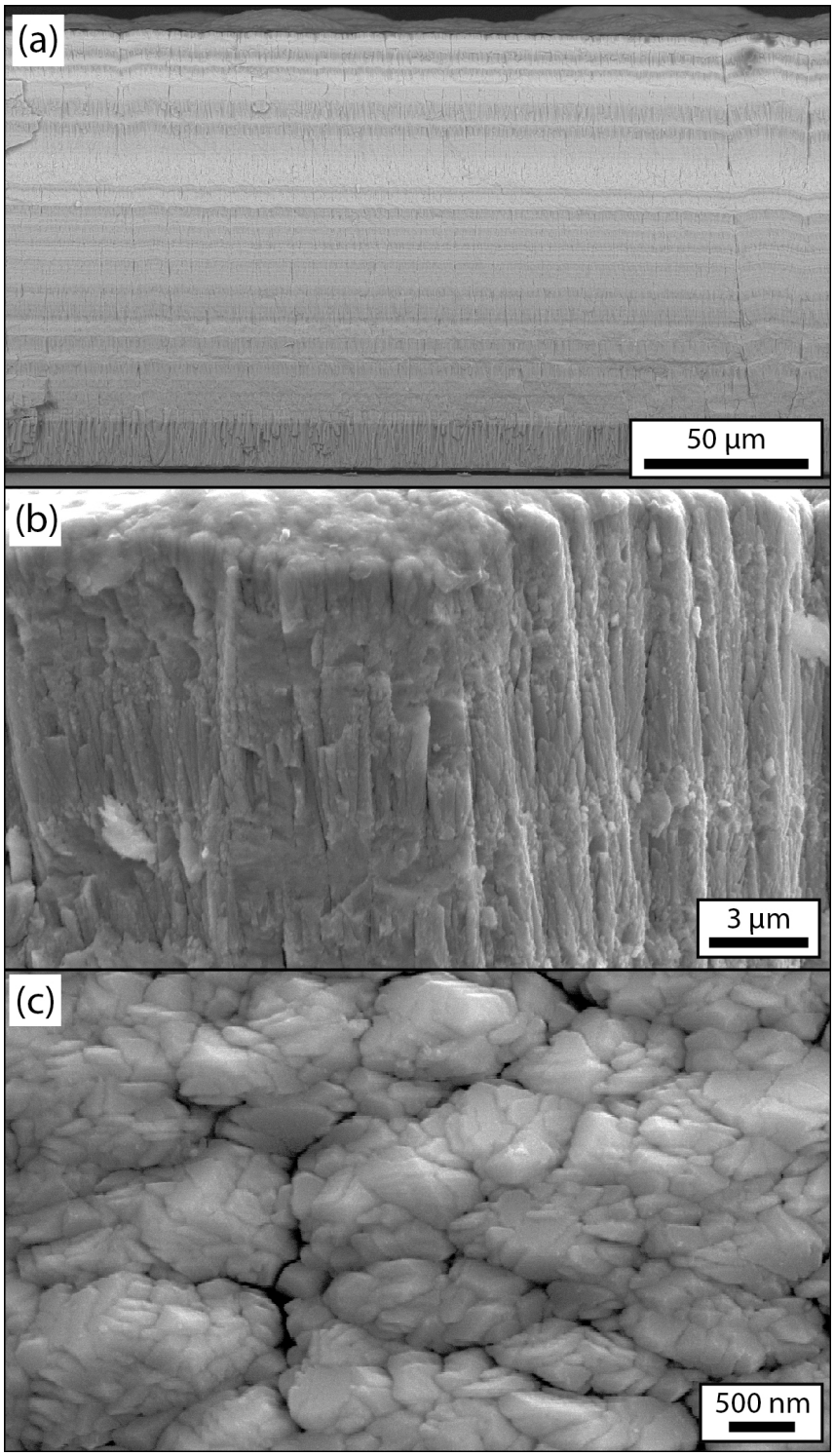

Figure 5.10: (a) Neither clearly defined columns nor intercolumnar gaps can be seen in a cross-sectional fracture surface from 15Yb25Ta coating. However, a higher magnification image near the surface, (b), reveals that a fine columnar structure is present. The tips of the columns, seen in (b) and (c), are too small for detailed structural analysis but generally appear to relatively blunt in comparison to that observed for 8YbSZ and 25Yb15Ta.

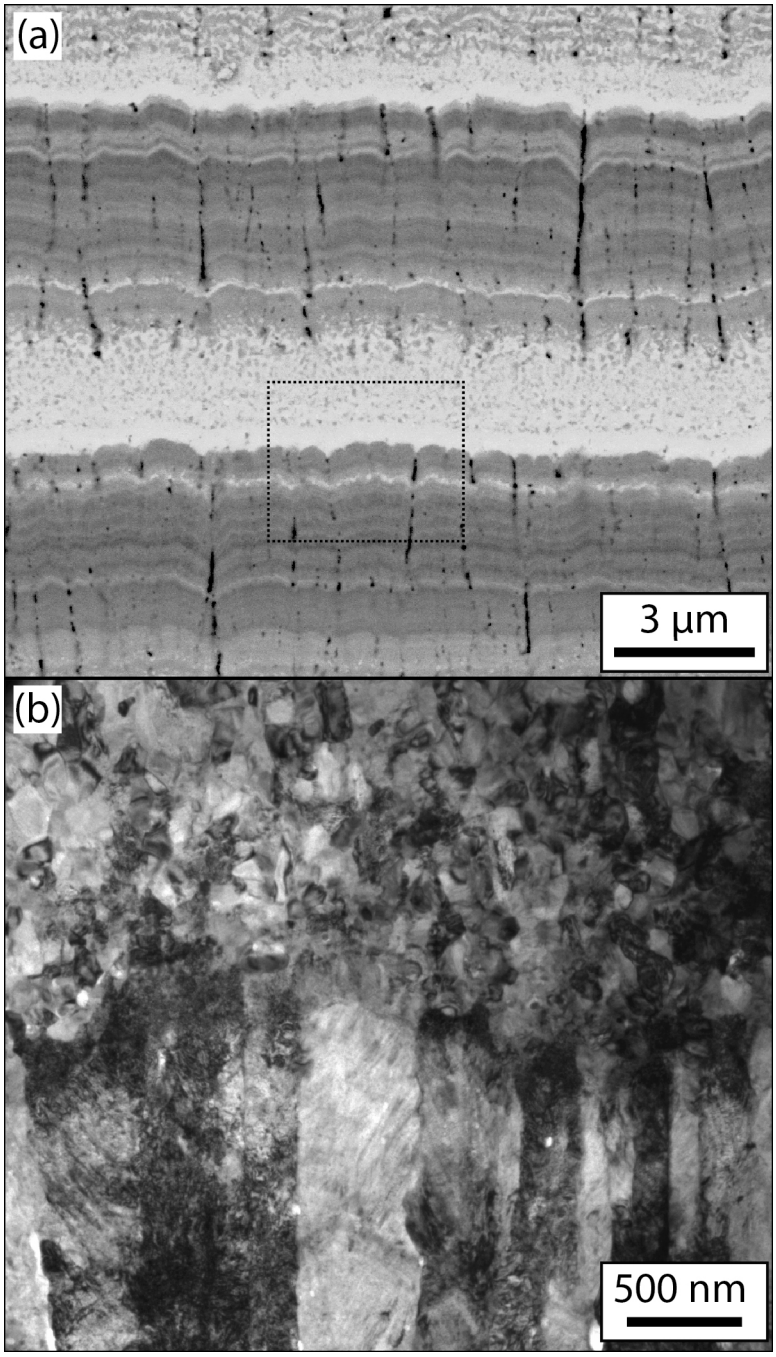

Figure 5.11: (a) A columnar structure is observed in the 15Yb25Ta coating in regions where the local composition is close to the nominal composition (dark regions). However, the columnar structure terminates in regions where the local composition is significantly enriched in $YbO_{1.5}$ and $TaO_{2.5}$ (bright bands). The TEM lamella taken from such a region, (b), clearly demonstrates the columnar microstructure in the dark regions and fine equiaxed grains in the bright regions. Therefore, the compositional fluctuations that occur upon deposition are deleterious to the columnar microstructure.

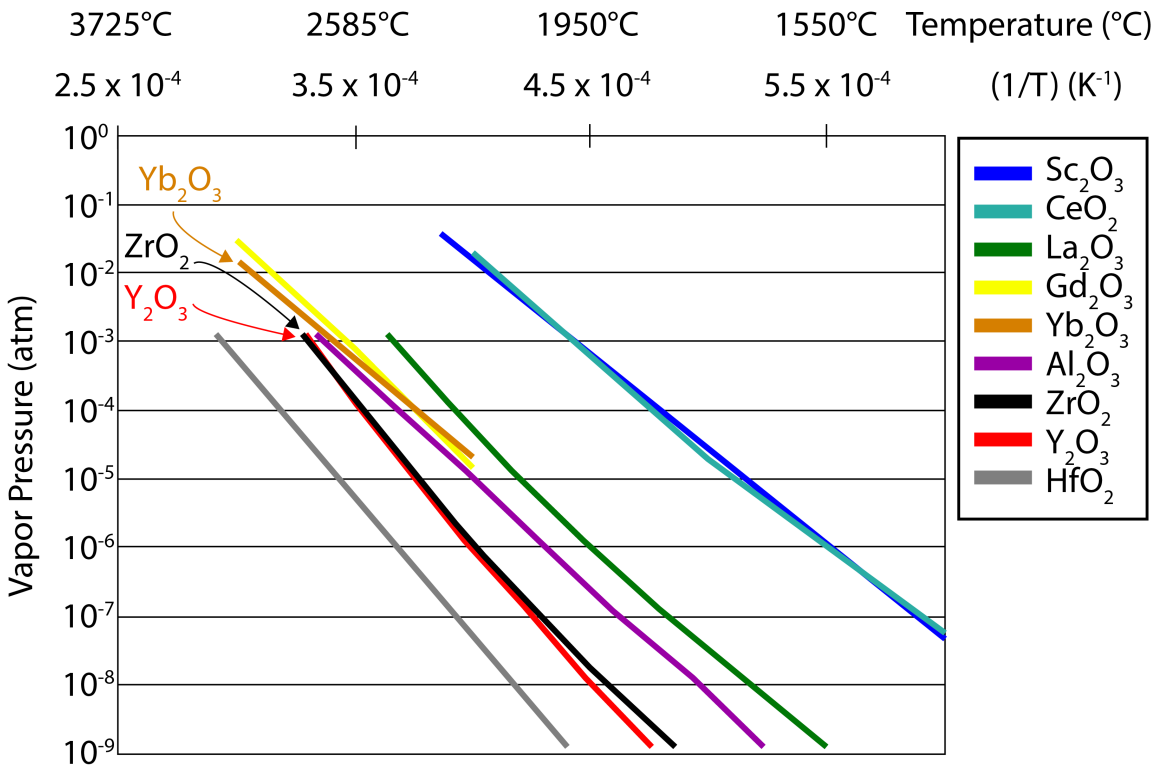

Figure 5.12: Vapor pressures of various rare-earth solid sesquioxides in addition to ZrO_2 and HfO_2 as a function of inverse temperature. Adapted from [126].

CHAPTER 6: MICROSTRUCTURE EVOLUTION AND PHYSICAL PROPERTIES OF ZrO_2-$(Y+Yb)O_{1.5}$-$TaO_{2.5}$ THERMAL BARRIER COATINGS

The compositional fluctuations described in the previous chapter exemplify one of the key issues hindering the implementation of ZrO_2-$REO_{1.5}$-$TaO_{2.5}$ (RE = rare-earth) materials in thermal barrier coatings (TBCs). Significant fluctuations in Zr^{4+} content are tolerable only on the trivalent dopant side of the ZrO_2-$RETaO_4$ quasi-binary, e.g. Figure 5.4 for RE=Yb, since the tetragonal phase produced in this region is non-transformable upon cooling from temperatures between 1250°C and 1500°C. Fluctuations into the Ta-rich side of the same system instead lead to the formation of a transformable tetragonal phase, and potentially the formation of phases that may be less strain tolerant because of anisotropic thermal expansion. A second issue is whether these compositional fluctuations have a detrimental effect on the desirable properties. It has been shown that the thermal conductivity varies only moderately over a relatively wide composition range in the phase fields including the tetragonal zirconia solid solution [12]. Little is known, however, about the effects of composition on the toughness of oxides within the ZrO_2-$RE^{3+}M^{5+}O_4$ quasi-binary or within the neighboring three-phase fields.

Much of the research performed to date has focused on ternary systems based on Y+Ta [13], Y+Nb [125,138] or comparisons between the latter [139-141], but seldom on Yb+Ta [72]. The patent literature claims desirable behavior for a wide range of trivalent stabilizers ($REO_{1.5}$, where RE is Sc, Y, La, and the lanthanides between Nd and Yb, or mixtures thereof), and short menu of pentavalent stabilizers ($MO_{2.5}$, where M is Ta or Nb, or mixtures thereof) [142,143]. There is evidently an interest in exploring quaternary and perhaps higher

order compositions [38,144,145], but the larger rare earths form tantalates or niobiates that exhibit much lower solubility than Y in tetragonal ZrO_2, and that reduces or eliminates the non-transformable region in that field. The smaller trivalent REs have more desirable phase stability behavior, and because of their larger mass they also result in further reductions in thermal conductivity [11].

A logical choice for this first study on quaternary compositions is the combination of Y+Yb, since both have similar chemical behavior and phase equilibria with ZrO_2 and Ta_2O_5, which facilitates understanding in the absence of a full quaternary phase diagram for the ZrO_2-$YO_{1.5}$-$YbO_{1.5}$-$TaO_{2.5}$ system. Of particular interest is the potential effect of Y and Yb additions on the deposition behavior since they both form tantalates of comparable stability with $TaO_{2.5}$ but do exhibit small differences in solubility in ZrO_2. Additionally, it is possible that they also modify differently the activity and vapor pressure of $TaO_{2.5}$ in the melt.

This chapter explores the microstructure evolution of a multi-phase ZrO_2-$(Y+Yb)O_{1.5}$-$TaO_{2.5}$ composition deposited by EB-PVD and aged at 1250°C and 1500°C, as well as the toughness and coefficient of thermal expansion of compacts fabricated from EB-PVD and precursor-derived powders of the same composition. Because of the similar phase equilibria quaternary compositions are plotted on the ZrO_2-$YO_{1.5}$-$TaO_{2.5}$ ternary diagram using the combined Y+Yb content, and often referred to in that manner. Comparisons are made with 8YSZ and a second set of quaternary compositions of the same oxides, both in the form of dense compacts. The results highlight compositions in this quaternary system that offer a promising path for TBC development [143,146].

6.1 Experimental Details

EB-PVD thermal barrier coatings of nominal composition ZrO_2-12$YO_{1.5}$-13$YbO_{1.5}$-14$TaO_{2.5}$ (in mole percent, hereafter 12Y13Yb14Ta or 25YY14T[4]) were provided by an industrial collaborator using proprietary process parameters. Free-standing specimens of these coatings underwent isothermal heat treatments in air at 1250°C and 1500°C as described in Chapter 3. After every aging step, x-ray diffraction (XRD) and Raman spectroscopy were performed at room temperature. The early stages of decomposition were monitored by analyzing the phases present in the coating after an exposure of 0.5 h and subsequently when the cumulative time reached 24, 100, and 400 h. To assist in phase identification standards were prepared to analyze the evolving XRD and Raman spectra, as well as calibration standards for TEM EDS. These standards include (i) a non-transformable single phase tetragonal composition, 16Y16Ta, (ii) a single phase fluorite (cubic) composition 30Y11Ta, (iii) a single phase tetragonal composition, 20Yb20Ta, (iv) a two-phase but predominantly monoclinic zirconia composition, 11Y8Ta, and (v) a single phase yttrium tantalate composition, 40Y40Ta. All of these compositions were synthesized by reverse co-precipitation from mixed precursor solutions [91] but the tetragonal phases were sintered at 1500°C for 24 h while the monoclinic and cubic ones was sintered at 1250°C for 24-100 h. The compositions were calibrated based on extramural ICP analysis (Dirats Laboratories, Westfield, MA).

Coatings in the as-deposited and fully aged (1250°C/400h) conditions underwent further characterization including electron probe microanalysis (EPMA), scanning electron

[4] Because the Y and Yb contents are not distinguished, when plotting on the phase diagram quaternary compositions are abbreviated by the combined content of Y + Yb (YY) and the content of Ta (T). All other compositions are denoted by the Y/Yb and Ta contents, omitting Zr. In most combined quaternary composition the Y:Yb ratio is approximately one.

microscopy (SEM), and transmission electron microscopy (TEM). All TEM lamellae from the coating were extracted at an angle of approximately 30° to the columnar growth direction in order to facilitate reaching the [111] zone axis for diffraction and phase analysis. The [111] zone axis was used for phase analysis as it contains reflections belonging to all three possible tetragonal variants.

Microindentation toughness testing was performed on two sets of compacts. The first set of compacts was made from 12Y13Yb14Ta (25YY14T) powders either synthesized by precursor methods or from EB-PVD deposits. The latter material was initially deposited onto graphite paddles, separated using a low temperature (650-900°C) pyrolysis heat treatment, and collected. The powders were compacted and densified into specimens for toughness testing using the methods described in Chapter 3. The second set of compacts was made from several quaternary compositions chosen to explore how toughness varies in the two-phase field $t + F$ and three-phase field $t + F + YT$ near the estimated limit of the non-transformable tetragonal phase field in the quaternary system. 11Y11Yb19Ta (22YY19T), 9Y9Yb15Ta (18YY15T), 10Y10Yb17Ta (20YY17T), 10Y10Yb15Ta (20YY15T), and 10Y10Yb20Ta (20YY20T) powders were synthesized from precursors and tested together with a baseline 8YSZ material. The compacts were fabricated via the same processing described for the 12Y13Yb14Ta compacts.

The bulk, linear coefficient of thermal expansion (CTE) was measured on 25 mm long bars of 25YY14T EB-PVD powder and 8YSZ precursor derived powder. The specimens were fabricated as described in Chapter 3.

6.2 Results

6.2.1 As-Deposited Microstructure

Figure 6.1(a) shows a cross-sectional overview of the as-deposited EB-PVD 25YY14T TBC in BSE imaging mode. A thin, 15 μm 8YSZ layer was deposited under the approximately 185 μm thick topcoat to enable thermochemical compatibility with the thermally grown oxide TGO. The 8YSZ also provides enhanced toughness in the vicinity of the TGO, where most failures due to cyclic oxidation initiate. The microstructure of the 25YY14T top coat is columnar, with similar features to those typical of 7-8YSZ EB-PVD TBCs [45]. However, the columns are somewhat broader and exhibit extensive internal segmentation, most evident at the tips as shown in Figure 6.1(a). The volume fraction of nominally intercolumnar porosity in the as-deposited state, as measured by image analysis on a TBC taper section, Figure 6.2,[5] is between 4-7%, which is in the lower end of the range reported for EB-PVD 7-8YSZ, [147,148] Relatively low temperature (1150°C) treatments, typically used after deposition in EB-PVD 7-8YSZ, lead to some sintering of the fine intracolumnar segmentation and increases in the measured intercolumnar porosity to ~9-11% (Figure 6.2).

A compositional profile of the coating measured by EPMA, Figure 6.1(b), shows the distribution of the combined rare earth content, ($YO_{1.5}$+$YbO_{1.5}$) and the Ta concentration throughout the thickness. There is compositional scatter in the 25YY14T layer, which, due to the larger atomic numbers of Yb and Ta relative to Zr and Y, results in Z-contrast variation seen in the BSE image in Figure 6.1(a). Although not shown explicitly in the EPMA data, the ytterbia and tantala contents consistently fluctuate approximately in phase (i.e. when the Yb content increases, so does the Ta,), similar to the observations made in

[5] Kindly provided by Dr. Vladimir Tolpygo from Honeywell Aerospace.

Chapter 4, whereas the yttria and tantala content always fluctuate out of phase, so that the $\Delta REO_{1.5}$:$\Delta TaO_{2.5}$ ratio relative to the nominal composition is approximately constant. Plotting the measured compositions every 5 μm onto the ZrO_2-$YO_{1.5}$-$TaO_{2.5}$ phase diagram in Figure 6.1(c) illustrates the scatter relative to the nominal composition (denoted by a star).[6] As a consequence of the compositional fluctuation, the coating composition is expected to oscillate between the two-phase *t*+*F* and three-phase *t*+*F*+*YT* phase regions, with small portions of the coating possibly falling into the transformable range, i.e. ZrO_2 contents above the shaded band in Figure 6.1(c).

XRD and Raman spectra for the as-deposited coating are presented in Figure 6.3. The plots include scans from (i) *t*-16Y16Ta, a nominally non-transformable tetragonal single-phase; (ii) *m*-11Y8Ta, a two-phase material containing a large majority of monoclinic zirconia (resulting from a large fraction of transformable *t*); (iii) *F*-30Y11Ta, a nominally single-phase fluorite (cubic); and (iv) *M*-40Y40Ta, a nominally single-phase monoclinic yttrium tantalate doped with zirconia. The non-primitive pseudocubic unit cell was used to index peaks belonging to the tetragonal zirconia phase. The XRD spectrum suggests that the as-deposited material is single phase with predominant peaks belonging to the $(200)_t$ and $(400)_t$ reflections near $2\theta = 35°$ and 74°. A high-resolution 2θ scan (Figure 6.4) revealed that the peak near 35° is slightly asymmetric, suggesting that there are small (ca. 0.03Å) variations in the local unit cell parameters. The large relative intensity of the $(200)_t$ and $(400)_t$ reflections is indicative of a [200] out-of-plane texture developed during deposition. XRD pole figure analysis performed on the coating using the (200) and (220) diffraction peaks,

[6] As noted earlier, the phase field boundaries at 1250°C are not known for the quaternary system, but the expected similarity of behavior between Y and Yb suggests that the 25YY14T composition should consist primarily of *t*+*F*, perhaps with a minor amount of $(Y,Yb)TaO_4$.

Figure 6.5, confirms the [200] out-of-plane texture and also reveals a well-defined in-plane texture as noted in an earlier study for 8YSZ [68]. The Raman spectrum of the as-deposited TBC, Figure 6.3(b), does not perfectly match either the tetragonal or fluorite standard spectra, likely due to a combination of texture in the coating, chemistry of the metastable phase, and cation ordering pattern, but the fact that the spectrum contains peaks belonging to the tetragonal phase, e.g. the peak at ~450 cm^{-1}, suggests that the as-deposited coating is tetragonal rather than cubic.

In order to examine the microstructure within each column in the as-deposited condition and confirm tetragonality, a TEM lamella was extracted where the EPMA indicated that the composition was close to the nominal, approximately 115 μm above the sapphire substrate as illustrated in Figure 6.1(a). A bright field image in Figure 6.6(a) shows the packing of columns and intercolumnar gaps in a scale finer than that typical of the standard 7-8YSZ coatings. The spread of in-plane crystal orientations was found to be ~20° by diffraction, in rough agreement with that inferred from the XRD pole figure in Figure 6.5. The average composition of the lamella, as measured by EDS, was 12.1±0.9%$YO_{1.5}$-15.8±1.7 %$YbO_{1.5}$-16.7±1.3 %$TaO_{2.5}$, slightly richer in both Yb and Ta compared to the nominal values. The [111] zone axis pattern (ZAP) of every column analyzed exhibited even-odd-odd type diffraction spots, which are characteristic of the tetragonal zirconia structure. Here again the ZAPs and reflection indices are referenced relative to the tetragonal pseudocubic unit cell. A typical [111] ZAP is shown in Figure 6.6(b) and exhibits three weak {211}-type reflections, suggesting the presence of three tetragonal variants. Dark field imaging was performed with those reflections in order to elucidate the scale and distribution of the tetragonal domains, shown in Figure 6.6. The microstructure is reminiscent of a combination of the mottled and

colony-like microstructures seen in other zirconia-based binaries [149] [132], with small tetragonal domains distributed throughout the entire volume of the grain. The fine scale of the tetragonal domains suggest they are largely coherent, giving rise to strains that could be responsible for the asymmetry of the as-deposited $(200)_t$ XRD peak. The entire area of each grain appears to be comprised of only the three tetragonal domains, but the low intensity of the tetragonal diffraction spots and the small scale of the observed domains (~10-20 nm in width) make it difficult to assess with complete confidence whether the material is comprised only of tetragonal phase. As seen in the DF images in Figure 6.6, it was found that two of the three tetragonal orientations comprise the large majority of the imaged grain volume. The same two tetragonal variants (relative to the columnar growth direction) were observed to predominate in the majority of the grains analyzed.

6.2.2 Evolution at 1250°C

The XRD and Raman plots in Figure 6.3 show the phase evolution as the coating is aged for progressively longer times at 1250°C. By 24 h the coating begins to show splitting of the original single (400) XRD peak near $2\theta = 74°$ into two peaks, arising from the partitioning of the initial metastable *t'* phase into the equilibrium cubic and tetragonal phases. After 24 h, no new peaks appear and no significant shifts in peak positions are detected in the spectrum. Notably, the predominant peaks after 400 cumulative hours at temperature are still (400)-type but now they are indexed to the equilibrium tetragonal and cubic phases, suggesting that the phase evolution at this temperature does not impact the texture developed during deposition, similar to the behavior reported for 8YSZ [68]. Concomitantly, the Raman spectrum after 400 h exhibits only the peaks characteristic of the tetragonal phase. Although one would expect evidence of the cubic phase in the Raman spectrum, which typically

manifests itself as a broad peak in the Raman response of the cubic phase in the ZrO_2-$YO_{1.5}$-$TaO_{2.5}$ system appears to be essentially featureless in the measured region. Most importantly, the lack of the characteristic doublet at ~180 cm^{-1} in the Raman scans confirms the absence of *m*-ZrO_2, and hence that the equilibrium tetragonal phase resulting from high-temperature aging [150], remains non-transformable.

In order to examine the microstructure within each column after aging, a TEM lamella was extracted at a location with composition close to the nominal value. The average composition, as determined from EDS, was 11.3±1.1%$YO_{1.5}$-13.8±1.3%$YbO_{1.5}$-15.2±1.4%$TaO_{2.5}$. Every segment of a column analyzed by diffraction in the TEM displayed a [111] ZAP similar to the one shown in Figure 6.7(b), containing one strong and two weak (211)-type reflections that suggest the presence of one dominant tetragonal variant. Notably, the dominant tetragonal variant in each grain analyzed always corresponded to one of the two prevalent variants observed in the as-deposited structure. The microstructures of the columns were observed to vary throughout the lamella, perhaps due to differences in the local chemical composition and structure, e.g. proximity to large pores, but generally appeared to consist of small, approximately 250 nm x 50 nm tetragonal crystallites, similar to the colony-like structure seen in the as-deposited coating but on a larger scale, surrounded by a secondary phase, Figure 6.7(c). Areas that did not illuminate under the dark field 2-beam conditions were presumed to be cubic phase based on the XRD information. To verify that the tetragonal grains were not cubic grains that had undergone the cubic-to-tetragonal transformation on cooling, high-resolution EDS chemical analysis was performed on areas analyzed by dark field. A chemical line scan through a region in the dark field micrograph in Figure 6.7(c) indicated that areas illuminated under dark field imaging had chemical

compositions with a 1:1 (Y+Yb):Ta ratio and areas not illuminated had a 2:1 (Y+Yb):Ta ratio, qualitatively consistent with the tetragonal and cubic phases, respectively, Figure 6.7(c). No diffraction or visual evidence of *m*-ZrO_2 could be found.

6.2.3 Evolution at 1500°C

Systematic aging treatments at 1500°C and complementary XRD and Raman analysis, Figures 6.8(a) and (b), revealed phase evolution nearly identical to that seen at 1250°C with the only notable differences being the much more rapid partitioning of the metastable phase, which is visible as quickly as 30 minutes in the XRD spectra, and the higher concentration of cubic phase at equilibrium. The analysis confirms that tetragonal phase stability against the monoclinic transformation is retained from 1250°C to 1500°C, in accordance with the ternary phase diagrams.

To examine the microstructure after aging a TEM lamella was extracted at a location with composition close to the nominal value as in the 1250°C treatment, Figure 6.9. The average EDS composition was 14.0±0.7%$YO_{1.5}$-12.3±0.8%$YbO_{1.5}$-12.5±0.6%$TaO_{2.5}$. The microstructure consists of large, micrometer-sized grains exhibiting either none or one strong (211)-type reflections in the [111] ZAP, indicative of each grain being either a single tetragonal or cubic crystal, Figure 6.9(a). The scale of each tetragonal or cubic grain is comparable to or larger than that of the original columnar segments but not larger than the columns themselves, and the misorientation between the equilibrated phases is within the range measured for columns in the as-deposited coating, suggesting that the grains grow from clusters of similarly oriented columnar segments.

6.2.4 Fracture Toughness

The calculated hardness and toughness values for the materials tested as powder-derived compacts are summarized in Table 1 and plotted in Figure 6.10. A comparison was first made between two versions of the 25YY14T composition, one prepared from powders generated by grinding of the EB-PVD material and one from precursor-derived powders. Representative indents for these compacts at the same magnification are shown in Figures 6.11(a) and (b), respectively. The micrographs show no indications of large-scale porosity in the precursor-derived sample but a significant amount of porosity in the EB-PVD specimen. Crushing of material underneath the indenter is evident in the latter and is likely the origin of the lower hardness relative to the precursor-derived sample. Considering that the measured crack lengths for both specimens were nearly identical but that the toughness scales as the square of the indent size, the porosity is likely responsible for the difference in the measured toughness of 25YY14T when fabricated using the two different powder feedstocks, 16±3 J/m^2 for the EB-PVD material vs. 8±3 J/m^2 for the precursor-derived material. It is thus expected that the value measured from the precursor-derived compact more accurately describes the intrinsic toughness of the equilibrated composition, which is significantly lower than that measured for t'-8YSZ in this study, 42±3 J/m^2.

It was hypothesized that the large fraction of cubic phase in the 25YY14T Ta composition was responsible for the low toughness. To test this and investigate how phase content influences indentation toughness, a number of quaternary compositions closer to the tip of the tetragonal phase field were synthesized from precursors. The positions of the compositions relative to the tip and their measured toughnesses can be seen in Figure 6.10. All of the tested compositions exhibited toughness approximately 2-4 times larger than the

25YY14T material nominally similar to the EB-PVD coating. The phase fractions could not be rigorously quantified due to a paucity of knowledge on the parameters of the crystal structures, which would be required for Rietveld refinement, and on the quaternary phase diagram, which would be required to estimate the phase fractions based on the measured compositions. Nevertheless, one may argue than that as the composition moves from the tip of the tetragonal phase field towards the cubic phase, the toughness decreases monotonically. The trend in toughness as the composition moves from the tip of the tetragonal phase field towards the tantalate phase field is less clear, but the toughness appears to stay closer to the value observed for the tetragonal phase.

6.2.5 Coefficient of Thermal Expansion

The mean CTE for 25YY14T is plotted alongside the mean CTE for 8YSZ in Figure 6.12. The CTE of the quaternary material is found to be lower than that of 8YSZ by about 0.5 ppm/K in the temperature range 200°C-1200°C. Although the specimens were heat treated prior to the initial measurement in order to allow the initial stages of sintering to occur, it was observed that each sample densified a small amount (<1%) each dilatometry cycle. It is likely that the decrease in the slope of the CTEs above ~1100°C is an artifact of this densification, and that the difference between the CTEs does not actually decrease in the range 1100-1200°C.

6.3 Discussion

The microstructure evolution and properties of 25YY14T and related compositions are best discussed in the context of what is known about the requirements and performance of conventional 8YSZ TBCs.

6.3.1 Microstructure Evolution During Deposition

It is first noted that both 25YY14T and 8YSZ exhibit columnar microstructures with a [200] out-of-plane texture and a [002] in-plane texture when deposited by EB-PVD. This is different than the [002] out-of-plane texture exhibited by the 25Yb15Ta coating in Chapter 5, which likely originates from the higher deposition temperature used in the 25Yb15Ta coating relative to the 25YY14T and 8YSZ coatings [68]. The columns in Figure 6.1(a) are somewhat broader and more internally segmented than those typical of 8YSZ, albeit not to the same extent as those in a related 20Yb20Ta coating reported earlier and deposited in the same evaporator [72]. The difference in morphology notwithstanding, the measured in-plane porosity in Figure 6.2 suggests that the quaternary TBC should exhibit adequate in-plane compliance, and hence strain tolerance under thermal cycling comparable to that in 8YSZ. Indeed, in plane elastic modulus measurements of similar EB-PVD coatings performed elsewhere reveal values consistent with those of 8YSZ [151]. It remains to be elucidated why the addition of Ta, or perhaps the combined addition of Y/Yb and Ta, modifies the development of the column morphology in these coatings.

The columns of both as-deposited coatings are also nominally single crystals, consisting of single-phase metastable, extended solid solutions. In the case of 8YSZ it is well established that each column is deposited as a single crystal of tetragonal phase, *t'* {Miller, 1982 #233}[48], and the texture develops by a process of evolutionary selection wherein columns with their ⟨100] direction oriented in the average direction of the incident vapor occlude others less favorably oriented. In principle, the same type of growth should be observed for the cubic or tetragonal forms of the zirconia solid solution depending on whether the deposition temperature falls above or below $T_0(c/t)$ for the composition of interest. Available

thermodynamic descriptions allow the calculation of $T_0(c/t)$ for the ZrO_2-$YO_{1.5}$ binary [17], but similar models are not yet available for the ZrO_2-$YO_{1.5}$-$YbO_{2.5}$-$TaO_{2.5}$ system, or even for the constituent ternaries. Even without accurate knowledge of the relationship between composition and $T_0(c/t)$ in the higher order systems, the experimental observations clearly indicate that the 25YY14T coating is tetragonal at room temperature. However, the observations do not explicitly illustrate whether the material was deposited as a tetragonal phase, since it is possible that it is deposited as a cubic phase that undergoes the $c \rightarrow t$ transformation on cooling. Details of the microstructure offer clues as to the identity of the as-deposited phase. The small scale of the tetragonal domains within each column supports the idea that the tetragonal domains form by a mechanism involving short-range ordering rather than, for instance, a displacive transformation. It is anticipated that the formation of the domains originates from the preference for short-range order between RE^{3+} and Ta^{5+} cations in the ZrO_2-$REO_{1.5}$-$TaO_{2.5}$ systems, as predicted by first principles calculations in Chapter 4. The domains represent regions of the material where the short-range ordering patterns are oriented in one of the three mutually orthogonal directions relative to the columnar [200] axis. If the domains formed on cooling from the $c \rightarrow t$ transformation, a process that would be facilitated by short-range diffusion of the cations, the generated domain structure would form to minimize strain energy. In this scenario, it would be expected that each column would contain a single prevalent tetragonal variant, since the biaxial stress state upon cooling would bias the growth of the variant with the c-axis out-of-plane. This is inconsistent with the experimental observation of two dominant tetragonal variants in each column (Figure 6.6). The two dominant variants are instead consistent with the scenario in which the tetragonal domains form upon deposition, since the [200] out-of-

plane texture would favor the growth of the two tetragonal variants with the c-axis in the plane of the coating. Therefore, it is hypothesized that the material is deposited as small tetragonal domains at temperature. The cubic phase observed by XRD can be viewed as a statistical average of nanoscale domains of the three tetragonal orientations. It is possible that the formation of tetragonal domains upon deposition may contribute to the increased segmentation of the columnar structure in the ZrO_2-$REO_{1.5}$-$TaO_{2.5}$ coatings relative to 8YSZ and YbSZ coatings.

6.3.2 Microstructure Evolution Upon Aging

Aging at ~1500°C causes *t'*-8YSZ to decompose into the equilibrium two-phase cubic and tetragonal microstructure, eventually leading to fully incoherent tetragonal grains, followed by monoclinic transformation on cooling [48]. In principle, this evolution also occurs at 1250°C but at considerably slower rates. In contrast, the ZrO_2-$(Y+Yb)O_{1.5}$-$TaO_{2.5}$ system contains a thermodynamically stable, non-transformable tetragonal phase field, which allows not only the creation of the stable, single-phase tetragonal materials, but also supersaturated structures that decompose upon aging into a mixture of phases containing the equilibrium, non-transformable tetragonal phase. The 25YY14T composition studied in this publication is an example of the latter. The equilibrium configuration of 25YY14T in the temperature range of interest, based on the phase constitution observed after 400 h at 1500°C (Figure 6.9), consists of micrometer sized cubic and non-transformable tetragonal crystals. The cubic and tetragonal crystals are inferred to be subgrains within each column owing to their similar orientation, which is thought to be inherited through the original, slightly misaligned, segmented structure. The cumulative evidence suggests that the microstructure evolution involves concomitant coarsening one of the two predominant tetragonal variants observed in

the as-deposited structure and redistributing the cations to achieve the equilibrium composition of both phases. The microstructure observed at 1250°C, consisting of nanometer sized tetragonal crystallites surrounded by cubic crystallites, with all three tetragonal variants still present but only one predominant, presumably represents an intermediate state, where slower diffusion rates have limited the redistribution of cations and growth of the grains. Given enough time at 1250°C, it is expected that the microstructure would evolve to a similar scale and morphology to that seen at 1500°C.

6.3.3 Properties and Influence on Durability

In addition to microstructure and phase stability, the physical and mechanical properties of the TBC material are critical to the durability of the coating since they determine the level of stresses and associated strain energy density arising form the thermal cycling, and the coating resistance to crack propagation. One important driving force for cracking is the compressive stress that develops upon cooling due to the difference in thermal expansion coefficient between the TBC ceramic and underlying superalloy. It was found that the difference between the mean coefficient of thermal expansion for the 25YY14T and 8YSZ materials is less than 0.5 ppm/K in the temperature range 200-1200°C. A simple thermomechanical model described elsewhere [152] can be used to estimate the difference in stored elastic energy between a TBC of 8YSZ and the quaternary material under spatially isothermal cycling conditions. If the CTE of the superalloy is ~15 ppm/K [153] and all other relevant parameters – coating modulus, Poisson ratio, and coating thickness – are kept constant, the decrease in the CTE of the quaternary TBC represents a 25% increase in the stored elastic energy relative to 8YSZ. The relatively small change in the CTE therefore drives a large increase in the energy release rate for delamination. In the more realistic

scenario involving a thermal gradient through the coating, the lower thermal conductivity of the 25YY14T TBC will change the temperature distribution so that the temperature near the TBC/TGO interface, which typically experiences the largest driving forces for delamination, is lower. The thermal excursion of the substrate, which dictates the stresses in the system, will be reduced and thus so will the maximum energy release rate in the TBC, corresponding to the TBC/TGO interface.

The preceding analysis suggests that the quaternary coating will require similar or increased toughness relative to 8YSZ in order to achieve similar durability. The total toughness of the coating is dictated by: (i) the intrinsic material toughness and (ii) the resistance to crack propagation resulting from the microstructural features, notably via crack deflection and crack bridging mechanisms induced by the columnar structure, as shown in segmented plasma sprayed coatings [66]. A few toughness measurements on APS microstructures have been accomplished [66,154,155] but similar measurements on EB-PVD coatings have been elusive owing to experimental limitations of the available techniques and the achievable coating thicknesses. Nevertheless, the similarities between the microstructures of 8YSZ and quaternary TBCs suggest that the contribution to the toughness from microstructural resistance should be similar, so that the intrinsic toughness provides insight into the relative fracture resistance. The intrinsic toughness of the 25YY14T material after 100 h at 1250°C, 8-16 J/m^2, is about a quarter to a half of that reported for 8YSZ. It is noteworthy that the measured toughness of the quaternary composition is consistent with the value of ~16 J/m^2 reported by Pitek et al. [16] for a similar composition in the ZrO_2-$YO_{1.5}$-$TaO_{2.5}$ ternary system, namely 22Y13Ta. The low toughness of both compositions is ascribed to their proximity to the fluorite phase field, which, when equilibrated, gives rise to a microstructure

dominated by the large fraction of the more brittle cubic phase. Preliminary investigations on several quaternary compositions showed that oxides with a (Y+Yb):Ta ratio closer to 1, so that the fraction of cubic phase is reduced to a minimum, can increase the toughness by a factor of at least 2. The results in Figure 6.10 suggest that the presence of $YTaO_4$ may not degrade the toughness of coatings based on the tetragonal zirconia solid solution as much as the presence of fluorite. Interestingly, the large toughnesses observed for the single tetragonal phase in the ternary, ~45-50 J/m^2 [13,16], which might be expected for the 18YY15T composition given its closer proximity to the tetragonal phase field, was not observed. Whether this is due to differences in processing and microstructure remains the subject of ongoing research. This topic, along with the trend between cubic and/or yttrium tantalate phase fraction and toughness will be discussed in the next chapter of this thesis.

6.4 Synopsis

A ZrO_2-$12YO_{1.5}$-$13YbO_{1.5}$-$14TaO_{2.5}$ composition of possible interest for TBC applications was deposited by EB-PVD. The coating exhibits a columnar microstructure and texture similar to state-of-the-art ZrO_2-$8YO_{1.5}$ TBCs, with each column being deposited as a single, supersaturated, cubic phase. Aging between 1250°C and 1500°C results in the growth of small, non-transformable tetragonal and cubic domains, which eventually coarsen to form separate cubic and tetragonal grains. Although compositional scatter during the deposition process results in small areas where the local composition was expected to be transformable to monoclinic on cooling, no evidence of monoclinic zirconia was found in the as-deposited or aged conditions.

One potential drawback of the 25YY14T material is its combination of lower CTE and toughness relative to 8YSZ, which suggests that it might be prone to enhanced

thermomechanical degradation. The smaller CTE of the quaternary composition leads to enhanced thermomechanical stresses on thermal cycling while the lower toughness results in a lower critical energy release rate necessary for crack propagation. Preliminary results suggest, however, that modifying the chemistry to be closer to the tetragonal phase field tip could enhance the toughness to values closer to that of the single, non-transformable tetragonal phase without sacrificing the stability of the tetragonal phase. The cumulative findings support the conclusion that multiphase quaternary ZrO_2-$(Y+Yb)O_{1.5}$-$TaO_{2.5}$ materials could have the requisite microstructural and thermomechanical properties and processability for phase stable thermal barrier coatings with enhanced temperature capabilities relative to the current industrial standard as long as the nominal composition and homogeneity can be maintained in a range where the tetragonal phase is dominant.

6.5 Tables and Figures

Table 6.1: Toughness and hardness for compositions and processing routes studied. (PD: precursor derived, SPS: spark plasma sintering, SF: sinter forging)

Material	Processing	Hardness H (GN•m^{-2})	Toughness G (J•m^{-2})	G std. dev. σ_G (J•m^{-2})
8YSZ	PD/SPS	13.5	42	3
25YY14T	EB-PVD/SF	7.4	16	1
25YY14T	PD/SF	14.2	8	1
18YY15T	PD/SF	12.0	21	1
20YY15T	PD/SF	12.0	17	1
20YY17T	PD/SF	12.0	15	1
22YY19T	PD/SF	8.8	23	1
20YY20T	PD/SF	8.4	31	3

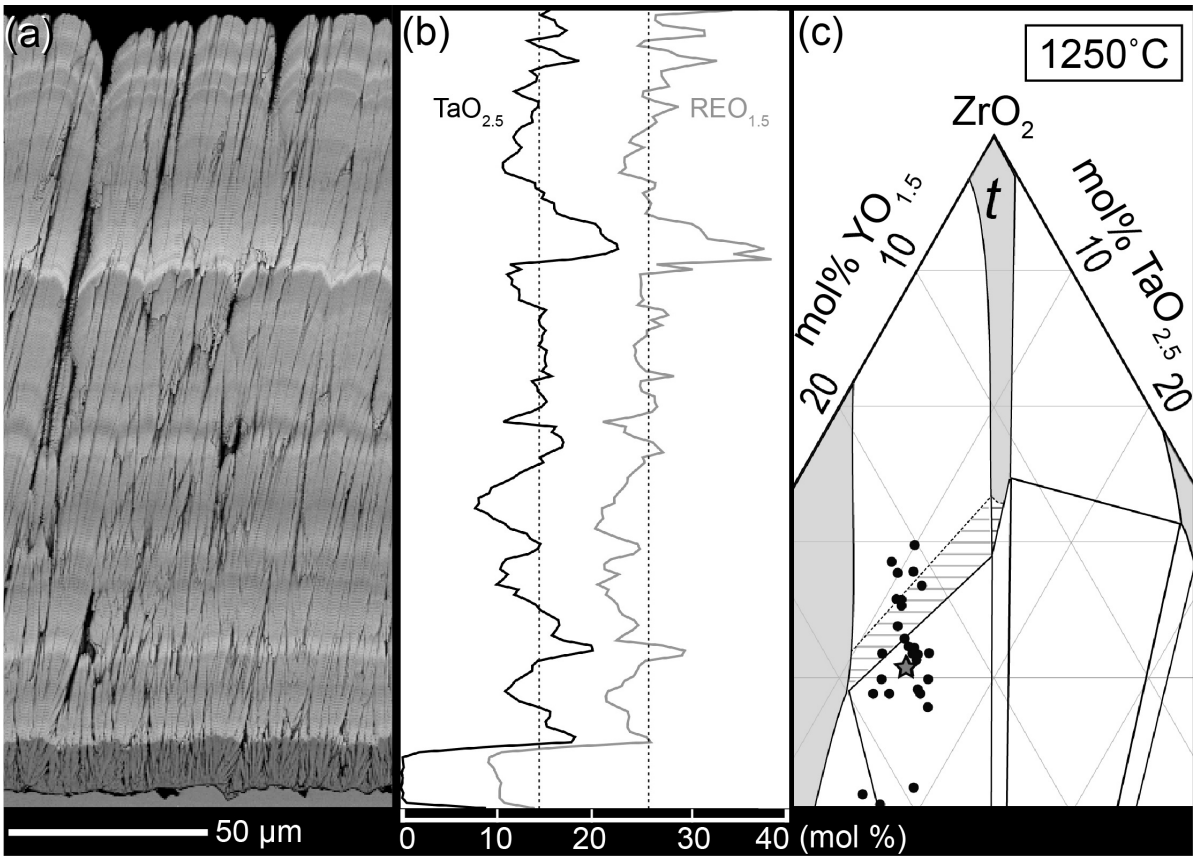

Figure 6.1: (a) BSE SEM analysis of the as-deposited 25YY14T TBC reveals a columnar microstructure with Z-contrast variations throughout the thickness of the coating. The changing contrast is linked to compositional fluctuations detected by EPMA, (b), and plotted in the 1250°C isothermal section (c). The dashed lines in (b) indicate the nominal composition and $REO_{1.5}$ is defined as $YO_{1.5}$ + $YbO_{1.5}$. The [111] ZA (e) of a column outlined by a dotted white box in the bright field image (d), which was extracted by FIB from the region marked in (a), reveals the presence of three tetragonal variants, one imaged in dark field in (f). Symbol key: m: monoclinic zirconia solid solution; t: tetragonal zirconia solid solution; F: cubic zirconia (fluorite) solid solution; YT: monoclinic yttrium tantalate.

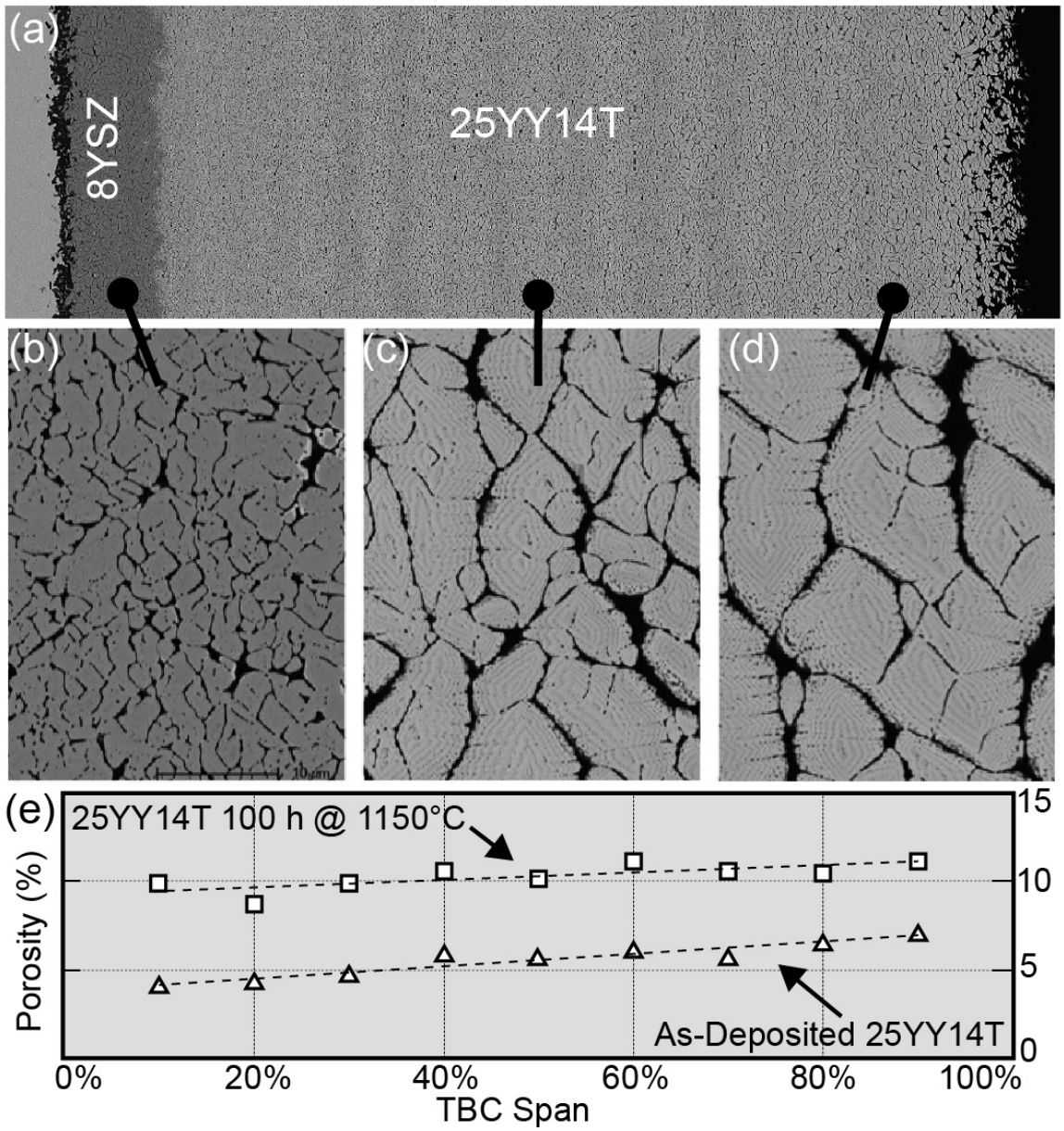

Figure 6.2: A backscattered electron image of the as-deposited TBC taper section that was used to characterize intercolumnar porosity, (a). (b), (c), and (d) show representative areas of the TBC at different points along the TBC span (10%, 40%, and 80%, respectively). The porosity in the as-deposited state and after aging for 100 h at 1150°C is displayed in (e), noting that 8YSZ coatings typically display ~7% intercolumnar porosity [68].

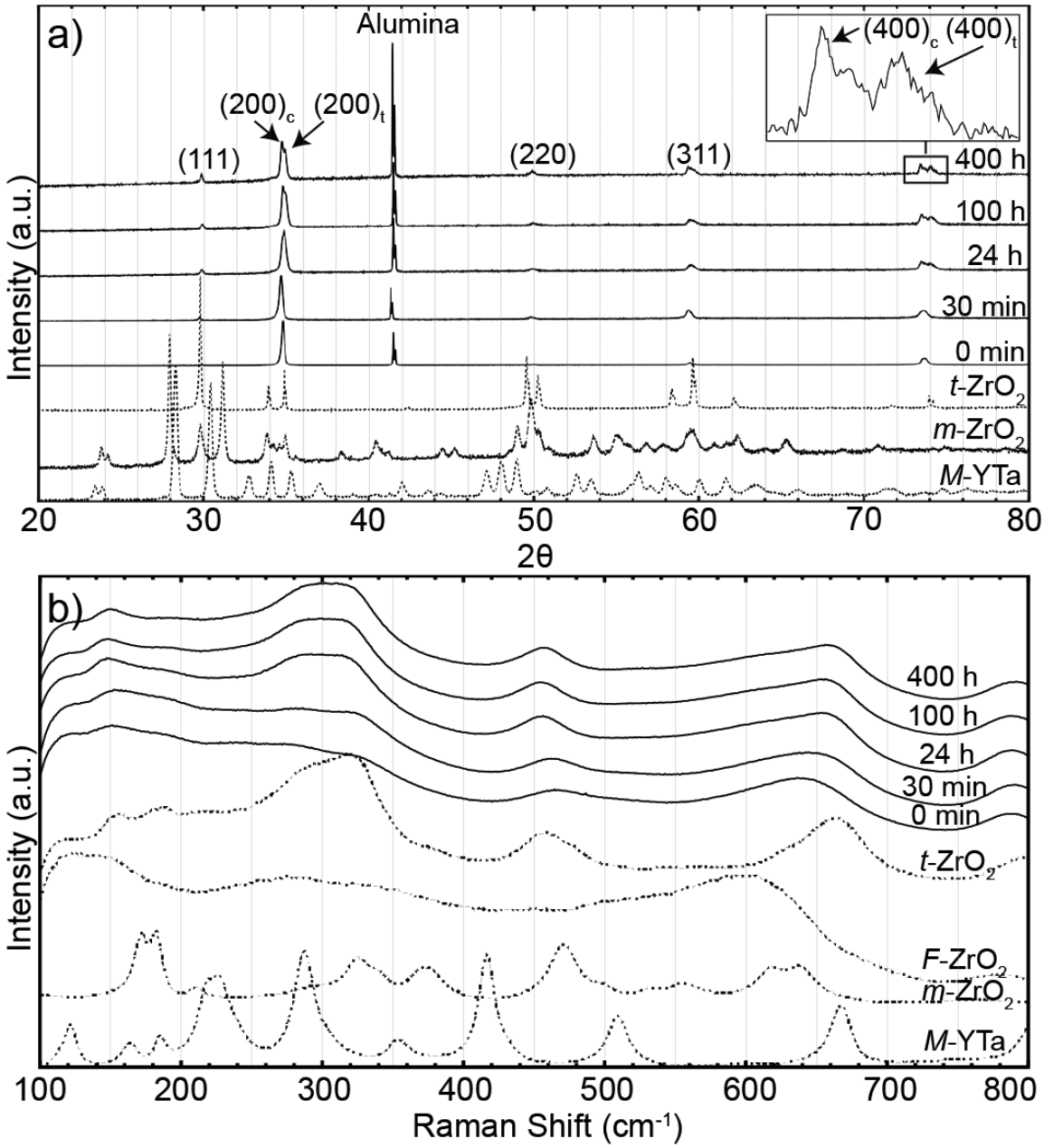

Figure 6.3: XRD (a) and Raman (b) scans of the 25YY14T coating in the as-deposited state and for various times after aging at 1250°C show no significant evidence of m-$YTaO_4$ nor m-ZrO_2. The coating's Raman profile in the as-deposited state is consistent with a tetragonal phase, as the cubic phase is not Raman active in this region. The splitting of the initially single (400) XRD peak after 400 h at 1250°C implies that the coating has partitioned into a two-phase tetragonal and cubic mixture. Symbol key: *m*-YTa: monoclinic yttrium tantalate; *m*-ZrO_2: 11Y8Ta monoclinic zirconia solid solution; *F*-ZrO_2: 30Y11Ta fluorite (cubic) zirconia solid solution; *t*-ZrO_2: 16Y16Ta non-transformable tetragonal solid solution.

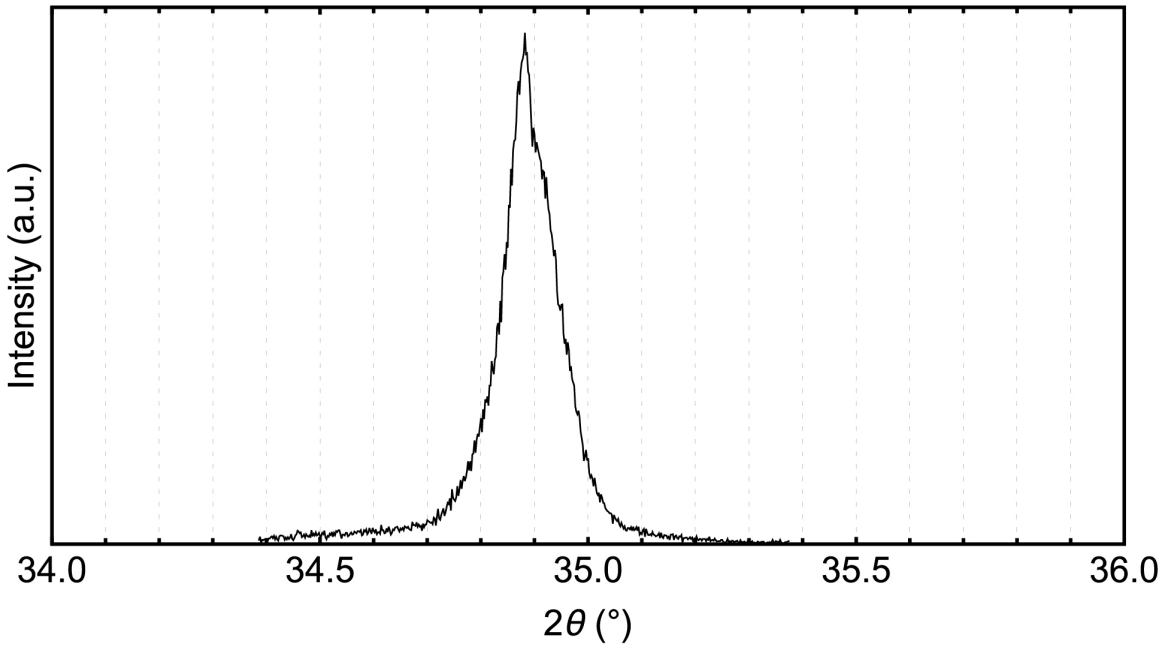

Figure 6.4: A high-resolution (step-size 0.002°) XRD scan of the 200 peak in the 25YY14T as-deposited coating exhibits asymmetry. Given that the beam was monochromated, the asymmetry reveals slight variations (ca. 0.03Å) in the unit cell parameters.

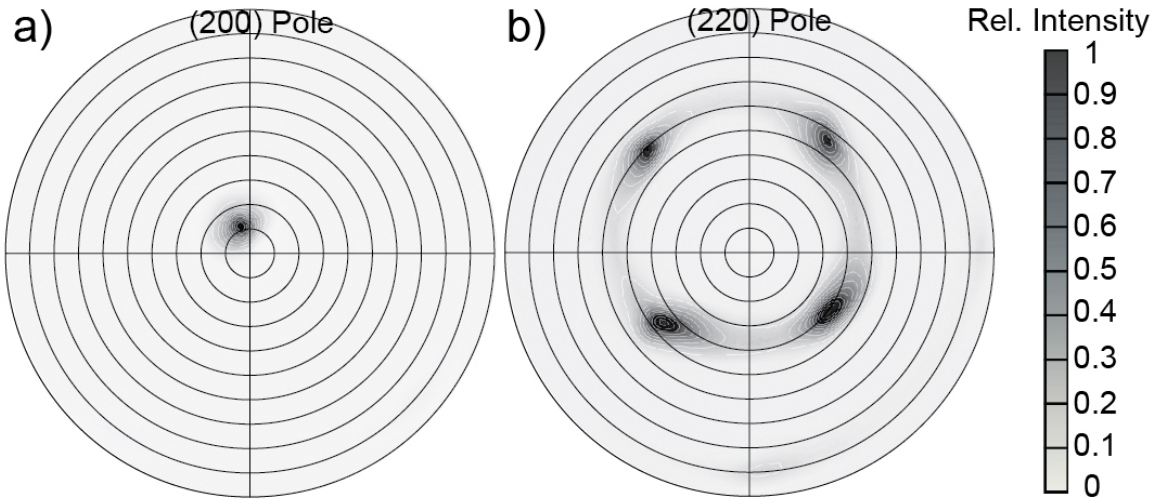

Figure 6.5: The observed pole figure for the (200) XRD peak in (a) indicates that the as-deposited 25YY14T coating exhibits a (200) out-of-plane texture with the direction of columnar growth rotated about 10° from the substrate normal, based on the positions of the pole. The (220) pole figure in (b) shows the single crystalline nature of the (220)-type poles and confirms that the coating also exhibits a single crystal in-plane texture.

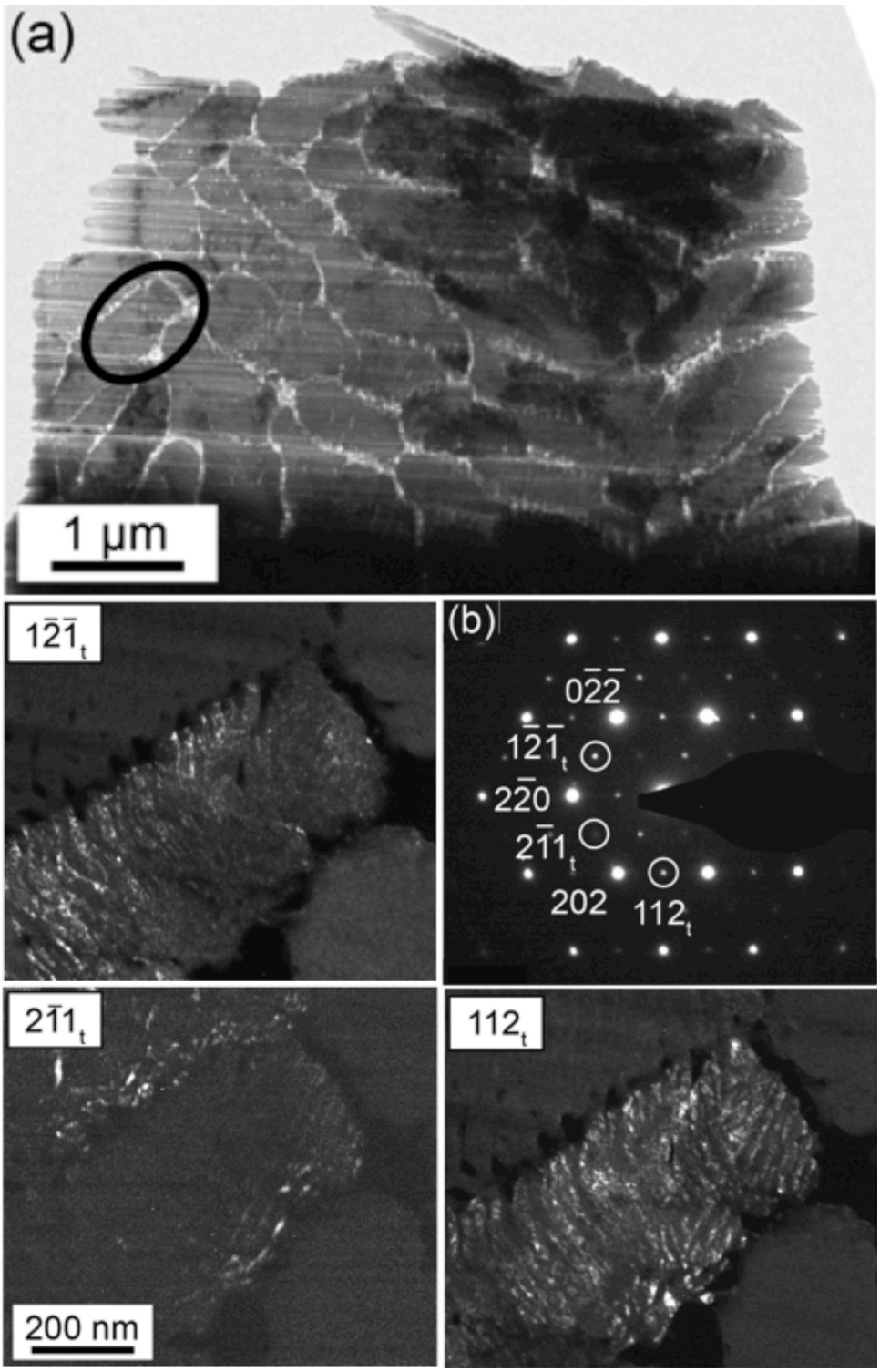

Figure 6.6: (a) BF overview image of the FIB lamella taken from the as-deposited coating. The [111] zone axis (b) of a single column outlined by a black circle in the BF image contains three (211)-type tetragonal diffraction spots. DF imaging using the tetragonal reflections, shown below the diffraction pattern, reveals the microstructure of the tetragonal domains.

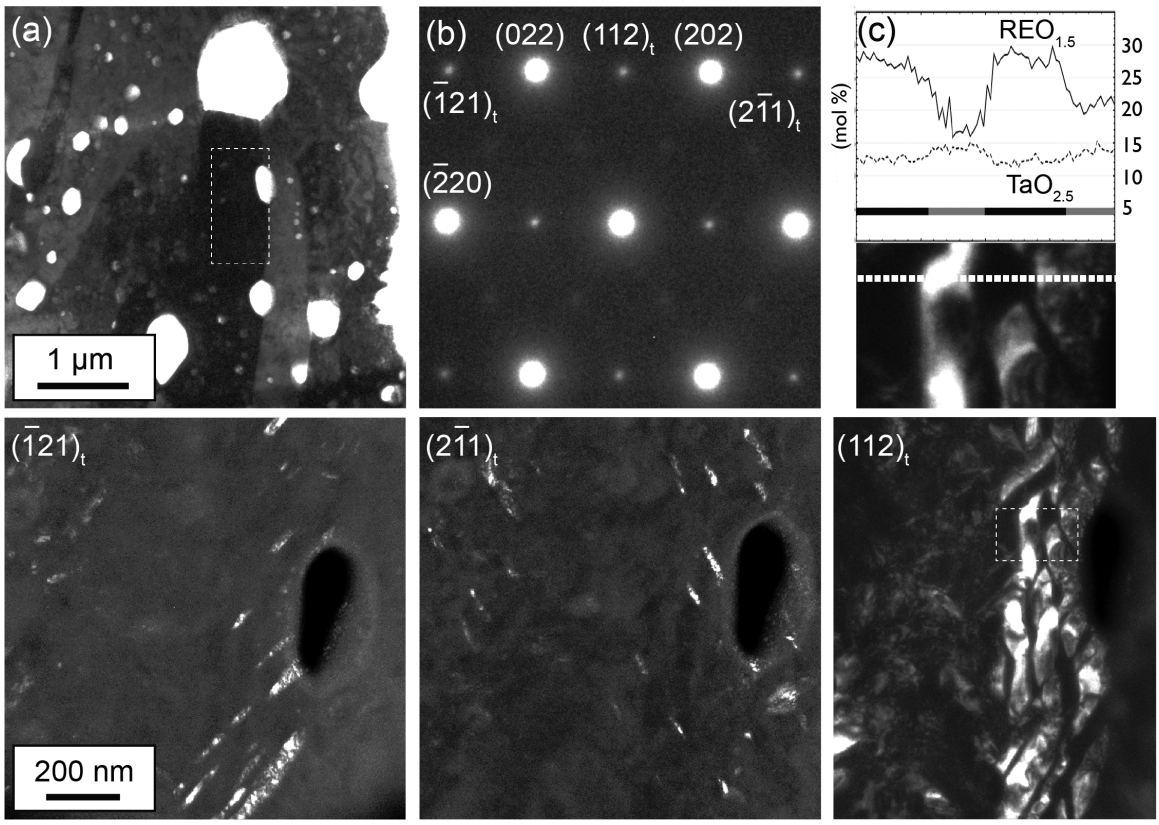

Figure 6.7: The [111] zone axis (b) of a single column outlined by a dashed white box in the BF image (a) after aging for 400 hours at 1250°C contains one major (211)-type diffraction spot, even though all three are present. DF imaging using the three tetragonal variants reveal small plate-like tetragonal precipitates surrounded by a secondary phase. An EDX chemical linescan taken from an area highlighted by a dashed white box in the (112) DF image and across a region shown by a white rectangle in (c) indicates that bright regions have an approximately 1:1 ratio of $(Y+Yb)O_{1.5}$:$TaO_{2.5}$ while dark regions have a 2:1 ratio, consistent with the idea that bright areas are the tetragonal phase and dark areas are the cubic phase.

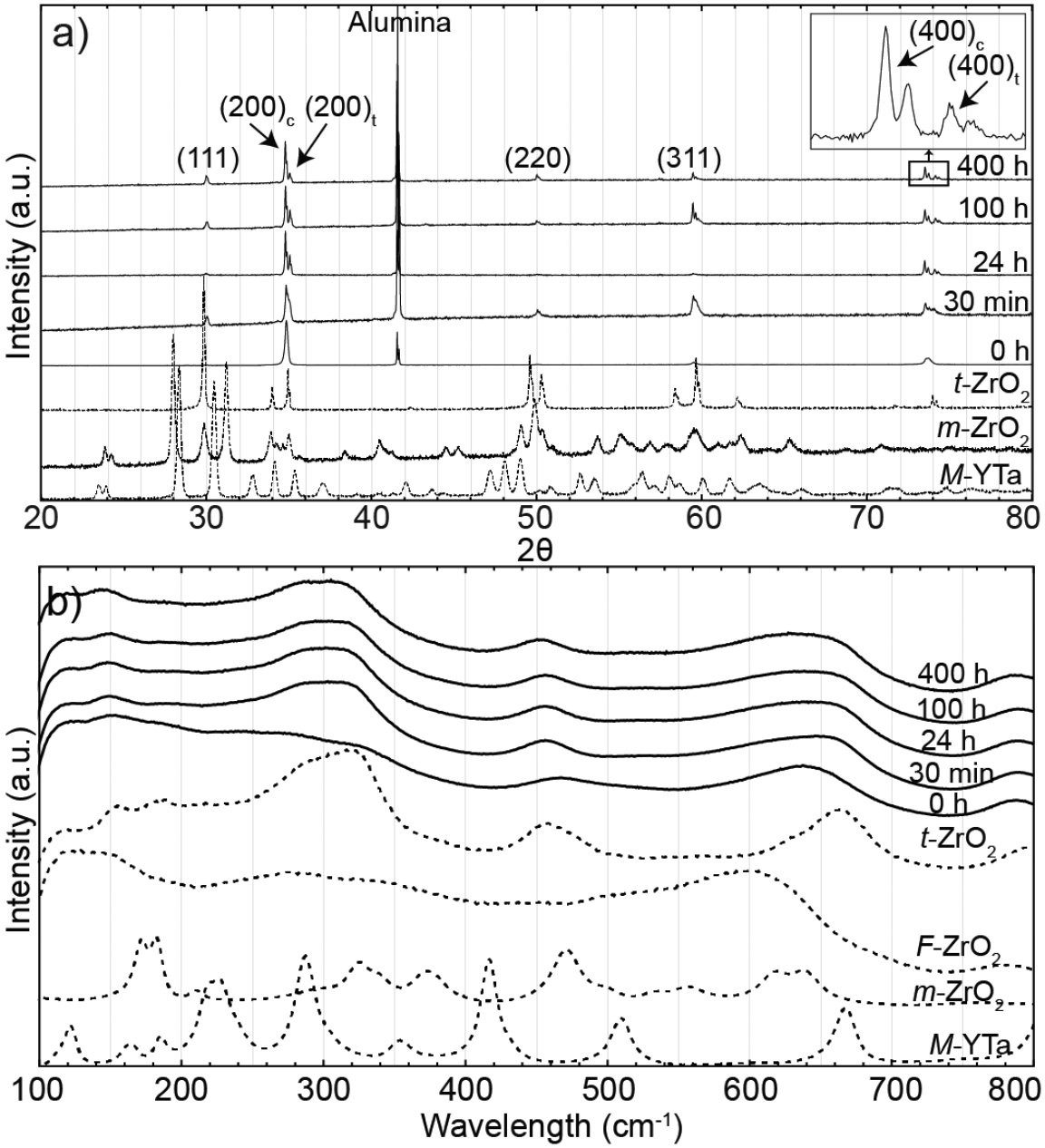

Figure 6.8: XRD (a) and Raman (b) scans of the 25YY14T coating in the as-deposited state and for various times after aging at 1500°C show no significant evidence of m-$YTaO_4$ nor m-ZrO_2. The coating's Raman profile in the as-deposited state is consistent with a tetragonal phase, as the cubic phase is not Raman active in this region. The split of the initially single (400) XRD peak shows the increased amounts of cubic phase relative to that seen at 1250°C. The doublets seen in the XRD spectra are attributed to secondary diffraction by copper $K_{\alpha 2}$ radiation.

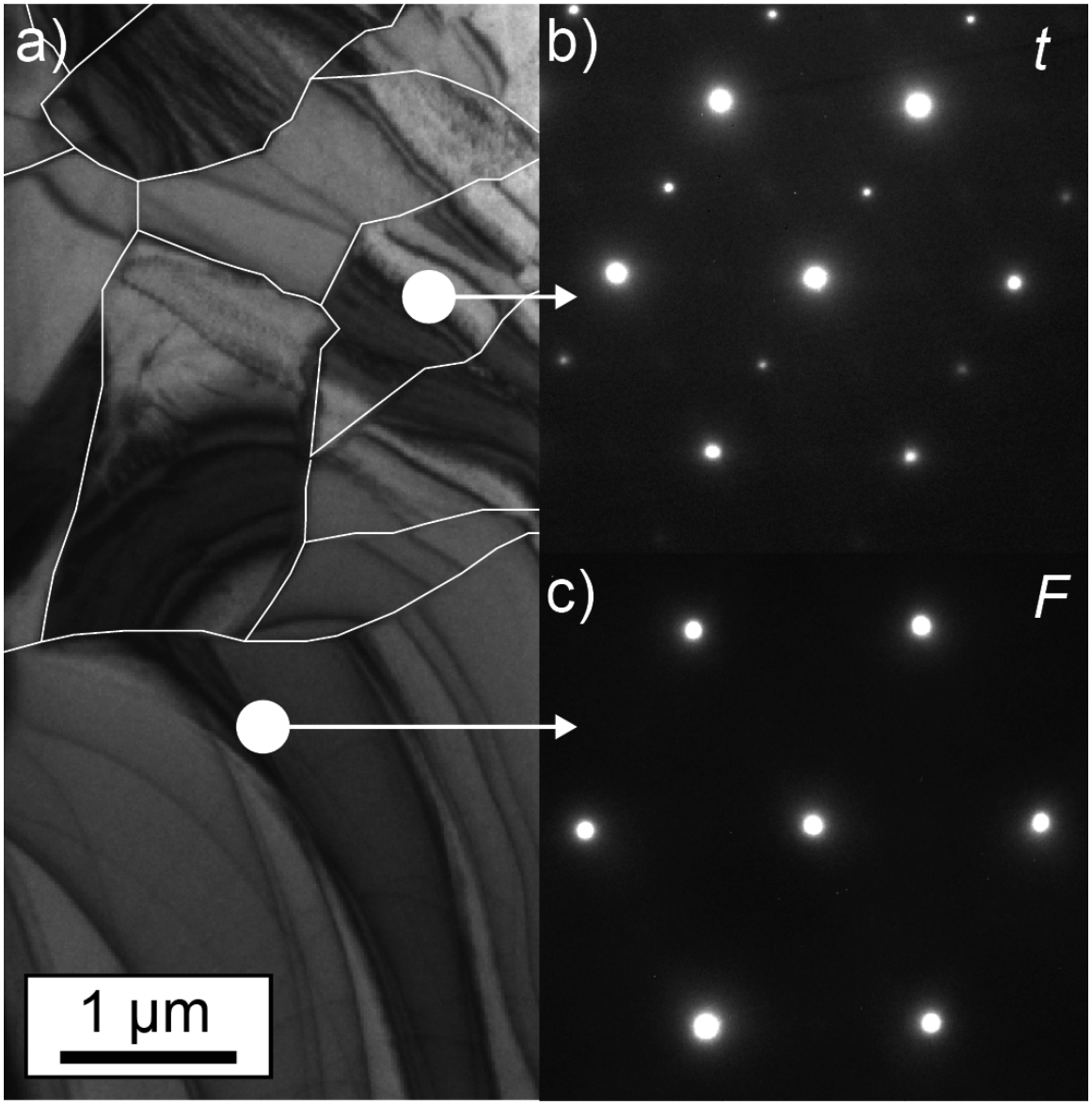

Figure 6.9: TEM BF reveals the microstructure of the 25YY14T TBC after 400 h at 1500°C, with individual grains outlined in white. The [111] ZA of each grain was consistent with a cubic or tetragonal single crystal structure.

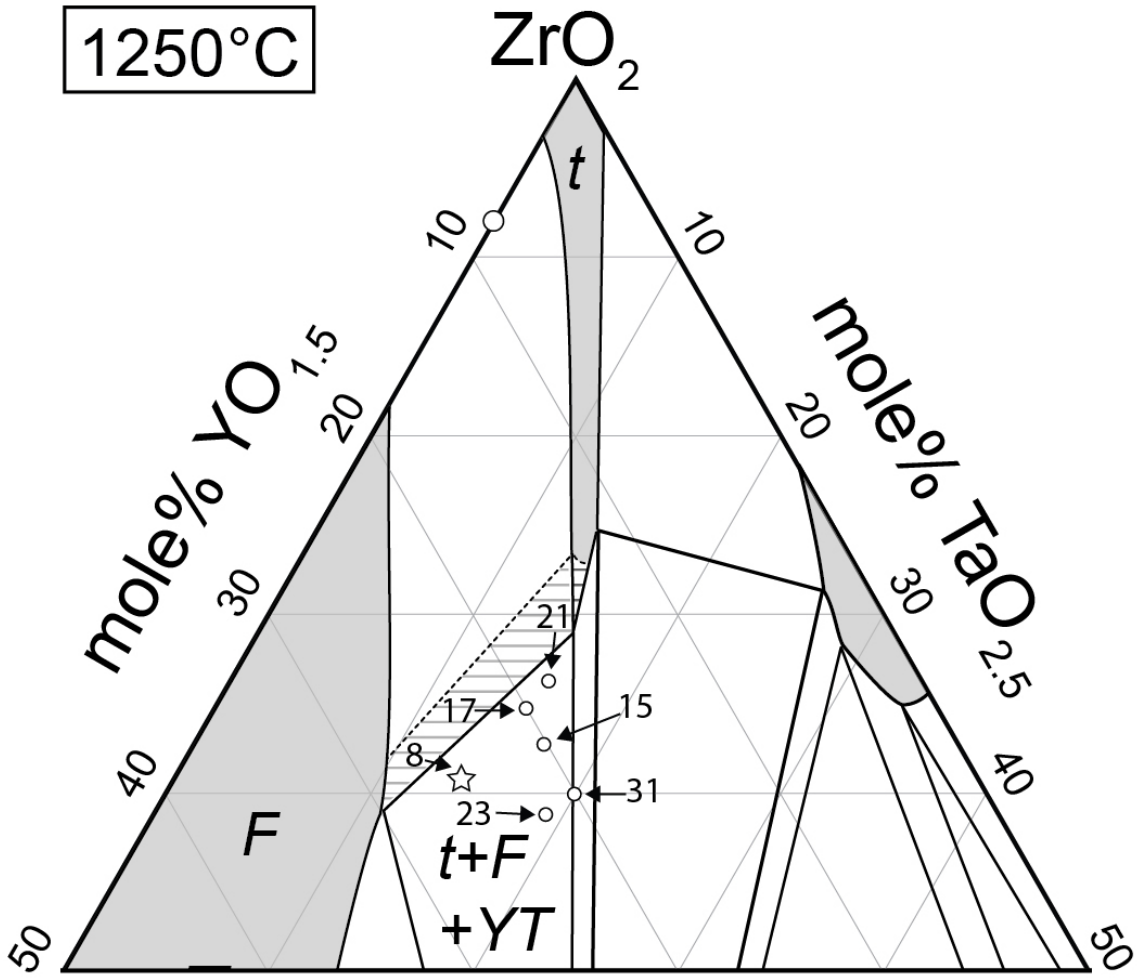

Figure 6.10: The quaternary compositions used to investigate toughness overlaid onto the 1250°C ZrO_2-$YO_{1.5}$-$TaO_{2.5}$ ternary phase diagram. The star represents the 25YY14T composition. Generally, as the amount of cubic phase increases relative to the tetragonal phase the indentation toughness decreases and as the amount of yttrium tantalate phase increases the toughness is similar, excluding the 10Y10Yb20Ta composition, which has unusually large toughness. Units are J/m^2.

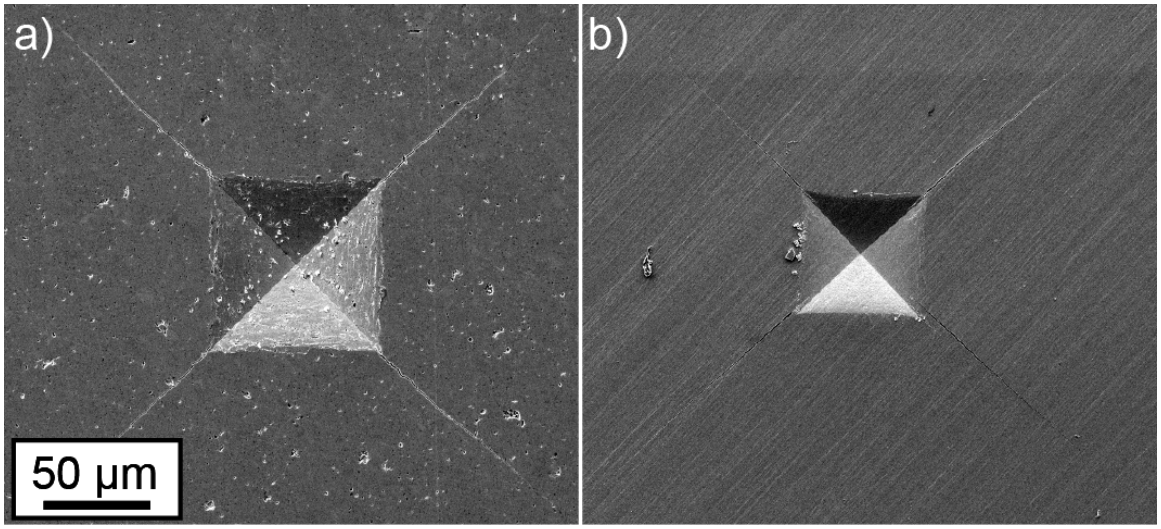

Figure 6.11: Representative indents for the 25YY14T (a) EB-PVD and (b) precursor-derived compacts using a 4 kg load. Porosity in the EB-PVD material results in an increased intent size relative to the dense, precursor-derived specimen, but the length of the cracks are similar.

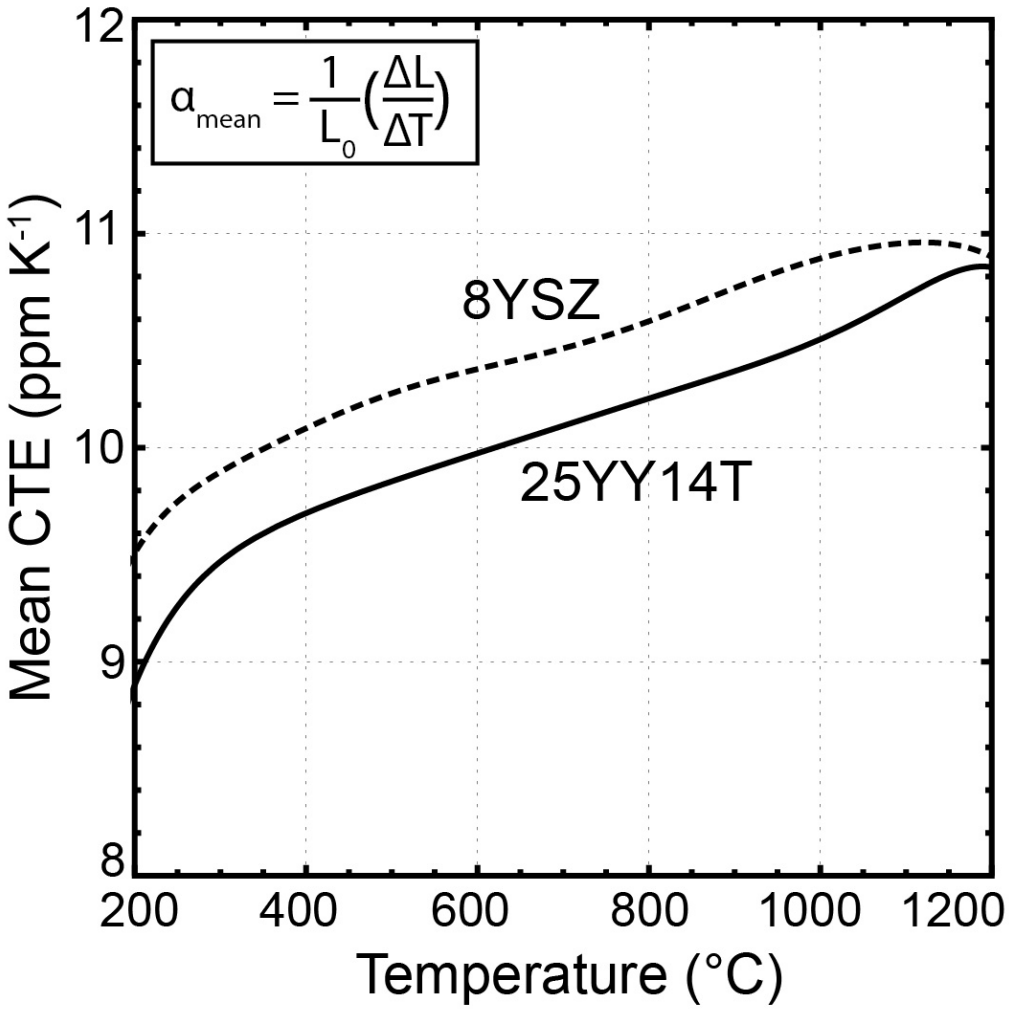

Figure 6.12: The mean CTE for 8YSZ is about 0.5 ppm larger than α_m for 25YY14T throughout a wide temperature range. The two values appear get close to one another near T = 1100-1200°C, but this could be caused by small amounts of sintering experienced in the CTE specimens at these temperatures.

CHAPTER 7: TOUGHNESS OF MULTI-PHASE MATERIALS IN THE ZrO_2-$YO_{1.5}$-$TaO_{2.5}$ SYSTEM

Compositional variability in ZrO_2-(Y/Yb)$O_{1.5}$-$TaO_{2.5}$ thermal barrier coatings (TBCs) processed by electron beam physical vapor deposition (EB-PVD) precludes the deposition of a TBC within the narrow single-phase *t*-ZrO_2 field. It is possible, as it is in 8YSZ, to deposit a metastable, extended solid solution single phase with the tetragonal structure, but compositional fluctuations would inevitably lead to phase partitioning within those regions outside the single-phase field. Secondary phases expected at equilibrium include *c*-ZrO_2 and *M'*-$YTaO_4$, with the relative fraction of each depending on the nominal composition of the TBC and the amount of compositional scatter. The presence of these secondary phases is expected to influence the durability of the coating since they modify important mechanical properties such as toughness. Preliminary evidence presented in the previous chapter indicates that secondary *c*-ZrO_2 and *M'*-$YTaO_4$ phases degrade the intrinsic toughness of the thermal barrier oxide, but a rigorous study investigating the effect on toughness of adding secondary phases to *t*-ZrO_2 was not performed in the context of the quaternary compositions.

In this chapter, the toughness of ZrO_2-$YO_{1.5}$-$TaO_{2.5}$ materials in the three-phase $t + c + M'$ field is probed by indenting polycrystalline compacts sintered at 1250°C. The ternary system was selected because of the greater reliability of the information on phase equilibria and crystal structure, which is not as extensive in the ZrO_2-$YbO_{1.5}$-$TaO_{2.5}$ system or the quaternary system. The goal of the work is to elucidate the effect of adding secondary *c*-ZrO_2 and *M'*-$YTaO_4$ phases on the toughness of *t*-ZrO_2 as well as to investigate general connections between composition, microstructure, toughness, and toughening mechanisms.

The phase constitution, characteristic microstructural features, and toughness of the compacts are reported. Trends between toughness, phase fraction, and microstructure are examined. The role of fracture mode and associated propensity for toughening mechanisms like crack deflection are discussed.

7.1 Experimental Details

Oxide powders of varying composition within the ZrO_2-$YO_{1.5}$-$TaO_{2.5}$ system were synthesized by reverse co-precipitation, as described in Chapter 3. The synthesized compositions include four nearly along a tie-line connecting *t*-ZrO_2 and *c*-ZrO_2 as well as six nearly along a tie-line connecting t-ZrO_2 and *M'*-$YTaO_4$. Standardized electron probe microanalysis (EPMA) was used to measure the bulk composition of each powder. The standard was a 16.62Y16.59Ta material with chemistry determined by an extramural ICP analysis (Dirats Laboratories, Westfield, MA). The measured compositions are listed in Table 7.1.

Powders were consolidated into pellets by spark plasma sintering ("SPS", FCT Systeme, Rauerstein, Germany) and sinter forging ("SF", Oxy-gon, Epsom, New Hamsphire), as described in Chapter 3. Pellet densities were measured by Archimedes method using water as the immersion medium. To convert the absolute densities to relative densities, the theoretical density of each composition was determined using the measured composition, the predicted phase fractions from the isothermal slice of the phase diagram at 1250°C, and the estimated density of each phase. The latter was determined using the equilibrium composition from the isothermal slice of the phase diagram at 1250°C and the lattice parameters of the equilibrium phases determined by x-ray diffraction. Table 7.2 summarizes the lattice parameters and theoretical densities of each phase.

Complementary analysis of the porosity content was carried out by image segmentation on back-scattered electron micrographs of the pellet microstructures. Measurements of relative density based on the segmentations were typically within 1% of those obtained by Archimedes' method, suggesting that this method captures a statistically relevant fraction of the porosity. The segmentation also enabled quantitative information about the shape and size of the pores to be extracted. The pore shape was characterized using the circularity measure, $C = 4\pi A/P^2$, where A is the pore area and P is the pore perimeter. A circular pore has $A = \pi r^2$ and $P = 2\pi r$, so that $C = 1$. As the pore shape deviates from a perfect circle, the circularity measure decreases and therefore the "sharpness" of the pore is expected to increase.

The area-averaged crystallite size in each compact was determined by electron backscatter diffraction (EBSD). In order to ensure that the crystallite size was statistically relevant, the analyzed region always contained at least 50 grains, and usually many more.

Specimen toughness was estimated by microindentation using a Vickers indenter, as described in Chapter 3. The tortuosity of indentation cracks was calculated by considering only the near-tip portion of the crack (5-10 μm) and dividing the path length (arc length) of the crack segment by the distance between the ends of the crack segment.

7.2 Results

Compositions, phase fractions, relative densities, and toughness values are summarized in Table 7.1. Compacts made from compositions that exhibit essentially only one single-phase, namely 16.2Y15.9Ta, 29.4Y11.9Ta, and 39.6Y38.2Ta, are referred to by the majority phase, *t*, *c*, and *M'*, respectively, even though a small fraction of secondary phases may be present. Compacts with a significant fraction of at least two phases are referred to by their

composition. The processing route is appended to the compact name to distinguish between the two processing routes, e.g. *t*-SPS vs. *t*-SF. The following sections focus on detailing the constituent phases, characteristic microstructural features, toughness, and fracture behavior for each material.

7.2.1 Constituent Phases

All compositions of the sintered compacts, except one, are located in the three-phase $t + c + M'$ field (Figure 7.1). The exception, 35.9Y38.7Ta, is rich in Ta relative to the designed composition and is located in the three-phase $t + O + M'$ field. A comparison of the x-ray diffraction patterns for the SPS and SF samples with that from the reference materials confirms that only *t*, *c*, and *M'* phases are present above the detection limit (Figure 7.2). The XRD patterns of materials located along the $t + c$ tie-line exhibit prominent reflections belonging to the *t* and *c* phases. As the compositions move closer to the *c*-ZrO_2 phase field, the intensities of the cubic peaks increase and the intensities of the tetragonal peaks decrease, indicating that the fraction of cubic phase is increasing at the expense of the tetragonal phase. The ratios of the peak intensities for the tetragonal and cubic phases qualitatively appear to be consistent with the calculated phase fractions in Table 7.1, although a rigorous quantification of the peak intensities was not performed. No significant differences are observed between XRD spectra taken from SPS and SF compacts of the same composition. Therefore, the constituent phases of the materials along the $t + c$ tie-line and their relative fractions are close to those anticipated based on their measured compositions in Table 7.1 and are independent of processing route. Similar trends are observed in the XRD patterns of materials located along the $t + M'$ tie-line. No evidence of the *O* phase was found in the 35.9Y38.7Ta SF material.

7.2.2 Microstructure

The characteristic microstructural features of the compacts are the crystallite size and the size, shape, and content of porosity (Figure 7.3). The range of crystallite size spanned by the entire set of compacts was estimated by measuring the size of the grains in the *t*, *c*, and *M'* materials. The crystallite size encompasses roughly one order of magnitude, from ~0.25 to 2.5 μm (Figure 7.4(a)). The smallest crystallites were observed in the *M'* compacts ($d_{SPS} \approx$ 0.25 μm, $d_{SF} \approx 0.4$ μm), intermediately sized crystallites were found in the *t* compacts ($d_{SPS} \approx 0.6$ μm, $d_{SF} \approx 0.4$ μm), and the largest crystallites were observed in the *c* compacts ($d_{SPS} \approx$ 1 μm, $d_{SF} \approx 2.5$ μm). It is noted that compositions with a more comparable fraction of two-phases (e.g. 50%-50%) likely have smaller grain sizes than the predominately single-phase compositions. Nevertheless, the data indicates that the crystallite size differs by no more than a factor 3 between compacts of the same composition.

The relative density of the compacts ranges from 0.88 to 0.99 (Table 7.1). The highest densities are generally achieved in the SF samples, which display relative densities greater than 0.94 in all cases. Considering any single composition, the average pore size in the SPS materials is 1.5-2x that of the SF materials, although the *c* and *M'* materials are exceptions to this trend (Figure 7.4(b)). In addition to having larger pores, the SPS specimens also tend to exhibit lower circularity than the pores in the SF specimens (Figure 7.4(c)). In summary, the SPS compacts generally display higher porosity content as well as larger and sharper pores.

7.2.3 Toughness

The toughness of the approximately single-phase *t*-ZrO_2 compacts varies from about 20-25 J/m^2 for *t*-SF to about 35-40 J/m^2 for *t*-SPS (Figure 7.5(a)), suggesting that the toughness is

sensitive to processing route and hence microstructure. As *c*-ZrO_2 is added to *t*-ZrO_2, the toughness drops rapidly and non-linearly to the low toughness of *c*-ZrO_2, ~5 J/m^2 (Figure 7.5(a)). Some variation in toughness between the *t* + *c* SPS and SF specimens is evident, suggesting, as before, that the toughness is sensitive to the processing route. The toughness of the SPS samples are generally larger but within a factor of two of the SF samples, and the absolute difference decreases with increasing *c*-ZrO_2 content. No difference in toughness is observed between *c*-SPS and *c*-SF (note that the two data points are overlapping on Figure 7.5(a).) Considering only a single processing route, the decrease in toughness with increasing *c*-ZrO_2 content is rapid enough that compositions with ~25% *c*-ZrO_2 exhibit toughness ~50% lower than that of pure *t*-ZrO_2.

In contrast, as *M'*-$YTaO_4$ is added to *t*-ZrO_2, the toughness is relatively unchanged, indicating the toughness is relatively insensitive to the phase fraction of *M'*, except perhaps in the very *t*-ZrO_2 rich portion of the tie-line (Figure 7.5(b)). The qualitatively different trend between toughness and phase fraction along the *t* + *M'* tie-line is likely related to the much larger toughness of *M'* compacts, ~20-25 J/m^2, in comparison to the *c* compacts. Although some variation in the toughness is evident between *t* + *M'* samples made by SPS and SF, neither processing route consistently produces specimens with higher toughness except when M' is only present in very small amounts.

7.2.4. Fracture Behavior

Fracture surfaces from the *t*, *c*, and *M'* materials reveal that the fracture mode can vary significantly between samples of different composition and processing route (Figure 7.6). For example, the *t*-SPS sample exhibits almost complete intergranular fracture while the *t*-SF sample exhibits a much larger degree of transgranular fracture. The (areal) percentage of

intergranular fracture for the *t*-SPS material based on these and similar images is estimated at ~90% and that for the *t*-SF material is ~50-60%. In contrast, the *c*-SPS and *c*-SF specimens both exhibit nearly complete transgranular fracture (>95%) and the *M'*-SPS and *M'*-SF compacts both exhibit a large degree of transgranular fracture (~80%). An important observation is that of the three materials, *t*, *c*, and *M'*, only compacts made from *t* display variable fracture mode with processing route and only compacts made from *t* exhibit substantial toughness variation with processing route. Therefore, considering any single composition, the fracture mode appears to be tied to the toughness of the compact and increased amounts of intergranular fracture correlate with higher toughness.

Variation in fracture mode is accompanied by changes to the prevalence of toughening mechanisms reflected in the extent of crack deflection, microcracking, grain bridging, and grain pullout. Manifestations of these toughening mechanisms are observed in the near-tip region of indentation cracks (Figure 7.7). The *t*-SPS specimen, which exhibits the highest amount of intergranular fracture, displays a prominent amount of crack deflection as well as numerous examples of microcracking, grain bridging, and grain pullout in a relatively short (<10 μm) crack segment (Figure 7.7(a)). The *t*-SF specimen, which exhibits a relatively lower incidence of intergranular fracture compared to *t*-SPS, qualitatively displays markedly fewer instances of the toughening mechanisms (Figure 7.7(b)). The reduced tendency for crack deflection is demonstrated by the reduced tortuosity of the cracks, ~1.1 for *t*-SF vs ~1.3 for *t*-SPS. Instances of the toughening mechanisms were found in all investigated samples that displayed a significant fraction of intergranular fracture, e.g. *M'*-SF (Figure 7.7(c)), but not in samples that displayed complete transgranular fracture, e.g. *c*-SF (Figure

7.7(d)). Therefore, the prevalence of the toughening mechanisms is linked to the propensity for intergranular fracture.

7.3 Discussion

Two salient findings arise from the reported observations: (a) trends between toughness and phase constitution are different along the $t + c$ and $t + M'$ tie-lines and (b) variation in toughness with processing route appears to be related to the variations in microstructure, which influences the fracture mode and prevalence of toughening mechanisms like crack deflection, microcracking, and grain bridging. The remainder of this chapter focuses on: (1) quantitatively assessing the trends in toughness with phase constitution and microstructure by fitting the collected data to a phenomenological model, (2) evaluating the statistical validity of the trends between toughness, phase constitution, and microstructure within the context of the model, (3) examining the significance of the observed fracture behavior on the current understanding of toughness and toughening mechanisms in the single-phase materials, and (4) highlighting implications of toughness trends with phase constitution on the durability of ZrO_2-$REO_{1.5}$-$TaO_{2.5}$ (RE = rare-earth) thermal barrier coatings.

7.3.1 Phenomenological Model

A comprehensive review of the literature reveals the lack of a sufficiently general micromechanics model that predicts toughness of multi-phase materials from the toughness of the constituent phases, phase fractions, and relevant microstructure parameters such as porosity content. In an effort to provide insight, the following phenomenological model is proposed to extract trends between toughness, phase constitution, and microstructure:

$$G = G_0 e^{Ax+By} \cdot (1+Cz) \,, \tag{7.1}$$

where G is the toughness, x is the fraction of c phase, y is the fraction of M' phase, z is porosity content, and G_0, A, B, and C are fitting constants. The grain size was not used in the model since the grain size was not collected for every compact. Whereas it is expected that various features of the porosity such as the location, size, and sharpness contribute to the impact on toughness, the model utilizes only the porosity content for simplicity and because it is expected to be the feature of the porosity that most influences the toughness. The effect of porosity was modeled as a linear function since the observed porosity contents, ~0-12%, encompass a relatively small range. The best fit yields the following values for the fitting constants: $G_0 = 27.4 \pm 3.0$ J/m^2, $A = -2.2 \pm 0.4$, $B = -0.4 \pm 0.2$, and $C = 3.0 \pm 2.0$ (mean value ± standard error). The residuals between the observed and predicted toughness values are generally small (root mean squared error ~4.3 J/m^2) and the correlation coefficient R^2 is close to unity, 0.96 (Figure 7.5(c)).

7.3.2 Evaluation of Trends Between Toughness, Phase Constitution, and Microstructure

Trends between toughness and phase constitution are reflected by the fitting coefficients A and B in the model, with A relating to the $t + c$ tie-line and B relating to the $t + M'$ tie-line. Negative values indicate that toughness decreases with increasing fraction of secondary phase (c or M') and the magnitude describes the severity of the toughness decrease. When the fractions of the secondary phase are zero, the toughness is equal to G_0, the toughness of a fully dense tetragonal compact. The mean values and standard errors for A and B reveal that the effect on toughness of adding c to t is different than that of adding M' to t at the 95% confidence level (± 2 standard errors). The more negative value of A suggests that additions of M' are less detrimental to the toughness than additions of c.

The calculated trends between toughness and phase fraction along each tie-line exhibit the anticipated shape based on the indentation results: additions of *c* to *t* produce rapid, non-linear decreases in toughness and additions of *M'* to *t* do not substantially affect the toughness (Figure 7.5(a) and (b)). The trends can also be applied to the toughness of the quaternary compositions in Chapter 6 (Figure 7.8). The RMS error of the calculated toughness values for the quaternary compositions is ~4.5 J/m^2, which is similar to the RMS of the model in the ternary system and therefore suggests that the model is valid for the quaternary system. Notably, the model does an excellent job in predicting the toughness of the 25YY14T composition discussed in detail in Chapter 6. The poor prediction of the 20YY20T composition is likely related to the elevated toughness of the composition relative to the toughness observed for similar ternary compositions (Figure 7.5(b)). Given that the quaternary compacts were assumed to be fully dense to perform these toughness calculations, it is possible that the 20YY20T contains a significant amount of porosity that changes the fracture behavior relative to that observed in the ternary system.

Trends between toughness and microstructure are reflected by the fitting coefficient *C* in the model, with positive values indicating that toughness increases with increasing porosity content. The results for the mean value and standard error of *C* suggest that there is no global relationship between toughness and porosity content at the 95% confidence level, since the confidence interval includes both negative and positive values ([-1.0 to 7.0]). This does not necessarily mean that toughness is independent of microstructure, but rather that the dependence on microstructure is more complex than that captured by the model fitting. Given the hypothesis that the variation in toughness with processing route is related to the fracture mode and prevalence of related toughening mechanisms, potentially significant

factors that are not considered in the model are the grain size, the mechanical properties of the grain boundaries, and the magnitude of residual thermal stresses. The grain boundary strength and toughness can strongly influence the fracture mode, as has been shown for structural ceramics like Si_3N_4 [156,157] and SiC [158]. Residual thermal stresses arising from anisotropy in coefficient of thermal expansion and elastic modulus are known to play an important role in the toughness generated by microcracking, grain bridging, and grain pullout in structural ceramics such as Al_2O_3 [159-161] and SiC [158]. Since the compacts tested in this work exhibit multiple phases of varying composition and crystal structure as well as differing phase constitution, a diversity of residual stresses and grain boundary properties are expected. This is reflected by the diversity of fracture behavior in the single-phase compacts (Figure 7.6). When no significant residual stresses are anticipated due to crystal symmetry, e.g. in *c*-SF, the compact fractures almost completely transgranularly; instead, when symmetry residual stresses are present, the fracture morphology depends significantly on the identities of the phases, e.g. *t*-SF vs. *M'*-SF, which exhibited differing amounts of intergranular fracture (~50-60% vs ~20%) but similar relative density, pore size, pore circularity, and crystallite size. It is generally expected that the characteristics of the porosity modify the residual stresses and grain boundary properties, but the effect on toughness likely depends on composition because of the above considerations. A model rooted in micromechanics is needed to capture these effects.

7.3.3 Implications on Toughness and Toughening Mechanisms of Single-Phase Materials

The toughness of dense, single-phase *t* compacts predicted by the model, ~27 J/m^2, is substantially lower than previous estimates of similar non-transformable compositions equilibrated at 1500°C, ~40-53 J/m^2 [13,16]. The relatively large toughness previously

observed has been ascribed to ferroelastic switching [16]. The results in this study do not negate the possibility of ferroelastic switching but suggest that crack deflection, microcracking, grain bridging, and grain pullout can contribute significantly to the toughness of polycrystalline *t* compacts. The disparity in toughness between *t*-SPS and *t*-SF, ~15 J/m^2, serves as an estimate of the toughening generated by these mechanisms under the assumption that any toughening produced by ferroelastic switching is comparable in both materials, which is justifiable given the similarity in crystallite size. This factor of ~1.6 difference is well within the range of toughening that has been observed on other structural ceramics by crack deflection [158,162,163], microcracking [159,164-167], and grain bridging [160], each of which can increase toughness by a factor of two or more. It follows that the relatively larger toughness estimated in [13,16] could also originate from mechanisms besides ferroelastic switching, but the paucity of information related to microstructure, fracture mode, and fracture pathways in the tested compacts prohibits a more detailed analysis. One important inference from this work is that comprehensive characterization of specimen microstructure and fracture behavior should be presented together with indentation toughness data.

The toughness of *M'* has not been previously reported and is predicted by the model to be ~18 J/m^2. The relatively high toughness in comparison to *c* (predicted to be ~3 J/m^2 by the model) suggests that one or more toughening mechanisms are active and the analysis of the fracture mode and fracture pathways demonstrates that crack deflection, microcracking, and grain bridging contribute to the toughness. It is possible, however, that other toughening mechanisms are operative or could be operative for different microstructures. For example, previous first principles calculations detailing the shape of the energy landscape for *M'* at 0

K suggest that ferroelastic switching is a viable toughening mechanism [168]. A more detailed investigation into the toughness of *M'* is needed to determine whether mechanisms besides those reported in this publication are operative.

7.3.2 Implication on Durability of ZrO_2-$REO_{1.5}$-$TaO_{2.5}$ TBCs

Since the resistance of TBCs to various fracture-type failure mechanisms is linked to the toughness of the thermal barrier oxide, the observed trends between toughness and phase constitution have important implications for the durability of ZrO_2-$REO_{1.5}$-$TaO_{2.5}$ coatings [6]. The toughness of *t* estimated in this work is lower than that characteristic of polycrystalline 8YSZ, ~40 J/m^2 [27,75] and therefore suggests that coatings made from non-transformable tetragonal compositions have marginally lower durability than state-of-the-art 8YSZ TBCs. The presence of secondary phases in *t* coatings, which originate from compositional fluctuations during EB-PVD processing, modifies the toughness. The reported chemical profiles for a coating with nominal composition in the *t* phase field indicate that the equilibrium phase fractions vary approximately from 0.5-1 for *t*, 0-0.3 for *c*, and 0-0.25 for *M'*, producing local toughness that varies from approximately ~13-27 J/m^2 [72]. Accordingly, the compositional fluctuations can degrade the local toughness by as much as a factor of one half and the average toughness by roughly one quarter. Consequently, the durability of TBCs based on non-transformable *t* is likely only moderately degraded by compositional variation.

7.4 Synopsis

This study has investigated toughness and toughening mechanisms of ZrO_2-$YO_{1.5}$-$TaO_{2.5}$ materials in the three-phase *t* + *c* + *M'* field by indenting polycrystalline compacts sintered at 1250°C. The toughness is dependent on composition and microstructure and the effect of

each can be comparable. The influence of composition arises from the relative fractions of the phases present at equilibrium and the differences between their intrinsic toughness. The influence of microstructure appears to originate from variations in the fracture pathway and the related propensity for crack deflection, microcracking, grain pullout, and grain bridging. Important implications on the current understanding of toughness and toughening mechanisms of ZrO_2-$REO_{1.5}$-$TaO_{2.5}$ (RE = rare-earth) materials and thermal barrier coatings are:

- A number of toughening mechanisms are found to contribute to the toughness of polycrystalline compacts fabricated from compositions in the three-phase *t* + *c* + *M'* field. The toughening mechanisms were previously unreported for these materials. This finding advocates the need for comprehensive characterization of microstructure and fracture pathways in conjunction with toughness measurements in order to understand the diversity of operative toughening mechanisms.
- TBCs based on non-transformable tetragonal compositions could have lower durability than previously expected. The toughness of the single-phase material at 1250°C varies from ~20-40 J/m^2 depending on microstructure, with the lower bound representing a significant decrease relative to the toughness previously reported [13,16]. Secondary phases arising with compositional variation associated with electron beam physical vapor deposition further degrade the average toughness by a factor of about one quarter.

7.5 Tables and Figures

Table 7.1: Relative phase fractions, relative density, and toughness of all compositions tested in this work. (Key: SPS = spark plasma sintering, SF = sinter forging, * = fraction of orthorhombic phase, ** = density measured using image thresholding on micrographs instead of Archimedes' method)

Composition	*t* phase fraction	*c* phase fraction	*M'* phase fraction	SPS Relative Density	SPS Toughness (J/m^2)	SF Relative Density	SF Toughness (J/m^2)
16.2Y15.9Ta	0.96	0.02	0.02	0.94	40.5 ± 2.9 34.8 ± 1.9	0.97	23.7 ± 2.1 22.1 ± 2.4
19.3Y15.1Ta	0.75	0.22	0.03	0.89	22.1 ± 1.2 22.7 ± 4.0	0.98	15.3 ± 1.2
22.5Y14.2Ta	0.52	0.45	0.03	0.90 0.96	16.2 ± 1.2 6.9 ± 1.1	0.99	8.6 ± 0.5
29.4Y11.9Ta	0.04	0.94	0.02	0.97	4.2 ± 0.4	0.95	5.0 ± 0.2
19.3Y18.4Ta	0.82	0.07	0.11	0.93 0.93 0.88	22.9 ± 1.2 19.9 ± 1.8 29.1 ± 0.8	0.96	25.2 ± 1.4
24.5Y21.6Ta **24Y21.9Ta**	0.58 0.61	0.16 0.14	0.26 0.25	0.95 -	27.5 ± 1.6 -	- 0.94	- 22.2 ± 1.6
29.3Y27.4Ta	0.42	0.09	0.49	0.88 0.96	22.2 ± 1.9 17.1 ± 0.8	-	-
39.6Y38.2Ta	0.04	0.02	0.94	0.89 0.91	25.5 ± 1.7 19.3 ± 0.7	-	-
35.9Y38.7Ta	0.15	0.08*	0.77	-	-	0.98**	26.5 ± 2.0

Table 7.2: Nominal chemistry, lattice parameters, and densities for each phase as determined using the methods described in the experimental methods section.

Phase	Nominal Chemistry	Lattice Parameters (Å)	Theoretical Density (g/cm^3)
t	15.7Y15.4Ta	a = 5.11 c = 5.24	6.63
c	30Y11Ta	a = 5.16	6.42
M'	41Y41Ta	a = 5.29 b= 5.47 c = 5.11 ß = 96.79°	7.19

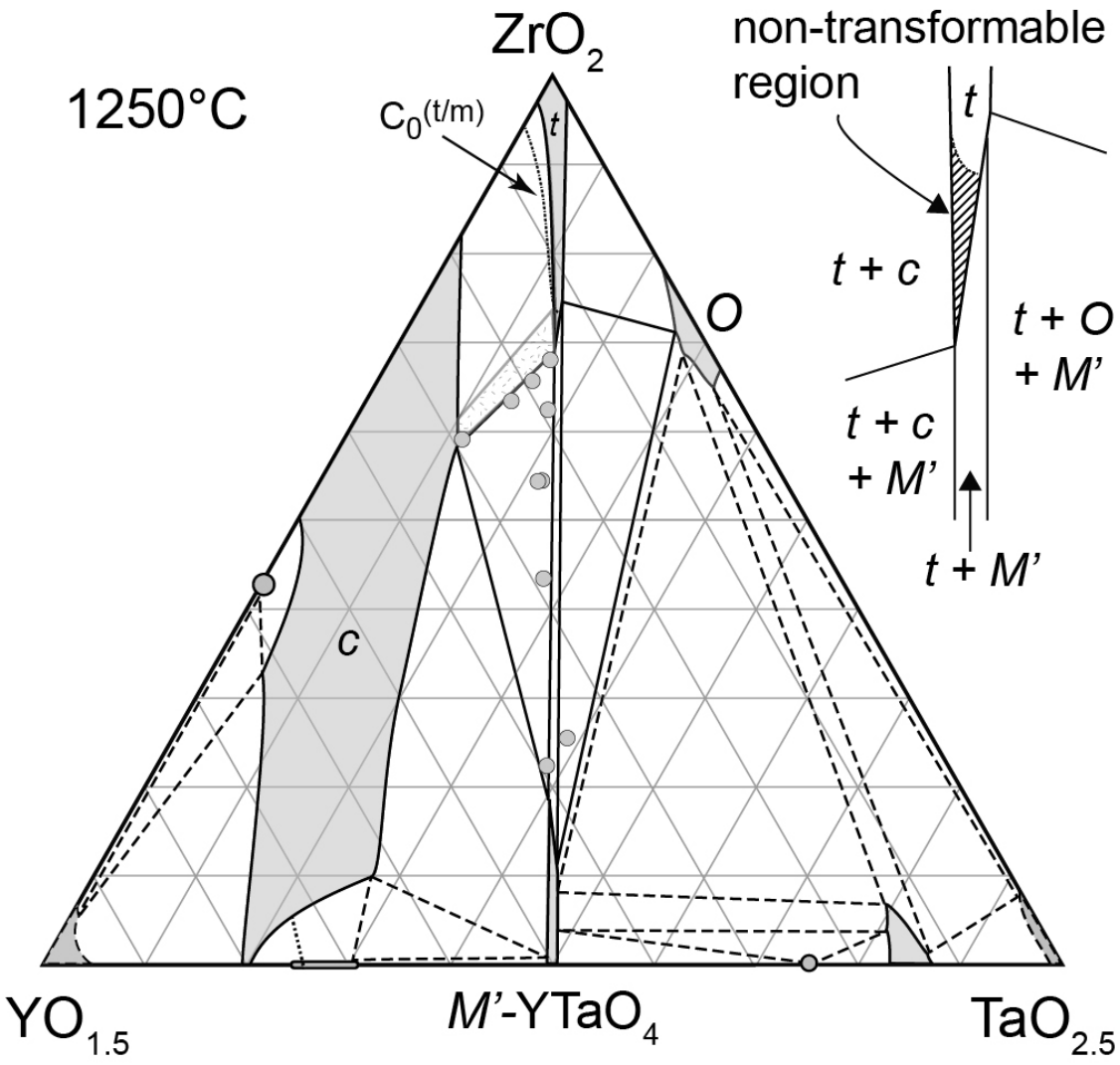

Figure 7.7: Compositions located at the tip of the tetragonal phase field in the ZrO_2-$YO_{1.5}$-$TaO_{2.5}$ system are non-transformable to *m*-ZrO_2 on cooling, a desirable trait for thermal barrier coating materials. The region of non-transformability is clearly illustrated by a hatched region in the inset on the top right, which shows a high magnification view of the tip. Overlaid grey dots in the *t + c + M'* three-phase field on the phase diagram show the measured compositions for the compacts tested in this work. One material near the *M'*-$YTaO_4$ phase field, whose chemistry deviated significantly from the designed composition, falls into the *t + O + M'* three-phase field.

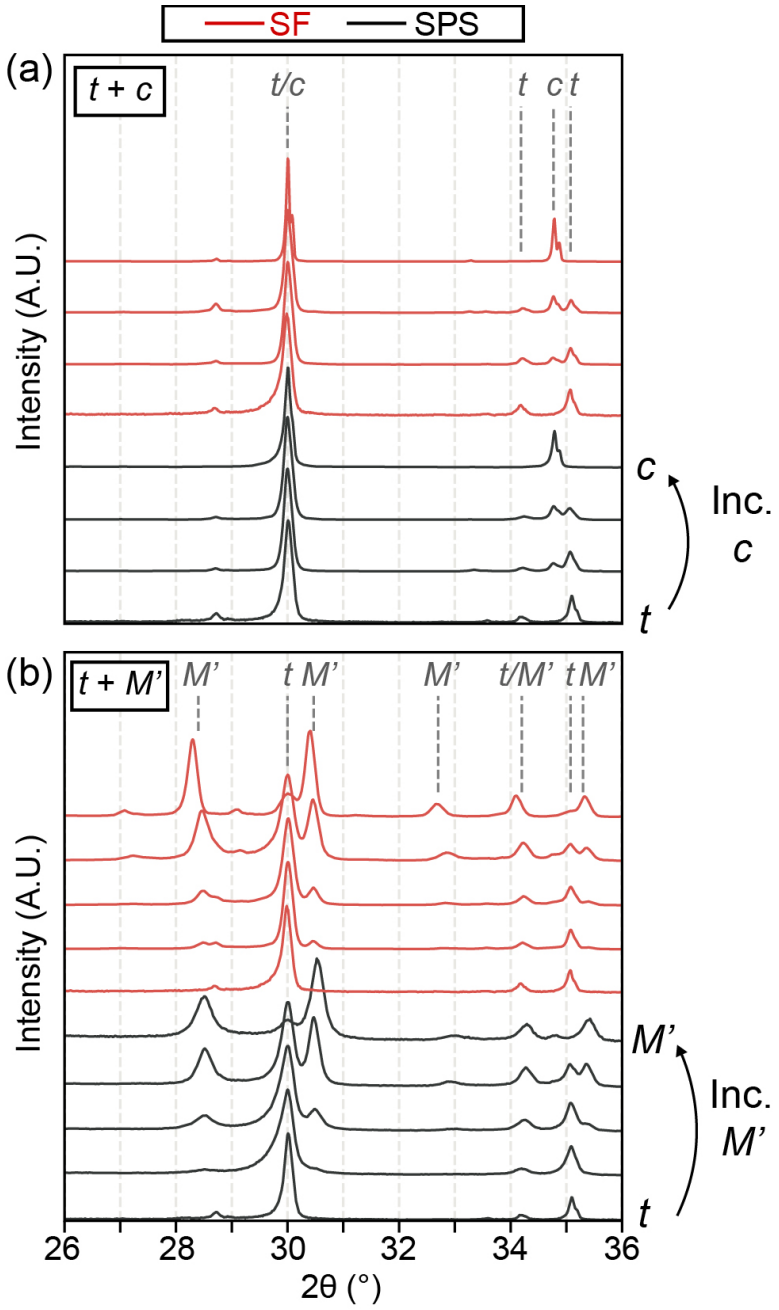

Figure 7.2: XRD spectra taken from materials approximately along tie-lines connecting the (a) $t + c$ phases and (b) $t + M'$ phases show the expected phases in qualitatively the correct fraction based on their composition. For each processing route, SPS in red and SF in black, the bottommost spectrum is the approximately single-phase t-ZrO_2 sample, the topmost spectrum is the approximately single-phase c-ZrO_2 or M'-$YTaO_4$ sample, and the middle spectra are the multi-phase samples in ascending order of increasing secondary phase content. Small, unlabeled peaks are diffraction from secondary $W_{K\alpha}$ radiation. The peak shift in the 35.9Y38.7Ta SF material (top composition in the $t + M'$ series) is likely due to the different composition of the M' phase in the three-phase $t + M' + O$ field relative to that in the $t + c + M'$ field.

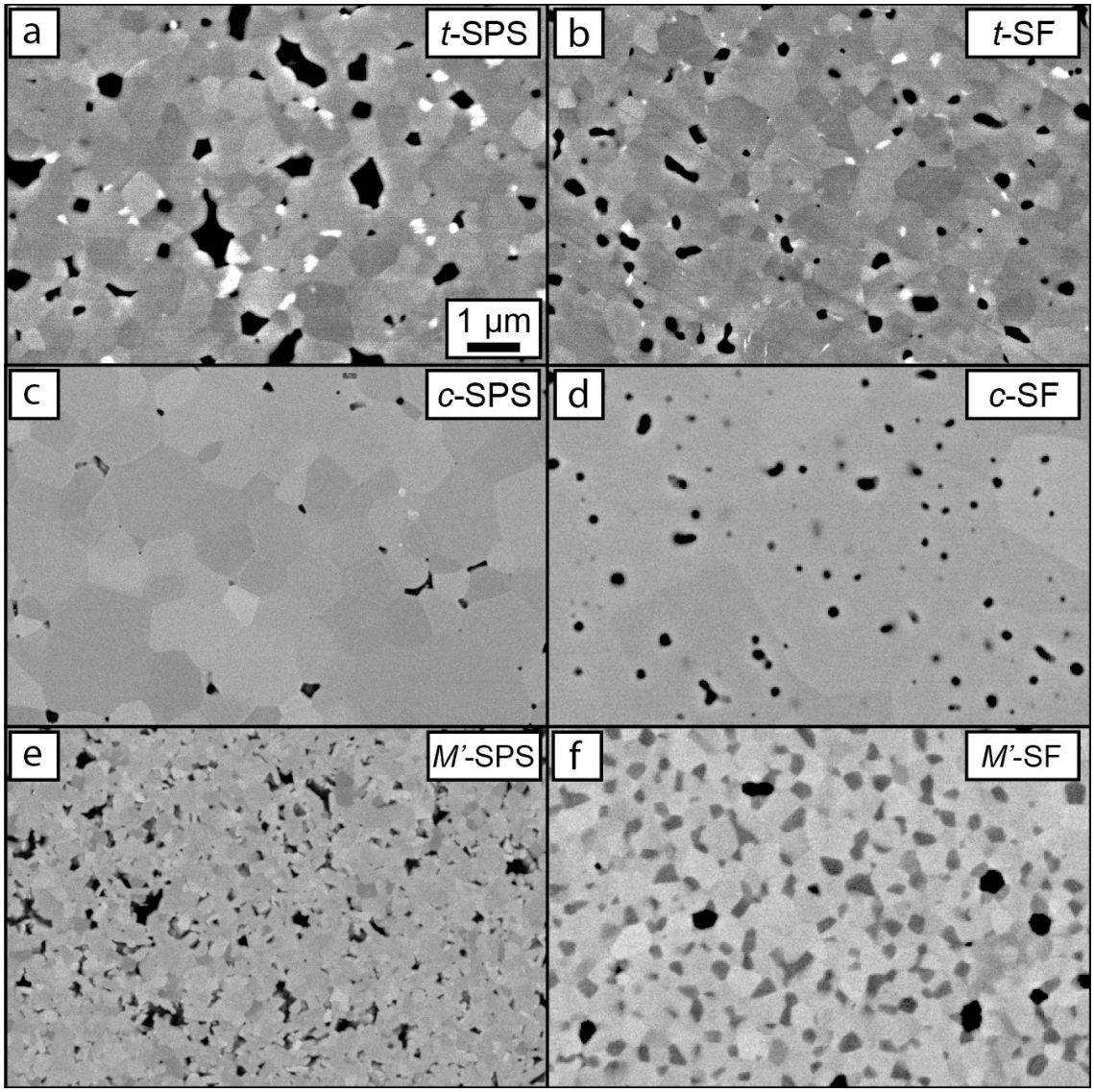

Figure 7.3: Back scattered electron micrographs from the approximately single-phase materials give an overall sense for the range of observed microstructures. The contrast in the images is attributed to both Z-contrast and orientation contrast. Since the depicted materials are close to single-phase, with the exception of the *M'*-SF (35.9Y38.7Ta) material, which has ~20% *t*-ZrO_2, the majority of the contrast is from differing orientation of the crystallites. However, some secondary phases can be seen in the materials. In all cases, the brightest crystallites are *M'*-$YTaO_4$, the crystallites of intermediate contrasts are *t*-ZrO_2 or *c*-ZrO_2 depending on the composition, and the dark regions are porosity.

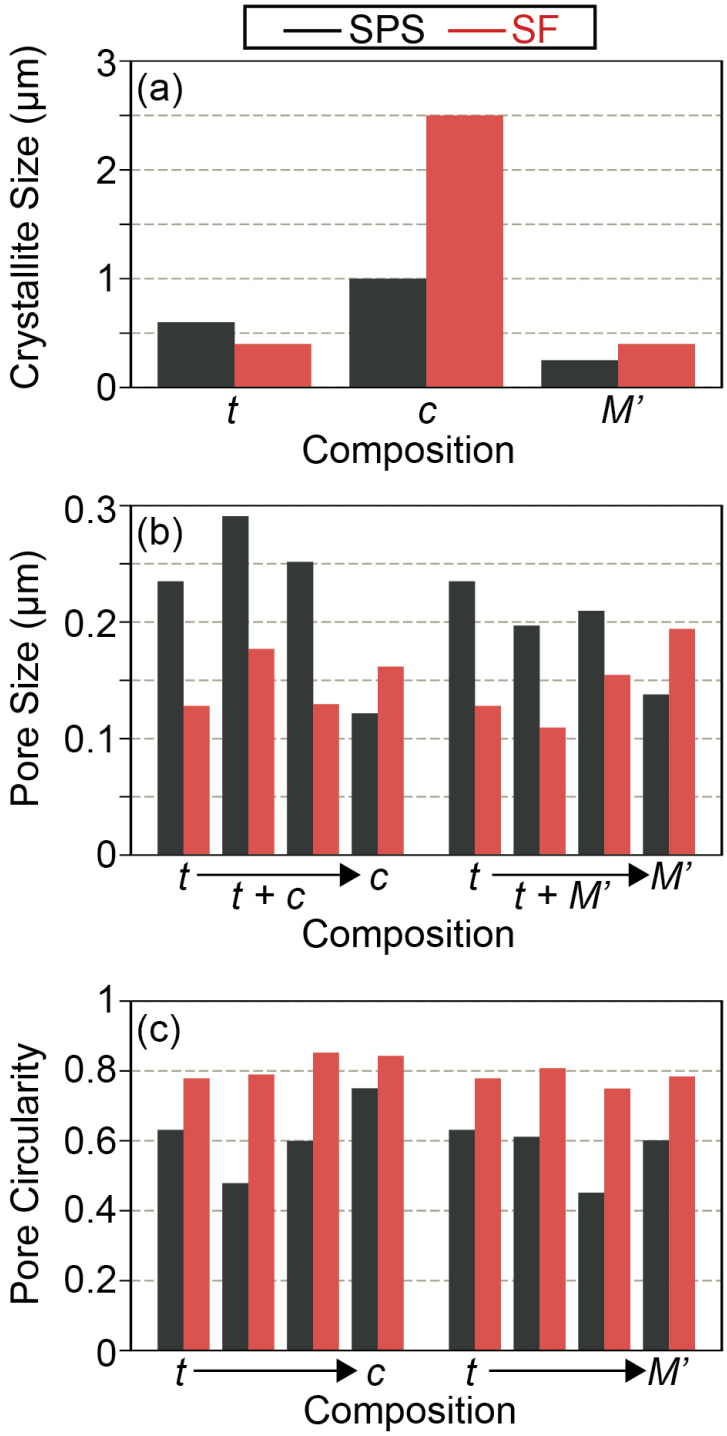

Figure 7.4. Plots showing the (a) crystallite size, (b) pore size, and (c) pore circularity for the tested specimens give a sense for how the relevant microstructural features vary as a function of composition and processing route. Whereas no clear trends arise for how the crystallite size varies with composition or processing route, it is clear that specimens made by SPS generally have larger and sharper (less circular) pores than specimens made by SF. Data from the 29.3Y27.4Ta-SPS compact (along the *t* + *M'* tie-line) has been excluded from (b) and (c) since a counterpart SF compact could not be fabricated.

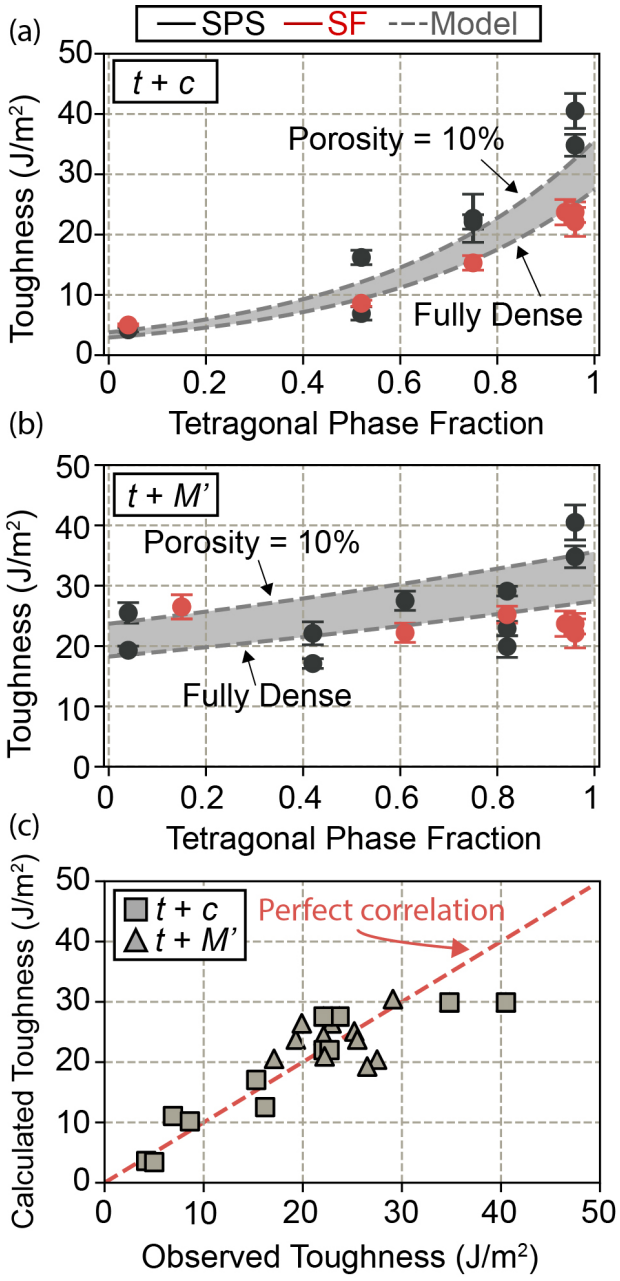

Figure 7.5: The toughness of the compacts generally decreases with increasing fraction of (a) *c* and (b) *M'* phases, even though some variation in toughness is evident between samples made by SPS versus SF. The decrease in toughness is much more rapid along the tie-line connecting *t* + *c* than *t* + *M'*, likely due to the lower toughness of the *c* phase compared to the *M'* phase. The model that was fit to the toughness and microstructure data predicts the toughness of the compacts reasonably well, (c). The gray, dashed lines in (a) and (b) represent predictions from the model for the two tie-lines at two different levels of porosity, 0% and 10%.

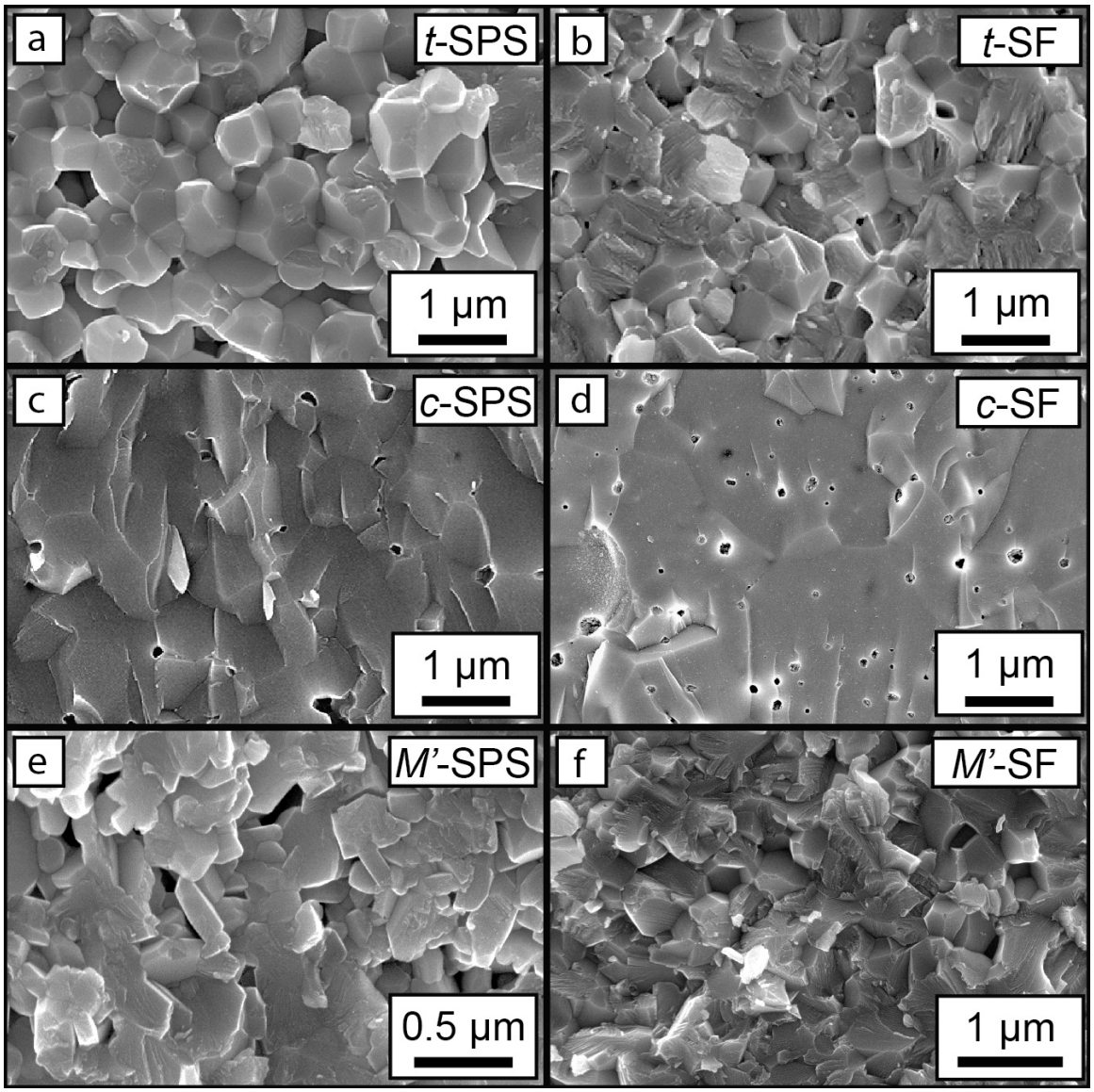

Figure 7.6: The fracture surface from the *t*-SPS specimen, (a), shows substantially more intergranular fracture (~90%) than the *t*-SF specimen (~50-60%), (b). The (c) *c*-SPS, (d) *c*-SF, (e) *M'*-SPS, and (f) *M'*-SF (35.9Y38.7Ta) specimens exhibit primarily transgranular fracture (>95%, >95%, 80%, 80%).

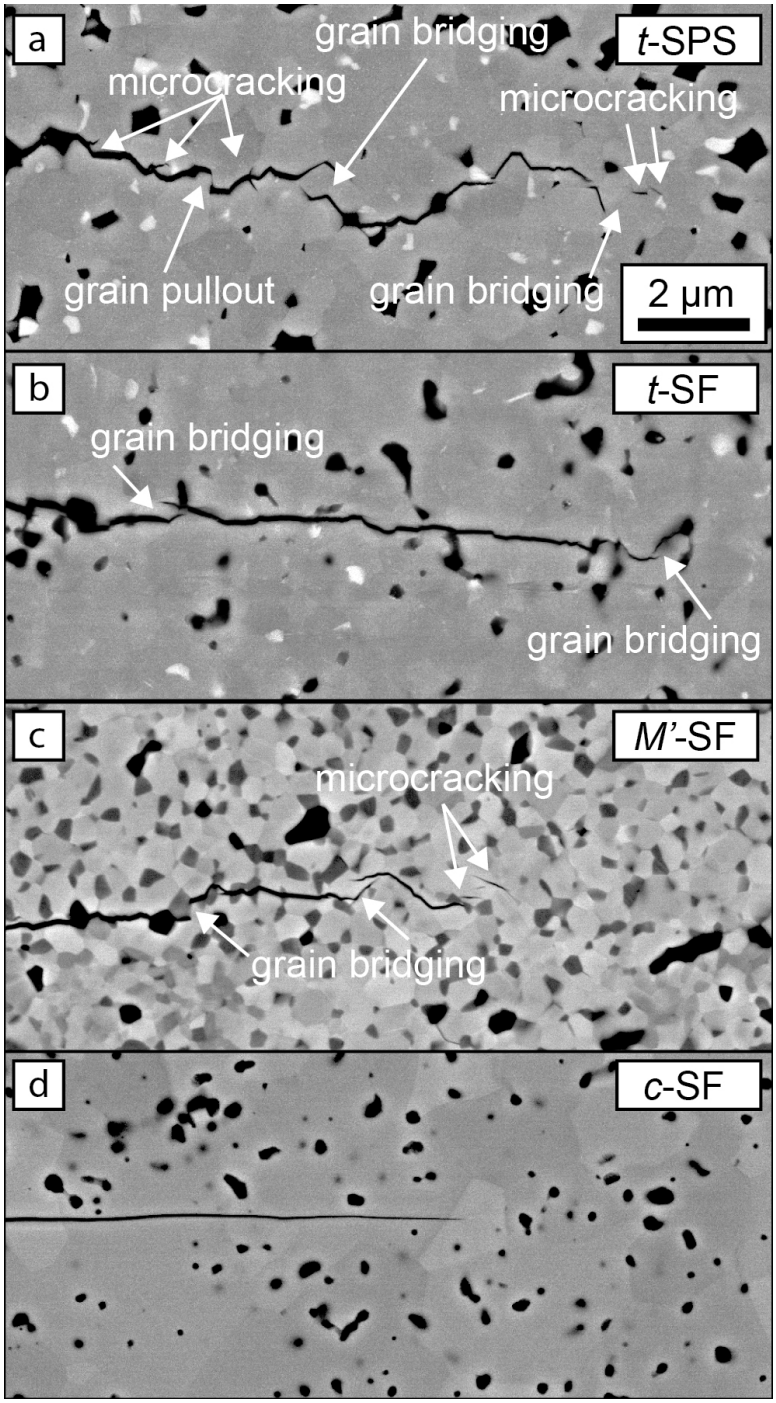

Figure 7.7: Compacts that displayed a significant amount of intergranular fracture on their fracture surfaces, such as *t*-SPS, *t*-SF, and *M'*-SF, also displayed evidence of toughening mechanisms such as crack deflection, microcracking, grain bridging, and grain pullout. Instances of these mechanisms are highlighted above by arrows, except for crack deflection, which can be identified by looking at the progression of the crack throughout the microstructure. No evidence of these toughening mechanisms was found in compacts that exhibited transgranular type fracture, e.g. *c*-SF.

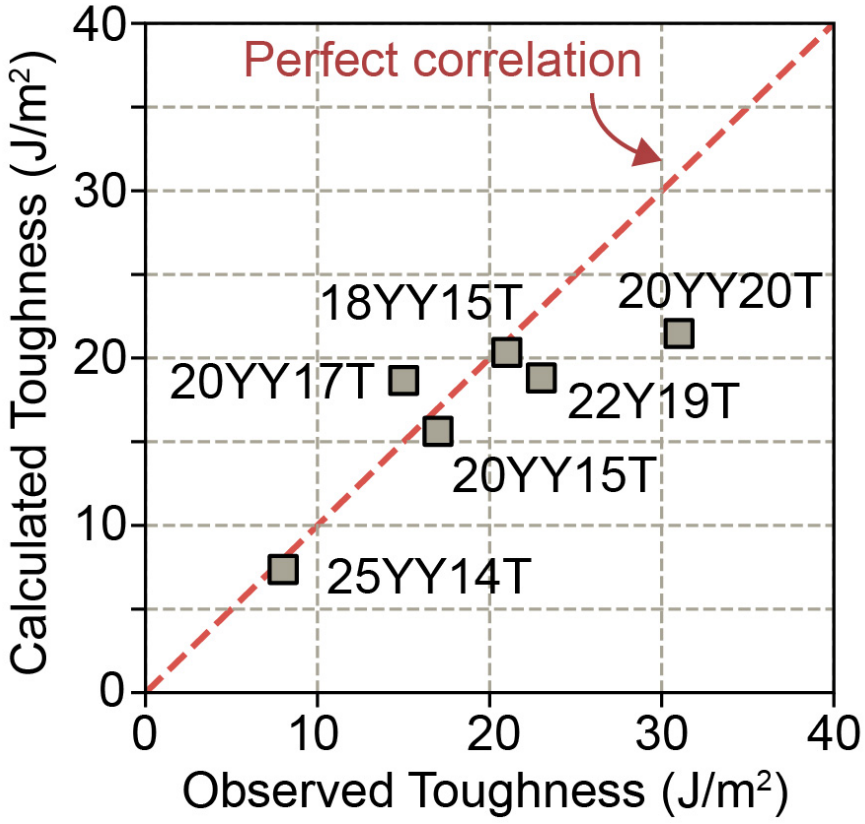

Figure 7.8 The RMS error of predicted toughness values for the quaternary compacts from Chapter 6, ~4.5 J/m^2, is similar to that observed for compacts in the ternary system, suggesting that the model performs well on quaternary compositions in the three-phase *t* + *c* + *M'* field. To perform these calculations, each pellet was assumed to be fully dense and the phase fractions were calculated using the ternary ZrO_2-$YO_{1.5}$-$TaO_{2.5}$ phase equilibria.

CHAPTER 8: MICROSTRUCTURE OF NON-TRANSFORMABLE *t*-ZrO_2

The previous chapter revealed that polycrystalline compacts containing the non-transformable tetragonal phase in the ZrO_2-$YO_{1.5}$-$TaO_{2.5}$ system exhibit toughness that is sensitive to microstructure. While it was found that the relationship between microstructure and toughness partly originates from toughening mechanisms like crack deflection and microcracking, it is possible that other mechanisms also contribute to the toughness. Ferroelastic domain switching is one mechanism of particular interest [6,76], as it is known to be operative in the tetragonal phase belonging to the ZrO_2-$YO_{1.5}$ system and therefore could also be operative in the non-transformable tetragonal phase [16]. However, there is a paucity of microstructural observations supporting ferroelastic behavior in these materials, partly because of the complex microstructures left after deformation. Understanding the ferroelasticity of the non-transformable tetragonal zirconia-based phases has the potential to improve the durability of thermal barrier coatings based on these materials, since it might be possible to tune and control microstructure to improve the toughness of the thermal barrier oxide.

It is expected that short-range order between Y^{3+} and Ta^{5+} cations predicted by first-principles calculations in Chapter 4 significantly influences the ferroelastic behavior of non-transformable tetragonal materials. The energetic preference to have the ordering pattern oriented in a specific direction relative to the tetragonal c-axis suggests that short-range cation diffusion is required to generate toughening by ferroelastic switching, since the ordering pattern needs to be rearranged along the new direction of the c-axis in the switched domain. If the ordering pattern is not rearranged, it is possible that domains revert back to

their original orientation once the stress driving switching is released, which would not produce any appreciable toughening. Given that cation diffusion is limited at room temperature, short-range ordering likely hinders ferroelastic switching and therefore reduces the toughening generated by it. Furthermore, it is possible that the short-range order influences the microstructure of each tetragonal crystallite by modifying the domain structure, with accompanying effects on the toughening.

This chapter focuses on investigating the grain-level microstructure of compacts based on the non-transformable tetragonal phase in order to determine if there is any microstructural evidence of ferroelastic behavior. Transmission electron microscopy (TEM) specimens were extracted from multiple locations on the surface of the indented *t*-SPS and *t*-SF compacts described in Chapter 7 to probe the structure prior to and following indentation. The spark plasma sintered (SPS) and sinter forged (SF) specimens exhibit grains both near and far away from microindentations that contain submicron-sized, twin-related domains. Each domain contains a secondary domain structure present on an extremely fine scale. The evolution of the domain structure and potential implications on toughness of the non-transformable tetragonal phase are discussed.

8.1 Experimental Details

Specimens for TEM analysis, prepared using a focused ion beam system (FIB) as discussed in Chapter 3, were extracted from two locations relative to the micro-indentation impressions on the *t*-SPS and *t*-SF compacts described in Chapter 7. The first location contained part of a micro-indentation crack near its tip, assuring that the section resides outside the plastic zone of the indentation but within the process zone of the crack. The second location contained undeformed material far away (>500 μm) from the indentation

impressions. Bright field imaging, dark field imaging, and selected area electron diffraction (SAED) were used to explore the microstructure of each extracted lamella at the length scale of hundreds of nanometers. Fourier filtering and reconstruction of high-resolution transmission electron (HR-TEM) images was used to investigate the crystallographic structure at the nanometer scale. High-angle annular dark field (HAADF) imaging mode on a scanning tunneling electron microscope (STEM) was used to probe the compositional homogeneity of the materials.

8.2 Results

A key characteristic of the *t*-SPS and *t*-SF compact microstructures is the presence of grains that contain multiple submicron domains. Examples are outlined in the low magnification images of the lamellas extracted from the *t*-SPS sample near an indentation crack tip (Figures 8.1) as well as the *t*-SPS and *t*-SF samples in regions containing undeformed material (Figures 8.2 and 8.3). Grains exhibiting this structure are recognized by sharp, linear boundaries that separate adjacent domains (Figure 8.4). The domains are anisotropic in shape and their average size is similar to the crystallite size measured for the *t*-SPS and *t*-SF compacts in Chapter 6, ~600 nm and ~400 nm, respectively.

Diffraction analysis reveals that adjacent domains exhibit a twin relationship. Figure 8.5 illustrates this for two domains in the heart-shaped grain near the middle of Figure 8.4. In this figure, the lamella has been tilted such that the grain is oriented along the [111] zone axis. The twin relationship is evident in the [111] zone axis patterns by the similar location of the fundamental 220-type diffraction spots, indicating a shared orientation of the cation sublattice, and the varied location of the most intense 211-type diffraction spots, indicating differing orientations of the tetragonal c-axis (Figure 8.5(b) and (c)). The twin boundary is

perpendicular to the nearly vertical reciprocal lattice 220-type vector in the diffraction patterns, suggesting that the twin boundary is a {220} plane. The fundamental 220-type and superlattice 211-type diffraction spots can be used to image the entire grain and each individual domain. Dark field imaging using one of the fundamental 220-type reflections results in the entire grain lighting up in a relatively uniform contrast (Figure 8.5(d)) whereas imaging using one of the superlattice 211-type reflections results in a single domain lighting up in contrast (Figure 8.5(e)). In both dark field images, small contrast variations are observed, suggesting that there is additional structure at a very fine scale.

A second, extremely fine domain structure, visible only through Fourier filtering and reconstruction of HRTEM images, is present within each tetragonal crystallite. Figure 8.6 shows one such Fourier analysis performed near the horizontal twin boundary shown in Figure 8.5 and along the same [111] zone axis. The global fast Fourier transform (FFT) of the HRTEM image in Figure 8.6(a), which is akin to the diffraction pattern from the imaged region, contains two dominant 211-type superlattice reflections that indicate two dominant orientations of the tetragonal c-axis (Figure 8.6(b)). Although not visible in Figure 8.6(a), the twin boundary can be detected by analyzing the change in the local FFT throughout the HRTEM image. The dashed box in Figure 8.6(a) gives an idea of the size of the box used to calculate the local FFTs. Figures 8.6(c-e) illustrate the FFTs as the box is moved from the top of the image to the bottom. A single dominant set of superlattice reflections is noted in the FFTs from the top and bottom of the image, but the dominant set changes from those circled in green in the inset in Figure 8.6(f) to those circled in red. Both sets of reflections have roughly equal intensity in the middle of the image (Figure 8.6(d)), suggesting that domain boundary is near the middle of the HRTEM micrograph. Placing virtual apertures

over the individual sets of superlattice reflections in the global FFT and computing the inverse FFT (IFFT) allows one to probe the structure of the material in a manner similar to dark field imaging (Figure 8.6(f)). As expected from the local FFTs, the domain at the top of the image is dominated by a single tetragonal variant colored in green and the domain at the bottom of the image is dominated by a second tetragonal variant colored in red. However, the IFFT images reveal two additional notable features of the domain structure. The first is the presence of all three tetragonal variants within each domain, although the two non-dominant variants are present in small proportions. The second is that each domain is composed of many smaller nano-domains that are visible as connected patches of similar color in Figure 8.6(f). Due to the diffuse nature of the domains and the possibility of domain overlap throughout the thickness of the lamella, it is difficult to quantitatively estimate the size of the domains using image segmentation methods. Nevertheless, a qualitative estimate of the domain size based on the IFFT image suggests that the domains on either side of the twin boundary are approximately 2-10 nm. In other regions near the twin boundary, a more uniform dispersion of the three tetragonal variants is observed (Figure 8.7). The nano-structure persists away from the twin boundary and into the "bulk" volume of each domain (Figure 8.8). The structure in these "bulk" regions is representative of the majority of the volume in each grain and is largely dominated by a single tetragonal variant even though all three variants are detectable (Figure 8.8(c) and (d)). The size of the nano-domains is qualitatively similar to those near the twin boundary. The existence of all three tetragonal variants within each domain explains why the [111] zone axis patterns in Figure 8.4, which are taken well within a single domain, exhibit some faint intensity in each of the 211-type diffraction reflection locations.

The composition within a single domain fluctuates at a length scale of similar order to the size of the nano-domain structure. Due to the larger atomic number of Ta relative to Y and Ta, the compositional heterogeneity results in Z-contrast variation visible in HAADF STEM imaging mode (Figure 8.9). The contrast fluctuations are quantitatively captured by the intensity profiles taken along single atomic planes in Figure 8.9(c) and (d). The profiles differ from that expected for random solid solutions both in the variability of intensity on neighboring atomic columns (length scale ~0.5 nm) and in the fluctuations over multiple unit cells (length scale >5 nm). The lack of long-range periodicity in the contrast fluctuations at any relevant length scale suggests that the contrast variability originates from short-range ordering of the cations rather than formation of an ordered phase. Given that increasing contrast is tied to local Ta concentration, the short-range ordering must involve Ta^{5+} cations.

8.3 Discussion

The results confirm two characteristics of the non-transformable tetragonal zirconia microstructure that have been speculated within the community or hypothesized in this dissertation, namely the presence of a domain structure within tetragonal grains and the existence of short-range ordering involving Ta^{5+} cations in the tetragonal crystal structure. These topics merit further discussion within the context of: (i) understanding how the microstructure evolved from the initial precursor-derived powder and (ii) potential implications on ferroelastic switching. When applicable, connections are made to the first-principles calculations presented in Chapter 4 and to the toughness measurements presented in Chapter 7.

8.3.1 Microstructure Evolution

The relationship between crystal structure and chemical short-range ordering predicted for the tetragonal phase by first principles calculations in Chapter 4 provides the necessary foundation to understand the microstructure evolution of the *t*-SPS and *t*-SF materials. The calculations indicate an energetic preference to cluster Y^{3+} and Ta^{5+} cations into checkerboard-type layers along (001) planes. As a result, short-range ordering patterns based on this and related cation configurations are expected at finite temperatures in the tetragonal phase. An important feature of these ordering patterns is that the cation arrangement is correlated with the orientation of the c-axis. Contrast fluctuations observed in HAADF STEM imaging mode confirm the presence of short-range ordering involving Ta^{5+} in the tetragonal crystal structure and therefore support the hypothesis that the local atomic configuration of the material is consistent with that predicted by DFT, even though the HAADF images do not explicitly validate this conclusion (i.e. the exact nature of the ordering patterns cannot be confirmed with the HAADF images) (Figure 8.9). The existence of fine-scale domains several nanometers in size within each tetragonal crystallites, referred to as "nano-domains" in the results, reflects the result of short-range ordering. Each nano-domain represents a small region of material where the ordering pattern is coherent over a large enough length scale (~5-20 unit cells) to produce a single orientation of the tetragonal crystal structure.

The question arises as to how the more macroscopic domain structure, which is characterized by twin boundaries hundreds of nanometers in size in addition to nano-domains of all three tetragonal variants within each crystallite, forms from the precursor-derived powder, given the preference for short-range ordering. The starting configuration of

the powder following pyrolysis at 700°C is a nanocrystalline material where each grain is a single-phase solid solution [169]. The XRD spectrum of the powder indicates that the crystallites exhibit tetragonality in the as-pyrolyzed state and therefore that the material already contains tetragonal domains exhibiting some degree of short-range order (Figure 8.10). The process shows similarities to prior work on Y_2O_3, where poorly ordered bixbyite domains analogous to fluorite are produced from precursor pyrolysis at a similar temperature (~530°C). These domains are of a scale approximately 3-5 unit cells [169] and coarsen rapidly to a larger scale with further exposure to the pyrolysis temperature yielding larger crystalline domains where the original short range ordered regions are still distinguishable by anti-phase boundaries. The domains in the tetragonal phase are likely of a similar size or smaller even though the pyrolysis temperature is slightly higher since the ordering process in Y_2O_3 only requires anion vacancy diffusion and that in the tetragonal phase requires cation diffusion. Consequently, each grain is expected to contain multiple domains roughly of equal fractions of the three tetragonal variants, similar to the microstructure observed in Figure 8.7.

The SPS and SF processing drives coarsening of the crystallites under a uniaxial compressive stress. The global compressive load and local stresses produced by geometric constraint bias the growth of one of the three tetragonal variants in each crystallite in order to minimize strain energy. The growth of domains having preferred orientation is achieved by cation rearrangement in domains having undesirable orientation, which only requires short-range diffusion. The outcome is the microstructures observed in Figure 8.8, where domains of one tetragonal variant dominate each sub-grain. However, due to sluggish diffusion rates at the sintering temperature (1250°C), the cation ordering pattern will vary

throughout the structure. This naturally produces small regions where the cation arrangement is sufficiently random that a local cubic phase is produced, seen as dark areas in Figure 8.8, or the local orientation of the tetragonal c-axis differs from the global c-axis of the crystallite, recognized as the two variants present in minor proportions in Figure 8.8.

The large-scale twin boundaries visible in Figures 8.1, 8.2, and 8.3 are hypothesized to form on growth as a result of stresses associated with geometric constraint. The constraint stresses on any single grain vary both spatially and temporally throughout the sintering process. Twin boundaries are produced when the local stresses in a growing part of the crystallite are sufficiently different from the rest of the grain such that a second orientation of the tetragonal crystal structure is energetically preferred relative to the existing dominant orientation. The twinning process minimizes the local strain energy in the new portion of the grain. Similar to reorientation of the nano-domains as described above, twinning is achieved by reorienting the short-range ordering pattern relative to the existing, dominant orientation.

8.3.2 Implications on Ferroelastic Switching

Although the domain structure observed in the *t*-SPS and *t*-SF compacts suggests that the material could be toughened by ferroelastic switching, the existence of domains alone does not demonstrate an operative ferroelastic toughening mechanism since the domains observed are formed during processing and not as a result of interactions with the crack stress field. This is in contrast to the domains generated in materials like *t'*-8YSZ deposited by electron beam physical vapor deposition, which form only in regions close to indentation cracks and therefore are indicative of ferroelastic toughening [76]. Consequently, in order to establish ferroelastic switching as an operative toughening mechanism in the *t*-SPS and *t*-SF

specimens, a difference in domain structure between grains in undeformed, bulk material and grains within the process zone of a crack must be demonstrated. The switching process is expected to change the relative fraction of the three tetragonal variants in grains located nearby the crack. This could be achieved by two related mechanisms involving reorientation of the tetragonal nano-domains, requiring short-range diffusion of cations. In the first mechanism, a fraction of the nano-domains throughout the entirety of each crystallite switch in response to the crack stress field. In the second, only nano-domains located adjacent to the large-scale twin boundaries switch, producing movement of the boundaries and accommodation of the stress. The difference between the two processes is the spatial localization of switching in the latter.

To assess if the first mechanism is active, one can compare the relative fractions of the three tetragonal variants in the bulk regions of crystallites located near and far away from indentation cracks. The relative intensities of the 211-type diffraction spots in FFTs similar to those presented in Figures 8.6 - 8.8 serve as a measure of the relative fractions of each tetragonal variant. A key assumption in this method is that the FFTs computed from small volumes of material are assumed to be representative of the entire microstructure, which is justified given the assumption that the switching process is uniform throughout the material. The following estimates are calculated by first converting the FFT images, which is an array of complex numbers, into an array of real numbers by calculating the complex modulus at each point. The relative fraction of each tetragonal variant was computed using:

$$t_i = t_i / \left(t_1 + t_2 + t_3 \right) \tag{8.1}$$

where t_i is the maximum intensity of the 211-type diffraction spot of the i-th tetragonal variant. The average fraction of the three tetragonal variants in the t-SPS sample is $t_1 = 0.87$

$\pm$ 0.02, $t_2 = 0.06 \pm 0.02$, and $t_3 = 0.07 \pm 0.005$ for crystallites located in the bulk material and $t_1 = 0.85 \pm 0.03$, $t_2 = 0.07 \pm 0.01$, and $t_3 = 0.08 \pm 0.03$ for crystallites located near the crack, specifically in the heart-shaped grain in Figure 8.5(a). Although such a calculation only serves as a preliminary estimate of the relative fractions of each variant, the similarity between the relative proportions indicates that switching does not occur uniformly throughout crystallites nearby indentation cracks. It is noted that a more rigorous analysis would involve evaluating numerous locations in multiple grains, as well as utilizing an electron diffraction method capable of sampling a larger area of material, such as precession electron diffraction.

Determining if localized ferroelastic switching has occurred near the macroscopic twin boundaries is more challenging, since it is possible that the microstructure prior to deformation is similar to that following deformation except for the location of the twin boundaries. Consequently, it is difficult to establish if this mechanism occurs without knowing the location of the domain boundaries prior to indentation. One route towards ascertaining if switching occurs by this mechanism is to track the location of the domain boundaries i*n-situ* while performing a mechanical test. Ideally, this could be simultaneously while measuring the stress-strain response, which would provide another means to verify that ferroelastic switching has taken place. Such a test could be performed in a SEM equipped with a mechanical testing stage [170]. Utilization of a SEM provides versatility in terms of the diversity of specimen shapes, sizes, and thickness that can be used since electron transparency is not required as well as access to a number of detectors and sensors such as scanning transmission electron microscopy (STEM) detectors and electron back scatter diffraction (EBSD) detectors. Coupling an electron transparent specimen with a

STEM detector provides a means to actively track the population of the three tetragonal variants during deformation by monitoring the intensity of the tetragonal reflections in the [111] zone axis diffraction pattern, as well as various crystalline defects [171,172]. An EBSD detector would facilitate elucidating how crystalline orientation influences switching. Alternatively, it also possible that such a test could be performed in a TEM equipped with a mechanical testing stage [170]. Compared to *in-situ* testing with an SEM, utilization of a TEM has the advantage of higher resolution, which can be used for detailed analysis of dislocations, twins, and other crystalline defects, and access to x-ray energy-dispersive spectroscopy (XEDS) and electron energy loss spectroscopy (EELS), which can be used to connect mechanical behavior with local composition. This type of testing was used to discover the first evidence of domain wall motion in *M*-$YTaO_4$ containing transformation twins [50].

Lastly, it is worth noting that the toughening produced by ferroelastic switching in the non-transformable tetragonal phase may be strongly sensitive to temperature, since domain reorientation is facilitated by cation diffusion. As a result, it is possible that even if the low temperature toughness is lower than that characteristic of *t'*-8YSZ, the high temperature toughness could be similar or larger, with concomitant benefits to the durability of thermal barrier coatings based on the non-transformable tetragonal phase. *In-situ* mechanical testing in an SEM [173] or TEM, as described above but with a heating stage, may be able to clarify the role of temperature (at least up to several hundred °C) on ferroelastic switching.

8.4 Synopsis

Insight into the microstructure of the non-transformable tetragonal phase within the ZrO_2-$YO_{1.5}$-$TaO_{2.5}$ system has emerged from this study. Two domain structures at significantly

different length scales are observed within the *t*-SPS and *t*-SF compacts. A fraction of the tetragonal grains are composed of sub-micron, twin-related domains and each crystallite is composed of finer nanometer-sized domains. The domain structure forms during processing as a result of short-range order between yttrium and tantalum cations in the tetragonal crystal structure, as predicted by first-principles calculations (Chapter 4). Evidence of the short-range order is observed for the first time by HAADF STEM imaging. It is generally expected that a similar microstructure is present in all polycrystalline compacts fabricated from single-phase, non-transformable tetragonal compositions, even though the details of the structure, such as the crystallite size and density of twin boundaries, are likely dependent on processing conditions.

Although the existence of domains within the microstructure suggests that the material may be amenable to toughening by ferroelastic switching, direct evidence of switching was not found in the limited work undertaken here. Bulk regions of crystallites located far from and nearby indentation cracks have a similar proportion of the three tetragonal variants, suggesting that the crack stress field has not modified the microstructure. However, it is possible that switching occurs by movement of the macroscopic twin boundaries, in which case switching will not be evident from analysis of the microstructure following indentation. *In-situ* mechanical tests may be able to confirm such a mechanism, providing a route of investigation for future work. If ferroelastic switching were confirmed to be an operative toughening mechanism, this would represent a major contribution to the understanding of toughness in the non-transformable tetragonal phase.

Ferroelastic switching is hypothesized to occur by a reorientation of the tetragonal nano-domains. Since the orientation of the tetragonal crystal structure in the domains is tied to the

cation arrangement, the process likely requires the short-range diffusion of cations. Consequently, it is expected that the toughness provided by ferroelastic switching is significantly dependent on temperature.

8.5 Figures

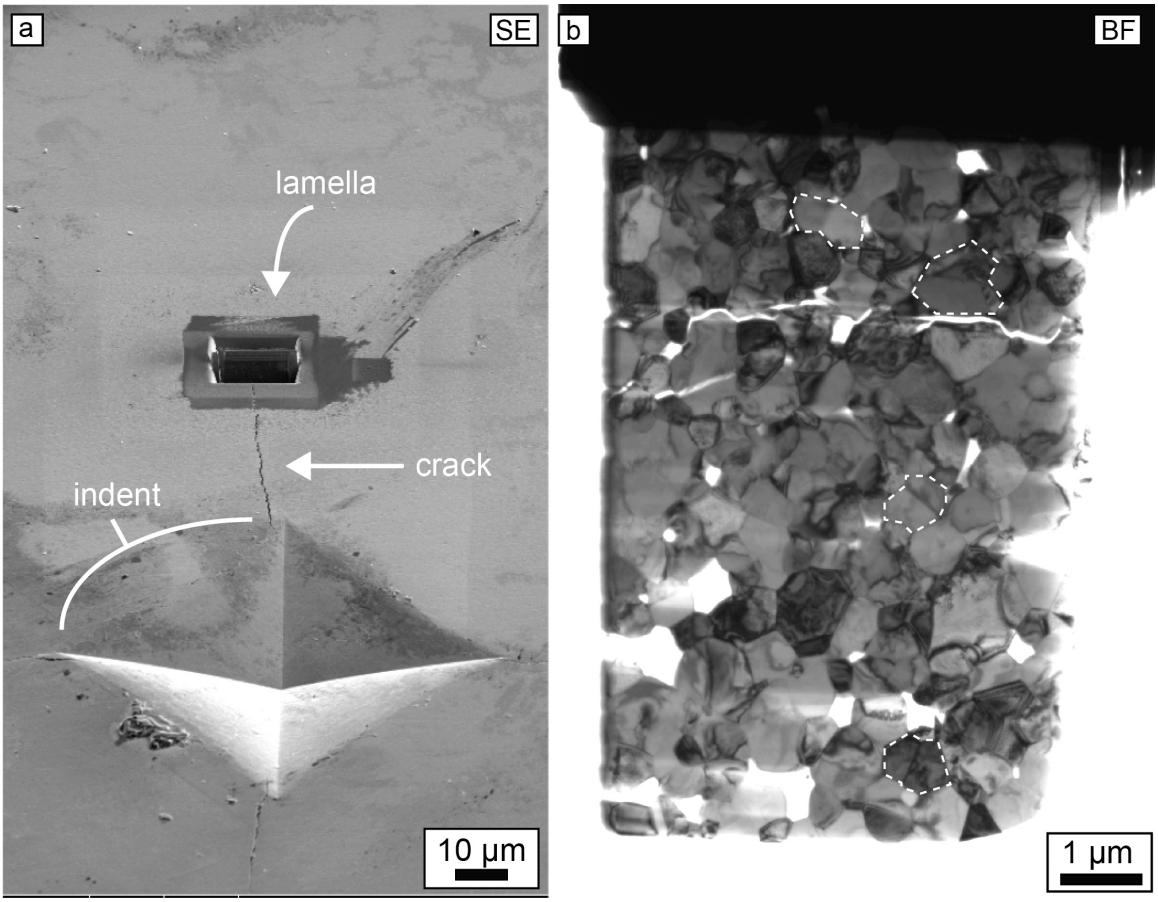

Figure 8.1: (a) A FIB lamella was extracted from a region containing a microindentation crack near its tip in the *t*-SPS sample. (b) Dashed white lines outline several grains containing submicron domains in the low magnification bright field image of the lamella, but many more grains can be found that exhibit the same structure. Note that the image in (b) is rotated so the surface of the specimen from which it was extracted in (a) would be on the right.

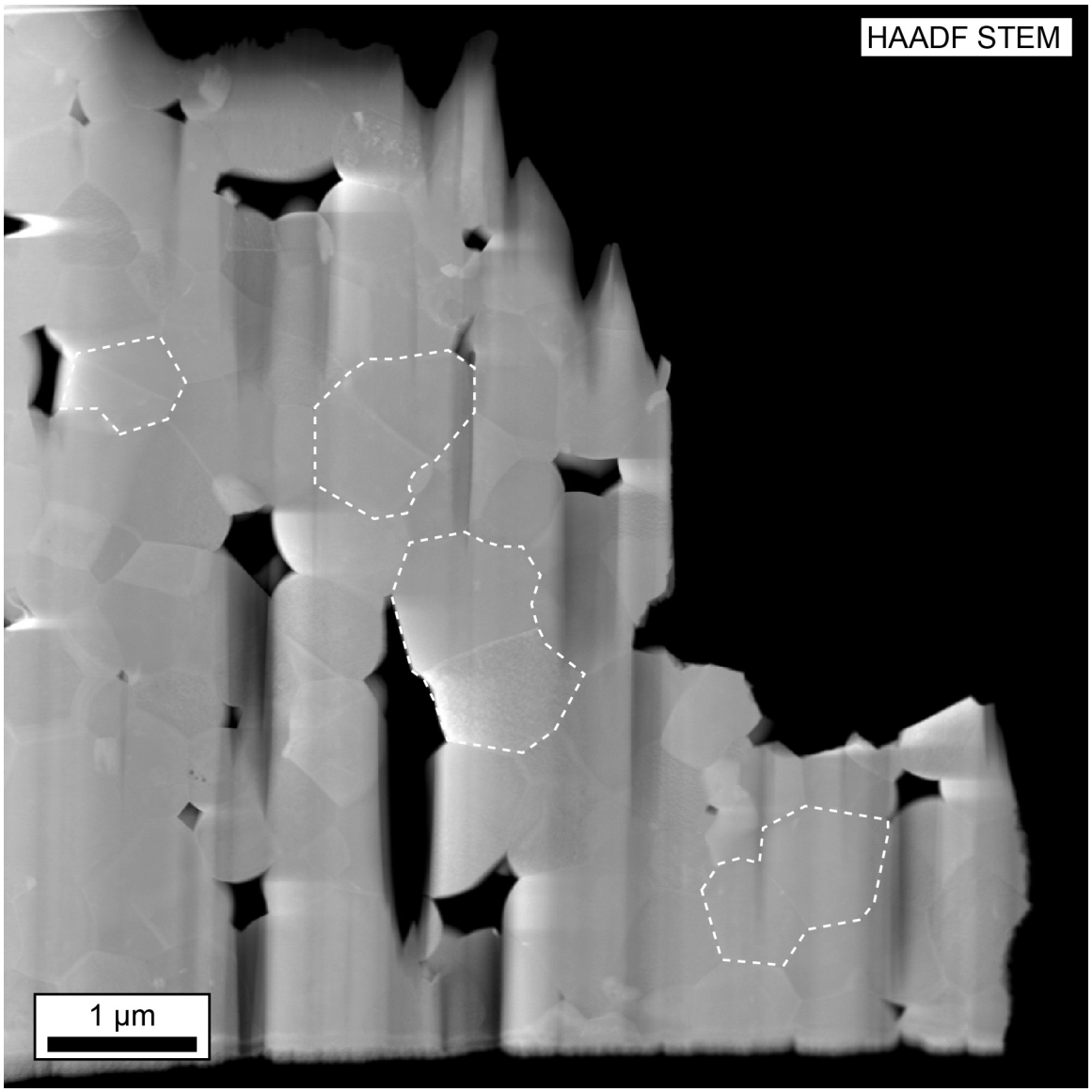

Figure 8.2: The TEM lamella extracted from the bulk, undeformed region of the *t*-SPS compact also contains grains exhibiting a submicron domain structure, suggesting that the formation of these domains is not associated with interactions with the crack stress field. Dashed white lines outline several grains containing domains.

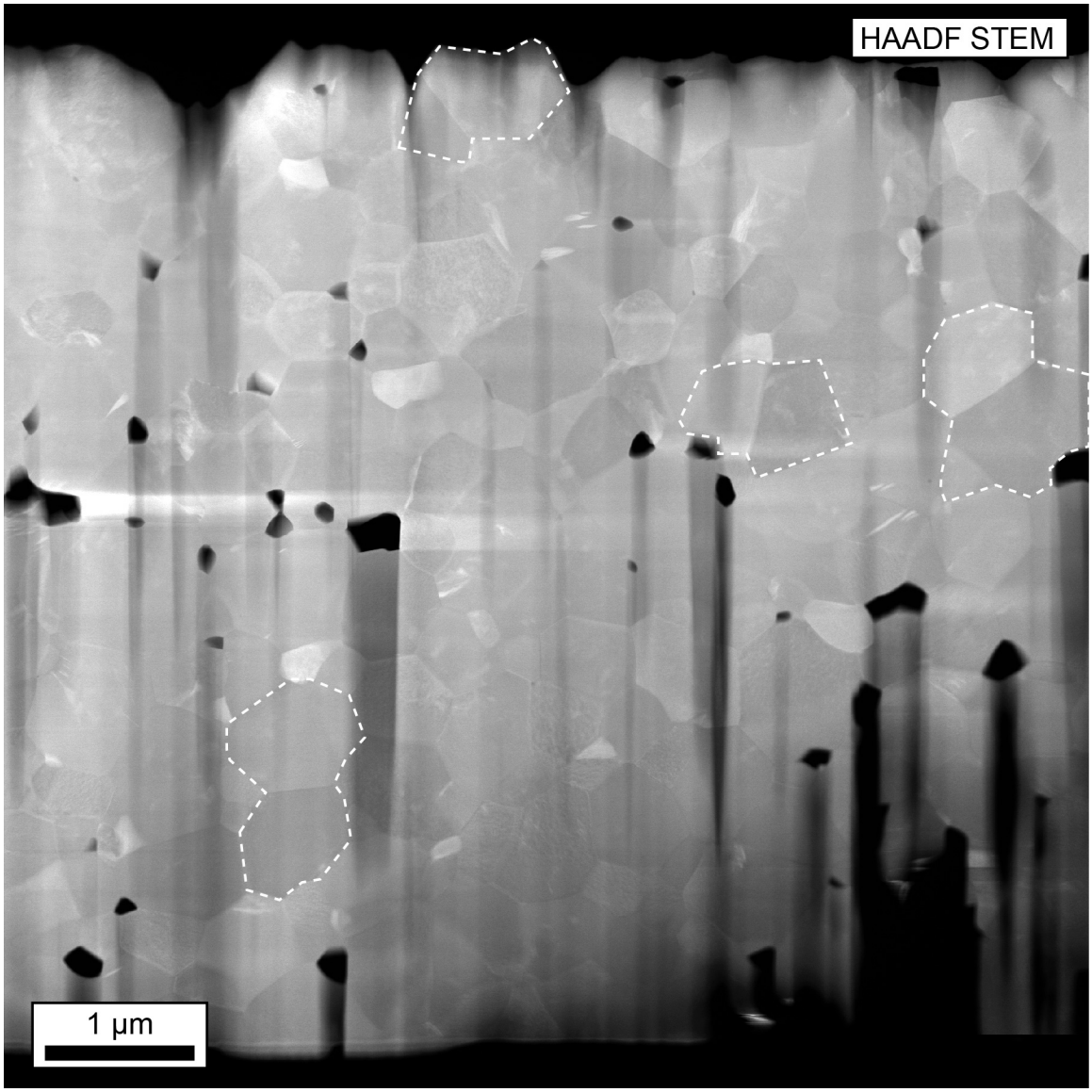

Figure 8.3: The TEM lamella extracted from the bulk, undeformed region of the *t*-SF compact similarly contains grains exhibiting a submicron domain structure, suggesting that the formation of the domains is not unique to the SPS process. Dashed white lines outline several grains containing domains.

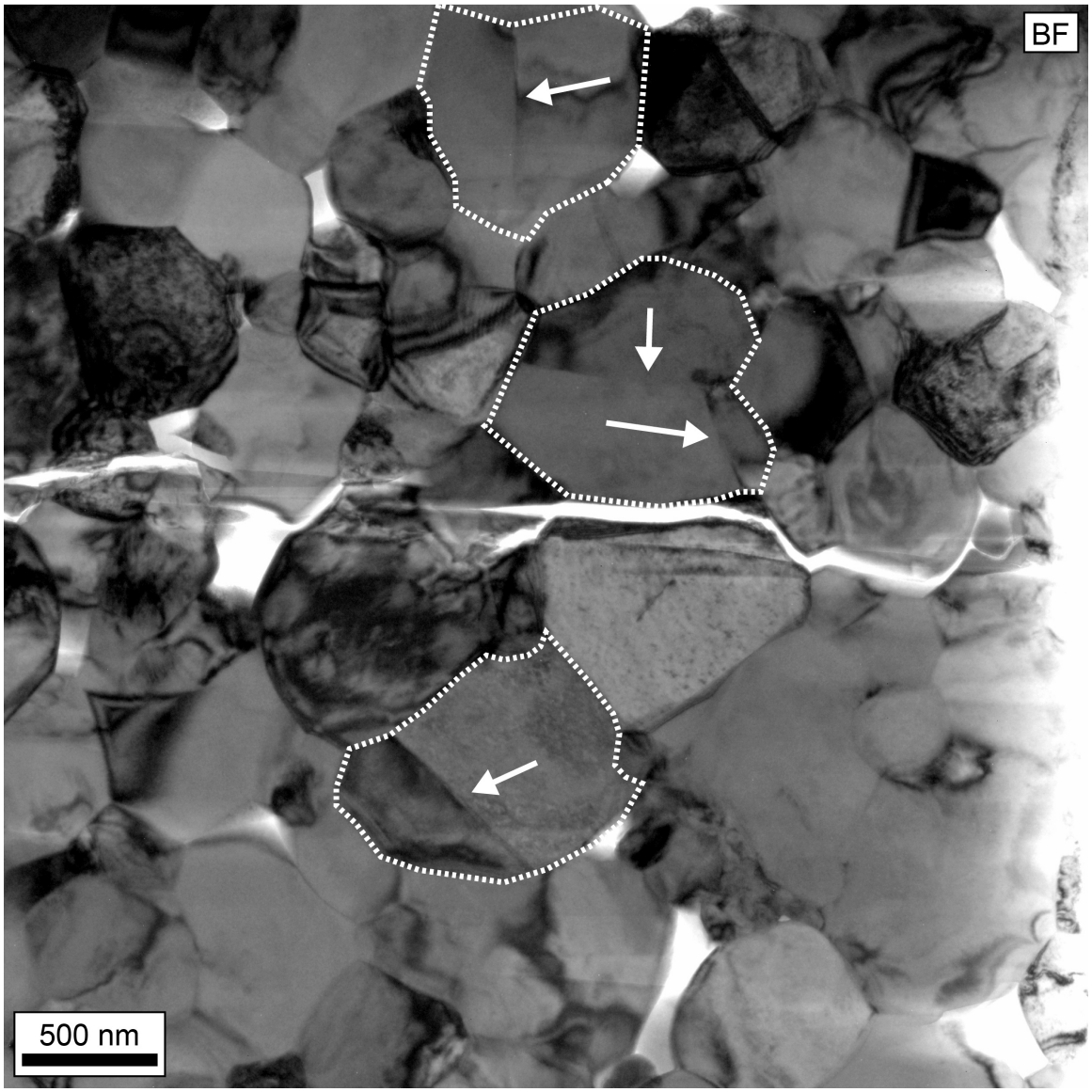

Figure 8.4: Several grains containing a submicron structure are outlined by a dashed white line in this higher magnification bright field image of the *t*-SPS lamella near the crack tip (Figure 8.1). White arrows point to the relatively straight domain boundaries. All subsequent micrographs were collected from the heart-shaped grain in the middle of the figure.

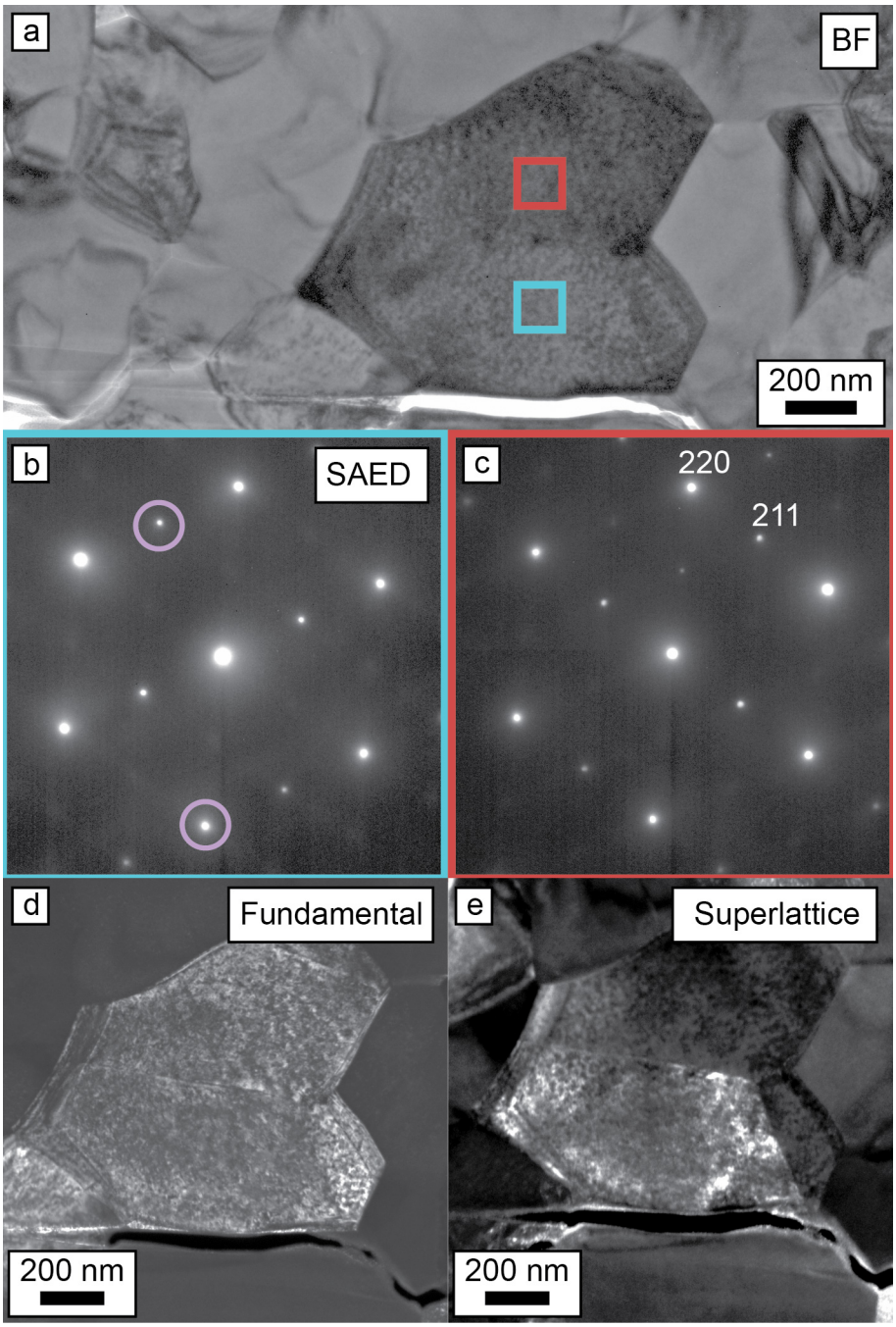

Figure 8.5: The red and teal boxes, which lie in two adjacent domains within the heart-shaped grain in (a), illustrate the location of the electron beam for the two [111] zone axis patterns shown in (b) and (c). Each SAED pattern exhibits a 211-type reflection, indicating that the domains have a tetragonal crystal structure, and the patterns are mirror images of one another across $\mathbf{g}_{220}$, indicating that the domains are twin-related and the twin boundary is a {220} plane. Dark field imaging using the fundamental 220-type reflection reveals the entire volume of the grain while that using the superlattice 211-type reflection reveals only the domain containing a particular orientation of the tetragonal crystal structure.

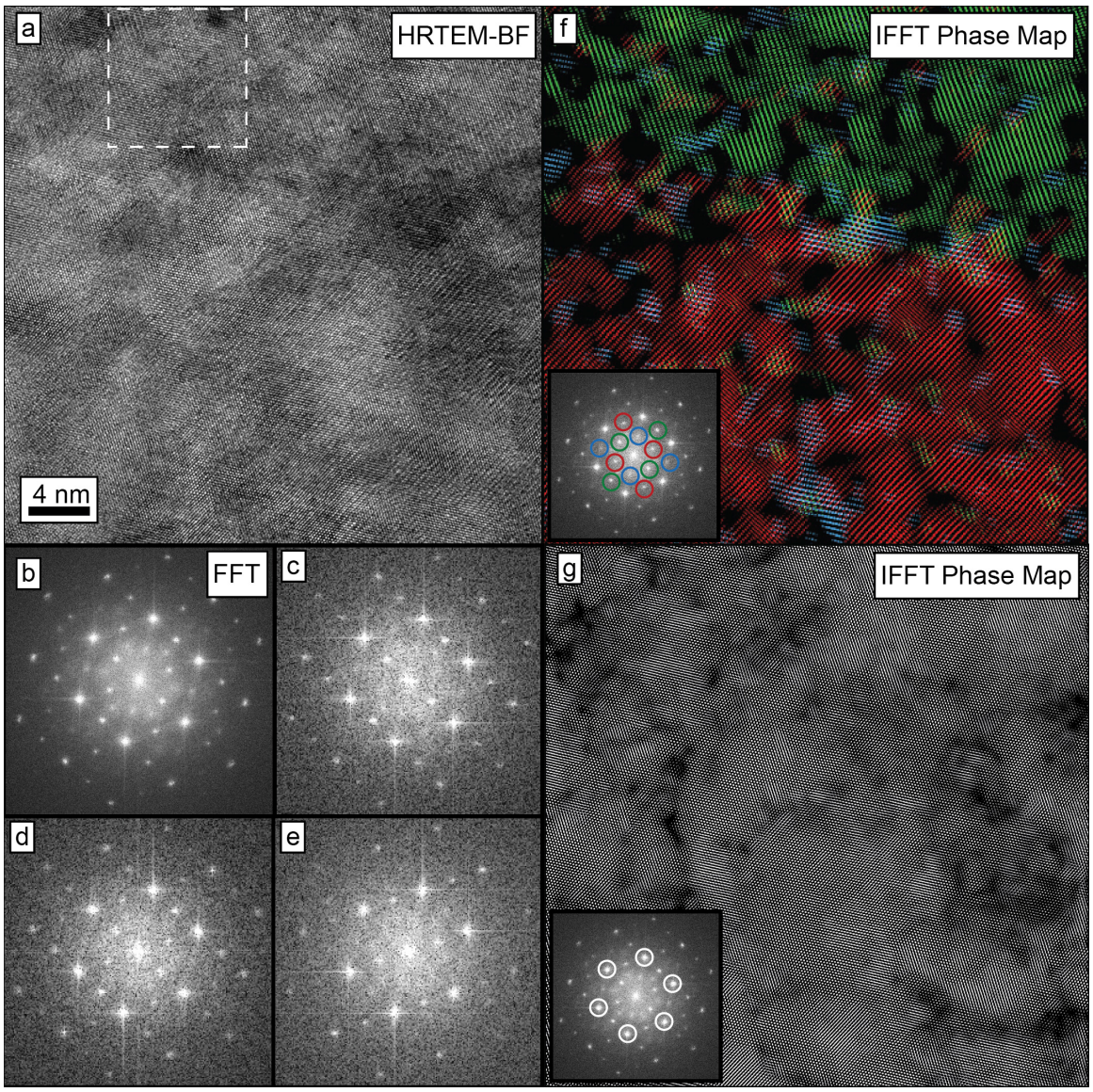

Figure 8.6: (a) An HRTEM image taken from a region containing the nearly horizontal twin boundary in the heart-shaped grain shown in Figure 8.5. (b) The FFT of the HRTEM image shows two intense 211-type reflections and therefore indicates that there are two dominant orientations of the tetragonal crystal structure. The dashed white line in (a) illustrates the size of the box used to compute the local FFT in several different parts of the image: (c) top, (d) middle, and (e) bottom. Based on the FFTs, a single orientation of the tetragonal phase dominates the top of the image, a single but different orientation of the tetragonal phase dominates the bottom of the image, and both orientations are present in roughly equal proportions in the middle of the image. The tetragonal superlattice reflections in (b) were used to produce (f) a phase map showing the microstructure of the three tetragonal variants, as shown in the inset. The color in the phase map reflects the orientation of the tetragonal domains. A similar IFFT phase map using only the fundamental reflections is shown in (g).

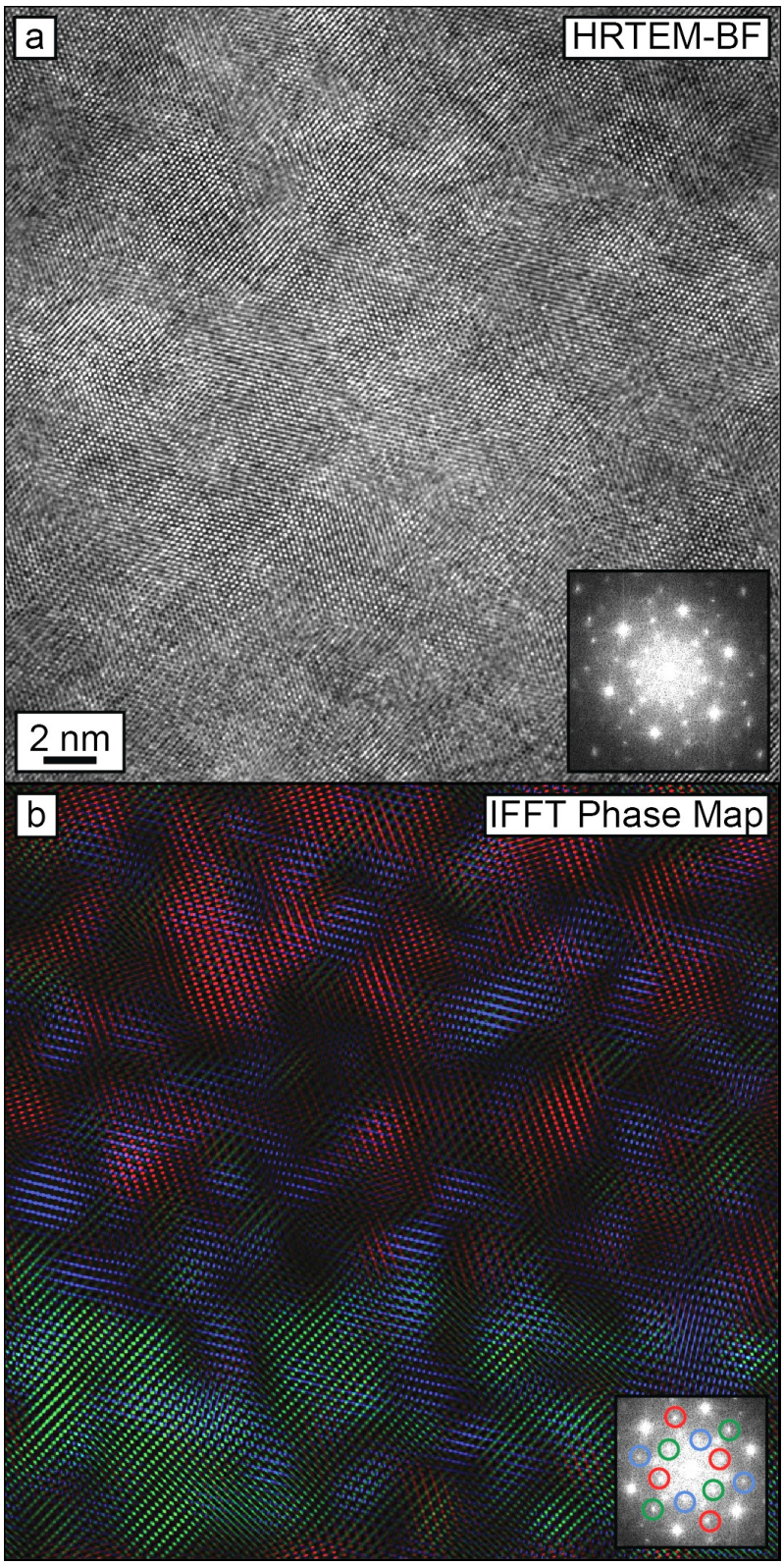

Figure 8.7: (a) HRTEM image and (b) corresponding IFFT phase map from a second region near the twin boundary shows a more equal proportion of all three tetragonal variants. The twin boundary is oriented similarly to that in Figure 8.6.

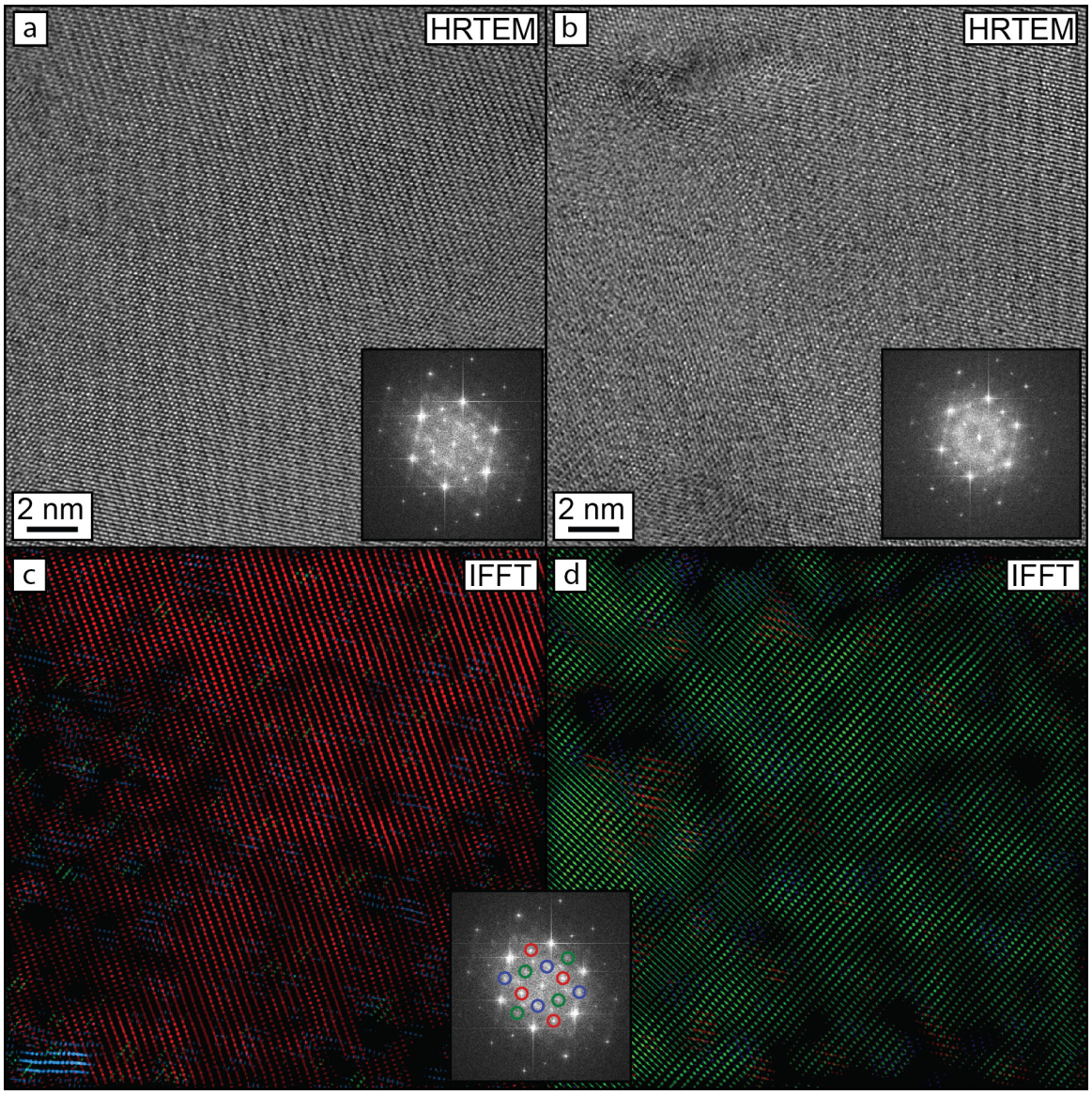

Figure 8.8: (a, b) HRTEM images and (c, d) corresponding IFFT phase maps from regions far from the twin boundary analyzed in Figure 8.6 (i.e. in the bulk of the two adjacent domains). All three tetragonal variants are observed in each region, but a single variant dominates the majority of the investigated area. The nano-domain structure is visible.

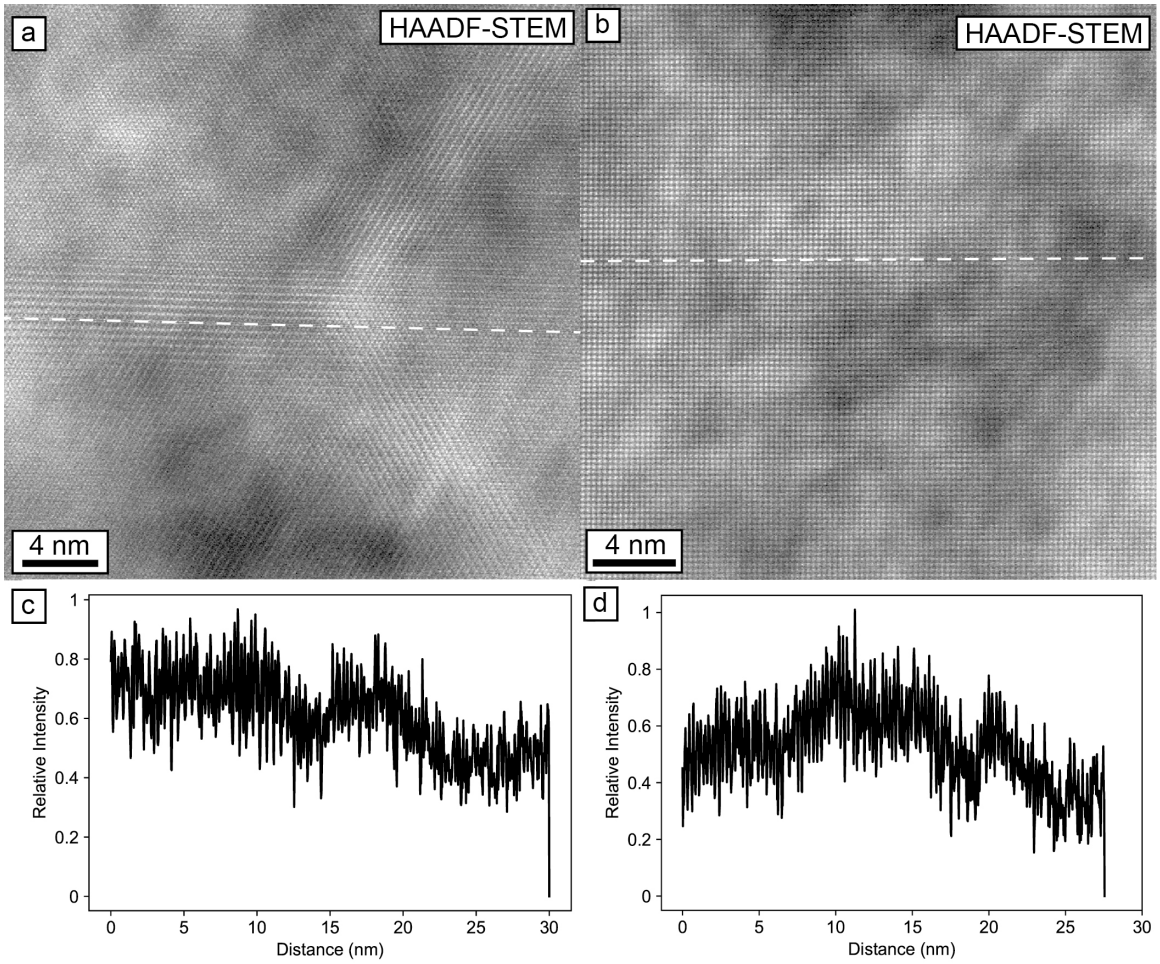

Figure 8.9: Contrast fluctuations observed in the HAADF STEM images of the heart-shaped grain in Figure 8.5 along the (a) 111 zone axis and (b) 100 zone axis originate from a non-uniform distribution of Ta^{5+} cations. Dashed white lines in (a) and (b) show atomic columns from which the intensity profiles in (c) and (d) were created. The profiles exhibit significant variations in intensity between neighboring atomic columns and over nanometer-sized length scales.

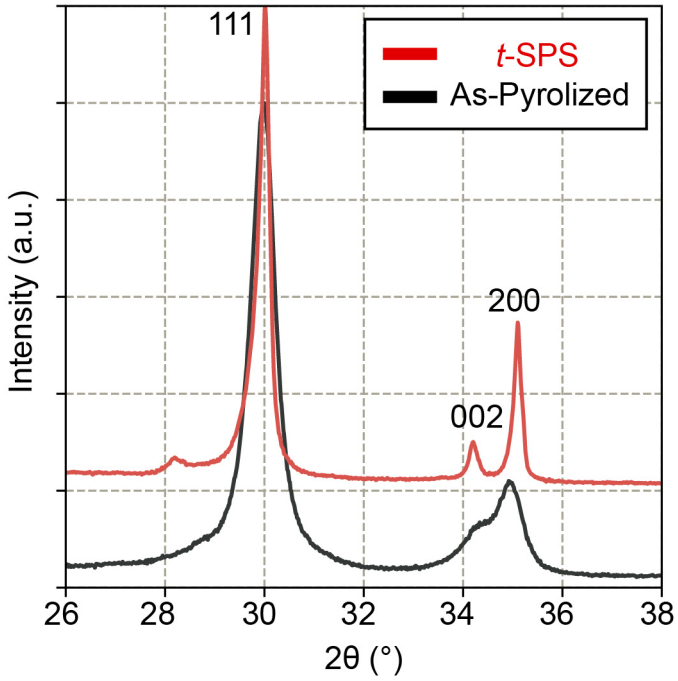

Figure 8.10: The XRD spectrum from the 16.2Y5.9Ta powder in the as-pyrolyzed state exhibits splitting of the 200-type fluorite peaks, indicating that the structure is tetragonal.

CHAPTER 9: CONCLUSIONS AND OUTLOOK

The primary objective of this dissertation was to gain a deeper understanding of fundamental relationships between crystal structure, phase equilibria, microstructure, and toughness in ZrO_2-(Y/Yb)$O_{1.5}$-$TaO_{2.5}$ thermal barrier oxides and to use the acquired knowledge to provide insight into issues pertaining to the implementation of these compositions in next-generation thermal barrier coating (TBC) systems.

Short-range order in the *t*-ZrO_2 solid solution serves as a foundation to understand much of the material behavior reported in this work, including several aspects related to deposition behavior during vapor processing (EB-PVD), microstructure evolution, and toughness. While previous studies had already hypothesized cation ordering in tetragonal ZrO_2-$YO_{1.5}$-$NbO_{1.5}$ materials, the current study provides the first experimental evidence of short-range order in tetragonal ZrO_2-$YO_{1.5}$-$TaO_{2.5}$ materials, as well as insight into the specific ordering patterns that are energetically preferred. High angle annular dark field images of non-transformable tetragonal compositions in the ZrO_2-$YO_{1.5}$-$TaO_{2.5}$ system show contrast fluctuations occurring over a length scale of 1-10 nm, indicating that short-range order involving Ta^{5+} is present at room temperature. The observations are consistent with first-principles calculations that predict a strong tendency for yttrium and tantalum cations to cluster into checkerboard-type layers and related configurations in the tetragonal phase. An important conclusion from the calculations is that cation-based short-range ordering is likely a general feature of the tetragonal phase in all ZrO_2-$REO_{1.5}$-$TaO_{2.5}$ (RE = rare-earth) systems, with the strength of the attractive interactions is dependent on rare-earth choice.

Investigations into the processability of ZrO_2-$REO_{1.5}$-$TaO_{2.5}$ materials by vapor deposition highlighted the challenges associated with producing industrial-scale EB-PVD coatings. It

was shown that ZrO_2-$YbO_{1.5}$-$TaO_{2.5}$ EB-PVD coatings exhibit significant compositional fluctuations originating from the higher vapor pressure of $YbO_{1.5}$-$TaO_{2.5}$ suboxides relative to ZrO_2 suboxides during deposition. Similar fluctuations are expected in vapor deposited coatings of all ZrO_2-$REO_{1.5}$-$TaO_{2.5}$ materials, though the character of the compositional scatter depends on the activity of $REO_{1.5}$-$TaO_{2.5}$ suboxides in the melt and hence the strength of the attractive interactions between RE^{3+} and Ta^{5+}. The compositional variation is undesirable from the point of view of phase stability, as local parts of the coating may drift into a region of the phase diagram where a transformable tetragonal phase is expected, as well as from the point of view of strain tolerance, as the formation of secondary phases can prevent the development of a well-defined columnar structure. The fluctuations become more severe with increasing $TaO_{2.5}$ concentration, such that an adequate combination of phase stability and strain tolerance is displayed only in coatings made from compositions with $REO_{1.5}$:$TaO_{2.5} \geq 1$.

Studies characterizing the microstructure evolution of ZrO_2-$(Y/Yb)O_{1.5}$-$TaO_{2.5}$ EB-PVD TBCs confirmed that coatings made from compositions within the suitable design space exhibit superior phase stability than state-of-the-art coatings based on ZrO_2-8 ± 1 mol% $YO_{1.5}$ (8YSZ). A novel aspect of this work was that it considered a TBC with nominal composition in the multi-phase *t* + *c* (+ *M'*) phase field as opposed to the single-phase *t*-ZrO_2 field reported in a previous investigation. The $12YO_{1.5}$-$13YbO_{1.5}$-$14TaO_{2.5}$ coating exhibited many similarities to *t'*-8YSZ coatings, including a comparable columnar morphology and crystallographic texture, but the microstructure evolution was significantly different. Each column was deposited as a single crystal composed of small domains of three tetragonal variants rather than a single domain of a single tetragonal variant. The structure is

produced by short-range ordering between $(Y/Yb)^{3+}$ and Ta^{5+} either at the deposition temperature or upon cooling. The crystallites coarsen upon aging but remain non-transformable to the monoclinic phase for at least 400 h at 1250°C and 1500°C. Due to the location of the composition within the multi-phase field, crystallites of the *c*-ZrO_2 phase grow concurrently with the tetragonal phase and degrade the toughness of the material. The combination of lower toughness and lower coefficient of thermal expansion relative to 8YSZ suggests that the coating might be more susceptible to thermomechanical degradation.

The low toughness of the $12YO_{1.5}$-$13YbO_{1.5}$-$14TaO_{2.5}$ material prompted an extensive study examining the relationship between toughness and phase constitution in the three-phase *t* + *c* + *M'* field. Microindentation toughness tests revealed that the toughness of polycrystalline compacts based on the non-transformable tetragonal phase drops rapidly with increasing fraction of *c*-ZrO_2 but is not significantly affected by the fraction of *M'*-$YTaO_4$. The results have important implications on the development of TBCs based on ZrO_2-$REO_{1.5}$-$TaO_{2.5}$ materials in the three-phase field: (i) TBC compositions should be located as close as possible to the tie-line connecting *t*-ZrO_2 and *M'*-$RETaO_4$ without sacrificing phase stability, since these compositions exhibit optimal toughness, and (ii) compositional fluctuations in ZrO_2-$(Y/Yb)O_{1.5}$-$TaO_{2.5}$ EB-PVD coatings are not expected to severely impact the toughness of the coatings when the nominal composition is close to the *t* + *M'* tie-line, since the variation is oriented nearly along a line of constant *c*-ZrO_2 phase fraction.

The tests also showed that a number of previously unreported toughening mechanisms, such as crack deflection, grain bridging, and microcracking, contribute to the toughness of polycrystalline compacts. The toughening mechanisms arise from thermal stresses developed during cooling and the associated effects on crack propagation pathways (i.e.

transgranular vs. intergranular fracture). As a result, the microstructure of the material can significantly impact the measured toughness value. For example, the toughness of polycrystalline compacts based on the tetragonal phase varied from ~20-40 J/m^2. An important conclusion from this finding is that a significant fraction of the measured toughness of the tetragonal phase can be derived from toughening mechanisms other than ferroelastic switching, which has been the presumed mechanism responsible for the desirable toughness of 8YSZ and related tetragonal compositions, including the non-transformable tetragonal phase in the ZrO_2-$(Y/Yb)O_{1.5}$-$TaO_{2.5}$ systems.

The final investigation pursued microstructural evidence of ferroelastic toughening in the indented tetragonal compacts. Detailed TEM investigations revealed that at least some fraction of the tetragonal grains both near and far away from indentation cracks contain sub-micron, twin-related domains and each crystallite contains finer nanometer-sized domains. The domain structure forms during processing as a result of the short-range order between yttrium and tantalum cations in the tetragonal crystal structure. Although the existence of domains within the microstructure suggests that the material may be amenable to toughening by ferroelastic switching, direct evidence of switching was not found. Bulk regions of crystallites located far from and nearby indentation cracks have a similar proportion of the three tetragonal variants, suggesting that the crack stress field has not modified the microstructure. However, it is possible that switching occurs by movement of the macroscopic twin boundaries, in which case switching will not be evident from analysis of the microstructure following indentation.

The work presented in this dissertation has generated considerable insight into fundamental structure-processing-properties relationships in ZrO_2-$(Y/Yb)O_{1.5}$-$TaO_{2.5}$ thermal barrier

oxides and coatings. The overarching conclusion from the investigation is that single and multi-phase TBCs based on ZrO_2-$(Y/Yb)O_{1.5}$-$TaO_{2.5}$ compositions in the three-phase *t* + *c* + *M'* field have the potential to outperform current state-of-the-art *t'*-8YSZ coatings despite challenges encountered during vapor deposition and anticipated lower toughness. However, continued efforts to elucidate whether or not ferroelastic switching is operative in the non-transformable tetragonal phase are necessary to identify routes for improved toughness. *In-situ* mechanical testing in an SEM with STEM capabilities may prove useful in simultaneously monitoring the stress-strain response, position of twin boundaries, and fractions of each tetragonal variant. Even if domain switching does not occur at room temperature, the possibility remains that it may be feasible at elevated temperature. Therefore, mechanical tests should be performed at various temperatures. Monte Carlo simulations investigating the distribution of cations within the tetragonal phase at relevant compositions and temperatures may be valuable in understanding trends in the mechanical behavior with temperature, since it is expected that short-range order between RE^{3+} and Ta^{5+} becomes less prevalent with increasing temperature. The cumulative studies may expose tunable variables, either in composition (including both rare-earth type and concentration) or in structure, that can be engineered to increase toughness. Understanding the influence of structure is particularly important in light of the substantially different microstructure of EB-PVD coatings in the as-deposited state and the anticipated different microstructure of air plasma spray (APS) coatings, although the latter remains the subject of future work.

REFERENCES

[1] International Energy Agency, 2017).
[2] I. A. T. Association, (2017).
[3] Advanced Turbine Systems, https://www.energy.gov/fe/science-innovation/clean-coal-research/hydrogen-turbines.
[4] C. G. Levi, Curr Opin Solid St M **8**, 77 (2004).
[5] D. R. Clarke, M. Oechsner, and N. P. Padture, Mrs Bull **37**, 891 (2012).
[6] A. G. Evans, D. R. Clarke, and C. G. Levi, J Eur Ceram Soc **28**, 1405 (2008).
[7] R. Vassen, M. O. Jarligo, T. Steinke, D. E. Mack, and D. Stover, Surf Coat Tech **205**, 938 (2010).
[8] R. A. Miller, J. L. Smialek, and R. G. Garlick, in *Science and Technology of Zirconia*, edited by A. H. Heuer, and L. W. Hobbs (The American Ceramic Society Inc., Ohio, 1981), pp. 241.
[9] D. R. Clarke and C. G. Levi, Annu Rev Mater Res **33**, 383 (2003).
[10] D. M. Lipkin, J. A. Krogstad, Y. Gao, C. A. Johnson, W. A. Nelson, and C. G. Levi, J Am Ceram Soc **96**, 290 (2013).
[11] Y. Shen, R. M. Leckie, C. G. Levi, and D. R. Clarke, Acta Mater **58**, 4424 (2010).
[12] A. M. Limarga, S. Shian, R. M. Leckie, C. G. Levi, and D. R. Clarke, J Eur Ceram Soc **34**, 3085 (2014).
[13] D. J. Kim and T. Y. Tien, J Am Ceram Soc **74**, 3061 (1991).
[14] C. A. Macauley, A. N. Fernandez, J. V. Van Sluytman, and C. G. Levi, J Eur Ceram Soc **38**, 4523 (2018).
[15] C. A. Macauley, A. N. Fernandez, and C. G. Levi, J Eur Ceram Soc **37**, 4888 (2017).
[16] F. M. Pitek and C. G. Levi, Surf Coat Tech **201**, 6044 (2007).
[17] O. Fabrichnaya, C. Wang, M. Zinkevich, C. G. Levi, and F. Aldinger, J Phase Equilib Diff **26**, 591 (2005).
[18] O. Fabrichnaya and F. Aldinger, Z Metallkd **95**, 27 (2004).
[19] M. H. Chen, J. C. Thomas, A. R. Natarajan, and A. Van der Ven, Phys Rev B **94** (2016).
[20] R. D. Shannon, Acta Crystallogr A **32**, 751 (1976).
[21] P. Li, I. W. Chen, and J. E. Pennerhahn, J Am Ceram Soc **77**, 118 (1994).
[22] P. Li and I. W. Chen, J Am Ceram Soc **77**, 1281 (1994).
[23] P. Li, I. W. Chen, and J. E. Pennerhahn, J Am Ceram Soc **77**, 1289 (1994).
[24] S. M. Ho, Mater Sci Eng **54**, 23 (1982).
[25] M. Yoshimura, Am Ceram Soc Bull **67**, 1950 (1988).
[26] D. J. Kim, J. W. Jang, and H. L. Lee, J Am Ceram Soc **80**, 1453 (1997).
[27] J. A. Krogstad, M. Lepple, and C. G. Levi, Surf Coat Tech **221**, 44 (2013).
[28] D. J. Kim, J Am Ceram Soc **73**, 115 (1990).
[29] W. D. Kingery, H. K. Bowen, and D. R. Uhlmann, *Introduction to Ceramics* (Wiley Interscience, New York, 1976).
[30] J. F. Bisson, D. Fournier, M. Poulain, O. Lavigne, and R. Mevrel, J Am Ceram Soc **83**, 1993 (2000).
[31] W. D. Kingery, J. Francl, R. L. Coble, and T. Vasilos, J Am Ceram Soc **37**, 107 (1954).

[32] A. Kulkarni, A. Vaidya, A. Goland, S. Sampath, and H. Herman, Mat Sci Eng a-Struct **359**, 100 (2003).
[33] P. G. Klemens and M. Gell, Mat Sci Eng a-Struct **245**, 143 (1998).
[34] C. B. Vining, W. Laskow, J. O. Hanson, R. R. Vanderbeck, and P. D. Gorsuch, J Appl Phys **69**, 4333 (1991).
[35] E. S. Toberer, A. Zevalkink, and G. J. Snyder, J Mater Chem **21**, 15843 (2011).
[36] C. J. Vineis, A. Shakouri, A. Majumdar, and M. G. Kanatzidis, Adv Mater **22**, 3970 (2010).
[37] J. R. Nicholls, K. J. Lawson, A. Johnstone, and D. S. Rickerby, Surf Coat Tech **151**, 383 (2002).
[38] D. Zhu and R. A. Miller, Thermal Conductivity and Sintering Behavior of Advanced Thermal Barrier Coatings, 2002.
[39] P. G. Klemens, Physica B **263**, 102 (1999).
[40] J. W. Fergus, Metallurgical and Materials Transactions E **1**, 118 (2014).
[41] D. R. Clarke, Surf Coat Tech **163**, 67 (2003).
[42] M. R. Winter and D. R. Clarke, Acta Mater **54**, 5051 (2006).
[43] H. F. Liu, S. L. Li, Q. L. Li, Y. M. Li, and W. X. Zhou, Solid State Sci **13**, 513 (2011).
[44] X. W. Song, M. Xie, S. L. An, X. H. Hao, and R. D. Mu, Scripta Mater **62**, 879 (2010).
[45] S. Sampath, U. Schulz, M. O. Jarligo, and S. Kuroda, Mrs Bull **37**, 903 (2012).
[46] A. F. Renteria, B. Saruhan, U. Schulz, H. J. Raetzer-Scheibe, J. Haug, and A. Wiedemann, Surf Coat Tech **201**, 2611 (2006).
[47] D. Y. Shin and A. Hamed, Wear **396**, 34 (2018).
[48] J. A. Krogstad, S. Kramer, D. M. Lipkin, C. A. Johnson, D. R. G. Mitchell, J. M. Cairney, and C. G. Levi, J Am Ceram Soc **94**, S168 (2011).
[49] J. A. Krogstad, R. M. Leckie, S. Kramer, J. M. Cairney, D. M. Lipkin, C. A. Johnson, and C. G. Levi, J Am Ceram Soc **96**, 299 (2013).
[50] C. A. Macauley, UC Santa Barbara, 2016.
[51] H. Yokokawa, N. Sakai, T. Kawada, and M. Dokiya, J Am Ceram Soc **73**, 649 (1990).
[52] H. G. Scott, Acta Crystallogr **B**, 281 (1977).
[53] A. Rouanet, Rev. Int. Hautes Tempe´r. Re´fract. **8**, 161 (1971).
[54] R. Darolia, Int Mater Rev **58**, 315 (2013).
[55] A. G. Evans, N. A. Fleck, S. Faulhaber, N. Vermaak, M. Maloney, and R. Darolia, Wear **260**, 886 (2006).
[56] R. G. Wellman and J. R. Nicholls, J Phys D Appl Phys **40**, R293 (2007).
[57] N. A. Fleck and T. Zisis, Wear **268**, 1214 (2010).
[58] C. A. Johnson, J. A. Ruud, R. Bruce, and D. Wortman, Surf Coat Tech **108**, 80 (1998).
[59] R. W. Jackson and M. R. Begley, Int J Solids Struct **51**, 1364 (2014).
[60] P. M. Kelly and L. R. F. Rose, Prog Mater Sci **47**, 463 (2002).
[61] J. Chevalier, L. Gremillard, A. V. Virkar, and D. R. Clarke, J Am Ceram Soc **92**, 1901 (2009).
[62] R. H. J. Hannink, P. M. Kelly, and B. C. Muddle, J Am Ceram Soc **83**, 461 (2000).

[63] A. G. Evans, D. R. Clarke, and C. G. Levi, in *Turbine Aerodynamics, Heat Transfer, Materials, and Mechanics*, edited by T. I. P. Shih, and V. Yang (The American Institute of Aeronautics and Astronautics (AIAA), 2014).
[64] M. J. Maloney, in *Turbine Forum*Nice-Port St. Laurent, France, 2006).
[65] R. Vassen, E. Traeger, and D. Stover, Int J Appl Ceram Tec **1**, 351 (2004).
[66] E. M. Donohue, N. R. Philips, M. R. Begley, and C. G. Levi, Mat Sci Eng a-Struct **564**, 324 (2013).
[67] U. Schulz, B. Saruhan, K. Fritscher, and C. Leyens, Int J Appl Ceram Tec **1**, 302 (2004).
[68] S. Terry, UCSB, 2001.
[69] T. E. Strangman, Thin Solid Films **127**, 93 (1985).
[70] K. D. Sheffler and D. K. Gupta, J Eng Gas Turb Power **110**, 605 (1988).
[71] S. M. Meier and D. K. Gupta, J Eng Gas Turb Power **116**, 250 (1994).
[72] J. V. Van Sluytman, S. Kramer, V. K. Tolpygo, and C. G. Levi, Acta Mater **96**, 133 (2015).
[73] A. G. Evans, J Am Ceram Soc **73**, 187 (1990).
[74] G. V. Srinivasan, J. F. Jue, S. Y. Kuo, and A. V. Virkar, J Am Ceram Soc **72**, 2098 (1989).
[75] T. A. Schaedler, R. M. Leckie, S. Kramer, A. G. Evans, and C. G. Levi, J Am Ceram Soc **90**, 3896 (2007).
[76] C. Mercer, J. R. Williams, D. R. Clarke, and A. G. Evans, P R Soc A **463**, 1393 (2007).
[77] A. Foitzik, M. Statwald-Klenke, and M. Ruhle, Z. Metallkd **84**, 397 (1993).
[78] D. Baither, M. Bartsch, B. Baufeld, A. Tikhonovsky, A. Foitzik, M. Ruhle, and U. Messerschmidt, J Am Ceram Soc **84**, 1755 (2001).
[79] D. Michel, L. Mazerolles, and M. P. Y. Jorba, J Mater Sci **18**, 2618 (1983).
[80] A. M. Bolon and M. M. Gentleman, J Am Ceram Soc **94**, 4478 (2011).
[81] C. Carbogno, C. G. Levi, C. G. Van de Walle, and M. Scheffler, Phys Rev B **90** (2014).
[82] C. J. Chan, F. F. Lange, M. Ruhle, J. F. Jue, and A. V. Virkar, J Am Ceram Soc **74**, 807 (1991).
[83] C. M. Phillippi and K. S. Mazdiyasni, J Am Ceram Soc **54**, 254 (1971).
[84] B. R. Lawn, *Fracture of Brittle Solids - Second Edition* (Cambridge University Press, 1993).
[85] G. R. Anstis, P. Chantikul, B. R. Lawn, and D. B. Marshall, J Am Ceram Soc **64**, 533 (1981).
[86] Z. Burghard, A. Zimmermann, J. Rodel, F. Aldinger, and B. R. Lawn, Acta Mater **52**, 293 (2004).
[87] Y. Du, Z. P. Jin, and P. Y. Huang, J Am Ceram Soc **74**, 1569 (1991).
[88] E. Tani, M. Yoshimura, and S. Somiya, J Am Ceram Soc **66**, 506 (1983).
[89] K. Wang, C. H. Li, H. Q. Dong, X. S. Ye, X. G. Lu, and W. Z. Ding, Metall Mater Trans A **41a**, 3525 (2010).
[90] M. H. Ciftcioglu and M. J. Mayo, Mater Res Soc Symp P **196**, 77 (1990).
[91] M. J. Mayo, Int Mater Rev **41**, 85 (1996).
[92] U. Anselmi-Tamburini, J. E. Garay, and Z. A. Munir, Scripta Mater **54**, 823 (2006).
[93] K. Lu, Int Mater Rev **53**, 21 (2008).

[94] D. R. Clarke and F. Adar, J Am Ceram Soc **65**, 284 (1982).
[95] A. International, West Conshohocken, PA.
[96] J. C. Thomas and A. Van der Ven, Phys Rev B **88** (2013).
[97] B. Puchala and A. Van der Ven, Phys Rev B **88** (2013).
[98] A. Van der Ven, J. C. Thomas, Q. C. Xu, and J. Bhattacharya, Math Comput Simulat **80**, 1393 (2010).
[99] G. Kresse and J. Hafner, Phys Rev B **49**, 14251 (1994).
[100] G. Kresse and J. Furthmuller, Comp Mater Sci **6**, 15 (1996).
[101] G. Kresse and J. Furthmuller, Phys Rev B **54**, 11169 (1996).
[102] G. Kresse, J Non-Cryst Solids **193**, 222 (1995).
[103] J. P. Perdew, K. Burke, and M. Ernzerhof, Phys Rev Lett **77**, 3865 (1996).
[104] G. Kresse and D. Joubert, Phys Rev B **59**, 1758 (1999).
[105] P. E. Blochl, Phys Rev B **50**, 17953 (1994).
[106] H. J. Monkhorst and J. D. Pack, Phys Rev B **13**, 5188 (1976).
[107] H. T. Stokes and D. M. Hatch, Journal of Applied Crystallography, 237 (2004).
[108] S. A. Mather and P. K. Davies, J Am Ceram Soc **78**, 2737 (1995).
[109] J. C. Thomas and A. Van der Ven, Phys Rev B **96** (2017).
[110] S. H. Guan, X. J. Zhang, and Z. P. Liu, J Am Chem Soc **137**, 8010 (2015).
[111] J. C. Thomas and A. Van der Ven, J Mech Phys Solids **107**, 76 (2017).
[112] J. Feng, S. Shian, B. Xiao, and D. R. Clarke, Phys Rev B **90** (2014).
[113] A. H. Larsen *et al.*, J Phys-Condens Mat **29**, 273002 (2017).
[114] R. Hoppe, Z Kristallogr **150**, 23 (1979).
[115] G. M. Wolten, Acta Crystall B-Stru **B 24**, 463 (1968).
[116] S. Shian, P. Sarin, M. Gurak, M. Baram, W. M. Kriven, and D. R. Clarke, Acta Mater **69**, 196 (2014).
[117] J. Bhattacharya and A. Van der Ven, Acta Mater **56**, 4226 (2008).
[118] H. P. Rooksby and E. A. D. White, Acta Crystallogr **16**, 888 (1963).
[119] L. H. Brixner and H. Y. Chen, J Electrochem Soc **130**, 2435 (1983).
[120] U. Schulz, B. Saint-Ramond, O. Lavigne, P. Moreno, A. vanLieshout, and A. Borger, in *28th International Conference on Advanced Ceramics and Composites: B* (The American Ceramic Society, Cocoa Beach, Florida, 2004).
[121] U. Schulz, S. G. Terry, and C. G. Levi, Mat Sci Eng a-Struct **360**, 319 (2003).
[122] H. Zhao, University of Virginia, 2009.
[123] H. B. Zhao, C. G. Levi, and H. N. G. Wadley, Surf Coat Tech **251**, 74 (2014).
[124] B. Saruhan, P. Francois, K. Fritscher, and U. Schulz, Surf Coat Tech **182**, 175 (2004).
[125] D. S. Almeida, C. R. M. Silva, M. C. A. Nono, and C. A. A. Cairo, Surf Coat Tech **200**, 2827 (2006).
[126] U. Schulz, K. Fritscher, C. Leyens, M. Peters, and W. A. Kaysser, Materialwiss Werkst **28**, 370 (1997).
[127] O. Unal, T. E. Mitchell, and A. H. Heuer, J Am Ceram Soc **77**, 984 (1994).
[128] J. M.W. Chase, C. A. Davies, J. J.R. Downey, D. J. Frurip, R. A. McDonald, and A. N. Syverud, edited by N. I. o. S. a. Technology1998).
[129] N. S. Jacobson, edited by NASACleveland, Ohio, 1989), p. 61.
[130] E. N. Kablov, V. L. Stolyarova, V. A. Vorozhtcov, S. I. Lopatin, O. B. Fabrichnaya, M. O. Ilatovskaya, and F. N. Karachevtsev, Rapid Commun Mass Sp **32**, 686 (2018).

[131] J. K. Gibson, J Phys Chem-Us **98**, 6063 (1994).
[132] J. M. Cairney, N. R. Rebollo, M. Ruhle, and C. G. Levi, Int J Mater Res **98**, 1177 (2007).
[133] J. A. Thornton, Annu Rev Mater Sci **7**, 239 (1977).
[134] U. Schulz, K. Fritscher, and M. Peters, Surf Coat Tech **82**, 259 (1996).
[135] S. M. Lakiza and L. M. Lopato, J Am Ceram Soc **80**, 893 (1997).
[136] S. M. Lakiza, Z. O. Zaitseva, and L. M. Lopato, Powder Metall Met C+ **47**, 338 (2008).
[137] Y. Yokogawa and M. Yoshimura, J Am Ceram Soc **74**, 2077 (1991).
[138] D. S. Almeida, C. R. M. Silva, M. C. A. Nono, and C. A. A. Cairo, Mat Sci Eng a-Struct **443**, 60 (2007).
[139] S. Raghavan, H. Wang, W. D. Porter, R. B. Dinwiddie, and M. J. Mayo, Acta Mater **49**, 169 (2001).
[140] B. Leclercq, R. Mevrel, V. Liedtke, and W. Hohenauer, Materialwiss Werkst **34**, 406 (2003).
[141] S. Raghavan, H. Wang, R. B. Dinwiddie, W. D. Porter, R. Vassen, D. Stover, and M. J. Mayo, J Am Ceram Soc **87**, 431 (2004).
[142] B. Leclercq, R. Mevrel, A. Azzopardi, A. Malie, and B. Saint-Ramond, edited by U. P. OfficeUSA, 2008).
[143] V. K. Tolpygo and W. Baker, (Honeywell International Inc., USA, 2017), p. 7.
[144] L. L. Sun, H. B. Guo, H. Peng, S. K. Gong, and H. B. Xu, Prog Nat Sci-Mater **23**, 440 (2013).
[145] Q. L. Li, X. Z. Cui, S. Q. Li, W. H. Yang, C. Wang, and Q. Cao, J Therm Spray Techn **24**, 136 (2015).
[146] V. K. Tolpygo, (Honeywell International Inc., USA, 2013), p. 10.
[147] A. Kulkarni *et al.*, Mat Sci Eng a-Struct **426**, 43 (2006).
[148] A. F. Renteria, B. Saruhan, J. Ilavsky, and A. J. Allen, Surf Coat Tech **201**, 4781 (2007).
[149] Y. Zhou, Q. L. Ge, T. C. Lei, and T. Sakuma, J Mater Sci **26**, 4461 (1991).
[150] Y. Shen and D. R. Clarke, J Am Ceram Soc **93**, 2024 (2010).
[151] D. R. Clarke, 2016).
[152] C. G. Levi, J. W. Hutchinson, M. H. Vidal-Setif, and C. A. Johnson, Mrs Bull **37**, 932 (2012).
[153] J. A. Haynes, B. A. Pint, W. D. Porter, and I. G. Wright, Mater High Temp **21**, 87 (2004).
[154] G. N. Heintze and R. Mcpherson, Surf Coat Tech **36**, 125 (1988).
[155] G. N. Heintze and R. Mcpherson, Surf Coat Tech **34**, 15 (1988).
[156] E. Y. Sun, P. F. Becher, K. P. Plucknett, C. H. Hsueh, K. B. Alexander, S. B. Waters, K. Hirao, and M. E. Brito, J Am Ceram Soc **81**, 2831 (1998).
[157] A. Ziegler, J. C. Idrobo, M. K. Cinibulk, C. Kisielowski, N. D. Browning, and R. O. Ritchie, Science **306**, 1768 (2004).
[158] N. P. Padture, J Am Ceram Soc **77**, 519 (1994).
[159] Y. Fu and A. G. Evans, Acta Metall Mater **30**, 1619 (1982).
[160] G. Vekinis, M. F. Ashby, and P. W. R. Beaumont, Acta Metallurgica Et Materialia **38**, 1151 (1990).
[161] D. Bleise and R. W. Steinbrech, J Am Ceram Soc **77**, 315 (1994).

[162] K. T. Faber and A. G. Evans, Acta Metall Mater **31**, 565 (1983).
[163] K. T. Faber and A. G. Evans, Acta Metall Mater **31**, 577 (1983).
[164] K. T. Faber, T. Iwagoshi, and A. Ghosh, J Am Ceram Soc **71**, C (1988).
[165] W. H. Gu, K. T. Faber, and R. W. Steinbrech, Acta Metallurgica et Materialia **40**, 3121 (1992).
[166] R. W. Steinbrech, J Eur Ceram Soc **10**, 131 (1992).
[167] D. K. M. Shum and J. W. Hutchinson, Mechanics of Materials **9**, 83 (1990).
[168] S. G. Heinze, A. R. Natarajan, C. G. Levi, and A. Van der Ven, Phys Rev Mater **2** (2018).
[169] J. V, M. Degraef, and C. G. Levi, Acta Metallurgica Et Materialia **42**, 1829 (1994).
[170] M. Legros, D. S. Gianola, and C. Motz, Mrs Bull **35**, 354 (2010).
[171] P. Callahan, J.-C. Stinville, E. Yao, M. P. Echlin, J. Shin, F. Wang, M. D. Graef, T. M. Pollock, and D. S. Gianola, Microscopy and Microanalysis **24**, 1836 (2018).
[172] P. G. Callahan, J. C. Stinville, E. R. Yao, M. P. Echlin, M. S. Titus, M. De Graef, D. S. Gianola, and T. M. Pollock, Ultramicroscopy **186**, 49 (2018).
[173] J. Tracy, A. Waas, and S. Daly, J Am Ceram Soc **98**, 1898 (2015).